

UNIVERSITY OF BELGRADE
FACULTY OF MECHANICAL ENGINEERING

Hamad AlKaabi

Aerodynamic Characteristics of Axi-
Symmetric Bodies in Non-Symmetric
Flow Fields

Ph.D. Dissertation
Belgrade, 2018.

УНИВЕРЗИТЕТ У БЕОГРАДУ
МАШИНСКИ ФАКУЛТЕТ БЕОГРАД

Hamad AlKaabi

АЕРОДИНАМИЧКЕ КАРАКТЕРИСТИКЕ
ОСНОСИМЕТРИЧНИХ ТЕЛА У НЕСИМЕТ-
РИЧНОМ СТРУЈНОМ ПОЉУ

Докторска дисертација

Београд, 2018.



Подаци о ментору и члановима комисије

Ментор: др Златко Петровић, редовни професор у пензији,
Универзитет у Београду, Машински факултет Београд

Комисија:

др Александар Симоновић, редовни професор, Универзитет у
Београду, Машински факултет Београд

др Иван Костић, редовни професор, Универзитет у Београду,
Машински факултет Београд

др Огњен Пековић, доцент, Универзитет у Београду, Машински
факултет Београд

др Слободан Ступар, редовни професор у пензији, Универзитет у
Београду, Машински факултет Београд

Датум одбране:



Aerodynamic Characteristics of Axi-Symmetric Bodies in Non-Symmetric Flow Fields

Summary: Governing equations for turbulent flows are reviewed. Spalart Allmaras turbulence model has been selected for aerodynamic calculations. Computation is performed on the adaptive computational grid. Pressure based method for computational convergence was selected. Computations were performed for various angles of attack and various command surface deflections. Calculated results were compared with results obtained by wind tunnel testing. Experimental setup and experimental model are described. Results are presented by aerodynamic coefficients and contour lines of the Mach numbers, pressures and velocities.

Keywords: Aerodynamic coefficients, Computational methods, Missile dynamics, Wind tunnel measurements.

Scientific Field: Mechanical engineering

Scientific Subfield: Missile Aerodynamics

UDK: 533.6.013.07:532.517.4(043.3)



Аеродинамичке карактеристике осносиметричних тела у несиметричном струјном пољу

Резиме: Приказане су основне једначине турбулентног струјања. Презентована је и примењена метода Спаларта и Алмараса. Прорачун је вршен на адаптивној прорачунској мрежи. Једначина по притиску је коришћена за остваривање конвергенције решења. Извршени су прорачуни за различите нападне углове и различите отклоне командних површина. Резултати добијени прорачуном су упоређени са резултатима добијеним аеротунелским мерењима. Описано је експериментално постројење и модел испитивања. Резултати су приказани дијаграмима аеродинамичких коефицијената и дијаграмима расподеле брзине, притиска и махових бројева.

Кључне речи: Аеродинамички коефицијенти, Динамика ракете, Аеротунелска мерења, Прорачунски методи.

Научна област: Машинство

Ужа научна област: Ваздухопловство

УДК: 533.6.013.07:532.517.4 (043.3)



Table of Contents

Contents

Table of Contents.....	I
List of Figures.....	IV
Acknowledgments.....	1
Abstract.....	2
1. Introduction.....	3
2. Governing Equations.....	5
2.1. Pressure based.....	5
2.2. Turbulence model - Spalart-Allmaras.....	7
2.3. Grid Adaptation.....	9
3. Axis Symmetric Body Application.....	15
3.1. Simulation conditions.....	15
3.1.1. Sign Convention for Control Surfaces.....	15
3.2. CAD Model preparation.....	16
3.2.1. Configuration Description.....	17
3.2.2. Model Technical Drawing.....	18
3.2.3. Model Simplification.....	18
3.3. Simulation setup.....	20
3.3.1. Domain definition.....	20
3.3.1.1. Boundary conditions.....	21
3.3.2. Baseline mesh.....	22
3.3.3. Air flow characteristics.....	27
3.3.4. Steady state flow.....	28
3.3.5. Turbulence model.....	28
3.4. Mesh adaptation.....	28
3.4.1. Pressure gradient method.....	29
4. Results Presentation.....	31
4.1. Coefficients.....	32
4.1.1. Pitch moment coefficients.....	32



4.1.2.	Normal force coefficients.....	33
4.1.3.	Axial force coefficients.....	34
4.1.4.	Roll Moment coefficients.....	35
4.2.	Contours.....	36
4.2.1.	Mach number contours.....	36
4.2.1.1.	No deflection.....	37
4.2.1.2.	10 degrees deflection.....	48
4.2.1.3.	15 degrees deflection.....	68
4.2.2.	Pressure contours.....	88
4.2.2.1.	No deflection.....	89
4.2.2.2.	10 degrees deflection.....	105
4.2.2.3.	15 degrees deflection.....	129
5.	Experiment Set up.....	153
5.1.	Wind tunnel facility.....	153
5.2.	Wind tunnel testing section.....	154
5.3.	Wind tunnel testing results.....	155
5.3.1.	Pitch moment coefficients.....	155
5.3.2.	Normal force coefficients.....	156
5.3.3.	Axial force coefficients.....	158
5.3.4.	Roll moment coefficients.....	159
6.	Semi Empirical Methods.....	160
6.1.	Missile DATCOM.....	164
6.1.1.	Pitch Moment Coefficients.....	164
6.1.2.	Normal Force Coefficients.....	165
6.1.3.	Axial Force Coefficients.....	166
7.	Results Comparison.....	167
7.1.	No deflection.....	168
7.2.	10 degrees deflection.....	172
7.3.	15 degrees deflection.....	176
8.	Conclusions.....	180
9.	References.....	182



10. Appendix A.....	185
10.1. Velocity contours.....	185
10.1.1. No deflection.....	185
10.1.2. 10 degrees deflection.....	190
10.1.3. 15 degrees deflection.....	196



List of Figures

Figure 1	First order difference of density.....	11
Figure 2	Second order difference of density.....	11
Figure 3	First order difference of pressure.....	12
Figure 4	Second order difference of pressure.....	12
Figure 5	First order difference of velocity.....	13
Figure 6	Second order difference of velocity.....	13
Figure 7	First order difference of entropy.....	14
Figure 8	Second order difference of entropy.....	14
Figure 9	Rear view of the positive pitch control deflection.....	16
Figure 10	CAD model of the simulated missile.....	17
Figure 11	Missile technical drawing.....	18
Figure 12	Control surface airfoil cross section.....	19
Figure 13	Optimized control surface airfoil section.....	19
Figure 14	Flow domain with boundary conditions.....	21
Figure 15	Baseline mesh sizing and volume table report.....	23
Figure 16	General baseline mesh controls.....	24
Figure 17	Advanced baseline mesh controls.....	26
Figure 18	Baseline mesh named selections.....	26
Figure 19	Baseline mesh side view.....	27
Figure 20	Baseline mesh before adaptation.....	30
Figure 21	Baseline mesh with cells of required refinement.....	30
Figure 22	Adapted mesh.....	31
Figure 23	CFD pitch moment coefficients.....	33
Figure 24	CFD normal force coefficients.....	34
Figure 25	CFD axial force coefficients.....	35
Figure 26	CFD roll moment coefficients.....	36
Figure 27	Mach number contours for 0 ° control deflection and angle of attack $\alpha = 0^\circ$	38
Figure 28	Mach number contours for 0 ° control deflection and angle of attack $\alpha = 2^\circ$	39
Figure 29	Mach number contours for 0 ° control deflection and angle of attack $\alpha = -2^\circ$	40
Figure 30	Mach number contours for 0 ° control deflection and angle of attack $\alpha = 4^\circ$	41
Figure 31	Mach number contours for 0 ° control deflection and angle of attack $\alpha = -4^\circ$	42
Figure 32	Mach number contours for 0 ° control deflection and angle of attack $\alpha = 6^\circ$	43
Figure 33	Mach number contours for 0 ° control deflection and angle of attack $\alpha = -6^\circ$	44



Figure 34 Mach number contours for 0 ° control deflection and angle of attack $\alpha = 8^\circ$	45
Figure 35 Mach number contours for 0 ° control deflection and angle of attack $\alpha = -8^\circ$	46
Figure 36 Mach number contours for 0 ° control deflection and angle of attack $\alpha = 10^\circ$	47
Figure 37 Mach number contours for 0 ° control deflection and angle of attack $\alpha = -10^\circ$	48
Figure 38 Mach number contours for 10 ° control deflection and angle of attack $\alpha = 0^\circ$	49
Figure 39 Mach number contours for 10 ° control deflection and angle of attack $\alpha = 2^\circ$	51
Figure 40 Mach number contours for 10 ° control deflection and angle of attack $\alpha = -2^\circ$	53
Figure 41 Mach number contours for 10 ° control deflection and angle of attack $\alpha = 4^\circ$	55
Figure 42 Mach number contours for 10 ° control deflection and angle of attack $\alpha = -4^\circ$	57
Figure 43 Mach number contours for 10 ° control deflection and angle of attack $\alpha = 6^\circ$	59
Figure 44 Mach number contours for 10 ° control deflection and angle of attack $\alpha = -6^\circ$	61
Figure 45 Mach number contours for 10 ° control deflection and angle of attack $\alpha = 8^\circ$	63
Figure 46 Mach number contours for 10 ° control deflection and angle of attack $\alpha = -8^\circ$	65
Figure 47 Mach number contours for 10 ° control deflection and angle of attack $\alpha = 10^\circ$	66
Figure 48 Mach number contours for 10 ° control deflection and angle of attack $\alpha = -10^\circ$	68
Figure 49 Mach number contours for 15 ° control deflection and angle of attack $\alpha = 0^\circ$	69
Figure 50 Mach number contours for 15 ° control deflection and angle of attack $\alpha = 2^\circ$	71
Figure 51 Mach number contours for 15 ° control deflection and angle of attack $\alpha = -2^\circ$	73
Figure 52 Mach number contours for 15 ° control deflection and angle of attack $\alpha = 4^\circ$	75
Figure 53 Mach number contours for 15 ° control deflection and angle of attack $\alpha = -4^\circ$	77
Figure 54 Mach number contours for 15 ° control deflection and angle of attack $\alpha = 6^\circ$	79
Figure 55 Mach number contours for 15 ° control deflection and angle of attack $\alpha = -6^\circ$	81



Figure 56 Mach number contours for 15 ° control deflection and angle of attack $\alpha = 8^\circ$	83
Figure 57 Mach number contours for 15 ° control deflection and angle of attack $\alpha = -8^\circ$	85
Figure 58 Mach number contours for 15 ° control deflection and angle of attack $\alpha = 10^\circ$	86
Figure 59 Mach number contours for 15 ° control deflection and angle of attack $\alpha = -10^\circ$	88
Figure 60 Static pressure contours for 0 ° control deflection and angle of attack $\alpha = 0^\circ$	89
Figure 61 Static pressure distribution along missile for 0 ° control deflection and angle of attack $\alpha = 0^\circ$	90
Figure 62 Static pressure contours for 0 ° control deflection and angle of attack $\alpha = 2^\circ$	91
Figure 63 Static pressure distribution along missile for 0 ° control deflection and angle of attack $\alpha = 2^\circ$	91
Figure 64 Static pressure contours for 0 ° control deflection and angle of attack $\alpha = -2^\circ$	92
Figure 65 Static pressure distribution along missile for 0 ° control deflection and angle of attack $\alpha = -2^\circ$	93
Figure 66 Static pressure contours for 0 ° control deflection and angle of attack $\alpha = 4^\circ$	94
Figure 67 Static pressure distribution along missile for 0 ° control deflection and angle of attack $\alpha = 4^\circ$	94
Figure 68 Static pressure contours for 0 ° control deflection and angle of attack $\alpha = -4^\circ$	95
Figure 69 Static pressure distribution along missile for 0 ° control deflection and angle of attack $\alpha = -4^\circ$	96
Figure 70 Static pressure contours for 0 ° control deflection and angle of attack $\alpha = 6^\circ$	97
Figure 71 Static pressure distribution along missile for 0 ° control deflection and angle of attack $\alpha = 6^\circ$	97
Figure 72 Static pressure contours for 0 ° control deflection and angle of attack $\alpha = -6^\circ$	98
Figure 73 Static pressure distribution along missile for 0 ° control deflection and angle of attack $\alpha = -6^\circ$	99
Figure 74 Static pressure contours for 0 ° control deflection and angle of attack $\alpha = 8^\circ$	100
Figure 75 Static pressure distribution along missile for 0 ° control deflection and angle of attack $\alpha = 8^\circ$	100
Figure 76 Static pressure contours for 0 ° control deflection and angle of attack $\alpha = -8^\circ$	101
Figure 77 Static pressure distribution along missile for 0 ° control deflection and angle of attack $\alpha = -8^\circ$	102



Figure 78 Static pressure contours for 0 ° control deflection and angle of attack $\alpha = 10^\circ$	103
Figure 79 Static pressure distribution along missile for 0 ° control deflection and angle of attack $\alpha = 10^\circ$	103
Figure 80 Static pressure contours for 0 ° control deflection and angle of attack $\alpha = -10^\circ$	104
Figure 81 Static pressure distribution along missile for 0 ° control deflection and angle of attack $\alpha = -10^\circ$	105
Figure 82 Static pressure contours for 10 ° control deflection and angle of attack $\alpha = 0^\circ$	106
Figure 83 Static pressure distribution along missile for 10 ° control deflection and angle of attack $\alpha = 0^\circ$	107
Figure 84 Static pressure contours for 10 ° control deflection and angle of attack $\alpha = 2^\circ$	108
Figure 85 Static pressure distribution along missile for 10 ° control deflection and angle of attack $\alpha = 2^\circ$	109
Figure 86 Static pressure contours for 10 ° control deflection and angle of attack $\alpha = -2^\circ$	111
Figure 87 Static pressure distribution along missile for 10 ° control deflection and angle of attack $\alpha = -2^\circ$	111
Figure 88 Static pressure contours for 10 ° control deflection and angle of attack $\alpha = 4^\circ$	113
Figure 89 Static pressure distribution along missile for 10 ° control deflection and angle of attack $\alpha = 4^\circ$	114
Figure 90 Static pressure contours for 10 ° control deflection and angle of attack $\alpha = -4^\circ$	115
Figure 91 Static pressure distribution along missile for 10 ° control deflection and angle of attack $\alpha = -4^\circ$	116
Figure 92 Static pressure contours for 10 ° control deflection and angle of attack $\alpha = 6^\circ$	117
Figure 93 Static pressure distribution along missile for 10 ° control deflection and angle of attack $\alpha = 6^\circ$	118
Figure 94 Static pressure contours for 10 ° control deflection and angle of attack $\alpha = -6^\circ$	119
Figure 95 Static pressure distribution along missile for 10 ° control deflection and angle of attack $\alpha = -6^\circ$	120
Figure 96 Static pressure contours for 10 ° control deflection and angle of attack $\alpha = 8^\circ$	122
Figure 97 Static pressure distribution along missile for 10 ° control deflection and angle of attack $\alpha = 8^\circ$	122
Figure 98 Static pressure contours for 10 ° control deflection and angle of attack $\alpha =$	124
Figure 99 Static pressure distribution along missile for 10 ° control deflection and angle of attack $\alpha = -8^\circ$	125



Figure 100 Static pressure contours for 10 ° control deflection and angle of attack $\alpha = 10^\circ$	126
Figure 101 Static pressure distribution along missile for 10 ° control deflection and angle of attack $\alpha = 10^\circ$	127
Figure 102 Static pressure contours for 10 ° control deflection and angle of attack $\alpha = -10^\circ$	128
Figure 103 Static pressure distribution along missile for 10 ° control deflection and angle of attack $\alpha = -10^\circ$	129
Figure 104 Static pressure contours for 15 ° control deflection and angle of attack $\alpha = 0^\circ$	130
Figure 105 Static pressure distribution along missile for 15 ° control deflection and angle of attack $\alpha = 0^\circ$	130
Figure 106 Static pressure contours for 15 ° control deflection and angle of attack $\alpha = 2^\circ$	132
Figure 107 Static pressure distribution along missile for 15 ° control deflection and angle of attack $\alpha = 2^\circ$	133
Figure 108 Static pressure contours for 15 ° control deflection and angle of attack $\alpha = -2^\circ$	134
Figure 109 Static pressure distribution along missile for 15 ° control deflection and angle of attack $\alpha = -2^\circ$	135
Figure 110 Static pressure contours for 15 ° control deflection and angle of attack $\alpha = 4^\circ$	136
Figure 111 Static pressure distribution along missile for 15 ° control deflection and angle of attack $\alpha = 4^\circ$	137
Figure 112 Static pressure contours for 15 ° control deflection and angle of attack $\alpha = -4^\circ$	138
Figure 113 Static pressure distribution along missile for 15 ° control deflection and angle of attack $\alpha = -4^\circ$	139
Figure 114 Static pressure contours for 15 ° control deflection and angle of attack $\alpha = 6^\circ$	140
Figure 115 Static pressure distribution along missile for 15 ° control deflection and angle of attack $\alpha = 6^\circ$	141
Figure 116 Static pressure contours for 15 ° control deflection and angle of attack $\alpha = -6^\circ$	143
Figure 117 Static pressure distribution along missile for 15 ° control deflection and angle of attack $\alpha = -6^\circ$	144
Figure 118 Static pressure contours for 15 ° control deflection and angle of attack $\alpha = 8^\circ$	145
Figure 119 Static pressure distribution along missile for 15 ° control deflection and angle of attack $\alpha = 8^\circ$	146
Figure 120 Static pressure contours for 15 ° control deflection and angle of attack $\alpha = -8^\circ$	147
Figure 121 Static pressure distribution along missile for 15 ° control deflection and angle of attack $\alpha = -8^\circ$	148



Figure 122 Static pressure contours for 15 ° control deflection and angle of attack $\alpha = 10^\circ$	149
Figure 123 Static pressure distribution along missile for 15 ° control deflection and angle of attack $\alpha = 10^\circ$	150
Figure 124 Static pressure contours for 15 ° control deflection and angle of attack $\alpha = -10^\circ$	152
Figure 125 Static pressure distribution along missile for 15 ° control deflection and angle of attack $\alpha = -10^\circ$	153
Figure 126 External view of the wind tunnel facility.....	154
Figure 127 Test section view during experiment preparation.....	155
Figure 128 Wind tunnel pitch moment coefficients.....	156
Figure 129 Wind tunnel normal force coefficients.....	157
Figure 130 Wind tunnel normal force coefficients - zoomed.....	157
Figure 131 Wind tunnel axial force coefficients.....	158
Figure 132 Wind tunnel roll moment coefficients.....	159
Figure 133 Lift coefficient for Missile DATCOM vs. other methods	161
Figure 134 Drag coefficient for Missile DATCOM vs. other methods	162
Figure 135 Pitch moment coefficient for Missile DATCOM vs. other methods.....	163
Figure 136 Missile DATCOM model	164
Figure 137 Missile DATCOM pitch moment coefficients	165
Figure 138 Missile DATCOM normal force coefficients	166
Figure 139 Missile DATCOM axial force coefficients.....	167
Figure 140 Normal force coefficient comparison for 0 ° control surface deflection.....	169
Figure 141 Pitch moment coefficient comparison for 0 ° control surface deflection.....	170
Figure 142 Axial force coefficient comparison for 0 ° control surface deflection.....	171
Figure 143 Roll moment coefficient comparison for 0 ° control surface deflection.....	172
Figure 144 Normal force coefficient comparison for 10 ° control surface deflection.....	173
Figure 145 Pitch moment coefficient comparison for 10 ° control surface deflection.....	174
Figure 146 Axial Force coefficient comparison for 10 ° control surface deflection.....	175
Figure 147 Roll moment coefficient comparison for 10 ° control surface deflection.....	176
Figure 148 Normal force coefficient comparison for 15 ° control surface deflection.....	177
Figure 149 Pitch moment coefficient comparison for 15 ° control surface deflection.....	178



Figure 150 Axial force coefficient comparison for 15 ° control surface deflection.....	179
Figure 151 Velocity contours for 0 ° control deflection and angle of attack $\alpha = 0^\circ$	185
Figure 152 Velocity contours for 0 ° control deflection and angle of attack $\alpha = 2^\circ$	185
Figure 153 Velocity contours for 0 ° control deflection and angle of attack $\alpha = -2^\circ$	186
Figure 154 Velocity contours for 0 ° control deflection and angle of attack $\alpha = 4^\circ$	186
Figure 155 Velocity contours for 0 ° control deflection and angle of attack $\alpha = -4^\circ$	187
Figure 156 Velocity contours for 0 ° control deflection and angle of attack $\alpha = 6^\circ$	187
Figure 157 Velocity contours for 0 ° control deflection and angle of attack $\alpha = -6^\circ$	188
Figure 158 Velocity contours for 0 ° control deflection and angle of attack $\alpha = 8^\circ$	188
Figure 159 Velocity contours for 0 ° control deflection and angle of attack $\alpha = -8^\circ$	189
Figure 160 Velocity contours for 0 ° control deflection and angle of attack $\alpha = 10^\circ$	189
Figure 161 Velocity contours for 0 ° control deflection and angle of attack $\alpha = -10^\circ$	190
Figure 162 Velocity contours for 10 ° control deflection and angle of attack $\alpha = 0^\circ$	190
Figure 163 Velocity contours for 10 ° control deflection and angle of attack $\alpha = 2^\circ$	191
Figure 164 Velocity contours for 10 ° control deflection and angle of attack $\alpha = -2^\circ$	191
Figure 165 Velocity contours for 10 ° control deflection and angle of attack $\alpha = 4^\circ$	192
Figure 166 Velocity contours for 10 ° control deflection and angle of attack $\alpha = -4^\circ$	192
Figure 167 Velocity contours for 10 ° control deflection and angle of attack $\alpha = 6^\circ$	193
Figure 168 Velocity contours for 10 ° control deflection and angle of attack $\alpha = -6^\circ$	193
Figure 169 Velocity contours for 10 ° control deflection and angle of attack $\alpha = 8^\circ$	194
Figure 170 Velocity contours for 10 ° control deflection and angle of attack $\alpha = -8^\circ$	194
Figure 171 Velocity contours for 10 ° control deflection and angle of attack $\alpha = 10^\circ$	195



Figure 172 Velocity contours for 10 ° control deflection and angle of attack $\alpha = -10^\circ$	195
Figure 173 Velocity contours for 15 ° control deflection and angle of attack $\alpha = 0^\circ$	196
Figure 174 Velocity contours for 15 ° control deflection and angle of attack $\alpha = 2^\circ$	196
Figure 175 Velocity contours for 15 ° control deflection and angle of attack $\alpha = -2^\circ$	197
Figure 176 Velocity contours for 15 ° control deflection and angle of attack $\alpha = 4^\circ$	197
Figure 177 Velocity contours for 15 ° control deflection and angle of attack $\alpha = -4^\circ$	198
Figure 178 Velocity contours for 15 ° control deflection and angle of attack $\alpha = 6^\circ$	198
Figure 179 Velocity contours for 15 ° control deflection and angle of attack $\alpha = -6^\circ$	199
Figure 180 Velocity contours for 15 ° control deflection and angle of attack $\alpha = 8^\circ$	199
Figure 181 Velocity contours for 15 ° control deflection and angle of attack $\alpha = -8^\circ$	200
Figure 182 Velocity contours for 15 ° control deflection and angle of attack $\alpha = 10^\circ$	200
Figure 183 Velocity contours for 15 ° control deflection and angle of attack $\alpha = -10^\circ$	201



Acknowledgments

I would like to take this opportunity to extend my appreciation and gratitude to their Highnesses The Leaders of The United Arab Emirates for their continuous support throughout my whole educational journey. Their continuous motivation has always boosted me to do my best for the United Arab Emirates. Moreover, I would like to thank Emirates Advanced Research and Technology Holdings for their support in completing this study.

Special thanks to all my family members who stood by my side during this journey. Without them I will never be where I am right now. In addition, I would like to express my greatest debt of gratitude to my late father Saif who encouraged me to start this whole journey before he passed away.

I would like to take this opportunity to extend my deepest gratitude to all friends who were there for me. I thank them for their continuous guidance, encouragement, and for pushing me further than I thought I could.

Moreover, I would like to express my gratitude to all the professors in the University of Belgrade for all the knowledge they provided. I would like to specially thank Professor Zlatko Petrovic, Professor Danilo Cuk, and Professor Jelena Svorcan who have been supporting me throughout my whole higher educational career. I greatly appreciate all the advice and guidance they have given me.



Abstract

This paper discusses an approach used for computational fluid dynamics simulation. The results of the approach are compared with experimental wind tunnel data for the same simulated model. The simulated model is a front canard control missile with wrap around tail fin stabilizer. The 0.4 Mach subsonic flow regime is used in the simulation. In addition, various flow simulations are performed for different angles of attack and pitch control deflection. The turbulence model used in the simulation is the Spalart Allmaras which proved to be optimum for the simulated flow conditions. The results are compared with experimental wind tunnel results to validate the approach used in the simulations. The approach is highly dependent on optimizing a custom mesh for each simulation based on the pressure gradient mesh adaptation in FLUENT.



1. Introduction

Accurate determination of aerodynamic coefficients for flying vehicles is very important. They are crucial during the design phase when flight simulations are made. In addition, they are crucial during the testing phase when flight tests are performed. Obtaining stability and control aspects of flying vehicles is a major challenge for aerodynamicists (1). Moreover, identification of missile aerodynamic coefficients is a popular field of research (2), (3), (4), and (5). Various methods exist to determine the coefficients theoretically and experimentally. The experimental methods of aerodynamic modelling can be summarized into two main groups: wind tunnel tests (6) and flight tests (7) and (8). In addition, the theoretical methods could be divided into two main groups as well: semi-empirical methods and computational fluid dynamics methods.

Computational fluid dynamics has become a major focus due to its unique potential in identifying the aerodynamic coefficients and visualizing fluid flow (9). Great efforts are being put in the research of how to simulate the flow that matches the flow of the flight test in order to obtain accurate values for the aerodynamic coefficients. The research is mainly focused on the setup of the problem. This includes generating the optimized 3D CAD model, selecting appropriate physics of the flow, optimization of the computational procedure, as well as the estimation of computational power required to perform such computationally intensive simulations.

The employed computational technique used can be separated into three major steps. First is the optimization of the CAD model. Second is the preparation of a suitable physics setup. Third is running repeated simulations utilizing pressure gradient mesh adaptation until reaching the convergence of the results.



The flow about axi-symmetric canard controlled missile with wrap around tail fin is simulated using ANSYS FLUENT. Moreover, the wrap around fins configurations is a major field of research (10). The simulations are performed for several angles of attack as well as several control deflections. All simulation results are then compared with experimental data obtained from the wind tunnel experiments.

High angle of attack simulations has always been a challenge for missiles aerodynamicists (11). However, good agreement between the CFD simulations and the experimental data for missiles with high angle of attack are found in (12). Flow of different missile configurations was also simulated by CFD methods and agreements are achieved in (13), (14), and (15).

In addition, canard controlled missiles is a major field of research in (16) and (17). However, it is very rare to find simulations for canard controlled missiles with the deflection of control surfaces coupled with high angle of attack.

The flow for Mach number 0.4 and for the angle of attack varying from -10 to 10 degrees is calculated in order to analyze the missile's static stability. In addition, canard pitch control deflections are simulated up to 15 degrees to capture the non-linearity, controllability, and maneuver capabilities of the missile. Exact conditions are replicated in the wind tunnel with full scale model to assess the accuracy and the quality of the calculated solution.



2. Governing Equations

2.1. Pressure based

ANSYS FLUENT flow simulations are categorized into two main solver types: pressure based and density based. Pressure based solver is used for all the simulations performed in this research. In pressure based solver, the pressure equation is continuously solved to obtain the velocity field until the solution converges. Both density based and pressure based utilize the same principle equations defined by Navier-Stokes (18).

The continuity equation is defined as:

$$\frac{\partial \rho}{\partial t} + \text{div}(\rho \mathbf{u}) = 0 \quad (1)$$

The momentum equation for x-component is defined as:

$$\frac{\partial(\rho u)}{\partial t} + \text{div}(\rho u \mathbf{u}) = -\frac{\partial p}{\partial x} + \text{div}(\mu \text{grad } u) \quad (2)$$

The momentum equation for y-component is defined as:

$$\frac{\partial(\rho v)}{\partial t} + \text{div}(\rho v \mathbf{u}) = -\frac{\partial p}{\partial y} + \text{div}(\mu \text{grad } v) \quad (3)$$



The momentum equation for z-component is defined as:

$$\frac{\partial(\rho w)}{\partial t} + \text{div}(\rho w \mathbf{u}) = -\frac{\partial p}{\partial z} + \text{div}(\mu \text{grad } w) \quad (4)$$

The energy equation used is:

$$\frac{\partial(\rho i)}{\partial t} + \text{div}(\rho i \mathbf{u}) = -p \text{div } \mathbf{u} + \text{div}(k \text{grad } T) + \Phi \quad (5)$$

Where p and ρ are defined as:

$$p = \rho RT \quad \text{and} \quad i = C_v T \quad (6)$$

All the impact in the internal energy equation due to the viscous stresses are represented in the dissipation function Φ

$$\Phi = \mu \left\{ \begin{array}{l} 2 \left[\left(\frac{\partial u}{\partial x} \right)^2 + \left(\frac{\partial v}{\partial y} \right)^2 + \left(\frac{\partial w}{\partial z} \right)^2 \right] \\ + \left(\frac{\partial u}{\partial y} + \frac{\partial v}{\partial x} \right)^2 + \left(\frac{\partial u}{\partial z} + \frac{\partial w}{\partial x} \right)^2 + \left(\frac{\partial v}{\partial z} + \frac{\partial w}{\partial y} \right)^2 \end{array} \right\} + \lambda (\text{div } \mathbf{u})^2 \quad (7)$$



Table 1 presents the variables used in the previous equations

Table 1 Navier-Stokes equations variables

Parameter	Description
ρ	Air density
\mathbf{u}	$u\vec{i} + v\vec{j} + w\vec{k}$ - Velocity vector
μ	Viscosity coefficient
i	Internal enthalpy
p	Pressure
T	Temperature
k	Heat conduction coefficient
c_v	Specific heat in constant volume
Φ	Dissipation function
λ	Second viscosity coefficient

2.2. Turbulence model - Spalart-Allmaras

The Spalart-Allmaras model (19) is a one-equation model that solves the kinematic eddy turbulent viscosity through the following transport equation

$$\begin{aligned} \frac{D\tilde{\nu}}{Dt} = & c_{b1}[1 - f_{t2}] \tilde{S} \tilde{\nu} + \frac{1}{\sigma} [\nabla \cdot ((\mathbf{u} + \tilde{\mathbf{v}}) \nabla \tilde{\nu}) + c_{b2} (\nabla \tilde{\nu})^2] \\ & - [c_{\omega 1} f_{\omega} - \frac{c_{b1}}{\kappa^2} f_{t2}] \left[\frac{\tilde{\nu}}{d} \right]^2 + f_{t1} \Delta U^2 \end{aligned} \quad (8)$$

Where $\tilde{\nu}$ is the working variable and should follow the transport equation. ν represents the molecular viscosity. The eddy turbulent viscosity is defined as ν_t

$$\nu_t = \tilde{\nu} f_{v1}, \quad f_{v1} = \frac{\chi^3}{\chi^3 + c_{v1}^3}, \quad \chi \equiv \frac{\tilde{\nu}}{\nu} \quad (9)$$



\tilde{S} is defined to be the vorticity magnitude and d is the closest wall distance.

$$\tilde{S} \equiv S + \frac{\tilde{v}}{\kappa^2 d^2} f_{v2}, \quad f_{v2} = 1 - \frac{\chi}{1 + \chi f_{v1}} \quad (10)$$

It is important to point out that the wall boundary condition is $\tilde{\mathbf{v}} = 0$ in Spalart-Allmaras turbulence model. The boundary condition in free stream ideally is $\tilde{\mathbf{v}} = 0$. However, $\tilde{\mathbf{v}} = 0$ provides problems in some solvers. Therefore, values below $\frac{v}{10}$ are considered to be acceptable.

f_{t1} and f_{t2} trip functions are defined as the following:

$$f_{t1} = c_{t1} g_t \exp\left(-c_{t2} \left(\frac{w_t^2}{\Delta U^2}\right) [d^2 + g_t^2 d_t^2]\right) \quad (11)$$

$$f_{t2} = c_{t3} \exp(-c_{t4} x^2) \quad (12)$$

Where d_t is defined as the distance between the trip to the field point. The wall vorticity located at the trip is defined as w_t . The velocity difference between the trip and the field point is defined as ΔU .

g_t is defined as the following:

$$g_t \equiv \min\left(0.1, \frac{\Delta U}{w_t \Delta x}\right)$$

Where Δx is defined as the spacing between the grids along the wall located at the trip.

Table 2 represents all the standard values of coefficients used in the Spalart Allmaras model.



Table 2 Spalart Allmaras coefficients

Model Constant	Value
c_{b1}	0.1355
σ	2/3
c_{b2}	0.622
κ	0.41
c_{w1}	$\frac{c_{b1}}{\kappa^2} + \frac{1 + c_{b2}}{\sigma}$
c_{w2}	0.3
c_{w3}	2
c_{v1}	7.1
c_{t1}	1
c_{t2}	2
c_{t3}	1.1
c_{t4}	2

2.3. Grid Adaptation

There are several ways of grid adaptation using different strategies and different equations. Grid Adaptation is commonly used in CFD simulations for missiles (20). In this paper, two dimensional Euler equations is used in the conservation law form for grid adaptation (21)

$$\frac{\partial U}{\partial t} = -\frac{\partial F}{\partial x} - \frac{\partial G}{\partial y} \quad (13)$$

Where U , F and G are defined as the following

$$U = \begin{bmatrix} \rho \\ \rho u \\ \rho v \\ E \end{bmatrix} \quad F = \begin{bmatrix} \rho u \\ \rho u u + p \\ \rho u v \\ \rho u h_o \end{bmatrix} \quad G = \begin{bmatrix} \rho v \\ \rho u v \\ \rho v v + p \\ \rho v h_o \end{bmatrix}$$

And



$$h_o = \frac{E+p}{\rho} = \frac{\gamma}{\gamma-1} \frac{p}{\rho} + \frac{1}{2}(u^2 + v^2) \quad (14)$$

Table 3 presents the variables used in the previous equations

Table 3 Grid adaptation equations' parameters

Parameter	Description
ρ	Density
u	x-direction velocity
v	y-direction velocity
E	Total internal energy
p	Pressure
h_o	Total enthalpy
γ	Ratio of specific heats

Choosing proper refinement parameter is crucial to assure optimized grid adaptation. Depending on the required results, different parameters are selected such as density, pressure, velocity and entropy. For example, choosing change of entropy, density, and pressure is preferred when studying shocks. In addition, the method of measuring the change of variable must be selected. First order difference and second order difference equations are the typical methods.

Figure 1 to Figure 8 represent the effect of refinement parameter choice which is examined for RAE 2822 airfoil for 3 degrees angle of attack along with Mach number 0.75.

Figure 1 and Figure 2 show the effect of grid refinement using density difference for both first and second order differences.

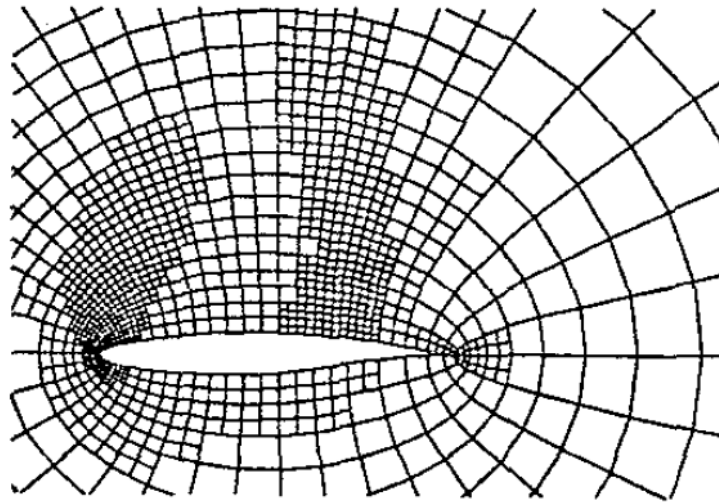


Figure 1 First order difference of density

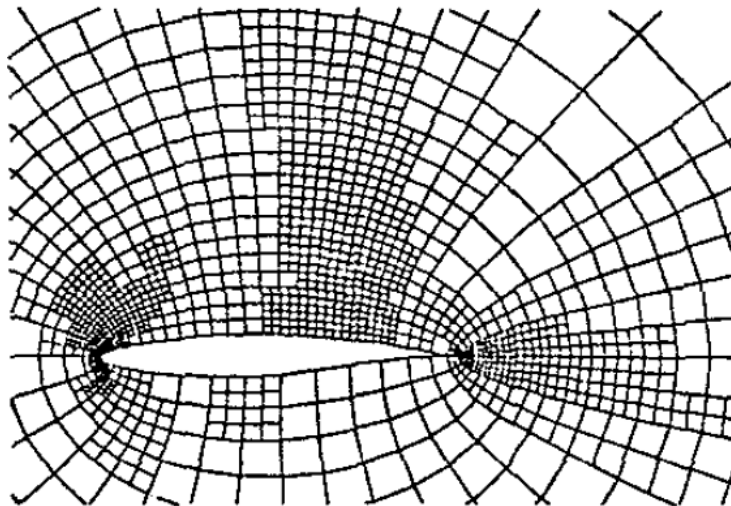


Figure 2 Second order difference of density

Figure 3 and Figure 4 show the effect of grid refinement using pressure difference for both first and second order differences.

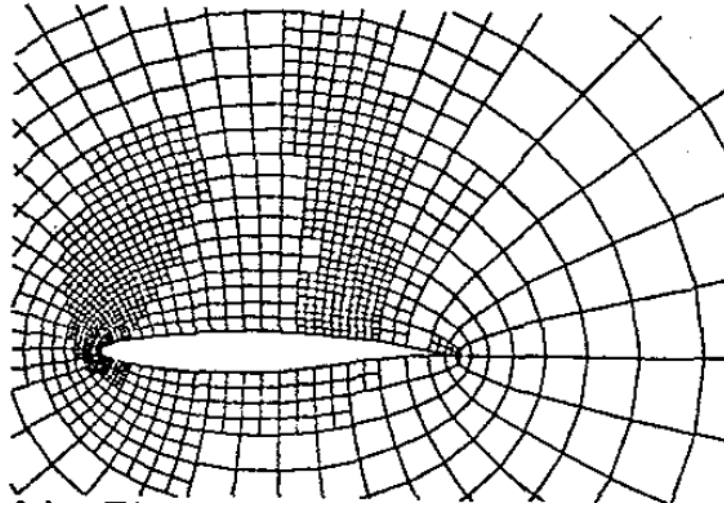


Figure 3 First order difference of pressure

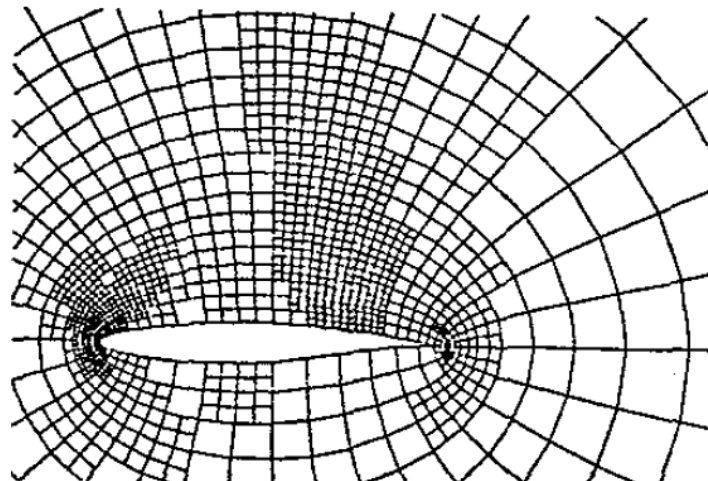


Figure 4 Second order difference of pressure

Figure 5 and Figure 6 show the effect of grid refinement using velocity difference for both first and second order differences.

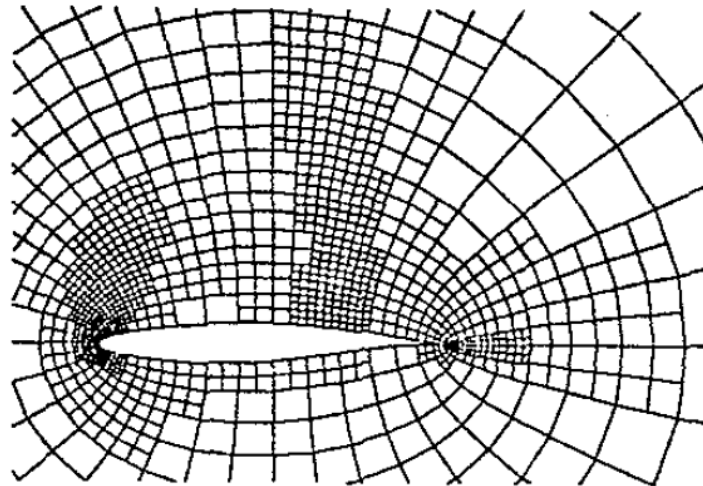


Figure 5 First order difference of velocity

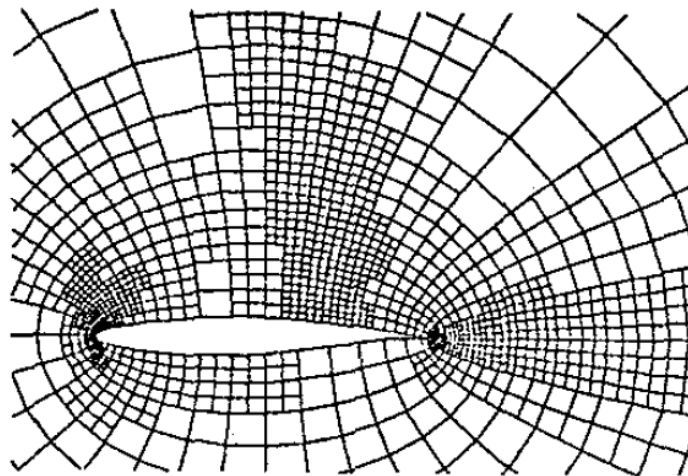


Figure 6 Second order difference of velocity

Figure 7 and Figure 8 show the effect of grid refinement using entropy difference for both first and second order differences.

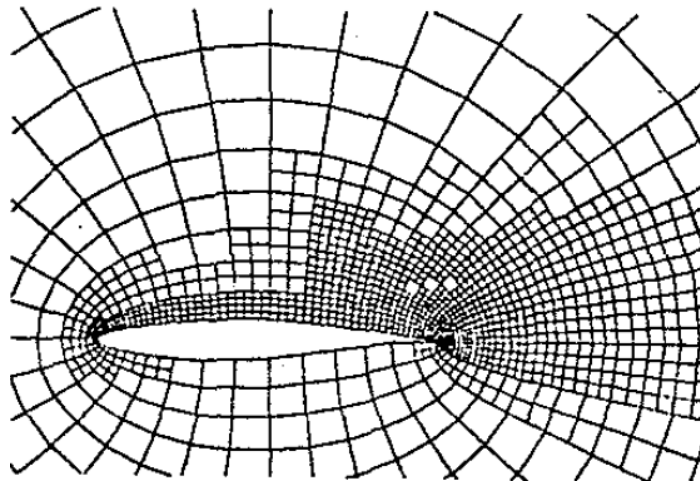


Figure 7 First order difference of entropy

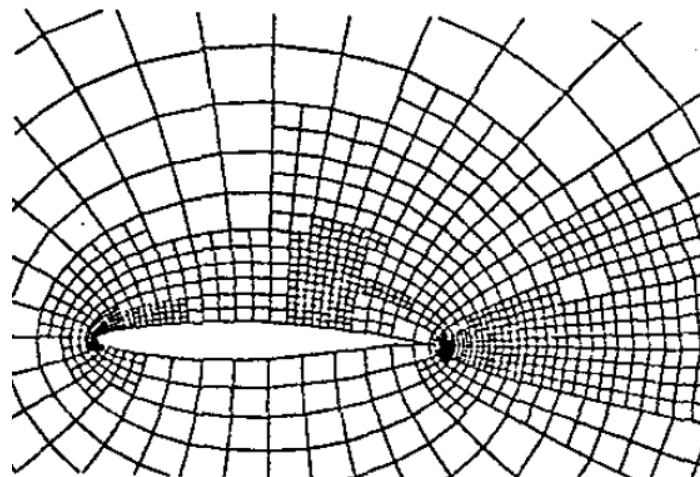


Figure 8 Second order difference of entropy



3. Axis Symmetric Body Application

3.1. Simulation conditions

In order to obtain sufficient data for the flight simulation aerodynamic model, several simulations were performed. They cover all the different cases of angle of attack as well as pitch control surfaces deflections. It is important to highlight that all the chosen conditions are identical to the conditions used in the wind tunnel testing to ensure accurate comparison.

Table 4 Simulated cases

	Angle of Attack	Pitch Deflection
Range	-10 to 10 degrees	0, 10, 15 degrees
Step Interval	2 degrees	N/A

3.1.1. Sign Convention for Control Surfaces

The model has two control surfaces to control motion in the pitch plane. The control surfaces are deflected according to each simulated case specified in Table 4 using the sign convention in Figure 9. The other two control surfaces are not deflected in any simulation since they are used for yaw plane motion control.

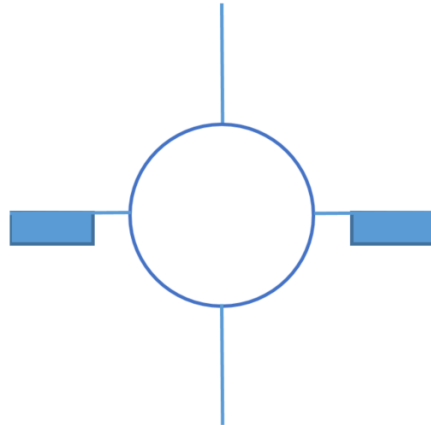


Figure 9 Rear view of the positive pitch control deflection

It is important to mention that Figure 9 shows the rear view of the model. Furthermore, the trailing edge of the control surface is represented by the lowered deflected panels.

3.2. CAD Model preparation

The CAD model used for the simulation is generated by CATIA using part design. The model is designed to be identical to the model tested in the wind tunnel. Figure 10 shows the full CAD model including all the aerodynamics surfaces.

It is important to point out that this model is a simplified model generated for simulation and not for production or any other type of model evaluation. As seen in Figure 10, the model does not include any screws or small details. Hence, the model seems like one homogeneous body. This is crucial to ensure smooth solution convergence as well as help gain accurate results as it will be explained later in this paper.



Figure 10 CAD model of the simulated missile

3.2.1. Configuration Description

The selected missile aerodynamic configuration is the canard controlled missile along with wrap around tail fin stabilizer. The control section consists of 4 canards for pitch, yaw, and roll control. Two canards are used to control motion in pitch plane while the other two are used to control motion in yaw plane as well as roll plane.

The tail fin section consists of 4 wrap around fins to ensure missile stability. The tail fins are selected to be wrap around due to the launcher requirements. They are also separated from the missile body with mechanical bearings to allow the tail fins to rotate freely around the body. One of the major challenges of the front canard controlled missile is the unwanted roll caused by the non-uniform flow disturbance from the front canards. Hence, the tail fins are freely rotating around the body without causing the missile body to roll.

3.2.2. Model Technical Drawing

The technical drawing of the simulated missile is shown in Figure 11. The drawing shows all the important dimensions of the missile such as full spans and chords of the canard control surfaces. All the dimensions are normalized by the caliber of the missile.

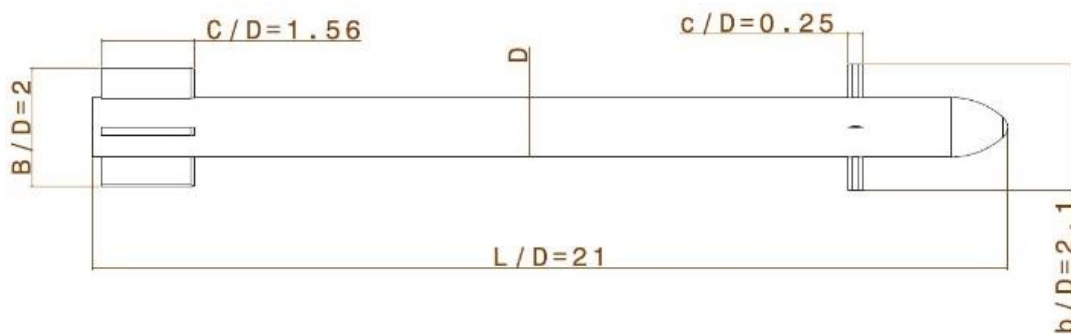


Figure 11 Missile technical drawing

3.2.3. Model Simplification

There are many details in the produced model that has no impact on the aerodynamic coefficients such as screw holes. In order to have efficient mesh size without sacrificing solution accuracy, it is significant to remove all those tiny details for the simulation. Therefore, the model is designed as a perfect tube without any holes.

The highest impact missile part on the aerodynamic coefficients are the aerodynamic control surfaces. The control surfaces proved to have significant impact on the mesh size. That is because they include smooth and round manufactured edges as shown in Figure 12.

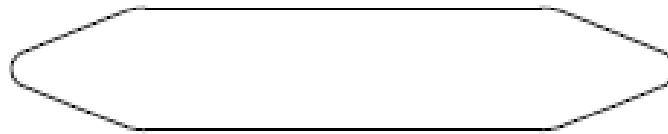


Figure 12 Control surface airfoil cross section

The idealized model of the control surface in Figure 12 is created to remove the details with small impact. The new optimized control surface airfoil section is six-line segments as shown in Figure 13. The removed details is proofed to have tiny impact as confirmed later in this paper.

The new optimized control surface airfoil section shown in Figure 13 has the potential to significantly reduce the mesh size. If the original control surface shown in Figure 12 were to be meshed, it would be important to significantly reduce the cells sizes near both leading and trailing edges. Moreover, those cell sizes will be identical along the full span of the 4 canards. Therefore, there will be an extreme increase in the overall mesh size.



Figure 13 Optimized control surface airfoil section



3.3. Simulation setup

Proper flow simulation requires proper flow model with proper air flow characteristics. The boundary surfaces locations as well as the computational grid specifications should be properly selected in order to assure accurate flow simulation.

3.3.1. Domain definition

The flow domain must be carefully specified in order to represent the real flow behavior. The inlet and outlet of the flow models are specified so that the simulated flow represents the real flow characteristics. The locations of the boundary condition surfaces are chosen carefully to ensure adequate flow volume.

The inlet, outlet, and sides are chosen to be significantly far from the simulated model. Increasing the volume of flow domain leads to the increase in mesh size. However, the meshing technique used significantly reduces the increase caused by high volume flow domain. The flow domain volume is $1.4744 \text{ e } +13 \text{ mm}^3$.

It is important to point out that the domain is defined for all the simulations with different cases. Usually simulations with high disturbances such as high angle of attack require different domain definitions. However, the domain defined shall cover all the simulated cases up to the extreme case of 10 degrees angle of attack along with 15 degrees control deflection.

3.3.1.1. Boundary conditions

The boundary conditions are selected to properly represent the flow characteristics, flow speed, as well as flow direction. The flow domain is selected to have cylindrical sides with inlet and outlet as shown in Figure 14

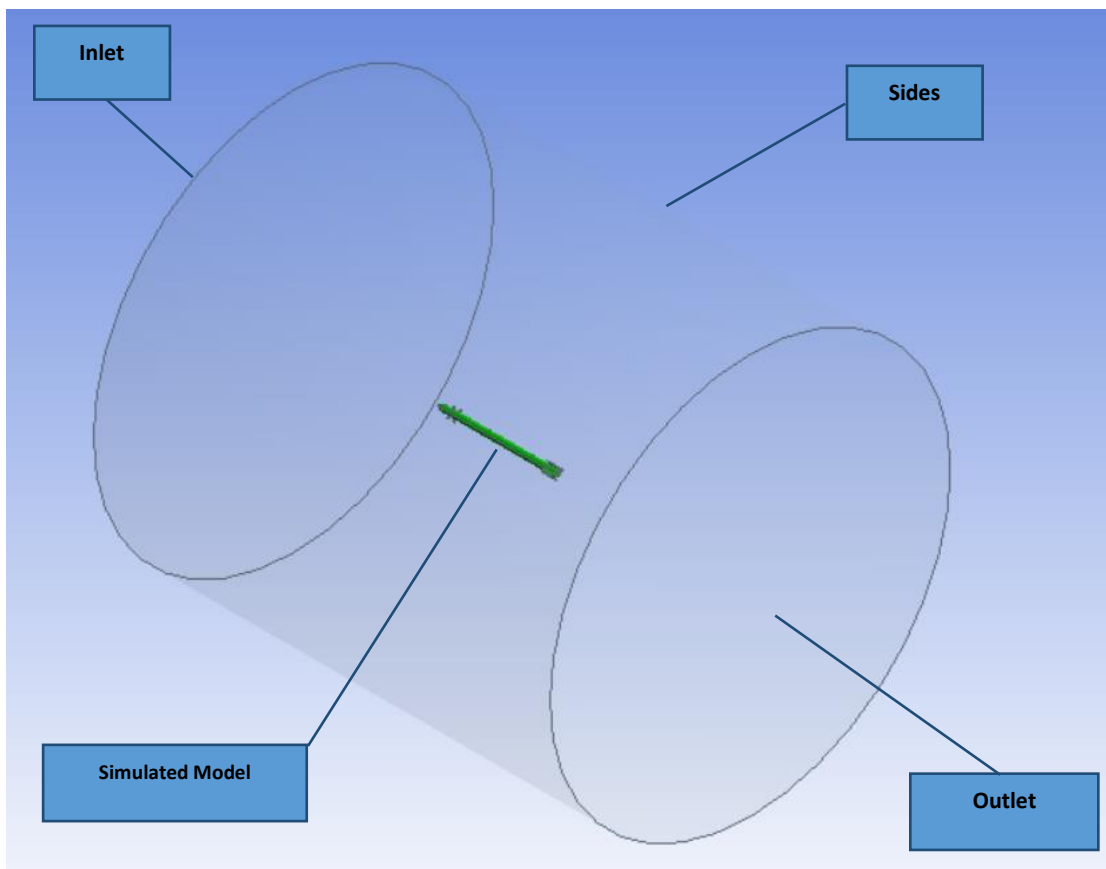


Figure 14 Flow domain with boundary conditions

(Note: Flow domain area is scaled down to show simulated model clearly)

All angles of attack are simulated by specifying the flow direction on all outer boundary surfaces. Components of the flow are defined according to the sine and cosine of angle of attack.



The inlet, sides, as well as outlet were set as pressure far-field with the following boundary conditions

Table 5 Boundary conditions parameters values

Parameter	value
M	0.4
p	90748 Pa
T	288.76 K
<i>u</i>	10

3.3.2. Baseline mesh

The baseline mesh is created to have the minimum possible number of cells without sacrificing the shape of the simulated model. It is important to highlight that this mesh is initial and not used to get the final results. That is because the mesh will be more optimized later in this paper for more accurate data.

The baseline mesh has 1162516 element cells with 211043 nodes. All the tables presented in the following figures in this section are screenshots from the automated ANSYS tables. The table in Figure 15 shows the general specifications of the mesh including mesh sizing and volume.



Object Name	Solid
State	Meshed
Graphics Properties	
Visible	Yes
Transparency	0.1
Definition	
Suppressed	No
Coordinate System	Default Coordinate System
Reference Frame	Lagrangian
Material	
Fluid/Solid	Defined By Geometry (Fluid)
Bounding Box	
Length X	20460 mm
Length Y	30291 mm
Length Z	30291 mm
Properties	
Volume	1.4744e+013 mm ³
Centroid X	7230. mm
Centroid Y	1.7419e-008 mm
Centroid Z	-8.4318e-009 mm
Statistics	
Nodes	211043
Elements	1162516
Mesh Metric	None

Figure 15 Baseline mesh sizing and volume table report

The baseline mesh is selected to be coarse mesh and the advanced size function is used on curvature. The inflation option used is smooth transition with transition ratio of 0.272. The maximum layers of inflation is set to be 5 with growth rate of 1.2. Figure 16 shows the general mesh controls used.



Sizing	
Use Advanced Size Function	On: Curvature
Relevance Center	Coarse
Initial Size Seed	Active Assembly
Smoothing	Medium
Transition	Slow
Span Angle Center	Fine
Curvature Normal Angle	Default (18.0 °)
Min Size	Default (23.6620 mm)
Max Face Size	Default (2366.20 mm)
Max Size	Default (4732.50 mm)
Growth Rate	Default (1.20)
Minimum Edge Length	2.05790 mm
Inflation	
Use Automatic Inflation	None
Inflation Option	Smooth Transition
Transition Ratio	0.272
Maximum Layers	5
Growth Rate	1.2
Inflation Algorithm	Pre
View Advanced Options	No
Assembly Meshing	
Method	None
Patch Conforming Options	
Triangle Surface Mesher	Program Controlled
Patch Independent Options	
Topology Checking	No
Advanced	
Number of CPUs for Parallel Part Meshing	Program Controlled
Shape Checking	CFD
Element Midside Nodes	Dropped
Straight Sided Elements	
Number of Retries	0
Extra Retries For Assembly	Yes
Rigid Body Behavior	Dimensionally Reduced
Mesh Morphing	Disabled
Defeaturing	
Pinch Tolerance	Default (21.2960 mm)
Generate Pinch on Refresh	No
Automatic Mesh Based Defeaturing	On
Defeaturing Tolerance	Default (11.8310 mm)

Figure 16 General baseline mesh controls

The major parts of the simulated model are sized carefully to optimize the mesh size without sacrificing data accuracy. However, the results accuracy are not the major concern when defining the baseline mesh. That is because the mesh is optimized later on for more accurate results.



The body cells face sizes are defined to be 10 mm. The lower face size is the better estimation of aerodynamic coefficients especially for skin friction drag. Refining the cells on the body has significant impact on the mesh size since the simulated model body is relatively long. Since the drag estimation is not the major interest of the simulations and increasing the mesh size is to be avoided, the body face mesh cells sizes are selected to be 10 mm.

The simulated model nose face size is selected to be 4 mm. 4 mm is sufficient to represent the curvature of the nose identical to the real model. Usually nose meshing has major impact on aerodynamic drag estimation.

The tail fin face size is set to be 3 mm. The tail fin of the simulated model has significant impact on the aerodynamic coefficients especially on the lateral aerodynamic coefficients. Hence, the small face sizes are selected for tail fin.

The canard control surfaces have the most impact on the lateral aerodynamic coefficients especially the control aerodynamic derivatives. However, there is no need for manual sizing of the mesh due to their simplified shape. The automatic program controlled meshing is sufficient to accurately represent their shape.

The body, nose, and tailfin mesh element sizes are specified in the table shown in Figure 17.



Object Name	Face Sizing	Face Sizing 2	Face Sizing 3
State	Fully Defined		
Scope			
Scoping Method	Named Selection		
Named Selection	Body	Nose	TailFin
Definition			
Suppressed	No		
Type	Element Size		
Element Size	10. mm	4. mm	3. mm
Behavior	Soft		
Curvature Normal Angle	Default		
Growth Rate	Default		
Local Min Size	Default (10. mm)	Default (4. mm)	Default (3. mm)

Figure 17 Advanced baseline mesh controls

The number of faces selected to be sized in the baseline mesh along with their named selections are shown in Figure 18. The number of faces are defined according to the CAD model imported from CATIA as well as the boundary conditions surfaces selected.

Object Name	Base	Body	canards	inlet	Nose	outlet	sides	TailFin
State	Fully Defined							
Scope								
Scoping Method	Geometry Selection							
Geometry	1 Face	2 Faces	28 Faces	1 Face	4 Faces	1 Face	24 Faces	
Definition								
Send to Solver	Yes							
Visible	Yes							
Program Controlled Inflation	Exclude							
Statistics								
Type	Imported							
Total Selection	1 Face	2 Faces	28 Faces	1 Face	4 Faces	1 Face	24 Faces	
Suppressed	0							
Used by Mesh Worksheet	No							

Figure 18 Baseline mesh named selections

The baseline mesh side view is shown in Figure 19. It is important to highlight that this view is cropped to show a zoomed version of the

simulated model. As seen in Figure 19, the cells towards the inlet, outlet, and sides are relatively higher in sizes. The baseline mesh does not consider flow disturbances such as angle of attack and control surface deflection. Hence, the baseline mesh is used for all angles of attack and control surface deflections. However, an optimization to the mesh is implemented on each case separately as explained later in this paper.

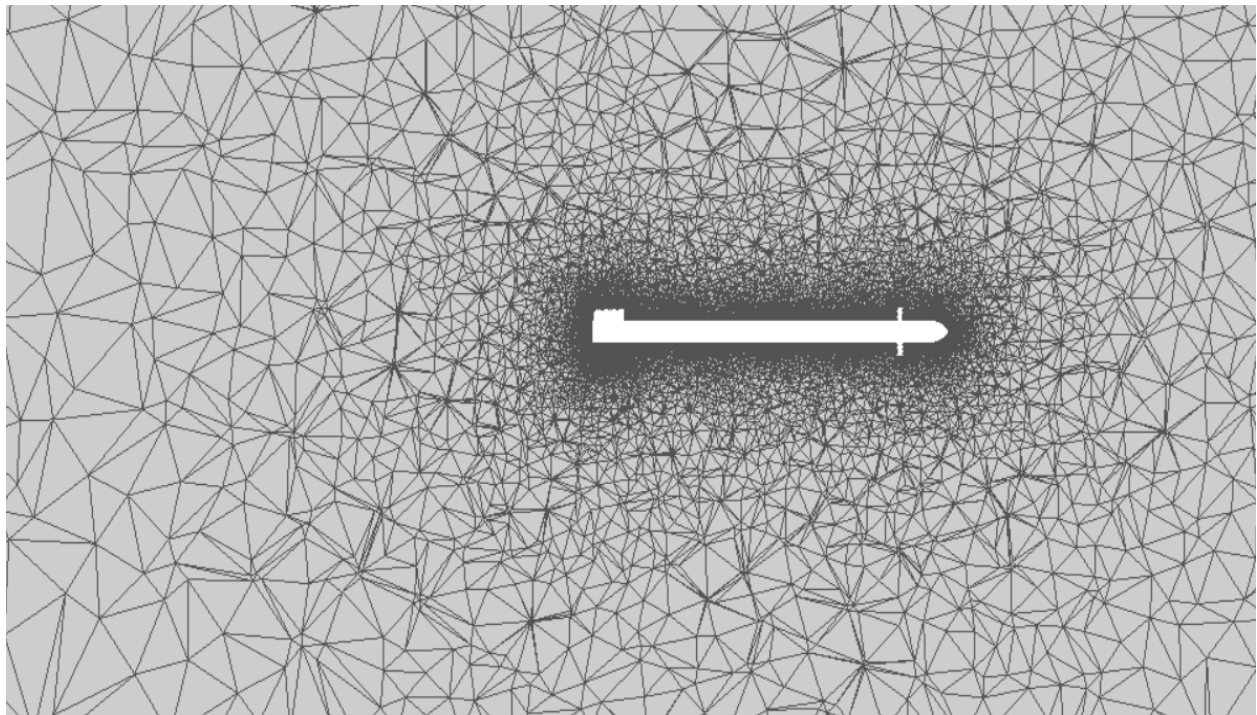


Figure 19 Baseline mesh side view

3.3.3. Air flow characteristics

The simulated fluid is selected to be air with ideal gas characteristics. The Sutherland's law is used for viscosity calculations. The Three Coefficient Method of Sutherland's law is used with the parameters presented in Table 6



Table 6 Sutherland's law parameters

Parameter	value
Reference viscosity	1.716e-05 [Kg/m-s]
Reference temperature	273.11 [K]
Effective temperature	110.56 [K]

3.3.4. Steady state flow

The simulated flow is selected to be steady state flow for most of the simulations. However, there are some simulations where transient flow is considered such as cases with high angles of attack coupled with high control surface deflections.

3.3.5. Turbulence model

The Spalart Allmaras turbulence model is used for all the simulations. The model is used with standard coefficients shown in Table 7

Table 7 Spalart Allmaras model coefficients used in simulation

Model Constant	value
C_{b1}	0.135
C_{b2}	0.622
C_{v1}	7.1
C_{w2}	0.3
C_{w3}	2.0

3.4. Mesh adaptation



Several methods can be used in FLUENT for mesh adaptation. The FLUENT mesh adaptation can be used based on several inputs such as the geometry and gradient values. They are used to adapt/optimize the mesh according to the selected technique by either refining or coarsening the mesh.

Mesh adaptation is usually used for solution optimization. Usually it captures all the details needed for mesh adaptation depending on the technique used. Mesh adaptation has the potential to significantly vary the size of the mesh. Hence, it should be used carefully.

3.4.1. Pressure gradient method

The gradient method is used in all simulations based on pressure gradient values in order to optimize the mesh. This method utilizes the pressure Euclidean norm along with a characteristics length scale according to the following equation (22).

$$|e_{il}| = (A_{cell})^{\frac{r}{2}} |\nabla f| \quad (15)$$

After running the simulation for a rough convergence of solution, the mesh is adapted by defining a pressure gradient threshold. Figure 20 and Figure 21 show the process mesh adaptation.

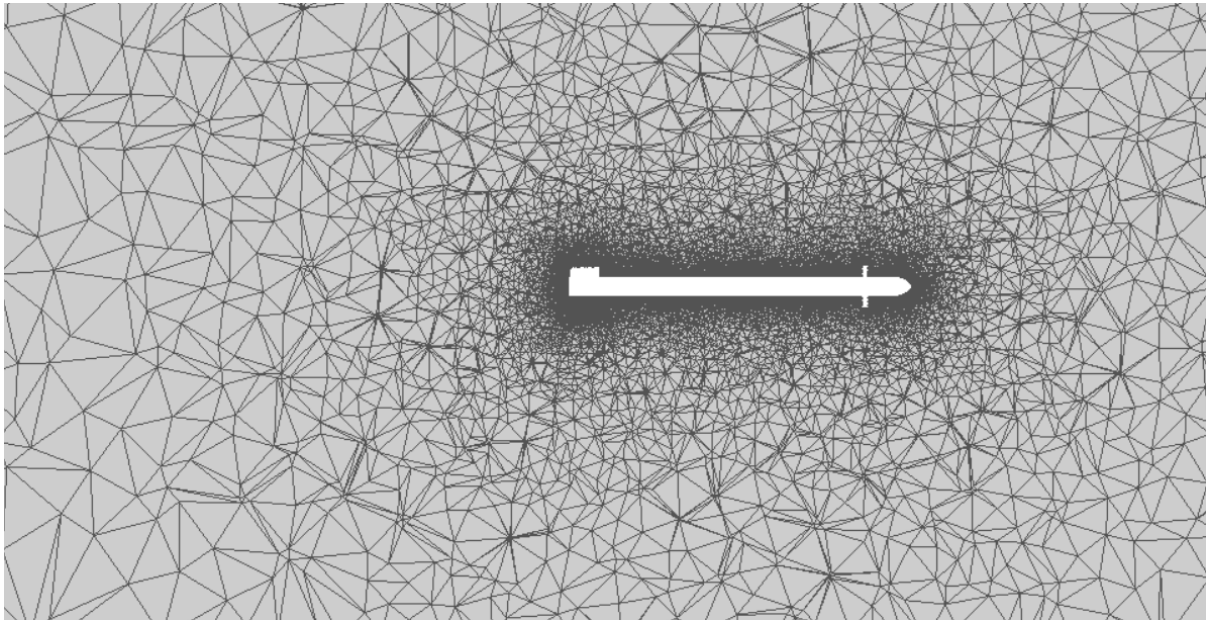


Figure 20 Baseline mesh before adaptation

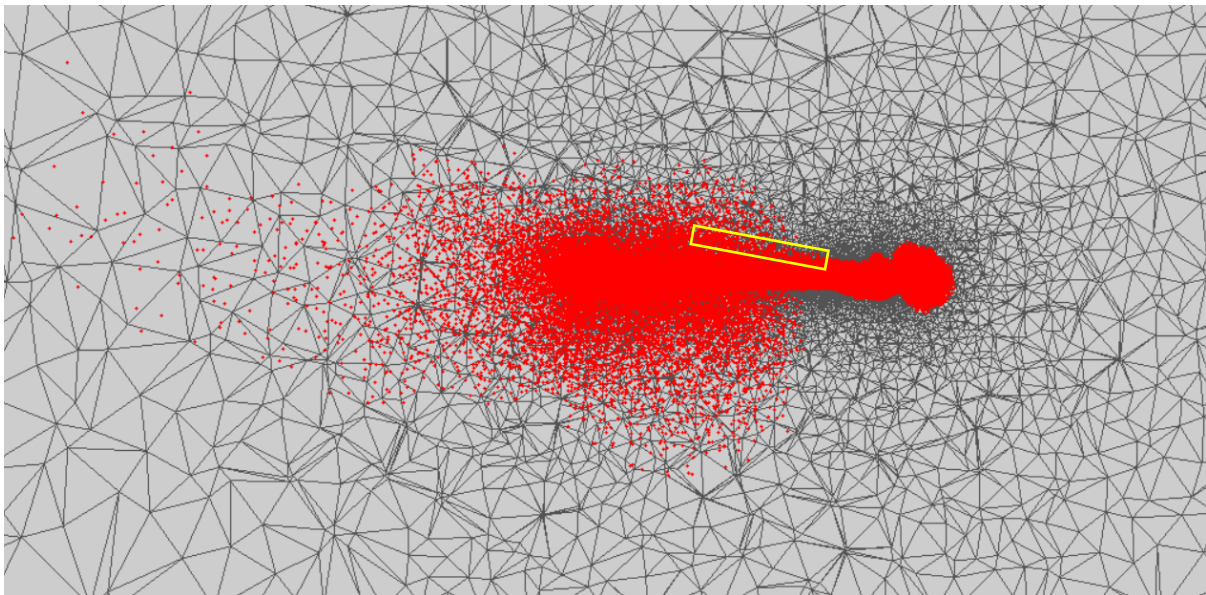


Figure 21 Baseline mesh with cells of required refinement

Figure 21 shows the baseline mesh with the areas [marked in red] that need refinement according to the specified threshold of pressure gradient. The flow changes with each angle of attack and control

deflection. Therefore, the adapted mesh is unique for each simulation case. The threshold of pressure gradient is selected so that the mesh size does not exceed 4 million cells.

The simulation case shown in Figure 21 is for 10 degrees angle of attack. It is important to highlight that the cells requiring adaptation follow the pressure gradient [marked in yellow].

Figure 22 shows the adapted mesh after applying pressure gradient method. It is important to point out that the changes in cells are not clearly visible. However, the mesh increased in size from 1.1 million to 4 million cells.

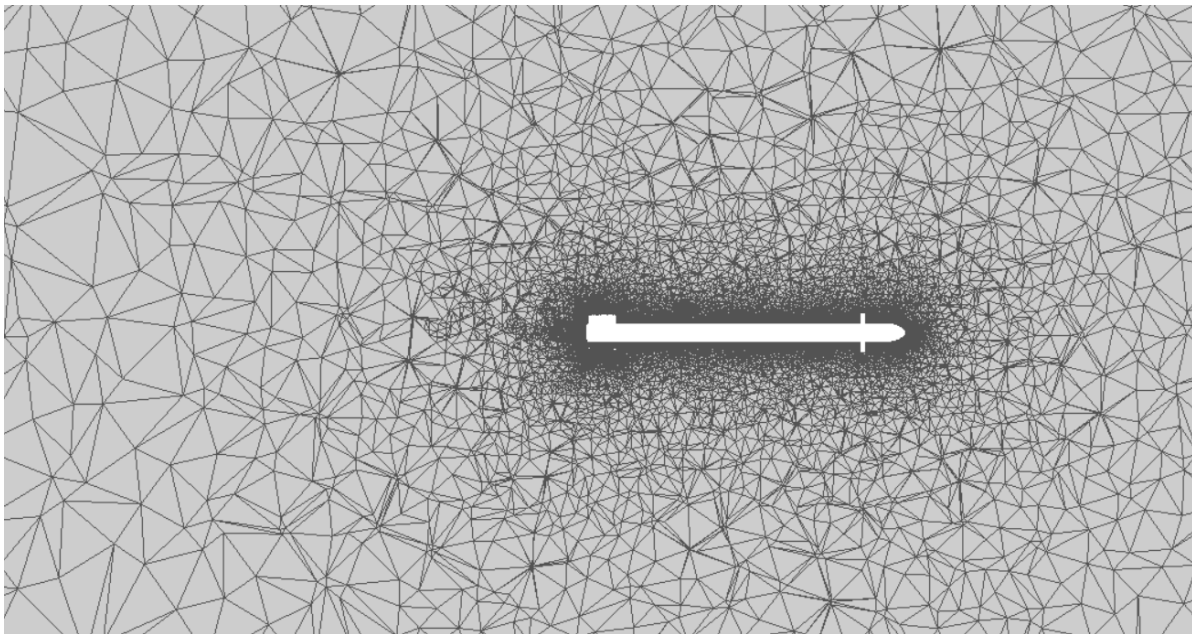


Figure 22 Adapted mesh

4. Results Presentation



The simulation is executed again after the mesh is optimized to obtain more optimized final results. The results are presented for all the simulation cases by forces, moments, and contours.

4.1. Coefficients

4.1.1. Pitch moment coefficients

The pitch moment coefficients are crucial due to their significant impact on static stability, controllability, as well as maneuver capability of the missile. Hence, several simulations are performed for different pitch control deflections up to 15 degrees. This allows for the comprehensive study of the full range of deflection capability. Moreover, it allows for the identification of the maximum control deflection angle without losing maneuver capability. It is important to point out that the moments are measured about a reference point located at 42% of the model length away from the model's nose tip.

Figure 23 shows the pitch moment coefficients vs. angles of attack for all control deflections. The pitch moment curve increases in value as the pitch control deflection increases. It is important to note that there is no significant increase of pitch moment curve between 10 degrees to 15 degrees especially towards high angle of attack. This proves that the missile's pitch moment control surfaces start to lose effectiveness near 15 degrees.

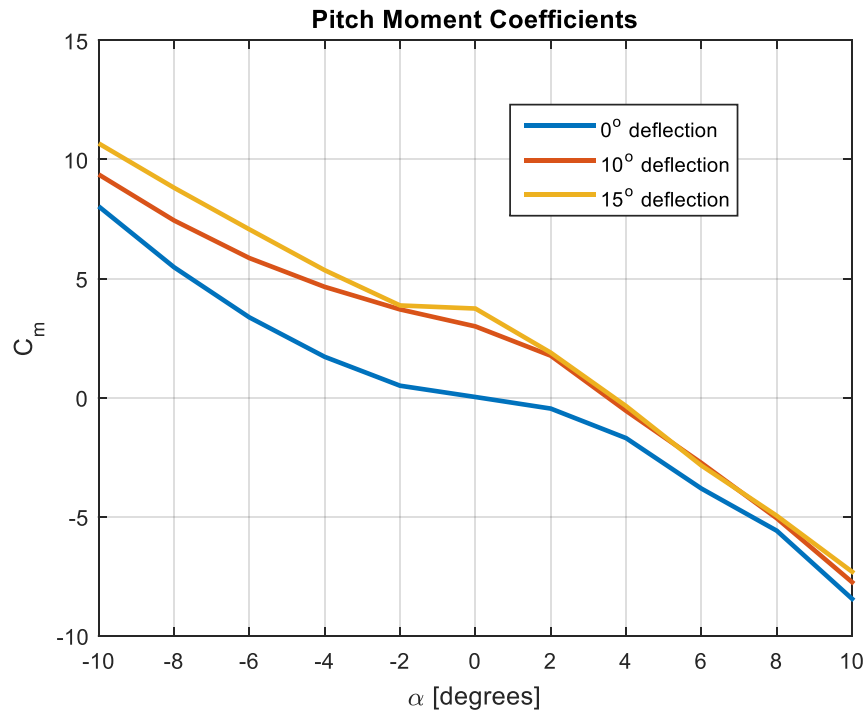


Figure 23 CFD pitch moment coefficients

4.1.2. Normal force coefficients

The lift force coefficient is important for the overall missile performance evaluation. The lift force coefficient helps in evaluating several performance parameters such as missile lift/drag ratio, stall speed, as well as maneuver capability.

The normal force coefficients for all control deflections vs. angles of attack are shown in Figure 24. It is important to note that the normal force coefficient curve of 10 and 15 degrees are almost identical. This proves that the missile starts to lose lift force when it approaches 15 degrees pitch control deflection.

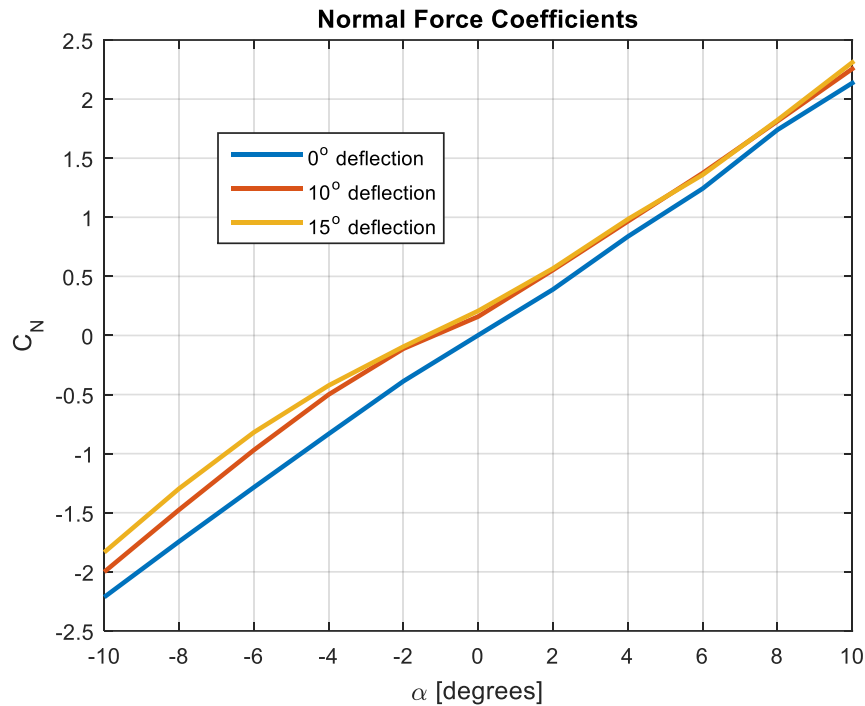


Figure 24 CFD normal force coefficients

By comparing Figure 23 and Figure 24, it is clear that the missile control surfaces effectiveness is improving as the control deflection increases. However, it is important to point out that there is no significant control effectiveness increase between 10 and 15 degrees control deflection. Therefore, it is concluded that the control deflection should not exceed 15 degrees to ensure the best control performance. This conclusion is supported by the simulation contours in the following sections.

4.1.3. Axial force coefficients

Figure 25 shows the axial force coefficients vs. angles of attack for all the control deflections determined by CFD simulations. The axial force curve increases in value as the pitch control deflection increases. It is important to note that there is a slight increase in the axial force coefficient for 10 and 15 degrees control deflection



towards high angle of attack. This increase is approximately 15% and 16% of the minimum axial force coefficient for 10 and 15 degrees control deflection respectively [increase between CA at angle of attack -10 degrees and 10 degrees].

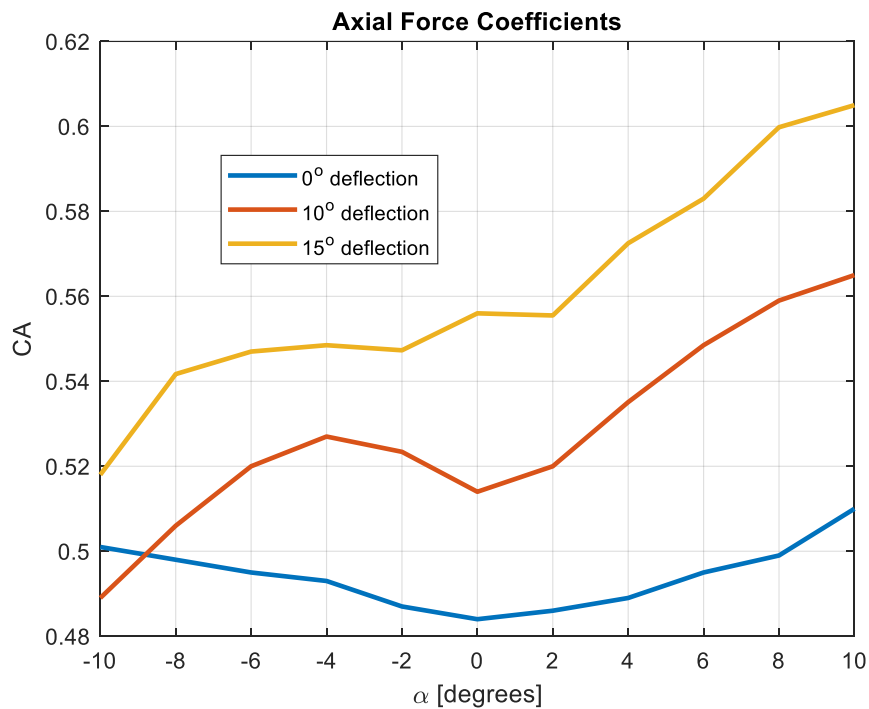


Figure 25 CFD axial force coefficients

4.1.4. Roll Moment coefficients

Figure 26 shows the roll moment coefficients vs. angles of attack for all the control deflections obtained by CFD simulations. The roll moment coefficient curves are almost identical and small in magnitude. It is important to point out that the control deflections simulation are for pitch plane control which means that there should be no roll moment. However, this roll is caused by the shape of tail fin [wrap



around fin]. Therefore, the plot in Figure 26 represent the wrap around fin effect on the roll plane.

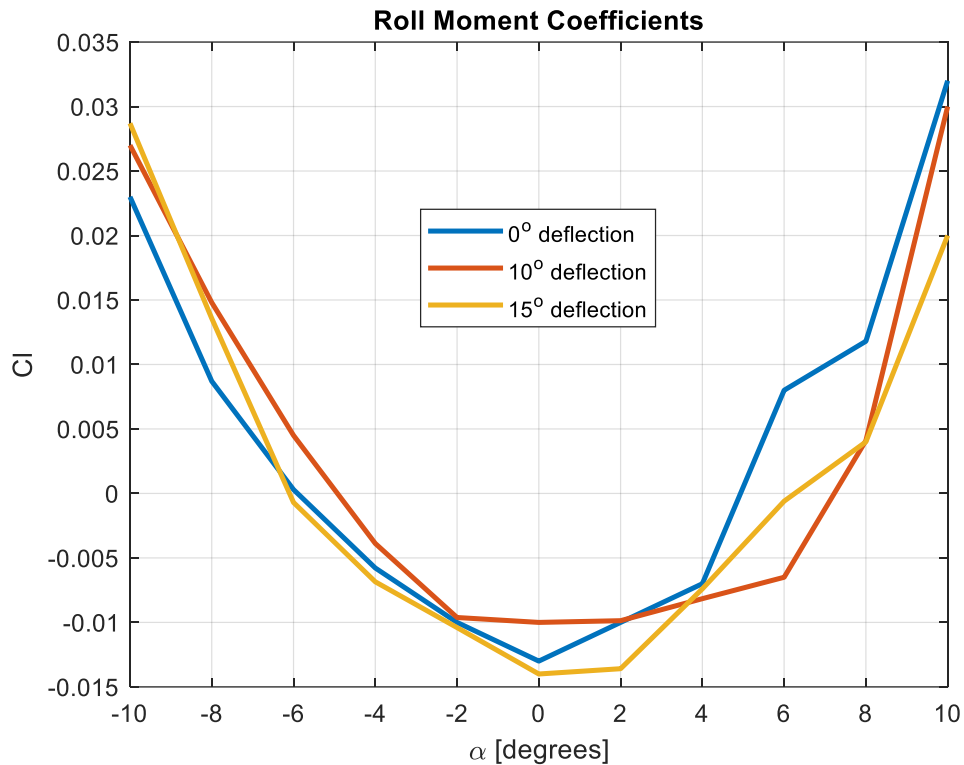


Figure 26 CFD roll moment coefficients

4.2. Contours

FLUENT is capable of presenting various types of contours such as Mach number, pressure, velocity, and temperature. However, The Mach number contours and pressure contours are chosen to be presented due to their major interest. In addition, velocity contours are provided in Appendix A

4.2.1. Mach number contours



The Mach number contours are crucial to evaluate the flow behavior of the simulation. They provide effective flow visualization which facilitates identifying significant performance parameters such as flow separation.

Various Mach number contours are generated due to several cases of control deflection and angles of attack. Angles of attack from 10 to -10 degrees are presented for each control deflection case. It is important to highlight that the increment size between each simulation case is 2 degrees angle of attack.

4.2.1.1. No deflection

The Mach number contours with 0 degree control surface deflection are presented in Figure 27 - Figure 37 for different angles of attack.

Figure 27 shows the simulation case with 0 degree angle of attack and 0 degree pitch control surface deflection. The contours shown in Figure 27 are expected since there are no significant flow disturbances caused by the control deflection or angle of attack.

There is no extraordinary flow behavior noticed in the contours shown in Figure 27. The regular flow characteristics at the base of the missile caused by the pressure drop is seen in Figure 27. This causes base drag on the missile.

Contours in Figure 27 show the Mach number drop towards the nose. This causes the pressure to rise at that point which leads to an increase in the drag nose component.

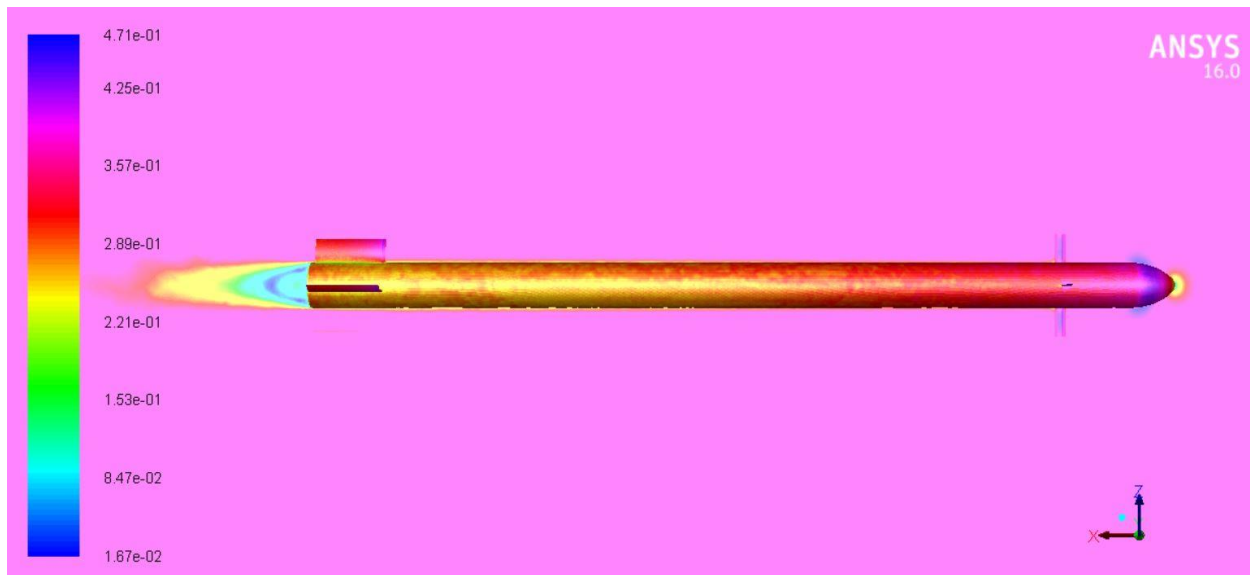


Figure 27 Mach number contours for 0 ° control deflection and angle of attack $\alpha = 0^\circ$

Figure 28 shows the simulation case with 2 degrees angle of attack and 0 degree pitch control surface deflection. The contours in Figure 28 show that the flow is starting to be disturbed especially behind the trailing edge of the pitch control surfaces.

The contours shown in Figure 28 indicate a drop in the Mach number towards the lower area of the front nose, control surfaces leading edge, and tail fin leading edge of the missile. This is caused by the angled flow represented by 2 degrees angle of attack. Hence, the pressure increases accordingly which results in extra drag on the missile. In addition, the Mach number drop results in an increased total normal force on the missile. This normal force acts upwards which is expected for positive angle of attack flow.

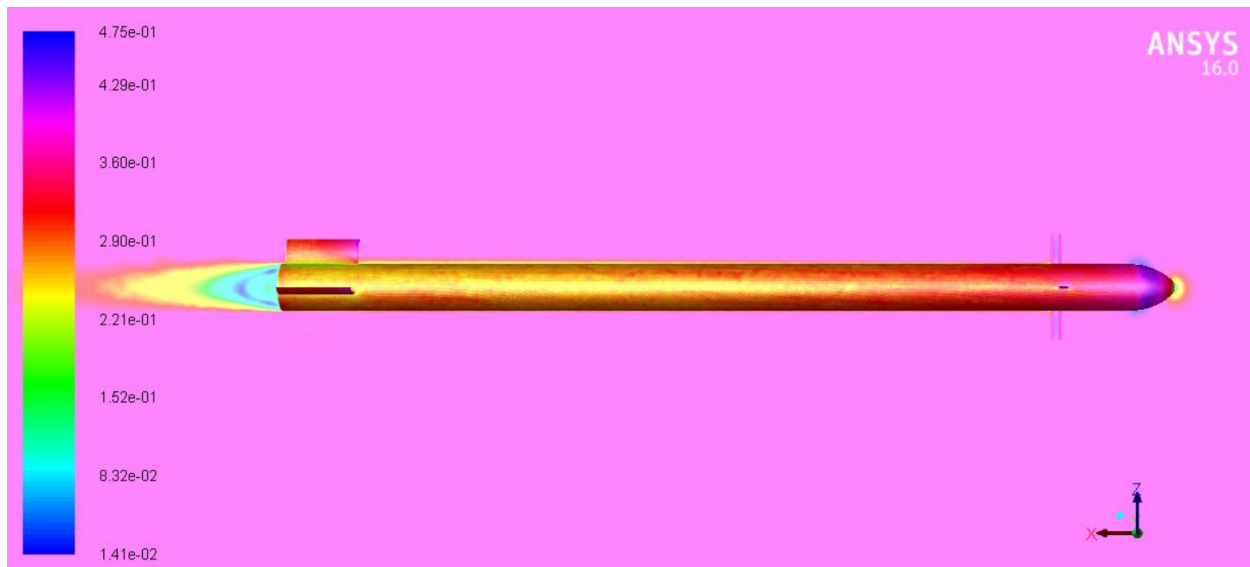


Figure 28 Mach number contours for 0 ° control deflection and angle of attack $\alpha = 2^\circ$

Figure 29 shows the simulation case with -2 degrees angle of attack and 0 degree pitch control surface deflection. The contours in Figure 29 show that the flow is starting to be disturbed especially behind the trailing edge of the pitch control surfaces.

The contours shown in Figure 29 indicate a drop in the Mach number towards the higher area of the front nose, control surfaces leading edge, and tail fin leading edge of the missile. This is caused by the angled flow represented by -2 degrees angle of attack. Hence, the pressure increases accordingly which results in extra drag on the missile. In addition, the Mach number drop results in an increased total normal force on the missile. This normal force acts downwards which is expected for negative angle of attack flow.

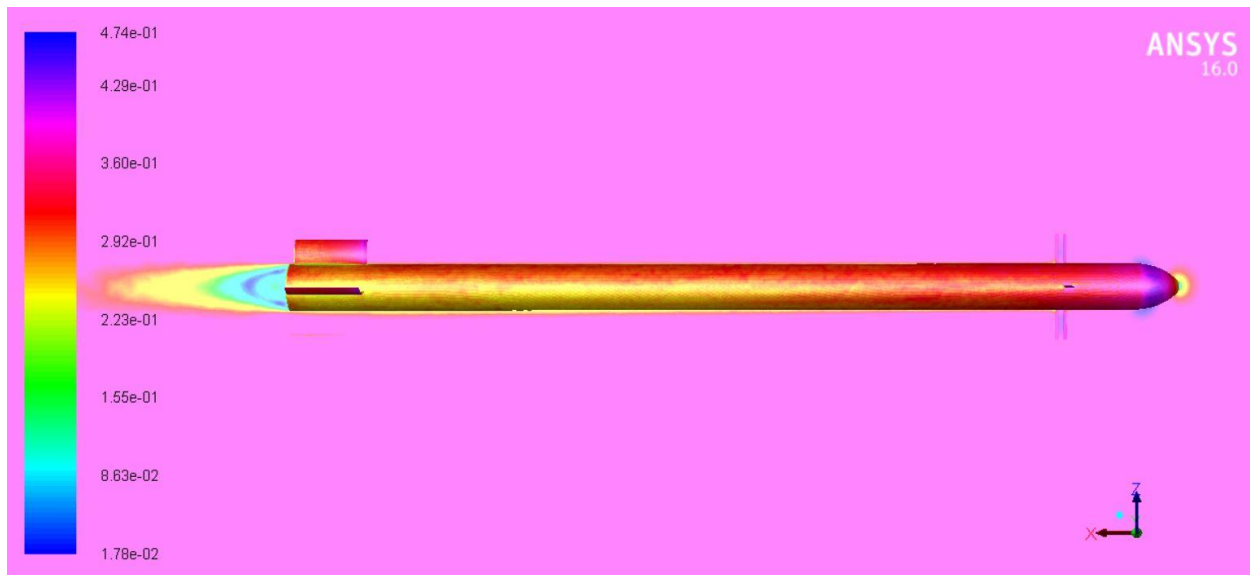


Figure 29 Mach number contours for 0° control deflection and angle of attack $\alpha = -2^\circ$

Figure 30 shows the simulation case with 4 degrees angle of attack and 0 degree pitch control surface deflection. The contours in Figure 30 show that the flow is starting to be disturbed especially behind the trailing edge of the pitch control surfaces.

The contours shown in Figure 30 indicate a drop in the Mach number towards the lower area of the front nose, control surfaces leading edge, and tail fin leading edge of the missile. This is caused by the angled flow represented by 4 degrees angle of attack. Hence, the pressure increases accordingly which results in extra drag on the missile. In addition, the Mach number drop results in an increased total normal force on the missile. This normal force acts upwards which is expected for positive angle of attack flow.

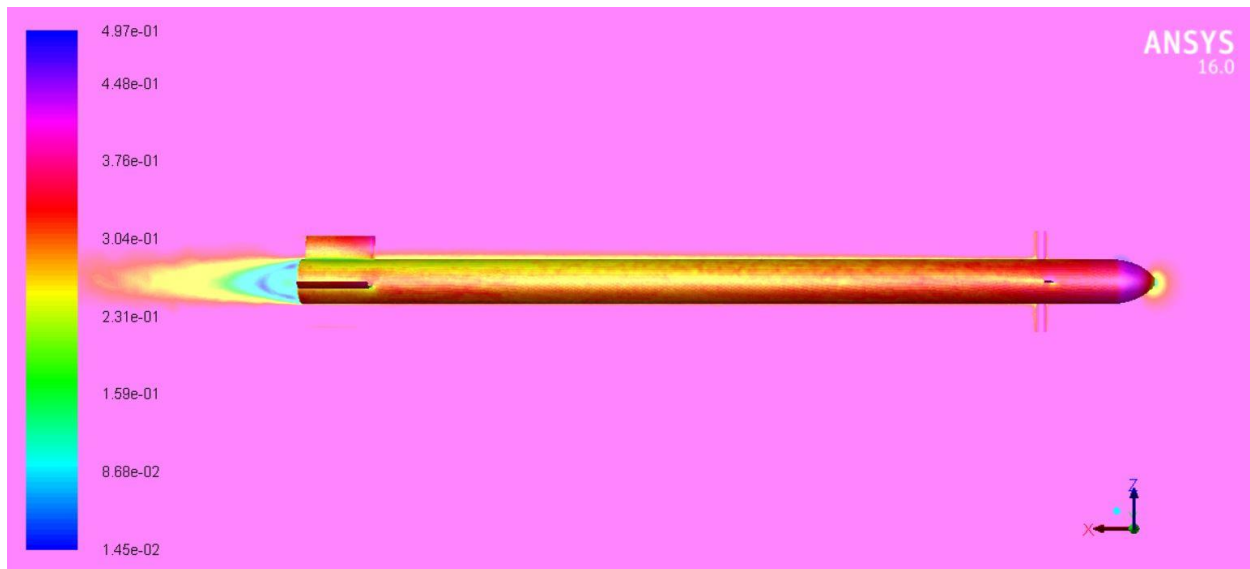


Figure 30 Mach number contours for 0 ° control deflection and angle of attack $\alpha = 4^\circ$

Figure 31 shows the simulation case with -4 degrees angle of attack and 0 degree pitch control surface deflection. The contours in Figure 31 show that the flow is starting to be disturbed especially behind the trailing edge of the pitch control surfaces.

The contours shown in Figure 31 indicate a drop in the Mach number towards the higher area of the front nose, control surfaces leading edge, and tail fin leading edge of the missile. This is caused by the angled flow represented by -4 degrees angle of attack. Hence, the pressure increases accordingly which results in extra drag on the missile. In addition, the Mach number drop results in an increased total normal force on the missile. This normal force acts downwards which is expected for negative angle of attack flow.



Figure 31 Mach number contours for 0° control deflection and angle of attack $\alpha = -4^\circ$

Figure 32 shows the simulation case with 6 degrees angle of attack and 0 degree pitch control surface deflection. The contours in Figure 32 show that the flow is starting to be disturbed especially behind the trailing edge of the pitch control surfaces.

The contours shown in Figure 32 indicate a drop in the Mach number towards the lower area of the front nose, control surfaces leading edge, and tail fin leading edge of the missile. This is caused by the angled flow represented by 6 degrees angle of attack. Hence, the pressure increases accordingly which results in extra drag on the missile. In addition, the Mach number drop results in an increased total normal force on the missile. This normal force acts upwards which is expected for positive angle of attack flow.



Figure 32 Mach number contours for 0 ° control deflection and angle of attack $\alpha = 6^\circ$

Figure 33 shows the simulation case with -6 degrees angle of attack and 0 degree pitch control surface deflection. The contours in Figure 33 show that the flow is starting to be disturbed especially behind the trailing edge of the pitch control surfaces.

The contours shown in Figure 33 indicate a drop in the Mach number towards the higher area of the front nose, control surfaces leading edge, and tail fin leading edge of the missile. This is caused by the angled flow represented by -6 degrees angle of attack. Hence, the pressure increases accordingly which results in extra drag on the missile. In addition, the Mach number drop results in an increased total normal force on the missile. This normal force acts downwards which is expected for negative angle of attack flow.



Figure 33 Mach number contours for 0 ° control deflection and angle of attack $\alpha = -6^\circ$

Figure 34 shows the simulation case with 8 degrees angle of attack and 0 degree pitch control surface deflection. The contours in Figure 34 show that the flow is starting to be disturbed especially behind the trailing edge of the pitch control surfaces.

The contours shown in Figure 34 indicate a drop in the Mach number towards the lower area of the front nose, control surfaces leading edge, and tail fin leading edge of the missile. This is caused by the angled flow represented by 8 degrees angle of attack. Hence, the pressure increases accordingly which results in extra drag on the missile. In addition, the Mach number drop results in an increased total normal force on the missile. This normal force acts upwards which is expected for positive angle of attack flow.



Figure 34 Mach number contours for 0° control deflection and angle of attack $\alpha = 8^\circ$

Figure 35 shows the simulation case with -8 degrees angle of attack and 0 degree pitch control surface deflection. The contours in Figure 35 show that the flow is starting to be disturbed especially behind the trailing edge of the pitch control surfaces.

The contours shown in Figure 35 indicate a drop in the Mach number towards the higher area of the front nose, control surfaces leading edge, and tail fin leading edge of the missile. This is caused by the angled flow represented by -8 degrees angle of attack. Hence, the pressure increases accordingly which results in extra drag on the missile. In addition, the Mach number drop results in an increased total normal force on the missile. This normal force acts downwards which is expected for negative angle of attack flow.



Figure 35 Mach number contours for 0 ° control deflection and angle of attack $\alpha = -8^\circ$

Figure 36 shows the simulation case with 10 degrees angle of attack and 0 degree pitch control surface deflection. The contours in Figure 36 clearly show greater disturbances behind the control surfaces comparing to the previous contours. This flow behavior is expected due to the angled flow caused by the 10 degrees angle of attack.

A greater decrease in Mach number contours is shown in Figure 36. This causes rise in pressure. Therefore, it increases drag. It also causes an increase of the missile's overall aerodynamic forces, such as the normal force. This is expected due to the increase of the angle of attack.

A greater decrease in Mach number contours is also seen in the leading edge of the tail fin as shown in Figure 36. Similarly, this contributes to the overall increase of the missile's aerodynamic forces.

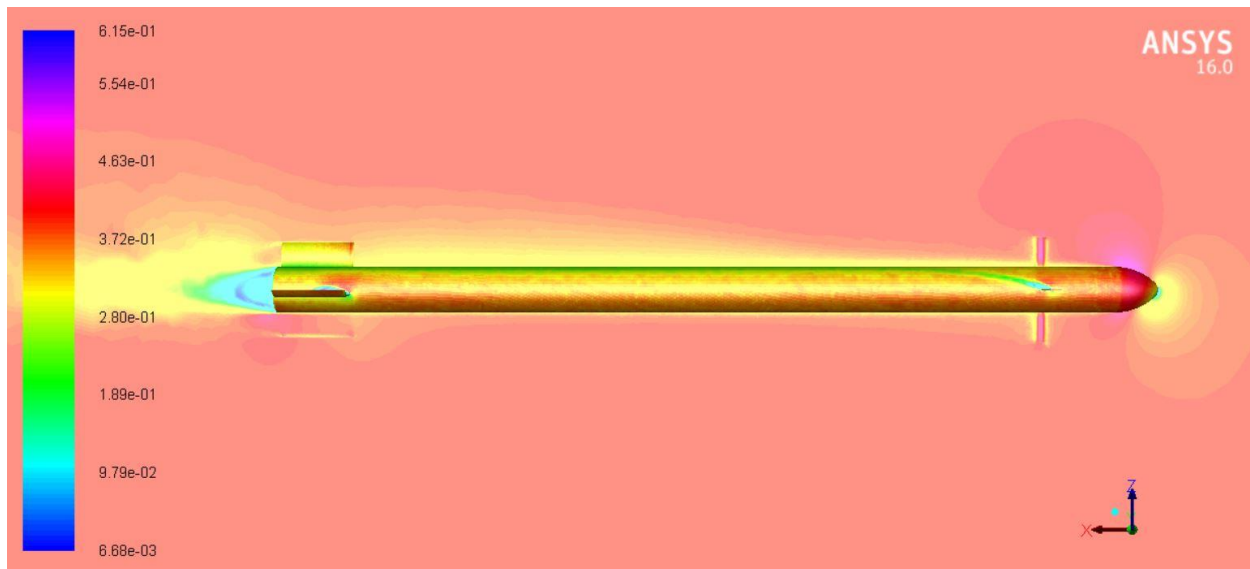


Figure 36 Mach number contours for 0 ° control deflection and angle of attack $\alpha = 10^\circ$

Figure 37 shows the simulation case with -10 degrees angle of attack and 0 degree pitch control surface deflection. The contours in Figure 37 show that the flow is starting to be disturbed especially behind the trailing edge of the pitch control surfaces.

The contours shown in Figure 37 indicate a drop in the Mach number towards the higher area of the front nose, control surfaces leading edge, and tail fin leading edge of the missile. This is caused by the angled flow represented by -10 degrees angle of attack. Hence, the pressure increases accordingly which results in extra drag on the missile. In addition, the Mach number drop results in an increased total normal force on the missile. This normal force acts downwards which is expected for negative angle of attack flow.

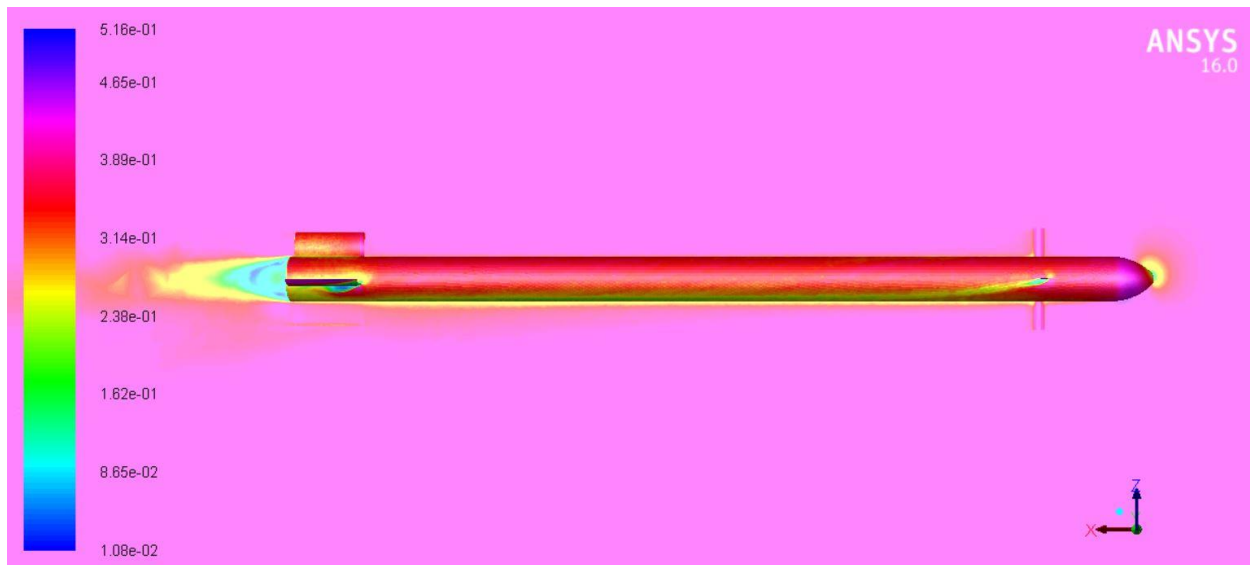


Figure 37 Mach number contours for 0° control deflection and angle of attack $\alpha = -10^\circ$

4.2.1.2. 10 degrees deflection

The Mach number contours with 10 degrees pitch control deflection are presented in Figure 38 - Figure 48 for different angles of attack.

Figure 38 shows the simulation case with 0 degree angle of attack and 10 degrees pitch control surface deflection. It is important to note that even with 0 degree angle of attack, there is a greater flow disturbance behind the control surfaces when comparing to the previous contours in Figure 27. This flow disturbance is due to the deflected control surface in the front.

The Mach number contours shown in Figure 38 do not show any extraordinary behavior around the nose as well as the tail fin. This is because of the zero angle of attack flow.



Figure 38 Mach number contours for 10 ° control deflection and angle of attack $\alpha = 0^\circ$

Figure 39 shows the simulation case with 2 degrees angle of attack and 10 degrees pitch control surface deflection. The contours show clear flow disturbance following the angled flow. The flow disturbance behind the control surfaces in these contours is greater than the contours in the Figure 28. This is caused by the control surface deflection.

It is important to point out that the flow facing the axis of the control surface is the sum of the 2 degrees angle of attack and the 10 degrees control deflection. Thus, the control surfaces are facing a total of 12 degrees angle of attack with respect to the chord line. That is why the disturbance is greater than the case in Figure 28 where the control deflection is 0 degree.

It is important to point out that the Mach number contours near the nose is identical to any simulation with 2 degrees angle of attack.



Therefore, the control deflection has no major effect on the nose Mach number contours distribution.

The contours shown in Figure 39 indicate a drop in the Mach number towards the lower area of the front nose and tail fin leading edge of the missile. This is caused by the angled flow represented by the 2 degrees angle of attack. Hence, the pressure increases accordingly which results in extra drag on the missile. In addition, the Mach number drop results in the increased normal force components on the missile. These normal force components act upward which is expected for positive angle of attack flow.

In addition, the normal force component acting on the control surfaces is directed upwards which can be seen in the flow disturbance direction behind the control surfaces. This is also caused by the Mach number drop seen in Figure 39.

Therefore, the total normal force acting on the missile is directed upwards. This supports the normal force coefficients results presented in Figure 24. The results imply that the missile's normal force goes to zero approximately near -2 degrees angle of attack. Thus, the missile's normal force is directed upwards for 2 degrees angle of attack. It is important to point out that -2 degrees angle of attack gives zero missile's normal force for both 10 and 15 degrees deflection.

According to the pitch moment coefficients results presented in Figure 23, this missile's trim angle of attack for 10 degrees deflection is approximately 4 degrees. Hence, the pitch moment acting on the missile is positive which corresponds to anti-clockwise moment direction

(pitch up direction). It is important to point out that the trim angle of attack is approximately identical for both 10 and 15 degrees deflection.

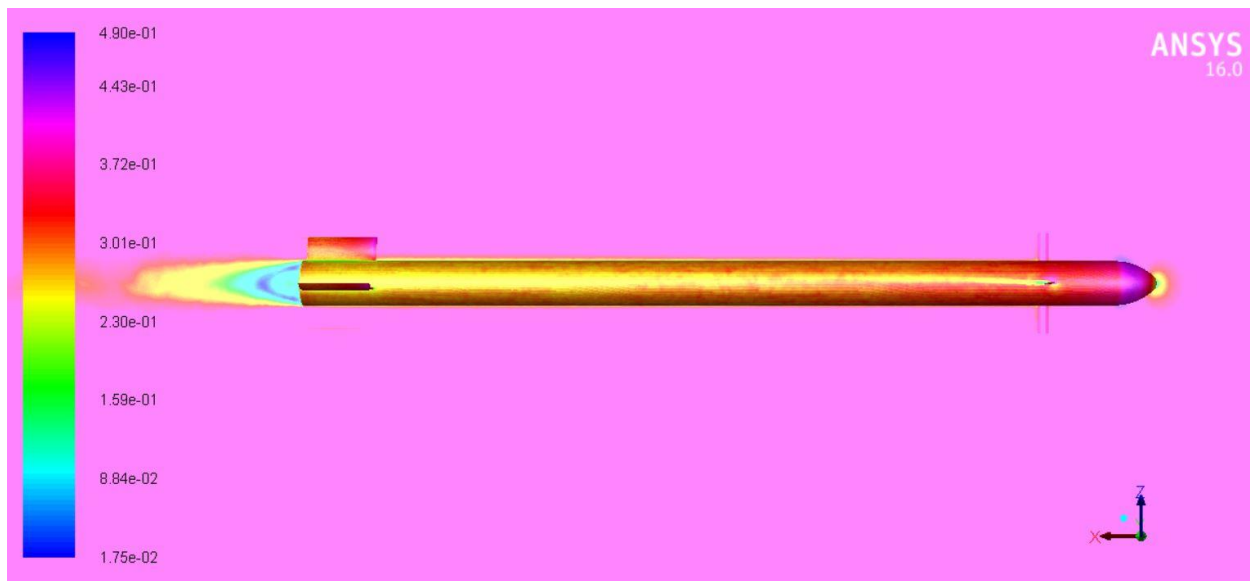


Figure 39 Mach number contours for 10 ° control deflection and angle of attack $\alpha = 2^\circ$

Figure 40 shows the simulation case with -2 degrees angle of attack and 10 degrees pitch control surface deflection. The contours show clear flow disturbance following the angled flow. The flow disturbance behind the control surfaces in these contours is greater than the contours in the Figure 29 which is caused by the control surface deflection as well.

It is important to point out that the flow facing the axis of the control surface is the sum of the -2 degrees angle of attack and the 10 degrees control deflection. Thus, the control surfaces are facing a total of 8 degrees angles of attack with respect to the chord line.



That is why the disturbance is greater than the case in Figure 29 where the control deflection is 0 degree.

It is important to point out that the Mach number contours near the nose is identical to any simulation with -2 degrees angle of attack. Therefore, the control deflection has no major effect on the nose Mach number contours distribution.

The contours shown in Figure 40 indicate a drop in the Mach number towards the higher area of the front nose and tail fin leading edge of the missile. This is caused by the angled flow represented by the -2 degrees angle of attack. Hence, the pressure increases accordingly which results in extra drag on the missile. In addition, the Mach number drop results in the increased normal force components on the missile. These normal force components act downwards which is expected for negative angle of attack flow.

In addition, the normal force component acting on the control surfaces is directed upwards which can be seen in the flow disturbance direction behind the control surfaces. This is also caused by the Mach number drop seen in Figure 40

However, the total normal force acting on the missile is zero which can be noticed in the overall flow disturbance along the full missile. This supports the normal force coefficients results presented in Figure 24. Thus, the missile's normal force is almost zero for flying condition of -2 degrees angle of attack and 10 degrees control deflection.

It is important to note that the simulated angle of attack here is lower than the trim angle of attack obtained from Figure 23. Hence,

the pitch moment acting on the missile is positive. This means that the pitch moment direction is anti-clockwise [pitch up direction] according to the selected axis system.

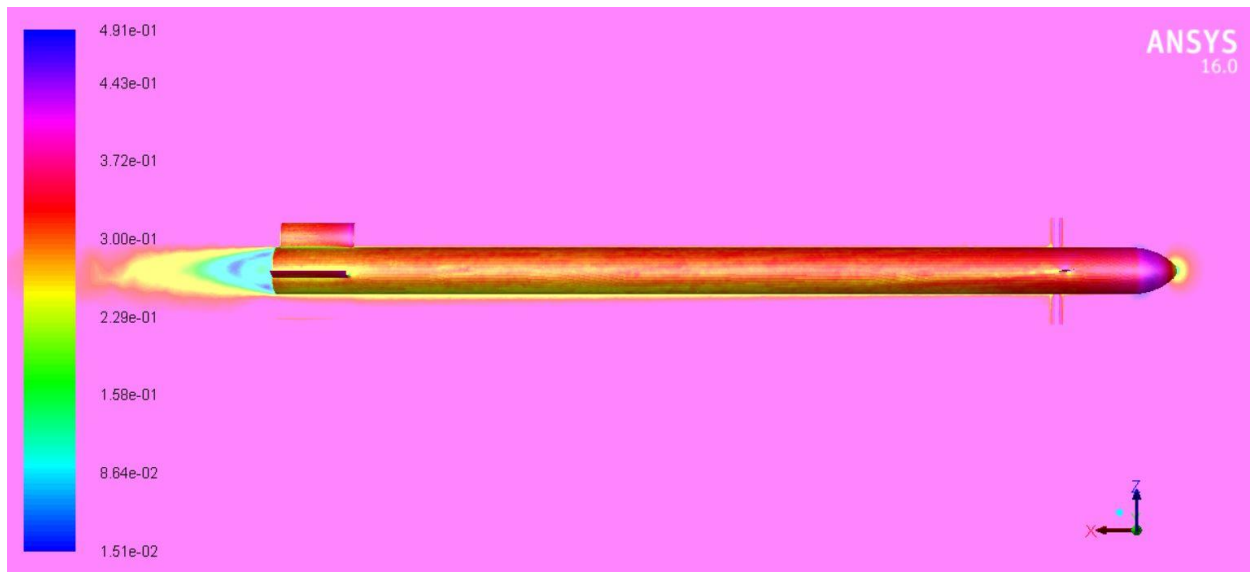


Figure 40 Mach number contours for 10 ° control deflection and angle of attack $\alpha = -2^\circ$

Figure 41 shows the simulation case with 4 degrees angle of attack and 10 degrees pitch control surface deflection. The contours show clear flow disturbance following the angled flow. The flow disturbance behind the control surfaces in these contours is greater than the contours in the Figure 30. This is caused by the control surface deflection.

It is important to point out that the flow facing the axis of the control surface is the sum of 4 degrees angle of attack and the 10 degrees control deflection. Thus, the control surfaces are facing a total of 14 degrees angles of attack with respect to the chord line.



That is why the disturbance is greater than the case in Figure 30 where the control deflection is 0 degree.

It is important to point out that the Mach number contours near the nose is identical to any simulation with 4 degrees angle of attack. Therefore, the control deflection has no major effect on the nose Mach number contours distribution.

The contours shown in Figure 41 indicate a drop in the Mach number towards the lower area of the front nose and tail fin leading edge of the missile. This is caused by the angled flow represented by 4 degrees angle of attack. Hence, the pressure increases accordingly which results in extra drag on the missile. In addition, the Mach number drop results in the increased normal force components on the missile. These normal force components act upwards which is expected for positive angle of attack flow.

In addition, the normal force component acting on the control surfaces is directed upwards which can be seen in the flow disturbance direction behind the control surfaces. This is also caused by the Mach number drop seen in Figure 41.

Therefore, the total normal force acting on the missile is directed upwards. This supports the normal force coefficients results presented in Figure 24. Thus, the missile's normal force is directed upwards for flying condition of 4 degrees angle of attack and 10 degrees control deflection.

According to the pitch moment coefficients results presented in Figure 23, this missile's trim angle of attack for 10 degrees deflection is approximately 4 degrees. Hence, the static pressure contours presented

in Figure 41 represents trim condition for 10 degrees control deflection. This means that the moments in front and behind the pitch moment axis cancel each other.



Figure 41 Mach number contours for 10 ° control deflection and angle of attack $\alpha = 4^\circ$

Figure 42 shows the simulation case with -4 degrees angle of attack and 10 degrees pitch control surface deflection. The contours show clear flow disturbance following the angled flow. The flow disturbance behind the control surfaces in these contours is greater than the contours in the Figure 31. This is caused by the control surface deflection as well.

It is important to point out that the flow facing the axis of the control surface is the sum of -4 degrees angle of attack and the 10 degrees control deflection. Thus, the control surfaces are facing a total of 6 degrees angles of attack with respect to the chord line.



That is why the disturbance is greater than the case in Figure 31 where the control deflection is 0 degree.

It is important to point out that the Mach number contours near the nose is identical to any simulation with -4 degrees angle of attack. Therefore, the control deflection has no major effect on the nose Mach number contours distribution.

The contours shown in Figure 42 indicate a drop in the Mach number towards the higher area of the front nose and tail fin leading edge of the missile. This is caused by the angled flow represented by -4 degrees angle of attack. Hence, the pressure increases accordingly which results in extra drag on the missile. In addition, the Mach number drop results in the increased normal force component on the missile. These normal force components act downwards which is expected for negative angle of attack flow.

In addition, the direction of the normal force component acting on the control surfaces is not clear in Figure 42. This is due to the interaction between positive control deflection with negative angle of attack.

Therefore, the total normal force acting on the missile is not clear in the contours shown in Figure 42. However, the normal force coefficients results presented in Figure 24 can be used to define the missile's normal force direction. Since the angle of attack is -4 degrees, the missile's normal force is directed downwards when the control surface deflection is 10 degrees.

It is important to note that the simulated angle of attack here is lower than the trim angle of attack obtained from Figure 23. Hence,

the pitch moment acting on the missile is positive. This means that the pitch moment direction is anti-clockwise [pitch up direction] according to the selected axis system.

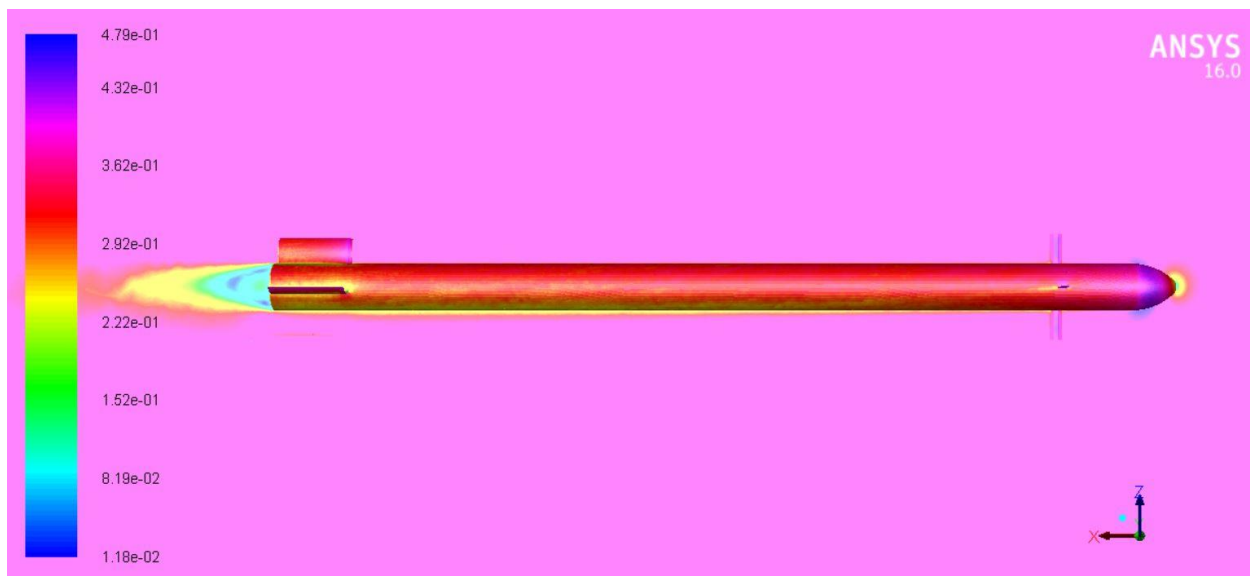


Figure 42 Mach number contours for 10 ° control deflection and angle of attack $\alpha = -4^\circ$

Figure 43 shows the simulation case with 6 degrees angle of attack and 10 degrees pitch control surface deflection. The contours show clear flow disturbance following the angled flow. The flow disturbance behind the control surfaces in these contours is greater than the contours in the Figure 32. This is caused by the control surface deflection.

It is important to point out that the flow facing the axis of the control surface is the sum of 6 degrees angle of attack and the 10 degrees control deflection. Thus, the control surfaces are facing a total of 16 degrees angles of attack with respect to the chord line.



That is why the disturbance is greater than the case in Figure 32 where the control deflection is 0 degree.

It is important to point out that the Mach number contours near the nose is identical to any simulation with 6 degrees angle of attack. Therefore, the control deflection has no major effect on the nose Mach number contours distribution.

The contours shown in Figure 43 indicate a drop in the Mach number towards the lower area of the front nose and tail fin leading edge of the missile. This is caused by the angled flow represented by 6 degrees angle of attack. Hence, the pressure increases accordingly which results in extra drag on the missile. In addition, the Mach number drop results in the increased normal force components on the missile. These normal force components act upwards which is expected for positive angle of attack flow.

In addition, the normal force component acting on the control surfaces is directed upwards which can be seen in the flow disturbance direction behind the control surfaces. This is also caused by the Mach number drop seen in Figure 43.

Therefore, the total normal force acting on the missile is directed upwards. This supports the normal force coefficients results presented in Figure 24. Thus, the missile's normal force is directed upwards for flying conditions of 6 degrees angle of attack and 10 degrees control deflection.

It is important to note that the simulated angle of attack here is greater than the trim angle of attack obtained from Figure 23. Hence, the pitch moment acting on the missile is negative. This means that

the pitch moment direction is clockwise [pitch down direction] according to the selected axis system.



Figure 43 Mach number contours for 10 ° control deflection and angle of attack $\alpha = 6^\circ$

Figure 44 shows the simulation case with -6 degrees angle of attack and 10 degrees pitch control surface deflection. The contours show clear flow disturbance following the angled flow. The flow disturbance behind the control surfaces in these contours is greater than the contours in the Figure 33 which is caused by the control surface deflection as well.

It is important to point out that the flow facing the axis of the control surface is the sum of -6 degrees angle of attack and the 10 degrees control deflection. Thus, the control surfaces are facing a total of 4 degrees angles of attack with respect to the chord line. That is why the disturbance is greater than the case in Figure 33 where the control deflection is 0 degree.



It is important to point out that the Mach number contours near the nose is identical to any simulation with -6 degrees angle of attack. Therefore, the control deflection has no major effect on the nose Mach number contours distribution.

The contours shown in Figure 44 indicate a drop in the Mach number towards the higher area of the front nose and tail fin leading edge of the missile. This is caused by the angled flow represented by -6 degrees angle of attack. Hence, the pressure increases accordingly which results in extra drag on the missile. In addition, the Mach number drop results in the increased normal force components on the missile. These normal force components act downwards which is expected for negative angle of attack flow.

In addition, the normal force component acting on the control surfaces is directed downwards which is clearly seen in the flow disturbance direction behind the control surfaces. This is also caused by the Mach number drop seen in Figure 44.

Therefore, the total normal force acting on the missile is directed downwards. This supports the normal force coefficients results presented in Figure 24. Thus, the missile's normal force is directed upwards for flying conditions of -6 degrees angle of attack and 10 degrees control deflection.

It is important to note that the simulated angle of attack here is lower than the trim angle of attack obtained from Figure 23. Hence, the pitch moment acting on the missile is positive. This means that the pitch moment direction is anti-clockwise [pitch up direction] according to the selected axis system.

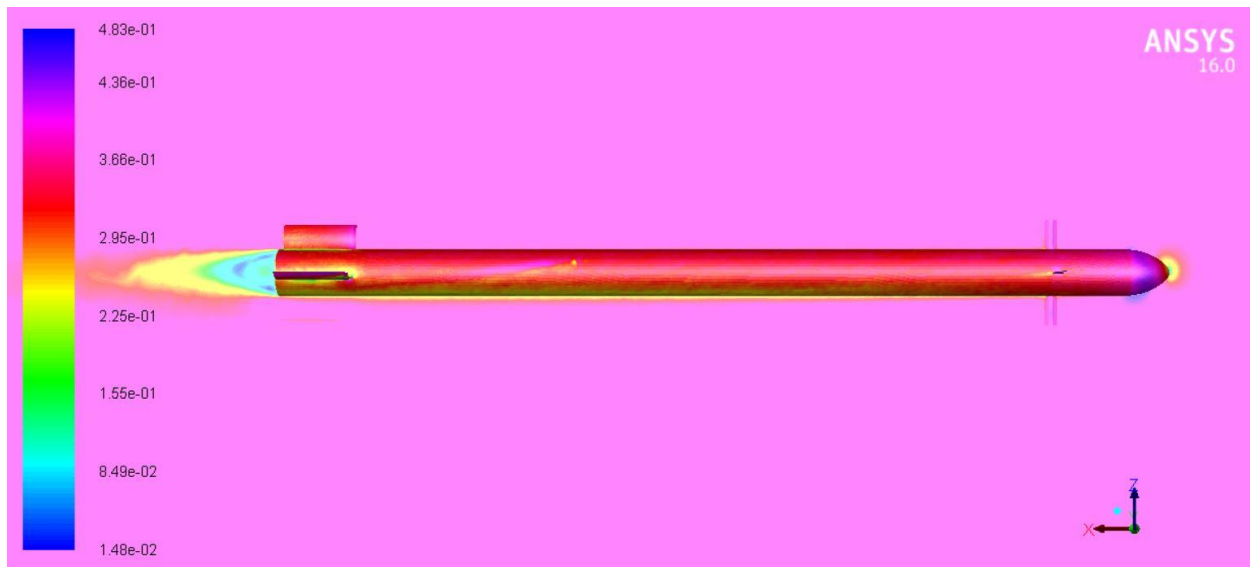


Figure 44 Mach number contours for 10 ° control deflection and angle of attack $\alpha = -6^\circ$

Figure 45 shows the simulation case with 8 degrees angle of attack and 10 degrees pitch control surface deflection. The contours show clear flow disturbance following the angled flow. The flow disturbance behind the control surfaces in these contours is greater than the contours in the Figure 34. This is caused by the control surface deflection as well.

It is important to point out that the flow facing the axis of the control surface is the sum of 8 degrees angle of attack and the 10 degrees control deflection. Thus, the control surfaces are facing a total of 18 degrees angles of attack with respect to the chord line. That is why the disturbance is greater than the case in Figure 34 where the control deflection is 0 degree.

It is important to point out that the Mach number contours near the nose is identical to any simulation with 8 degrees angle of attack.



Therefore, the control deflection has no major effect on the nose Mach number contours distribution.

The contours shown in Figure 45 indicate a drop in the Mach number towards the lower area of the front nose and tail fin leading edge of the missile. This is caused by the angled flow represented by 8 degrees angle of attack. Hence, the pressure increases accordingly which results in extra drag on the missile. In addition, the Mach number drop results in the increased normal force components on the missile. These normal force components act upwards which is expected for positive angle of attack flow.

In addition, the normal force component acting on the control surfaces is directed upwards which can be seen in the flow disturbance direction behind the control surfaces. This is also caused by the Mach number drop seen in Figure 45.

Therefore, the total normal force acting on the missile is directed upwards. This supports the normal force coefficients results presented in Figure 24. Thus, the missile's normal force is directed upwards for flying conditions of 8 degrees angle of attack and 10 degrees control deflection. In addition, the flow behind the control surfaces starts to separate which is clearly seen in Figure 45.

It is important to note that the simulated angle of attack here is greater than the trim angle of attack obtained from Figure 23. Hence, the pitch moment acting on the missile is negative. This means that the pitch moment direction is clockwise [pitch down direction] according to the selected axis system.



Figure 45 Mach number contours for 10 ° control deflection and angle of attack $\alpha = 8^\circ$

Figure 46 shows the simulation case with -8 degrees angle of attack and 10 degrees pitch control surface deflection. The contours show clear flow disturbance following the angled flow. The flow disturbance behind the control surfaces in these contours is greater than the contours in the Figure 35. This is caused by the control surface deflection as well.

It is important to point out that the flow facing the axis of the control surface is the sum of -8 degrees angle of attack and the 10 degrees control deflection. Thus, the control surfaces are facing a total of 2 degrees angles of attack with respect to the chord line. That is why the disturbance is greater than the case in Figure 35 where the control deflection is 0 degree.

It is important to point out that the Mach number contours near the nose is identical to any simulation with -8 degrees angle of attack.



Therefore, the control deflection has no major effect on the nose Mach number contours distribution.

The contours shown in Figure 46 indicate a drop in the Mach number towards the higher area of the front nose and tail fin leading edge of the missile. This is caused by the angled flow represented by -8 degrees angle of attack. Hence, the pressure increases accordingly which results in extra drag on the missile. In addition, the Mach number drop results in the increased normal force components on the missile. These normal force components act downwards which is expected for negative angle of attack flow.

In addition, the normal force component acting on the control surfaces is directed downwards which can be seen in the flow disturbance direction behind the control surfaces. This is also caused by the Mach number drop seen in Figure 46.

Therefore, the total normal force acting on the missile is directed downwards. This supports the normal force coefficients results presented in Figure 24. Thus, the missile's normal force is directed downwards for flying conditions of -8 degrees angle of attack and 10 degrees control deflection.

It is important to note that the simulated angle of attack here is lower than the trim angle of attack obtained from Figure 23. Hence, the pitch moment acting on the missile is positive. This means that the pitch moment direction is anti-clockwise [pitch up direction] according to the selected axis system.

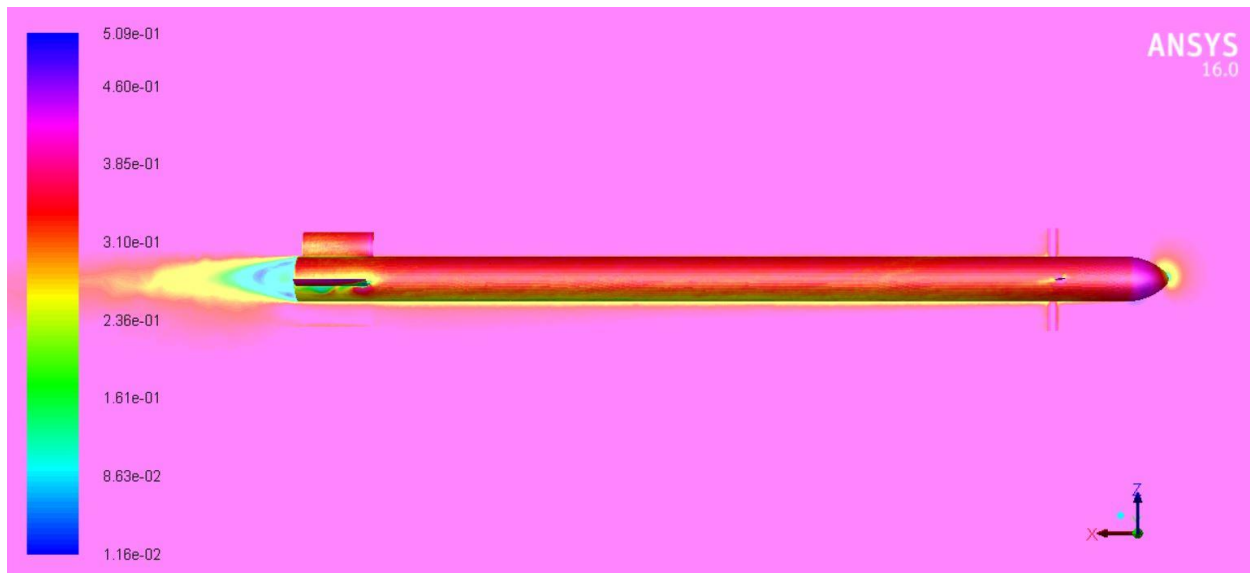


Figure 46 Mach number contours for 10 ° control deflection and angle of attack $\alpha = -8^\circ$

Figure 47 shows the simulation case with 10 degrees angle of attack and 10 degrees pitch control surface deflection. It is important to mention that the flow is starting to separate as highlighted by the black circle in Figure 47.

This flow behavior is expected due to the combined high angled flow generated by the deflected control surface and high angle of attack. 10 degrees angle of attack as well as 10 degrees control deflection results in 20 degrees flow angle with respect to the control surface chord line.

The Mach number contours towards the nose of the missile is identical to any simulation with angle of attack 10 degrees. However, the Mach number contours towards the tail fin are affected by the disturbed flow as seen in Figure 47.



Figure 47 Mach number contours for 10 ° control deflection and angle of attack $\alpha = 10^\circ$

Figure 48 shows the simulation case with -10 degrees angle of attack and 10 degrees pitch control surface deflection. The contours show clear flow disturbance following the angled flow. The flow disturbance behind the control surfaces in these contours is greater than the contours in the Figure 37. This is caused by the control surface deflection as well.

It is important to point out that the flow facing the axis of the control surface is the sum of -10 degrees angle of attack and the 10 degrees control deflection. Thus, the control surfaces are facing a total of 0 degree angles of attack with respect to the chord line. That is why the disturbance is greater than the case in Figure 37 where the control deflection is 0 degree.

It is important to point out that the Mach number contours near the nose is identical to any simulation with -10 degrees angle of attack.



Therefore, the control deflection has no major effect on the nose Mach number contours distribution.

The contours shown in Figure 48 indicate a drop in the Mach number towards the higher area of the front nose and tail fin leading edge of the missile. This is caused by the angled flow represented by -10 degrees angle of attack. Hence, the pressure increases accordingly which results in extra drag on the missile. In addition, the Mach number drop results in the increased normal force components on the missile. These normal force components act downwards which is expected for negative angle of attack flow.

In addition, the normal force component acting on the control surfaces is directed downwards which can be seen in the flow disturbance direction behind the control surfaces. This is also caused by the Mach number drop seen in Figure 48.

Therefore, the total normal force acting on the missile is directed downwards. This supports the normal force coefficients results presented in Figure 24. Thus, the missile's normal force is directed downwards for flying conditions of -10 degrees angle of attack and 10 degrees control deflection.

It is important to note that the simulated angle of attack here is lower than the trim angle of attack obtained from Figure 23. Hence, the pitch moment acting on the missile is positive. This means that the pitch moment direction is anti-clockwise [pitch up direction] according to the selected axis system.

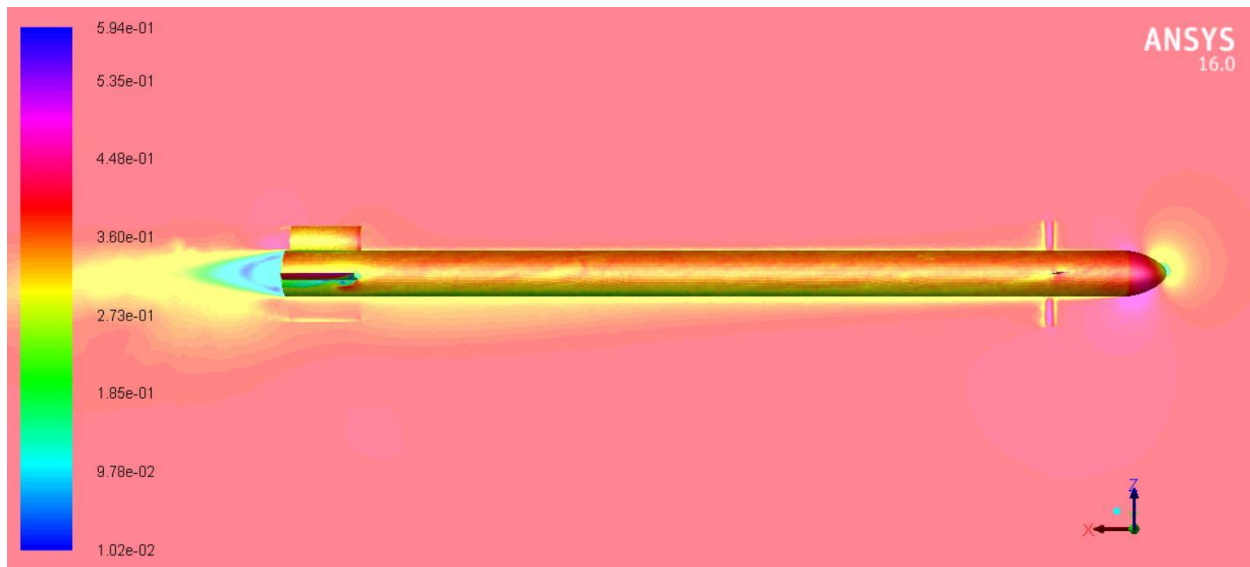


Figure 48 Mach number contours for 10 ° control deflection and angle of attack $\alpha = -10$

4.2.1.3. 15 degrees deflection

The Mach number contours with 15 degrees pitch control deflection are presented in Figure 49 - Figure 59 for different angles of attack.

Figure 49 shows the simulation case with 0 degree angle of attack and 15 degrees of pitch control surface deflection. The contours show great disturbance even though the angle of attack is 0 degree. This disturbance is due to the highly deflected pitch control surface.

The Mach number contours towards the nose shown in Figure 49 do not indicate any extraordinary behavior for angle of attack 0 degree. However, it is important to mention that the disturbance occurring near the leading edge of the tail fin is mainly caused by the high deflection of the front canard control surface.



Figure 49 Mach number contours for 15 ° control deflection and angle of attack $\alpha = 0^\circ$

Figure 50 shows the simulation case with 2 degrees angle of attack and 15 degrees pitch control surface deflection. The contours show clear flow disturbance following the angled flow. The flow disturbance behind the control surfaces in these contours is greater than the contours in the Figure 39. This is caused by the control surface deflection of 10 degrees.

It is important to point out that the flow facing the axis of the control surface is the sum of 2 degrees angle of attack and the 15 degrees control deflection. Thus, the control surfaces are facing a total of 17 degrees angles of attack with respect to the chord line. That is why the disturbance is greater than the case in Figure 39 where the control deflection is 10 degrees.

It is important to point out that the Mach number contours near the nose is identical to any simulation with 2 degrees angle of attack.



Therefore, the control deflection has no major effect on the nose Mach number contours distribution.

The contours shown in Figure 50 indicate a drop in the Mach number towards the lower area of the front nose and tail fin leading edge of the missile. This is caused by the angled flow represented by 2 degrees angle of attack. Hence, the pressure increases accordingly which results in extra drag on the missile. In addition, the Mach number drop results in the increased normal force components on the missile. These normal force components act upwards which is expected for positive angle of attack flow.

In addition, the normal force component acting on the control surfaces is directed upwards which can be seen in the flow disturbance direction behind the control surfaces. This is also caused by the Mach number drop seen in Figure 50.

Therefore, the total normal force acting on the missile is directed upwards. This supports the normal force coefficients results presented in Figure 24 which imply that the missile's normal force goes to zero approximately near -2 degrees angle of attack. Thus, the missile's normal force is directed upwards for 2 degrees angle of attack.

According to the pitch moment coefficients results presented in Figure 23, the missile's trim angle of attack for 15 degrees deflection is approximately 4 degrees. Hence, the pitch moment acting on the missile is positive which corresponds to anti-clockwise moment direction [pitch up direction]. It is important to point out that the trim angle of attack is approximately identical for both 10 and 15 degrees deflection.

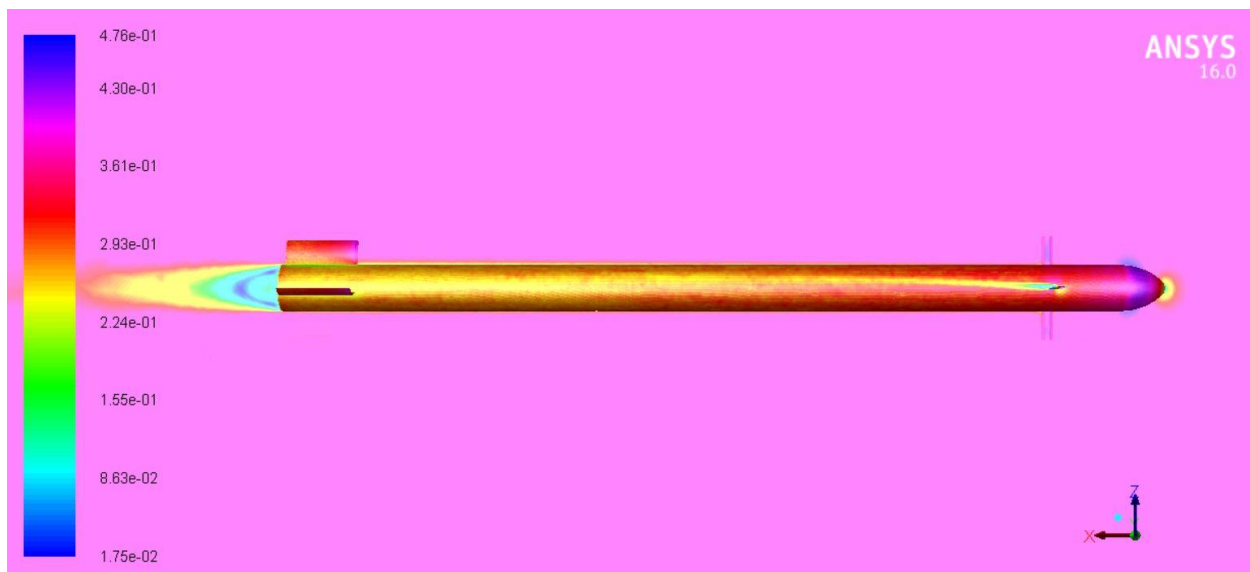


Figure 50 Mach number contours for 15 ° control deflection and angle of attack $\alpha = 2^\circ$

Figure 51 shows the simulation case with -2 degrees angle of attack and 15 degrees pitch control surface deflection. The contours show clear flow disturbance following the angled flow. The flow disturbance behind the control surfaces in these contours is greater than the contours in the Figure 40. This is caused by the control surface deflection as well.

It is important to point out that the flow facing the axis of the control surface is the sum of -2 degrees angle of attack and the 15 degrees control deflection. Thus, the control surfaces are facing a total of 13 degrees angles of attack with respect to the chord line. That is why the disturbance is greater than the case in Figure 40 where the control deflection is 10 degrees.

It is important to point out that the Mach number contours near the nose is identical to any simulation with -2 degrees angle of attack.



Therefore, the control deflection has no major effect on the nose Mach number contours distribution.

The contours shown in Figure 51 indicate a drop in the Mach number towards the higher area of the front nose and tail fin leading edge of the missile. This is caused by the angled flow represented by -2 degrees angle of attack. Hence, the pressure increases accordingly which results in extra drag on the missile. In addition, the Mach number drop results in the increased normal force components on the missile. These normal force components act downwards which is expected for negative angle of attack flow.

In addition, the normal force component acting on the control surfaces is directed upwards which can be seen in the flow disturbance direction behind the control surfaces. This is also caused by the Mach number drop seen in Figure 51.

However, the total normal force acting on the missile is zero which can be noticed in the overall flow disturbance along the full missile. This supports the normal force coefficients results presented in Figure 24. Thus, the missile's normal force is almost zero for flying condition of -2 degrees angle of attack and 15 degrees control deflection.

It is important to note that the simulated angle of attack here is lower than the trim angle of attack obtained from Figure 23. Hence, the pitch moment acting on the missile is positive. This means that the pitch moment direction is anti-clockwise [pitch up direction] according to the selected axis system.

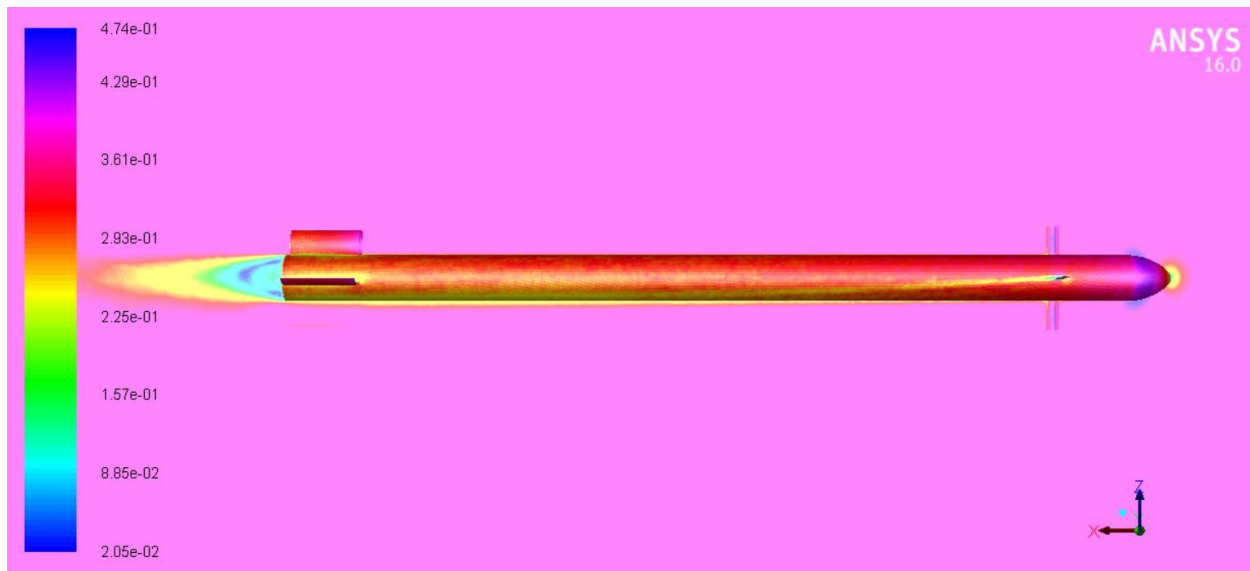


Figure 51 Mach number contours for 15 ° control deflection and angle of attack $\alpha = -2^\circ$

Figure 52 shows the simulation case with 4 degrees angle of attack and 15 degrees pitch control surface deflection. The contours show clear flow disturbance following the angled flow. The flow disturbance behind the control surfaces in these contours is greater than the contours in the Figure 41. This is caused by the control surface deflection of 10 degrees.

It is important to point out that the flow facing the axis of the control surface is the sum of 4 degrees angle of attack and the 15 degrees control deflection. Thus, the control surfaces are facing a total of 19 degrees angles of attack with respect to the chord line. That is why the disturbance is greater than the case in Figure 41 where the control deflection is 10 degrees.

It is important to point out that the Mach number contours near the nose is identical to any simulation with 4 degrees angle of attack.



Therefore, the control deflection has no major effect on the nose Mach number contours distribution.

The contours shown in Figure 52 indicate a drop in the Mach number towards the lower area of the front nose and tail fin leading edge of the missile. This is caused by the angled flow represented by 4 degrees angle of attack. Hence, the pressure increases accordingly which results in extra drag on the missile. In addition, the Mach number drop results in the increased normal force components on the missile. These normal force components act upwards which is expected for positive angle of attack flow.

In addition, the normal force component acting on the control surfaces is directed upwards which can be seen in the flow disturbance direction behind the control surfaces. This is also caused by the Mach number drop seen in Figure 52.

Therefore, the total normal force acting on the missile is directed upwards. This supports the normal force coefficients results presented in Figure 24. Thus, the missile's normal force is directed upwards for flying condition of 4 degrees angle of attack and 15 degrees control deflection.

According to the pitch moment coefficients results presented in Figure 23, the missile's trim angle of attack for 15 degrees deflection is approximately 4 degrees. Hence, the static pressure contours presented in Figure 52 represents trim condition for 15 degrees control deflection. This means that the moments in front and behind the pitch moment axis cancel each other.

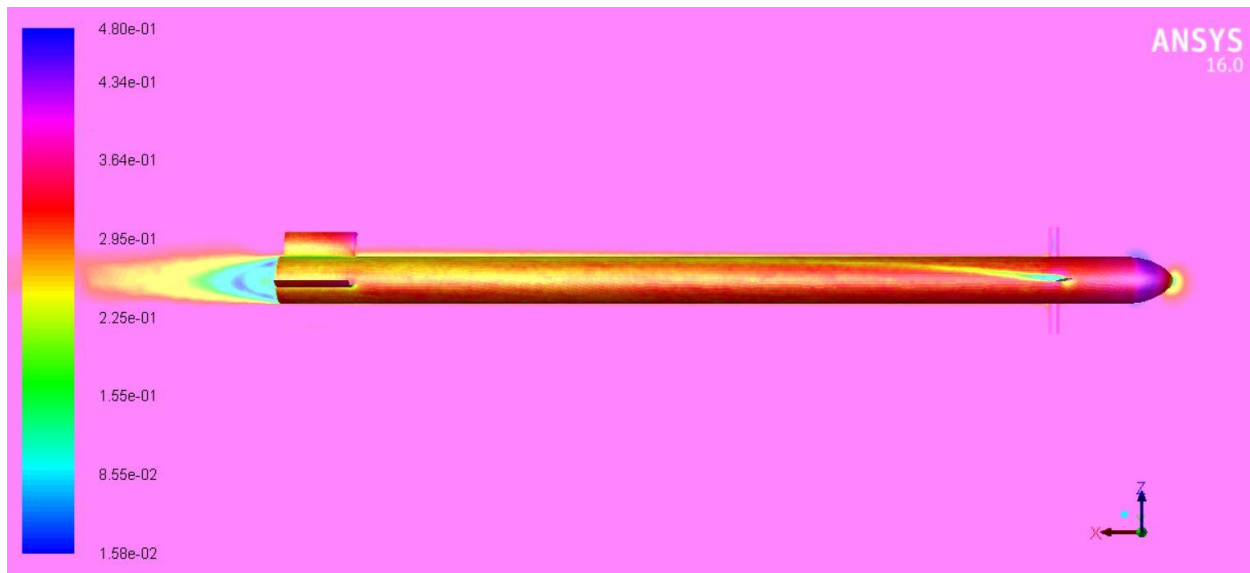


Figure 52 Mach number contours for 15 ° control deflection and angle of attack $\alpha = 4^\circ$

Figure 53 shows the simulation case with -4 degrees angle of attack and 15 degrees pitch control surface deflection. The contours show clear flow disturbance following the angled flow. The flow disturbance behind the control surfaces in these contours is greater than the contours in the Figure 42. This is caused by the control surface deflection of 10 degrees.

It is important to point out that the flow facing the axis of the control surface is the sum of -4 degrees angle of attack and the 15 degrees control deflection. Thus, the control surfaces are facing a total of 11 degrees angles of attack with respect to the chord line. That is why the disturbance is greater than the case in Figure 42 where the control deflection is 10 degrees.

It is important to point out that the Mach number contours near the nose is identical to any simulation with -4 degrees angle of attack.



Therefore, the control deflection has no major effect on the nose Mach number contours distribution.

The contours shown in Figure 53 indicate a drop in the Mach number towards the higher area of the front nose and tail fin leading edge of the missile. This is caused by the angled flow represented by -4 degrees angle of attack. Hence, the pressure increases accordingly which results in extra drag on the missile. In addition, the Mach number drop results in the increased normal force components on the missile. These normal force components act downwards which is expected for negative angle of attack flow.

In addition, the direction of the normal force component acting on the control surfaces is not clear in Figure 53. This is due to the interaction between positive control deflection with negative angle of attack.

Therefore, the total normal force acting on the missile is not clear in the contours shown in Figure 53. However, the normal force coefficients results presented in Figure 24 can be used to define the missile's normal force direction. Since angle of attack is -4 degrees, the missile's normal force is directed downwards when control surface deflection is 10 degrees.

It is important to note that the simulated angle of attack here is lower than the trim angle of attack obtained from Figure 23. Hence, the pitch moment acting on the missile is positive. This means that the pitch moment direction is anti-clockwise [pitch up direction] according to the selected axis system.

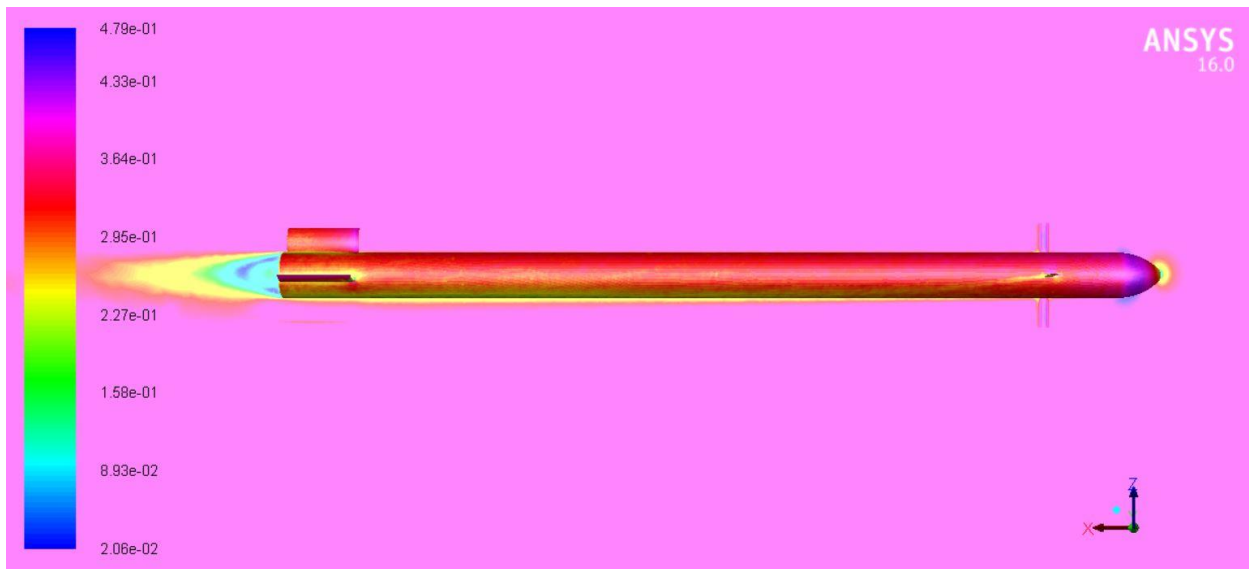


Figure 53 Mach number contours for 15 ° control deflection and angle of attack $\alpha = -4^\circ$

Figure 54 shows the case with 6 degrees angle of attack and 15 degrees pitch control surface deflection. The contours show clear flow disturbance following the angled flow. The flow disturbance behind the control surfaces in these contours is greater than the contours in the Figure 43. This is caused by the control surface deflection of 10 degrees.

It is important to point out that the flow facing the axis of the control surface is the sum of 6 degrees angle of attack and the 15 degrees control deflection. Thus, the control surfaces are facing a total of 21 degrees angles of attack with respect to the chord line. That is why the disturbance is greater than the case in Figure 43 where the control deflection is 10 degrees.

It is important to point out that the Mach number contours near the nose is identical to any simulation with 6 degrees angle of attack.



Therefore, the control deflection has no major effect on the nose Mach number contours distribution.

The contours shown in Figure 54 indicate a drop in the Mach number towards the lower area of the front nose and tail fin leading edge of the missile. This is caused by the angled flow represented by 6 degrees angle of attack. Hence, the pressure increases accordingly which results in extra drag on the missile. In addition, the Mach number drop results in the increased normal force components on the missile. These normal force components act upwards which is expected for positive angle of attack flow.

In addition, the normal force component acting on the control surfaces is directed upwards which can be seen in the flow disturbance direction behind the control surfaces. This is also caused by the Mach number drop seen in Figure 54.

Therefore, the total normal force acting on the missile is directed upwards. This supports the normal force coefficients results presented in Figure 24. Thus, the missile's normal force is directed upwards for flying conditions of 6 degrees angle of attack and 15 degrees control deflection.

It is important to note that the simulated angle of attack here is greater than the trim angle of attack obtained from Figure 23. Hence, the pitch moment acting on the missile is negative. This means that the pitch moment direction is clockwise [pitch down direction] according to the selected axis system.

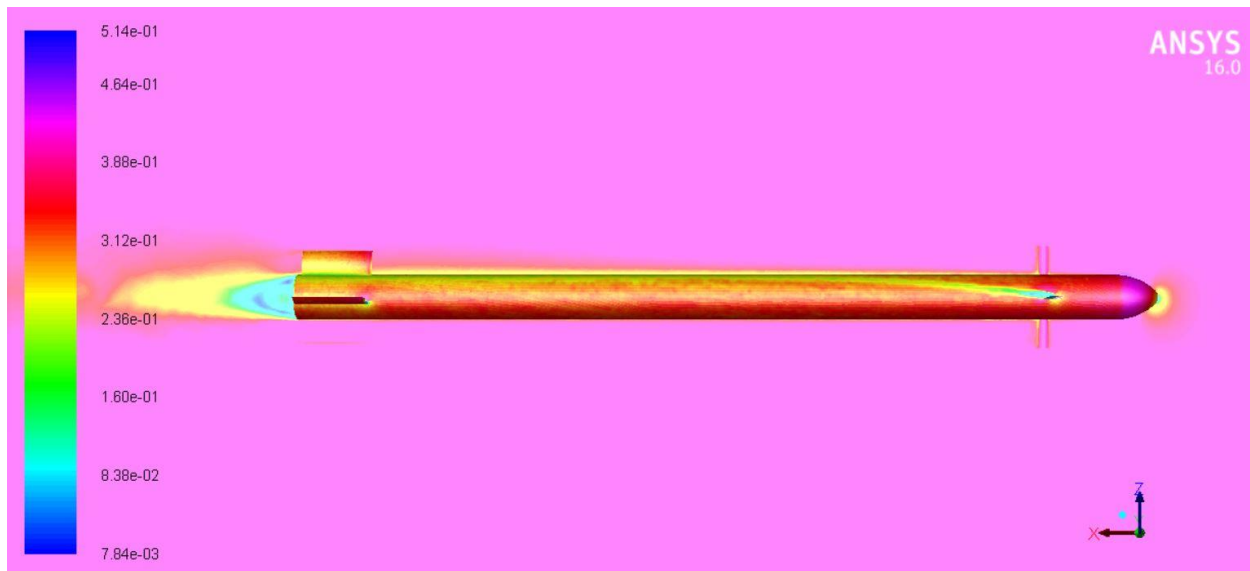


Figure 54 Mach number contours for 15 ° control deflection and angle of attack $\alpha = 6^\circ$

Figure 55 shows the simulation case with -6 degrees angle of attack and 15 degrees pitch control surface deflection. The contours show clear flow disturbance following the angled flow. The flow disturbance behind the control surfaces in these contours is greater than the contours in the Figure 44. This is caused by the control surface deflection of 10 degrees.

It is important to point out that the flow facing the axis of the control surface is the sum of -6 degrees angle of attack and the 15 degrees control deflection. Thus, the control surfaces are facing a total of 9 degrees angles of attack with respect to the chord line. That is why the disturbance is greater than the case in Figure 44 where the control deflection is 10 degrees.

It is important to point out that the Mach number contours near the nose is identical to any simulation with -6 degrees angle of attack.



Therefore, the control deflection has no major effect on the nose Mach number contours distribution.

The contours shown in Figure 55 indicate a drop in the Mach number towards the higher area of the front nose and tail fin leading edge of the missile. This is caused by the angled flow represented by -6 degrees angle of attack. Hence, the pressure increases accordingly which results in extra drag on the missile. In addition, the Mach number drop results in the increased normal force components on the missile. These normal force components act downwards which is expected for negative angle of attack flow.

In addition, the normal force component acting on the control surfaces is directed downwards which is seen in the flow disturbance direction behind the control surfaces. This is also caused by the Mach number drop seen in Figure 55.

Therefore, the total normal force acting on the missile is directed downwards. This supports the normal force coefficients results presented in Figure 24. Thus, the missile's normal force is directed upwards for flying conditions of -6 degrees angle of attack and 15 degrees control deflection.

It is important to note that the simulated angle of attack here is lower than the trim angle of attack obtained from Figure 23. Hence, the pitch moment acting on the missile is positive. This means that the pitch moment direction is anti-clockwise [pitch up direction] according to the selected axis system.

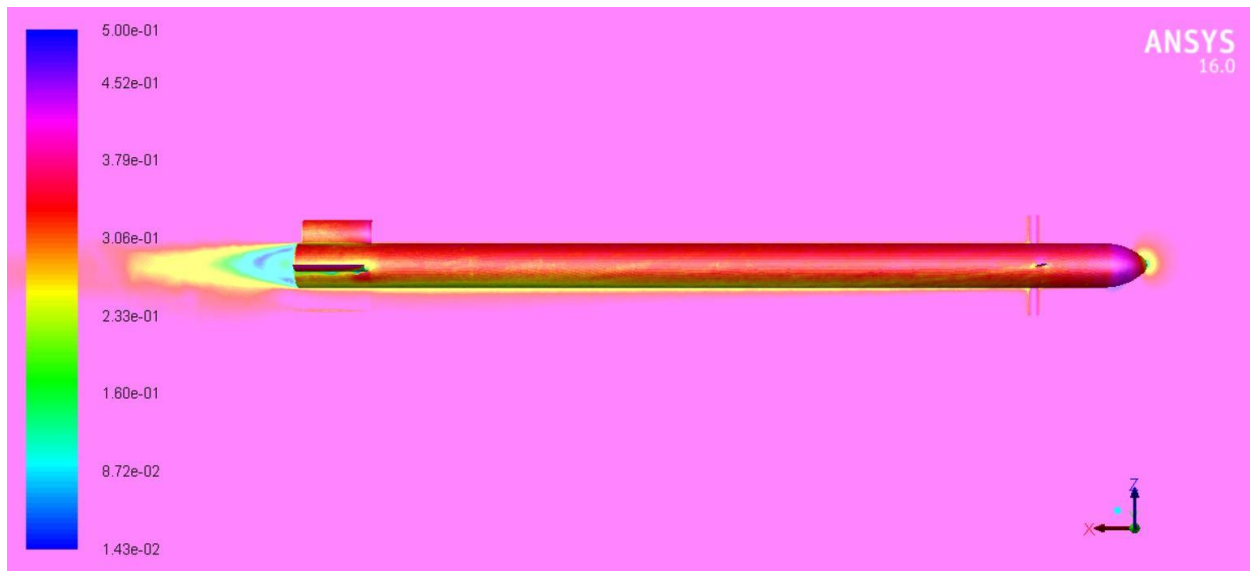


Figure 55 Mach number contours for 15 ° control deflection and angle of attack $\alpha = -6^\circ$

Figure 56 shows the simulation case with 8 degrees angle of attack and 15 degrees pitch control surface deflection. The contours show clear flow disturbance following the angled flow. The flow disturbance behind the control surfaces in these contours is greater than the contours in the Figure 45. This is caused by the control surface deflection of 10 degrees.

It is important to point out that the flow facing the axis of the control surface is the sum of 8 degrees angle of attack and the 15 degrees control deflection. Thus, the control surfaces are facing a total of 23 degrees angles of attack with respect to the chord line. That is why the disturbance is greater than the case in Figure 45 where the control deflection is 10 degrees.

It is important to point out that the Mach number contours near the nose is identical to any simulation with 8 degrees angle of attack.



Therefore, the control deflection has no major effect on the nose Mach number contours distribution.

The contours shown in Figure 56 indicate a drop in the Mach number towards the lower area of the front nose and tail fin leading edge of the missile. This is caused by the angled flow represented by 8 degrees angle of attack. Hence, the pressure increases accordingly which results in extra drag on the missile. In addition, the Mach number drop results in the increased normal force components on the missile. These normal force components act upwards which is expected for positive angle of attack flow.

In addition, the normal force component acting on the control surfaces is directed upwards which can be seen in the flow disturbance direction behind the control surfaces. This is also caused by the Mach number drop seen in Figure 56.

Therefore, the total normal force acting on the missile is directed upwards. This supports the normal force coefficients results presented in Figure 24. Thus, the missile's normal force is directed upwards for flying conditions of 8 degrees angle of attack and 15 degrees control deflection. In addition, the flow behind the control surfaces starts to separate which is clearly seen in Figure 56.

It is important to note that the simulated angle of attack here is greater than the trim angle of attack obtained from Figure 23. Hence, the pitch moment acting on the missile is negative. This means that the pitch moment direction is clockwise [pitch down direction] according to the selected axis system.

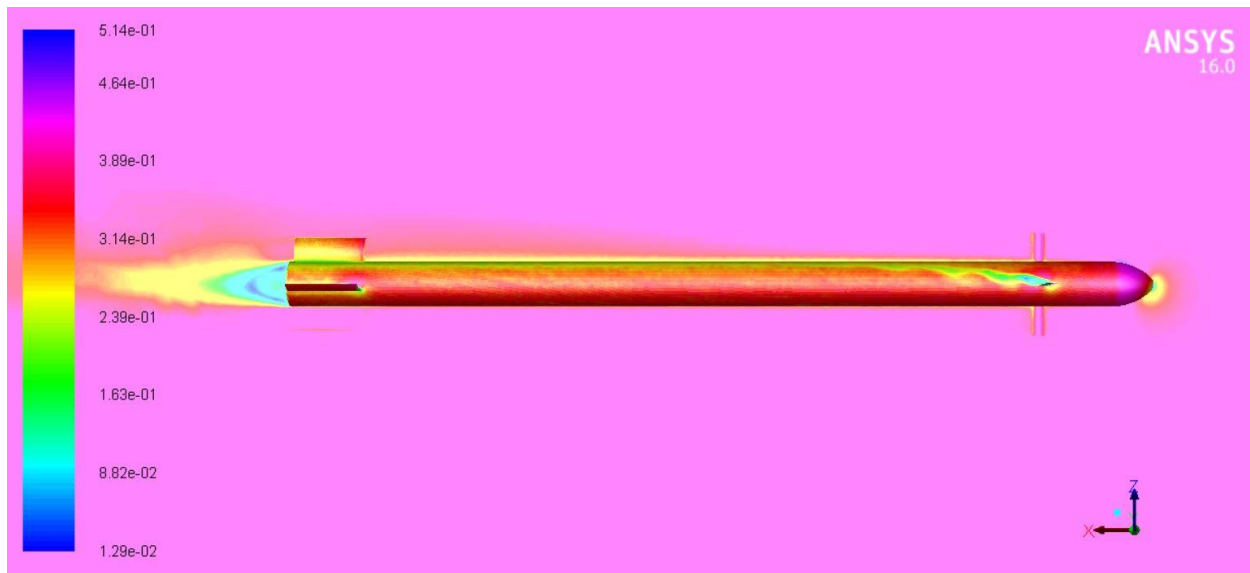


Figure 56 Mach number contours for 15 ° control deflection and angle of attack $\alpha = 8^\circ$

Figure 57 shows the simulation case with -8 degrees angle of attack and 15 degrees pitch control surface deflection. The contours show clear flow disturbance following the angled flow. The flow disturbance behind the control surfaces in these contours is greater than the contours in the Figure 46. This is caused by the control surface deflection of 10 degrees.

It is important to point out that the flow facing the axis of the control surface is the sum of -8 degrees angle of attack and the 15 degrees control deflection. Thus, the control surfaces are facing a total of 7 degrees angles of attack with respect to the chord line. That is why the disturbance is greater than the case in Figure 46 where the control deflection is 10 degrees.

It is important to point out that the Mach number contours near the nose is identical to any simulation with -8 degrees angle of attack.



Therefore, the control deflection has no major effect on the nose Mach number contours distribution.

The contours shown in Figure 57 indicate a drop in the Mach number towards the higher area of the front nose and tail fin leading edge of the missile. This is caused by the angled flow represented by -8 degrees angle of attack. Hence, the pressure increases accordingly which results in extra drag on the missile. In addition, the Mach number drop results in the increased normal force components on the missile. These normal force components act downwards which is expected for negative angle of attack flow.

In addition, the normal force component acting on the control surfaces is directed downwards which can be seen in the flow disturbance direction behind the control surfaces. This is also caused by the Mach number drop seen in Figure 57.

Therefore, the total normal force acting on the missile is directed downwards. This supports the normal force coefficients results presented in Figure 24. Thus, the missile's normal force is directed downwards for flying conditions of -8 degrees angle of attack and 15 degrees control deflection.

It is important to note that the simulated angle of attack here is lower than the trim angle of attack obtained from Figure 23. Hence, the pitch moment acting on the missile is positive. This means that the pitch moment direction is anti-clockwise [pitch up direction] according to the selected axis system.

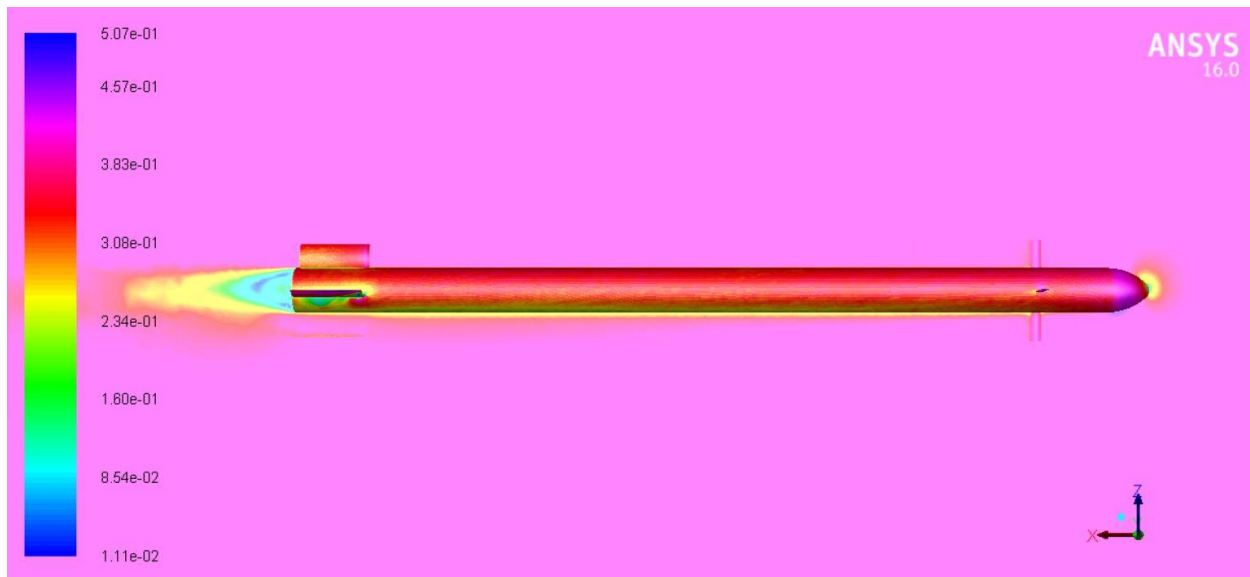


Figure 57 Mach number contours for 15 ° control deflection and angle of attack $\alpha = -8^\circ$

Figure 58 shows the simulation case with 10 degrees angle of attack and 15 degrees pitch control surface deflection. The flow separation is clearly seen behind the control surfaces shown in Figure 58. This indicates that the missile loses the control surface effectiveness.

The total of 25 degrees angled flow with respect to the control surface chord line faces the control surface. It is important to point out that this case includes the highest simulated angle of attack along with the highest pitch control surface deflection.

The Mach number contours towards the nose of the missile is identical to any simulation with angle of attack 10 degrees. However, the Mach number contours towards the tail fin are affected by the disturbed flow as seen in Figure 58.

It can be concluded that the missile control surfaces effectiveness is compromised when approaching 15 degrees control deflection with high

angle of attack. Therefore, this limit has to be considered when designing the autopilot for missile control.

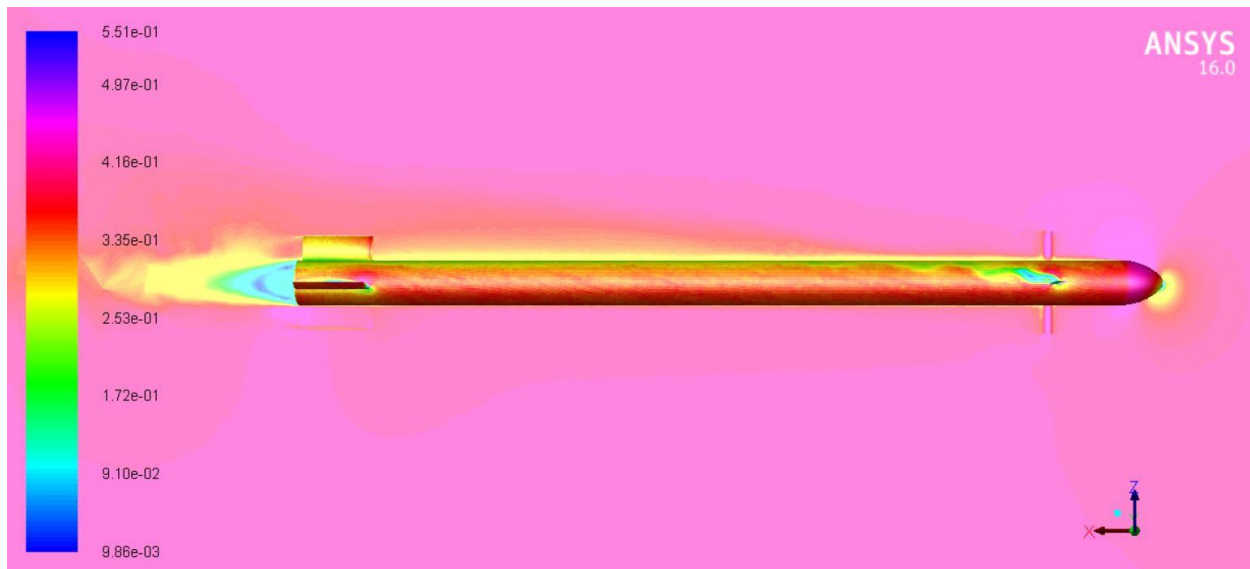


Figure 58 Mach number contours for 15 ° control deflection and angle of attack $\alpha = 10^\circ$

Figure 59 shows the simulation case with -10 degrees angle of attack and 15 degrees pitch control surface deflection. The contours show clear flow disturbance following the angled flow. The flow disturbance behind the control surfaces in these contours is greater than the contours in the Figure 48. This is caused by the control surface deflection of 10 degrees.

It is important to point out that the flow facing the axis of the control surface is the sum of -10 degrees angle of attack and the 15 degrees control deflection. Thus, the control surfaces are facing a total of 5 degrees angles of attack with respect to the chord line. That is why the disturbance is greater than the case in Figure 48 where the control deflection is 10 degrees.



It is important to point out that the Mach number contours near the nose is identical to any simulation with -10 degrees angle of attack. Therefore, the control deflection has no major effect on the nose Mach number contours distribution.

The contours shown in Figure 59 indicate a drop in the Mach number towards the higher area of the front nose and tail fin leading edge of the missile. This is caused by the angled flow represented by -10 degrees angle of attack. Hence, the pressure increases accordingly which results in extra drag on the missile. In addition, the Mach number drop results in the increased normal force components on the missile. These normal force components act downwards which is expected for negative angle of attack flow.

In addition, the normal force component acting on the control surfaces is directed downwards which can be seen in the flow disturbance direction behind the control surfaces. This is also caused by the Mach number drop seen in Figure 59.

Therefore, the total normal force acting on the missile is directed downwards. This supports the normal force coefficients results presented in Figure 24. Thus, the missile's normal force is directed downwards for flying conditions of -10 degrees angle of attack and 15 degrees control deflection.

It is important to note that the simulated angle of attack here is lower than the trim angle of attack obtained from Figure 23. Hence, the pitch moment acting on the missile is positive. This means that the pitch moment direction is anti-clockwise [pitch up direction] according to the selected axis system.

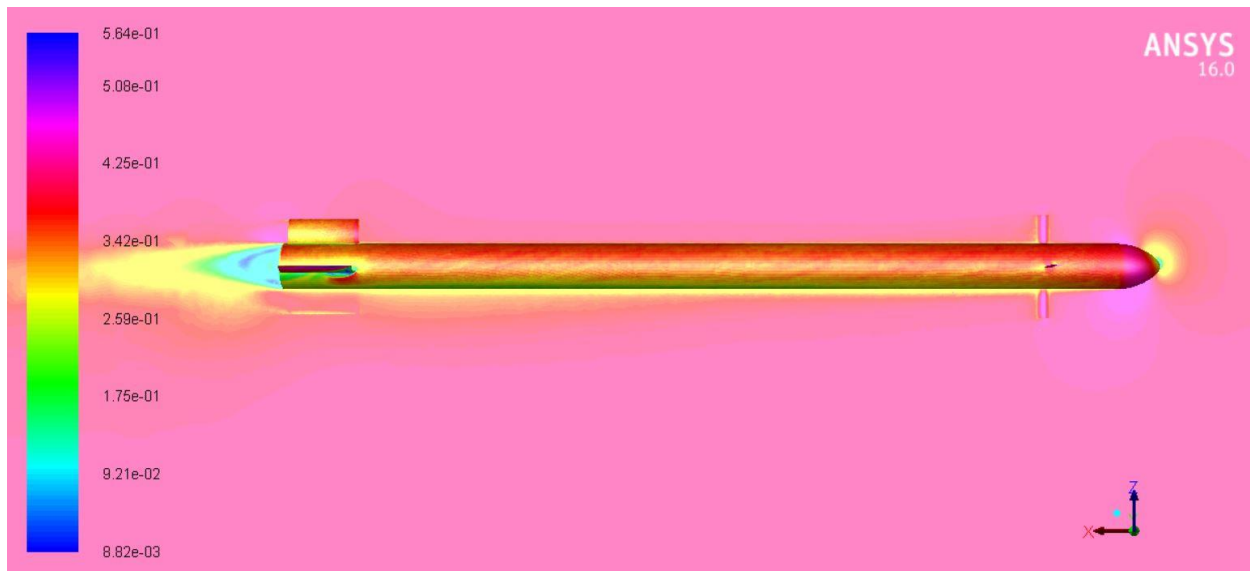


Figure 59 Mach number contours for 15 ° control deflection and angle of attack $\alpha = -10$

4.2.2. Pressure contours

Contours of static pressure are crucial to analyze flow simulation due to their high impact on the missile forces. They provide effective pressure distribution around the missile which helps to evaluate the missile aerodynamic performance.

Contours of static pressure can also be helpful when analyzing the missile's structure. They can provide inputs of the pressure distribution along all the missile parts. There are many methods of identifying load distribution along the missile parts. However, through pressure contours generated by FLUENT, exact pressure distribution throughout the whole model is generated. This should give an accurate results.

Various Mach number contours are generated due to several cases of control deflection and angles of attack. Angles of attack of 10 to -10 degrees are presented for each control deflection case. It is important to highlight that the increment size between each simulation case is 2 degrees angle of attack.

4.2.2.1. No deflection

Contours of static pressure with 0 degree control surface deflection are presented in Figure 60 - Figure 80 for different angles of attack.

Figure 60 shows the simulation case with 0 degree angle of attack and 0 degree pitch control surface deflection. The contours of pressure show regular pressure distribution for undisturbed flow with 0 degrees angle of attack.

Contours in Figure 60 show the increased pressure towards the tip of the missile which causes the nose component of the overall drag. The slight drop in pressure behind the trailing edges of the control surfaces can be seen in Figure 60 which also causes extra drag. The base drag effect can also be seen in Figure 60 through the pressure drop towards the missile's base.

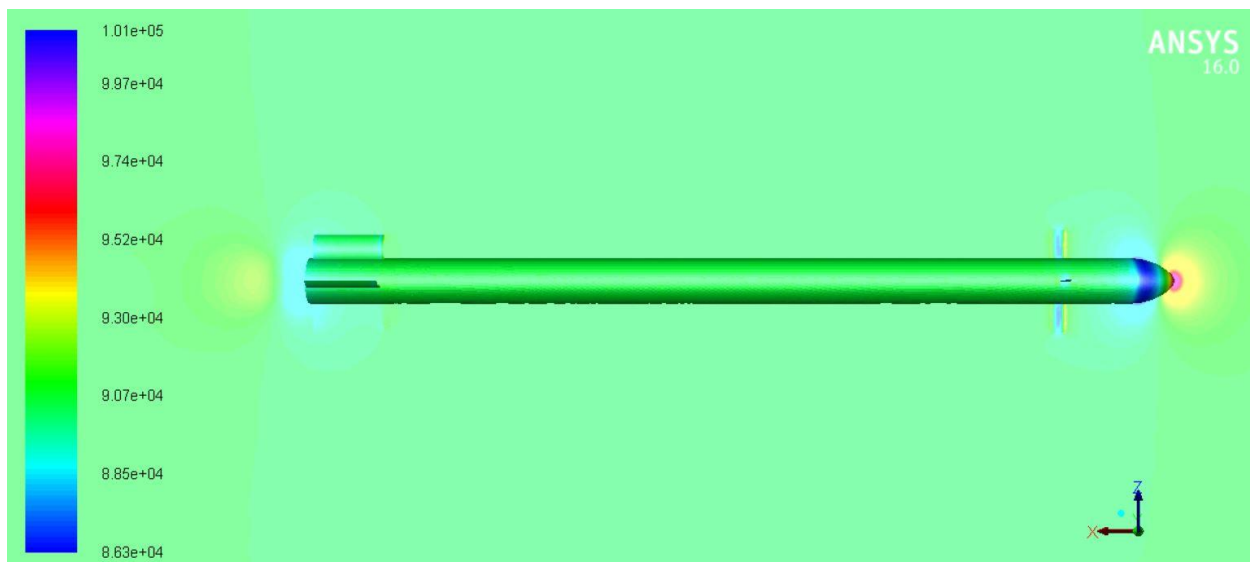


Figure 60 Static pressure contours for 0 ° control deflection and angle of attack $\alpha = 0^\circ$

Figure 61 shows the static pressure distribution along the whole missile's parts. The static pressure shows sudden increase in static pressure towards the nose, the canard control surfaces, and the tail fin. This is expected due to the direct exposure to the air flow.

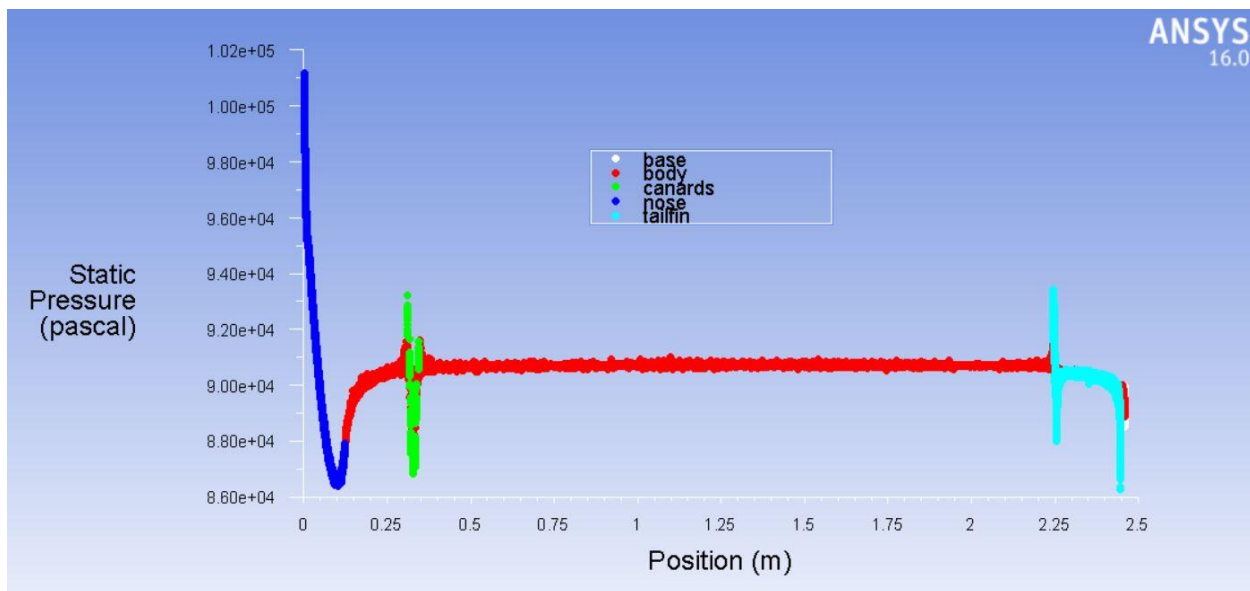


Figure 61 Static pressure distribution along missile for 0 ° control deflection and angle of attack $\alpha = 0^\circ$

Figure 62 shows the simulation case with 2 degrees angle of attack and 0 degree pitch control surface deflection. The contours of pressure in Figure 62 show increased pressure towards the lower part of the missile's nose due to the angled flow of 2 degrees.

The static pressure contours shown in Figure 62 show the pressure increase towards the lower area of the canards control surfaces and the tail fin. Hence, the force increases accordingly along the missile's axis which results in extra drag on the missile. In addition, the normal force increases due to the angled flow of 2 degrees. The base drag effects can also be seen in Figure 62 through the drop of static pressure contours in that area.

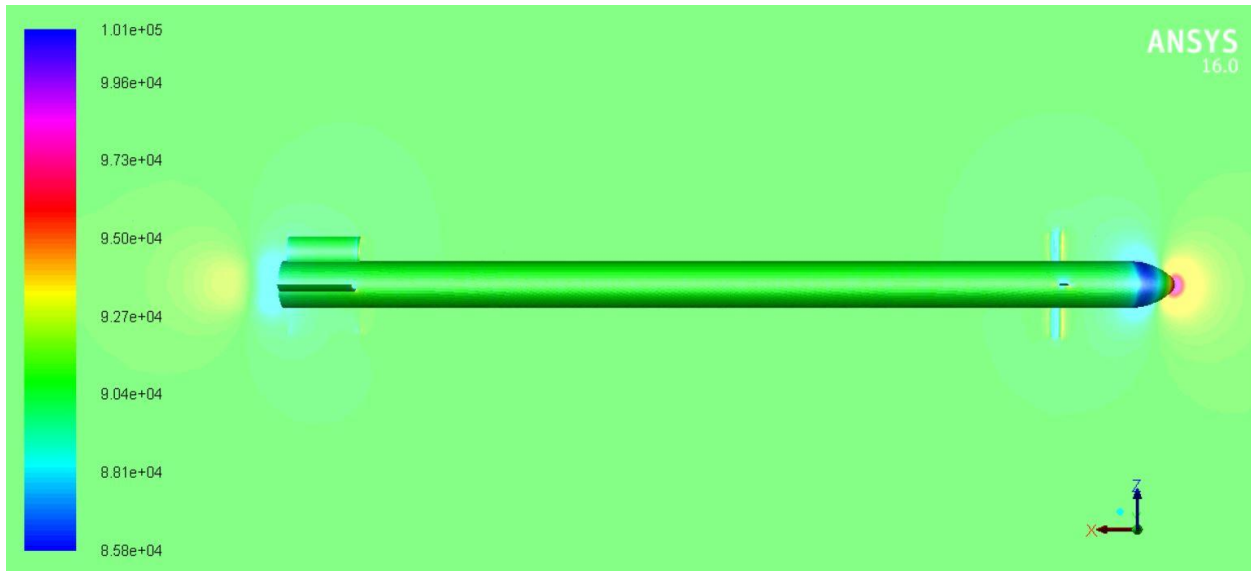


Figure 62 Static pressure contours for 0° control deflection and angle of attack $\alpha = 2^\circ$

Figure 63 shows the static pressure distribution along the whole missile's parts. The static pressure shows sudden increase in static pressure towards the nose, the canard control surfaces, and the tail fin. This is expected due to the direct exposure to the air flow.

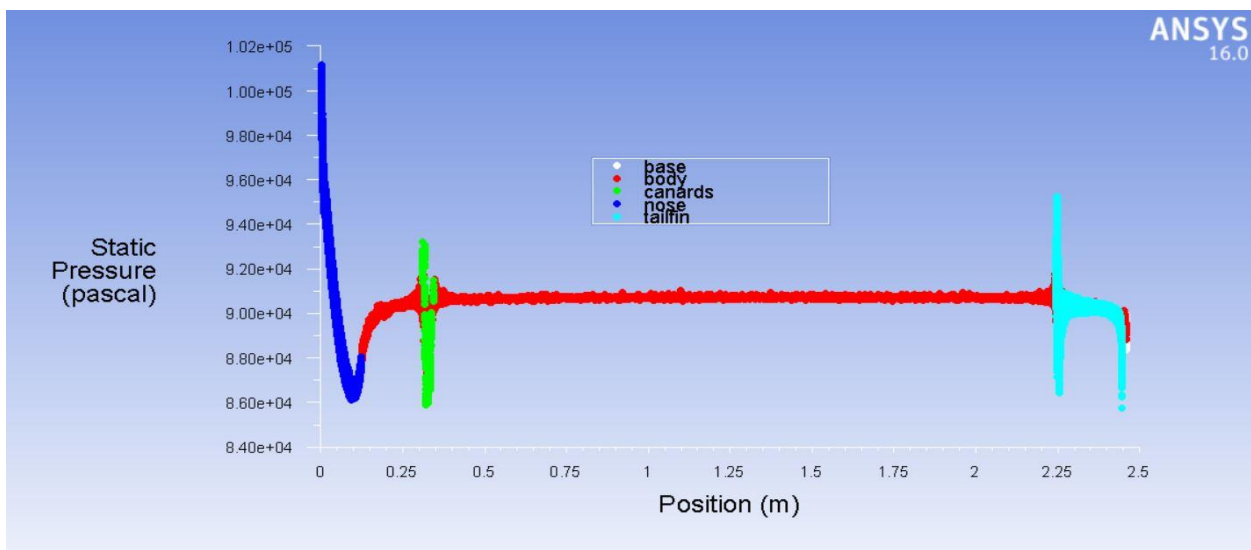


Figure 63 Static pressure distribution along missile for 0° control deflection and angle of attack $\alpha = 2^\circ$

Figure 64 shows the simulation case with -2 degrees angle of attack and 0 degree pitch control surface deflection. The contours of pressure in Figure 64 show increased pressure towards the upper part of the missile's nose due to the angled flow of -2 degrees.

The static pressure contours shown in Figure 64 show the pressure increase towards the upper area of the canards control surfaces and the tail fin. Hence, the force decreases accordingly which results in extra drag on the missile. In addition, the normal force decreases due to the angled flow of -2 degrees. The base drag effects can also be seen in Figure 64 through the drop of static pressure contours in that area.

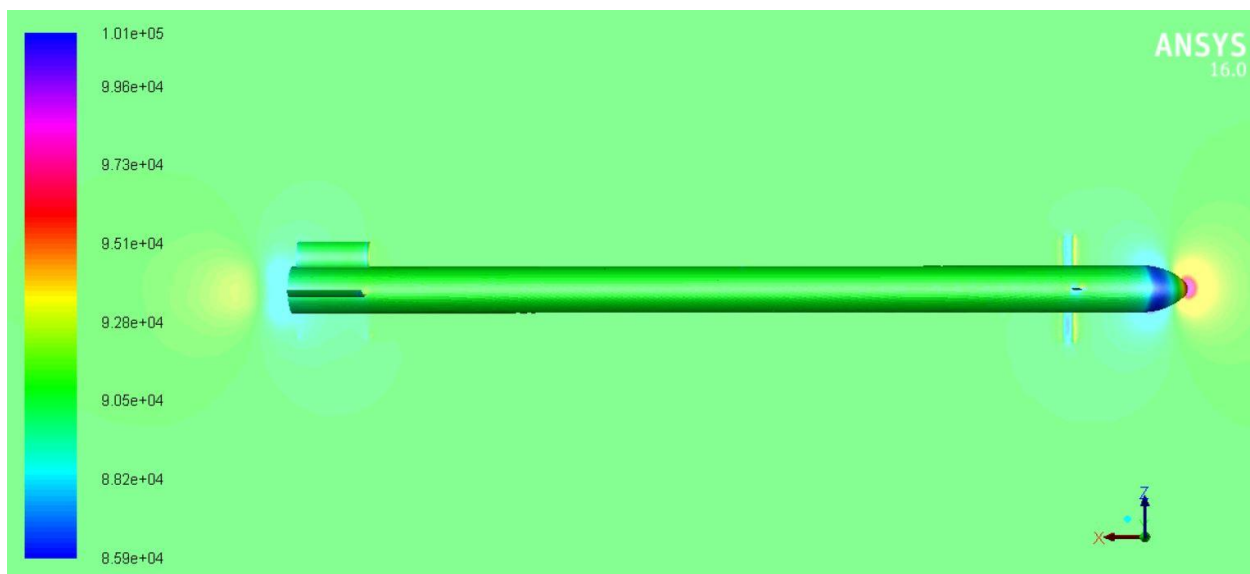


Figure 64 Static pressure contours for 0 ° control deflection and angle of attack $\alpha = -2^\circ$

Figure 65 shows the static pressure distribution along the whole missile's parts. The static pressure shows sudden increase in static

pressure towards the nose, the canard control surfaces, and the tail fin. This is expected due to the direct exposure to the air flow.

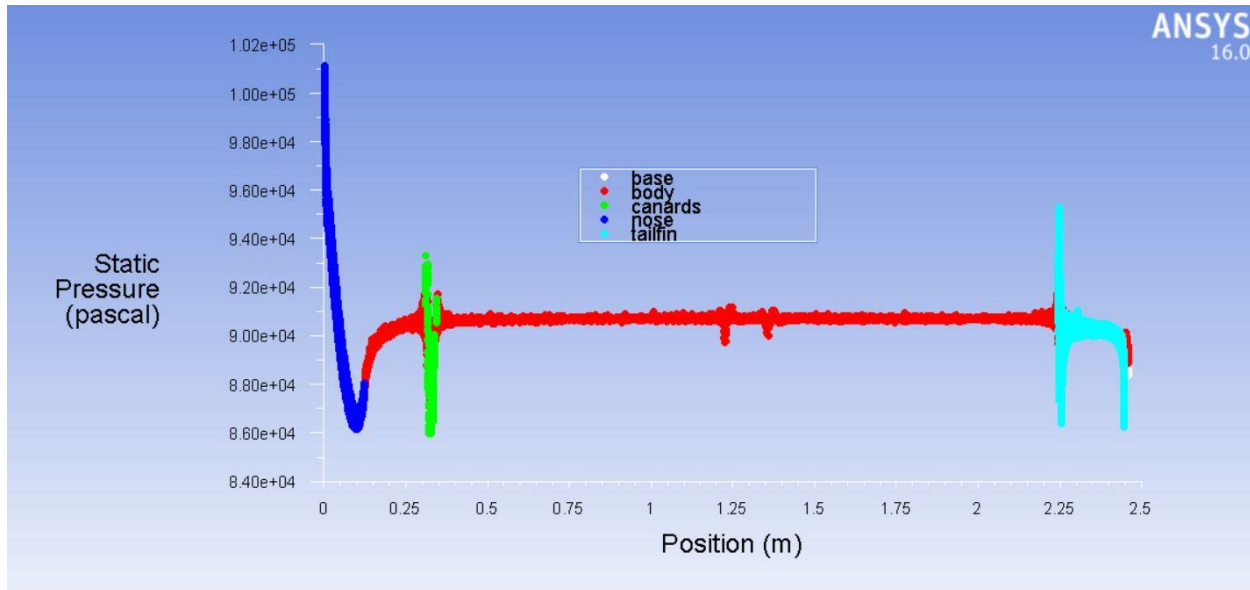


Figure 65 Static pressure distribution along missile for 0 ° control deflection and angle of attack $\alpha = -2^\circ$

Figure 66 shows the simulation case with 4 degrees angle of attack and 0 degree pitch control surface deflection. The contours of pressure in Figure 66 show increased pressure towards the lower part of the missile's nose due to the angled flow of 4 degrees.

The static pressure contours shown in Figure 66 show the pressure increase towards the lower area of the canards control surfaces and the tail fin. Hence, the force increases accordingly along the missile's axis which results in extra drag on the missile. In addition, the normal force increases due to the angled flow of 4 degrees. The base drag effects can also be seen in Figure 66 through the drop of static pressure contours in that area.

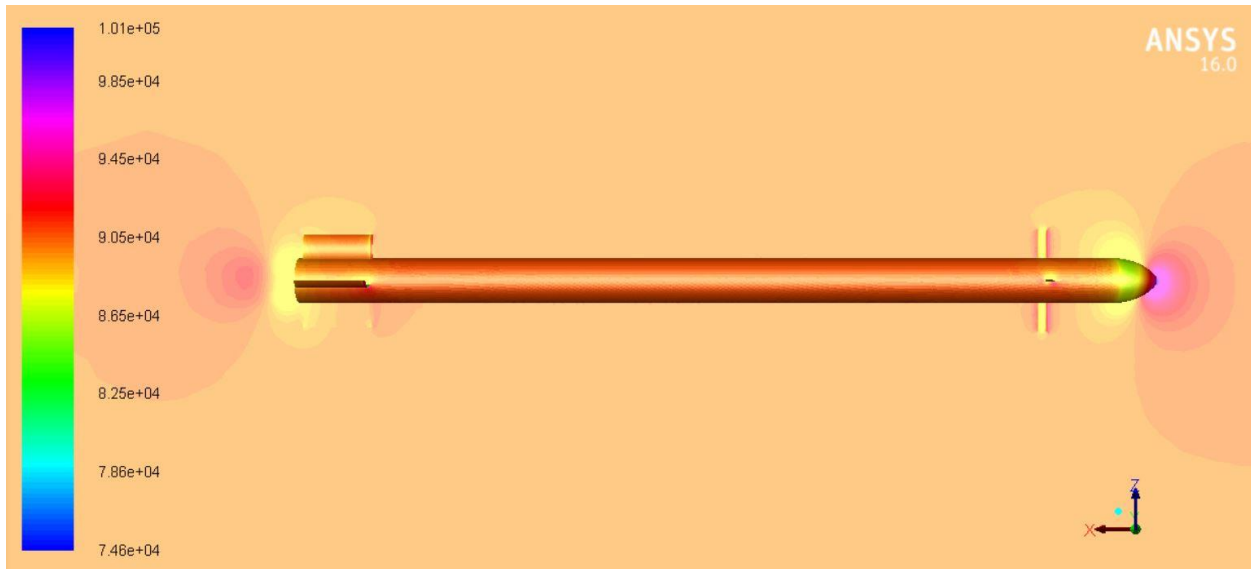


Figure 66 Static pressure contours for 0° control deflection and angle of attack $\alpha = 4^\circ$

Figure 67 shows the static pressure distribution along the whole missile's parts. The static pressure shows sudden increase in static pressure towards the nose, the canard control surfaces, and the tail fin. This is expected due to the direct exposure to the air flow.

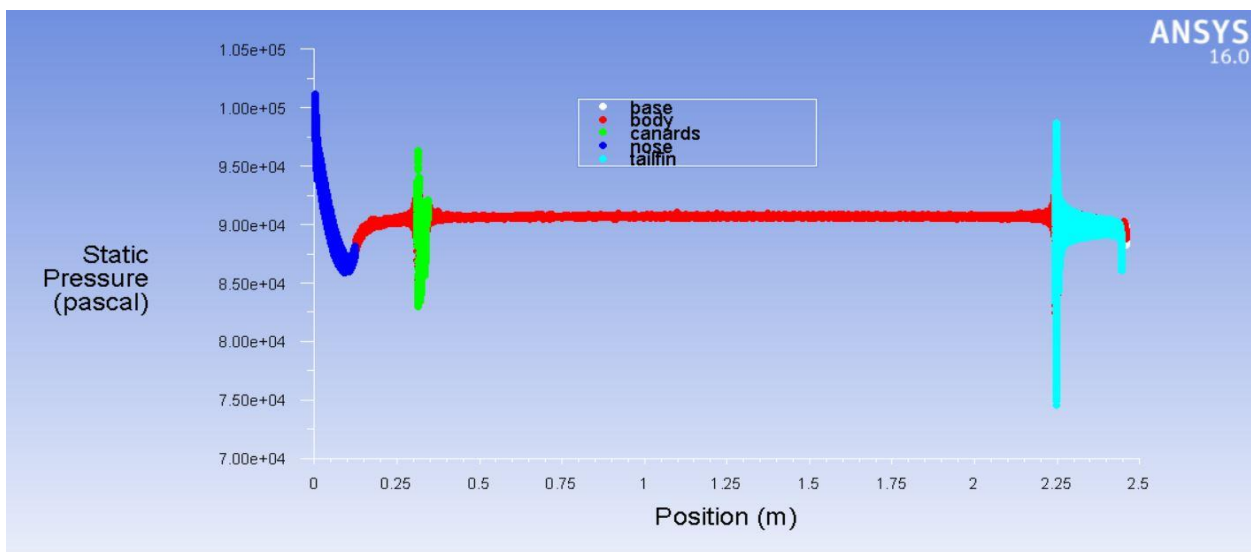


Figure 67 Static pressure distribution along missile for 0° control deflection and angle of attack $\alpha = 4^\circ$

Figure 68 shows the simulation case with -4 degrees angle of attack and 0 degree pitch control surface deflection. The contours of pressure in Figure 68 show increased pressure towards the upper part of the missile's nose due to the angled flow of -4 degrees.

The static pressure contours shown in Figure 68 show the pressure increase towards the upper area of the canards control surfaces and the tail fin. Hence, the force increases accordingly along the missile's axis which results in extra drag on the missile. In addition, the normal force decreases due to the angled flow of -4 degrees. The base drag effects can also be seen in Figure 68 through the drop of static pressure contours in that area.

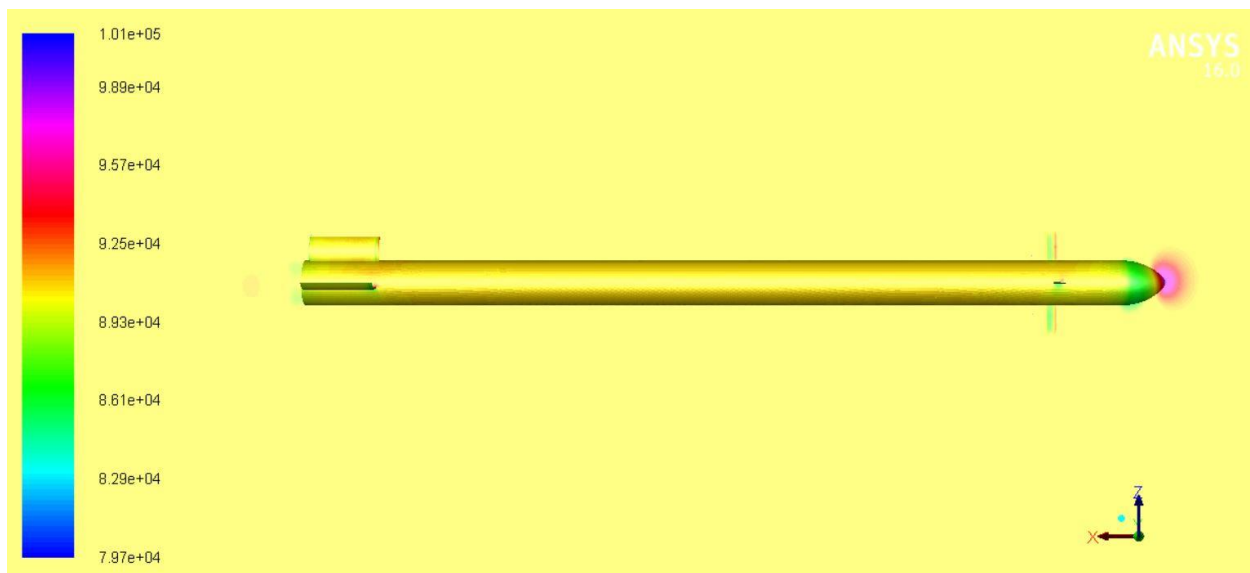


Figure 68 Static pressure contours for 0° control deflection and angle of attack $\alpha = -4^\circ$

Figure 69 shows the static pressure distribution along the whole missile's parts. The static pressure shows sudden increase in static pressure towards the nose, the canard control surfaces, and the tail fin. This is expected due to the direct exposure to the air flow.

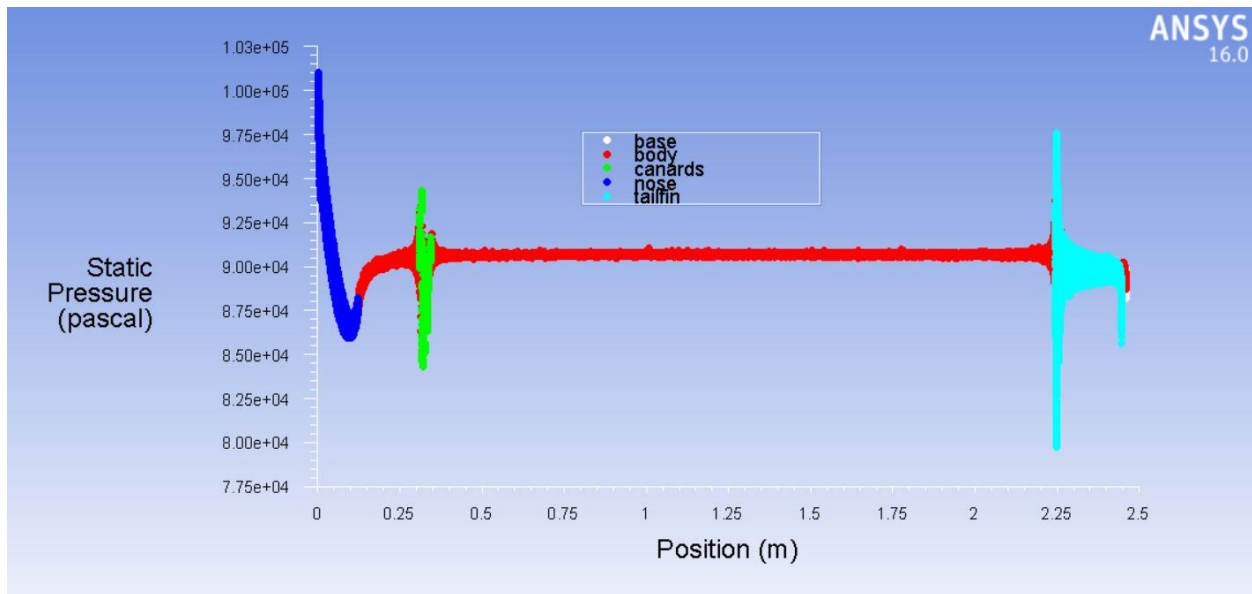


Figure 69 Static pressure distribution along missile for 0° control deflection and angle of attack $\alpha = -4^\circ$

Figure 70 shows the simulation case with 6 degrees angle of attack and 0 degree pitch control surface deflection. The contours of pressure in Figure 70 show increased pressure towards the lower part of the missile's nose due to the angled flow of 6 degrees.

The static pressure contours shown in Figure 70 show the pressure increase towards the lower area of the canards control surfaces and the tail fin. Hence, the force increases accordingly along the missile's axis which results in extra drag on the missile. In addition, the normal force increases upwards due to the angled flow of 6 degrees. The base drag effects can also be seen in Figure 70 through the drop of static pressure contours in that area.

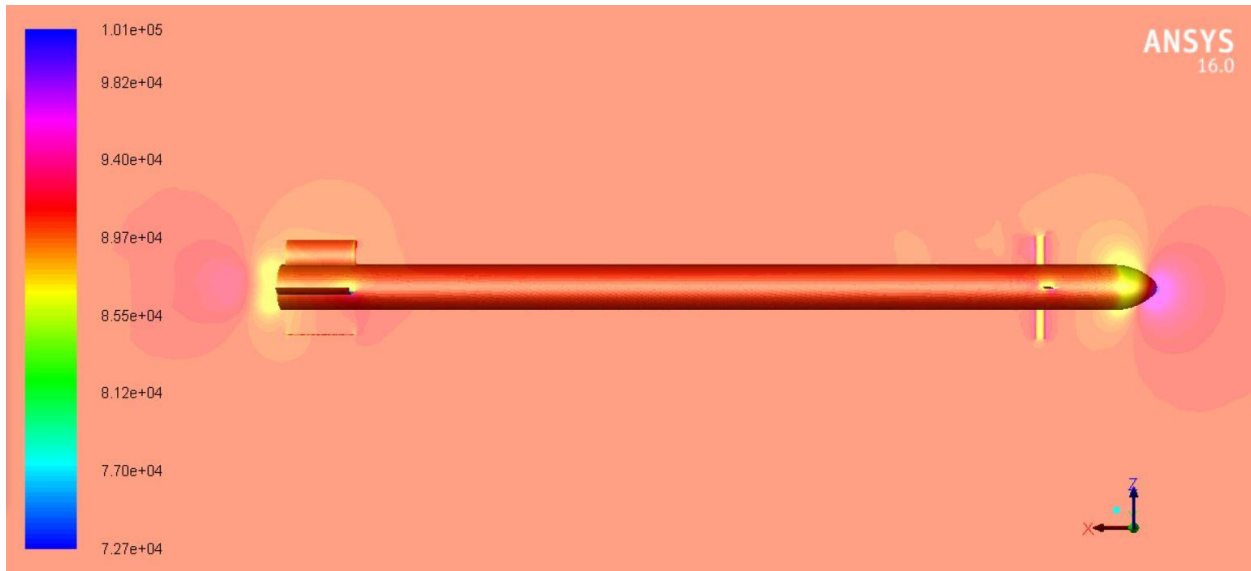


Figure 70 Static pressure contours for 0° control deflection and angle of attack $\alpha = 6^\circ$

Figure 71 shows the static pressure distribution along the whole missile's parts. The static pressure shows sudden increase in static pressure towards the nose, the canard control surfaces, and the tail fin. This is expected due to the direct exposure to the air flow.

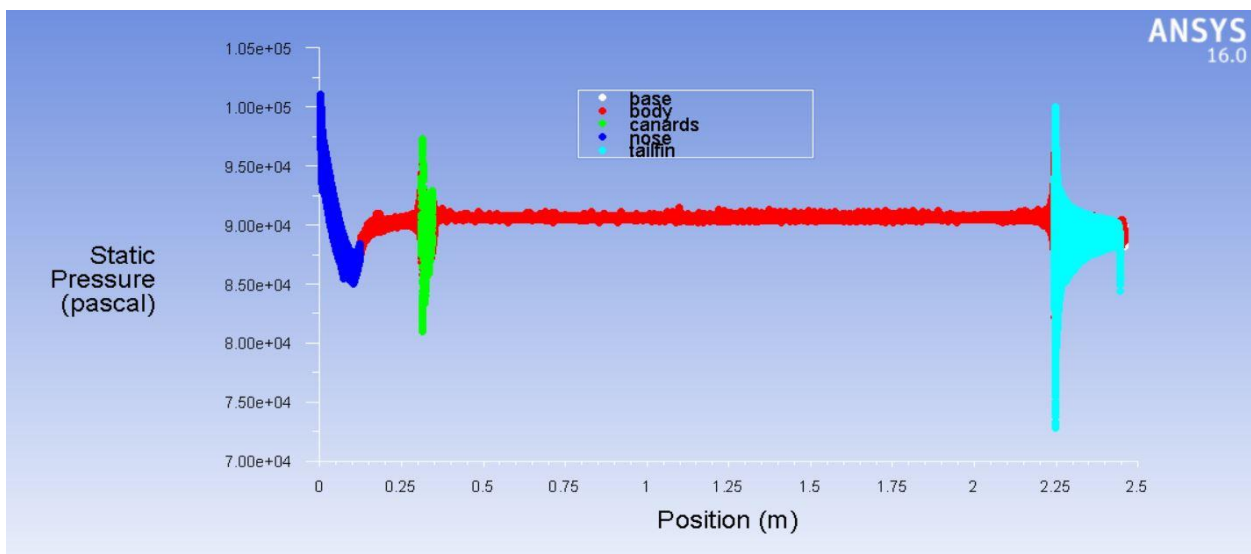


Figure 71 Static pressure distribution along missile for 0° control deflection and angle of attack $\alpha = 6^\circ$



Figure 72 shows the simulation case with -6 degrees angle of attack and 0 degree pitch control surface deflection. The contours of pressure in Figure 72 show increased pressure towards the upper part of the missile's nose due to the angled flow of -6 degrees.

The static pressure contours shown in Figure 72 show the pressure increase towards the upper area of the canards control surfaces and the tail fin. Hence, the force increases accordingly along the missile's axis which results in extra drag on the missile. In addition, the normal force decreases due to the angled flow of -6 degrees. The base drag effects can also be seen in Figure 72 through the drop of static pressure contours in that area.

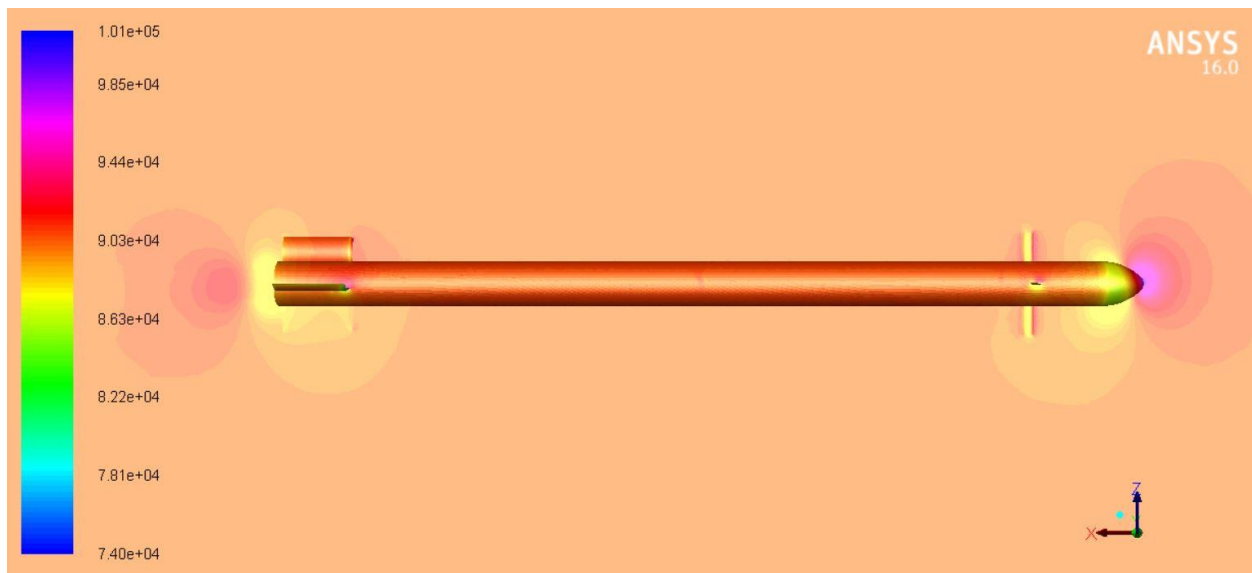


Figure 72 Static pressure contours for 0° control deflection and angle of attack $\alpha = -6^\circ$

Figure 73 shows the static pressure distribution along the whole missile's parts. The static pressure shows sudden increase in static pressure towards the nose, the canard control surfaces, and the tail fin. This is expected due to the direct exposure to the air flow.

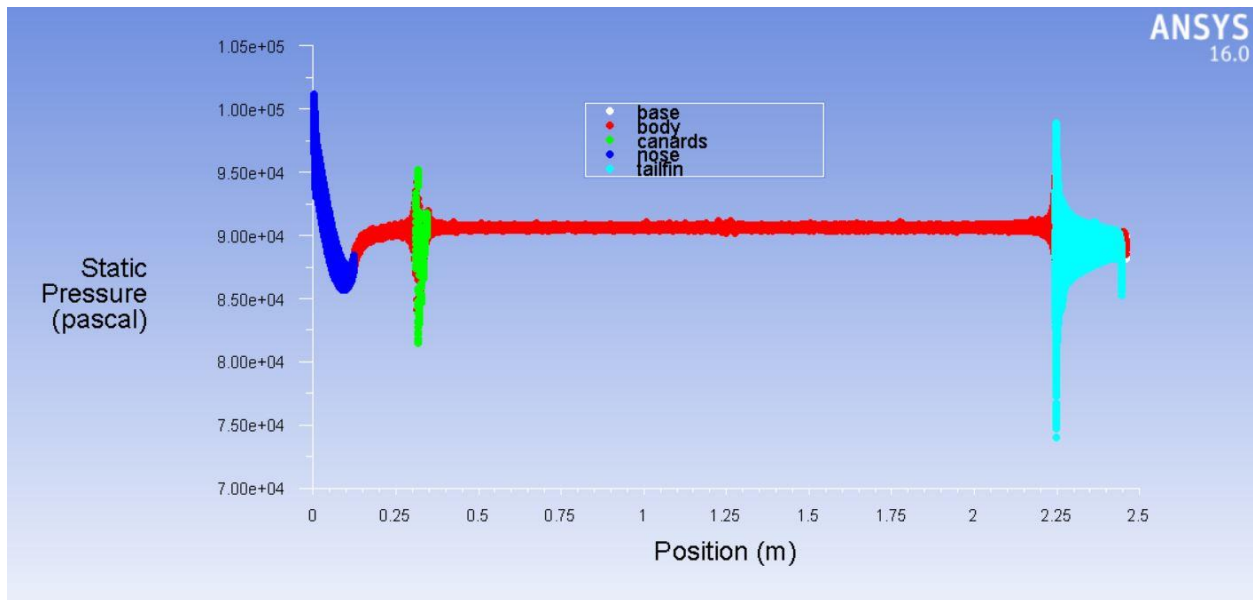


Figure 73 Static pressure distribution along missile for 0° control deflection and angle of attack $\alpha = -6^\circ$

Figure 74 shows the simulation case with 8 degrees angle of attack and 0 degree pitch control surface deflection. The contours of pressure in Figure 74 show increased pressure towards the lower part of the missile's nose due to the angled flow of 8 degrees.

The static pressure contours shown in Figure 74 show the pressure increase towards the lower area of the canards control surfaces and the tail fin. Hence, the force increases accordingly along the missile's axis which results in extra drag on the missile. In addition, the normal force increases upwards due to the angled flow of 8 degrees. The base drag effects can also be seen in Figure 74 through the drop of static pressure contours in that area.

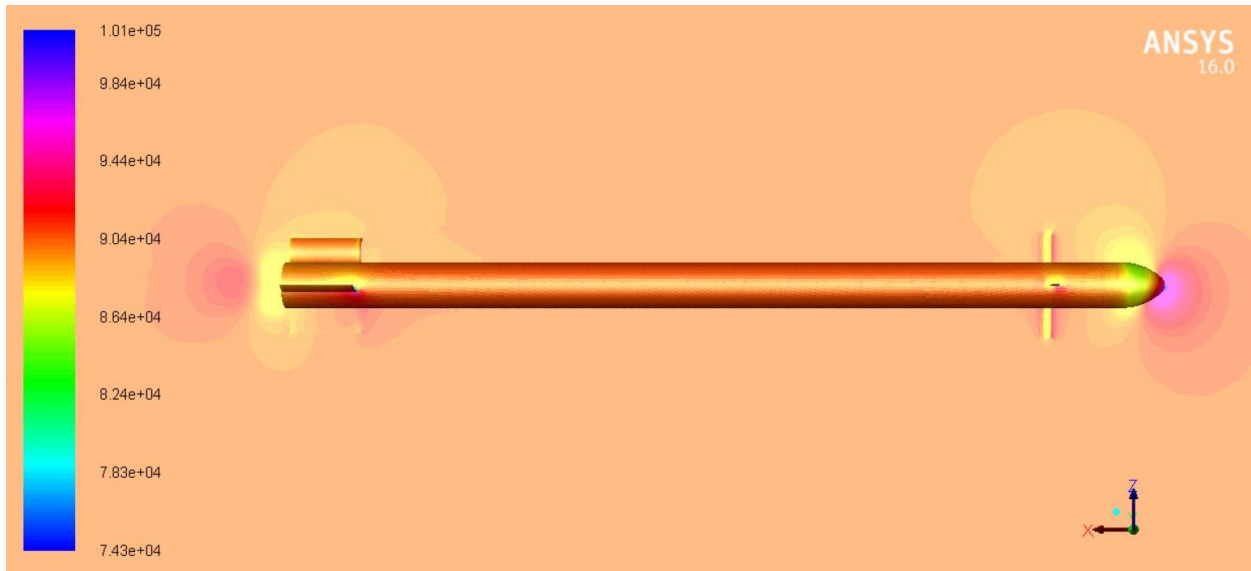


Figure 74 Static pressure contours for 0° control deflection and angle of attack $\alpha = 8^\circ$

Figure 75 shows the static pressure distribution along the whole missile's parts. The static pressure shows sudden increase in static pressure towards the nose, the canard control surfaces, and the tail fin. This is expected due to the direct exposure to the air flow.

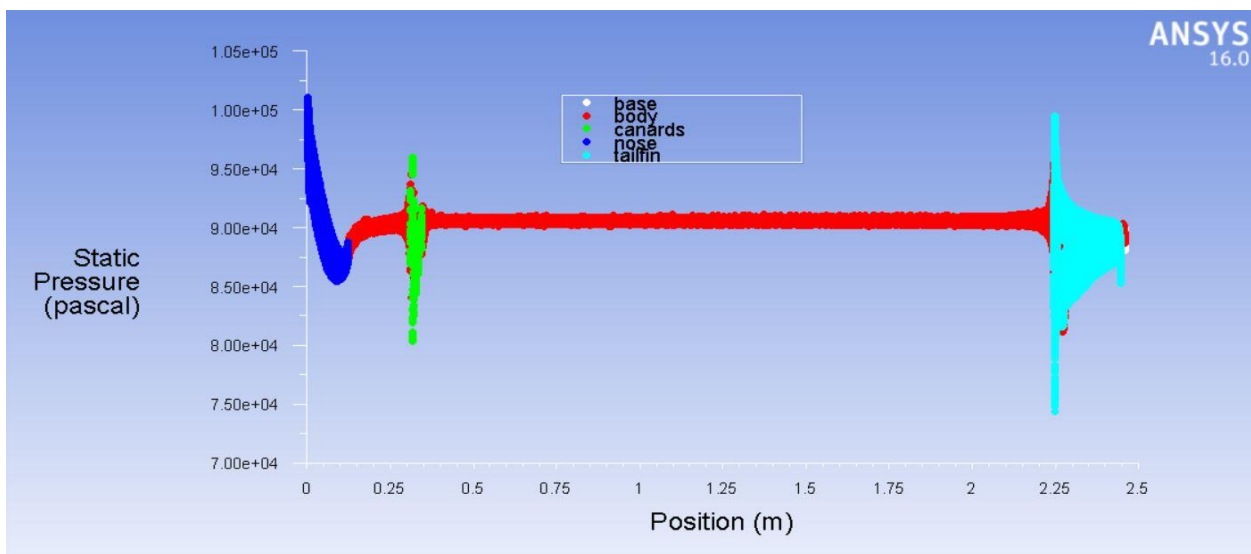


Figure 75 Static pressure distribution along missile for 0° control deflection and angle of attack $\alpha = 8^\circ$

Figure 76 shows the simulation case with -8 degrees angle of attack and 0 degree pitch control surface deflection. The contours of pressure in Figure 76 show increased pressure towards the upper part of the missile's nose due to the angled flow of -8 degrees.

The static pressure contours shown in Figure 76 show the pressure increase towards the upper area of the canards control surfaces and the tail fin. Hence, the force increases accordingly along the missile's axis which results in extra drag on the missile. In addition, the normal force decreases due to the angled flow of -8 degrees. The base drag effects can also be seen in Figure 76 through the drop of static pressure contours in that area.



Figure 76 Static pressure contours for 0° control deflection and angle of attack $\alpha = -8^\circ$

Figure 77 shows the static pressure distribution along the whole missile's parts. The static pressure shows sudden increase in static pressure towards the nose, the canard control surfaces, and the tail fin. This is expected due to the direct exposure to the air flow.

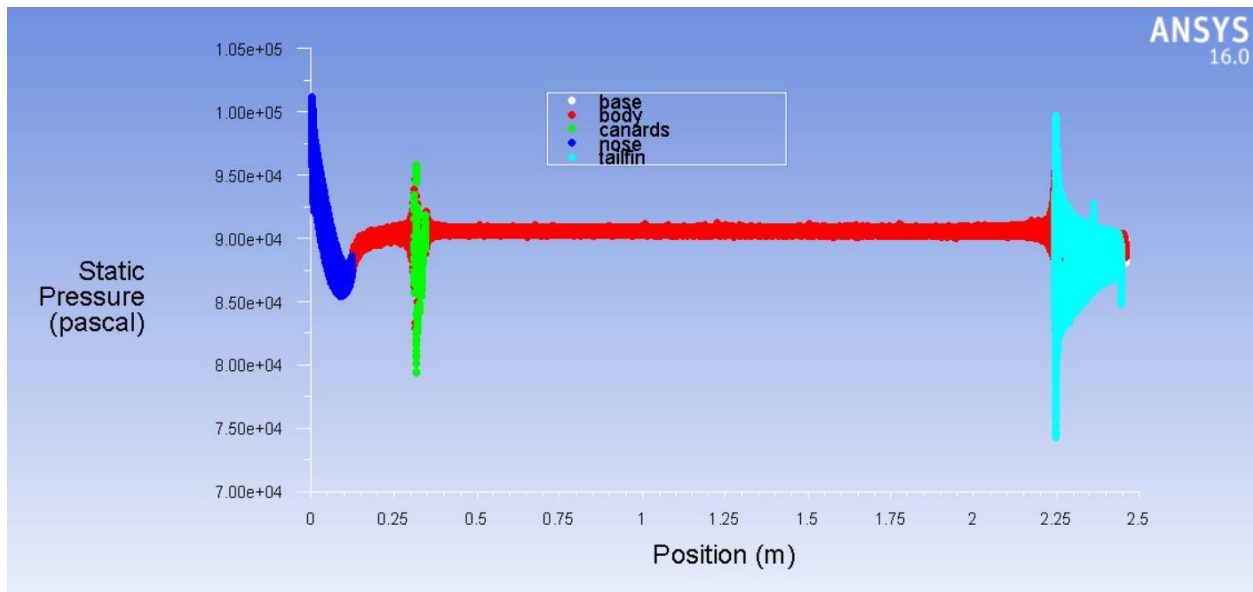


Figure 77 Static pressure distribution along missile for 0 ° control deflection and angle of attack $\alpha = -8^\circ$

Figure 78 shows the simulation case with 10 degrees angle of attack and 0 degree of pitch control surface deflection. The contours of pressure show greater pressure increase towards the lower area of the nose which indicates higher aerodynamic forces than the case in Figure 66.

The static pressure contours shown in Figure 78 show greater pressure increase towards the leading edges of the canard control surfaces as well as the tail. This is also caused by the angled flow of 10 degrees.

All these pressure increases towards nose, canards, as well as tail fin contribute to the overall drag of the missile, lift force, as well as pitch moment.

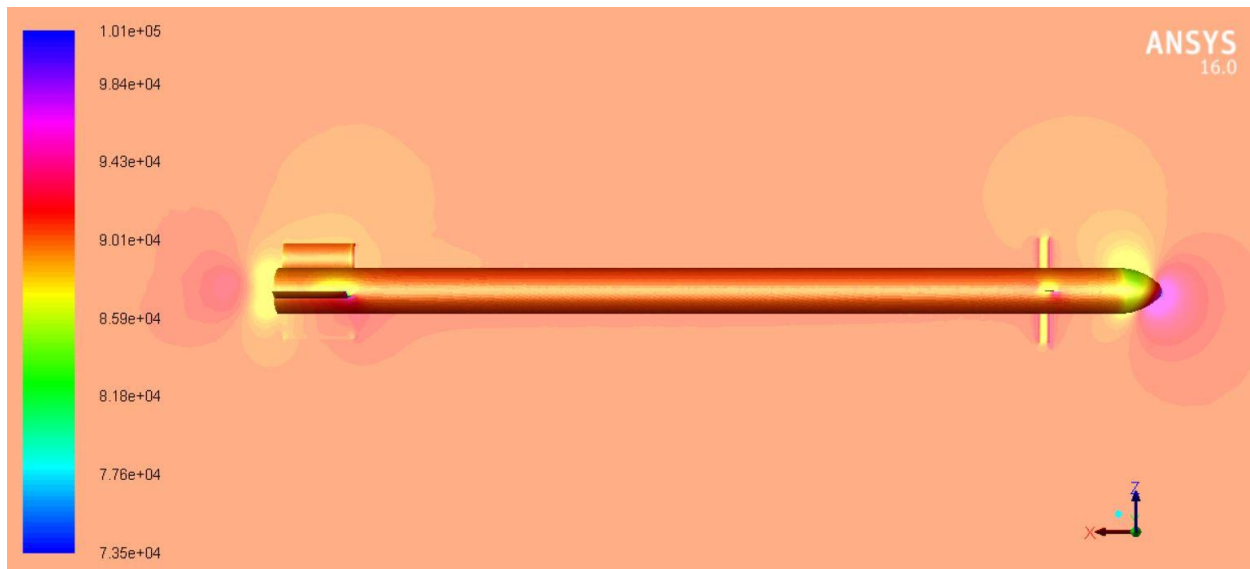


Figure 78 Static pressure contours for 0° control deflection and angle of attack $\alpha = 10^\circ$

Figure 79 shows the static pressure distribution along the whole missile's parts. The static pressure shows sudden increase in static pressure towards the nose, the canard control surfaces, and the tail fin. This is expected due to the direct exposure to the air flow.

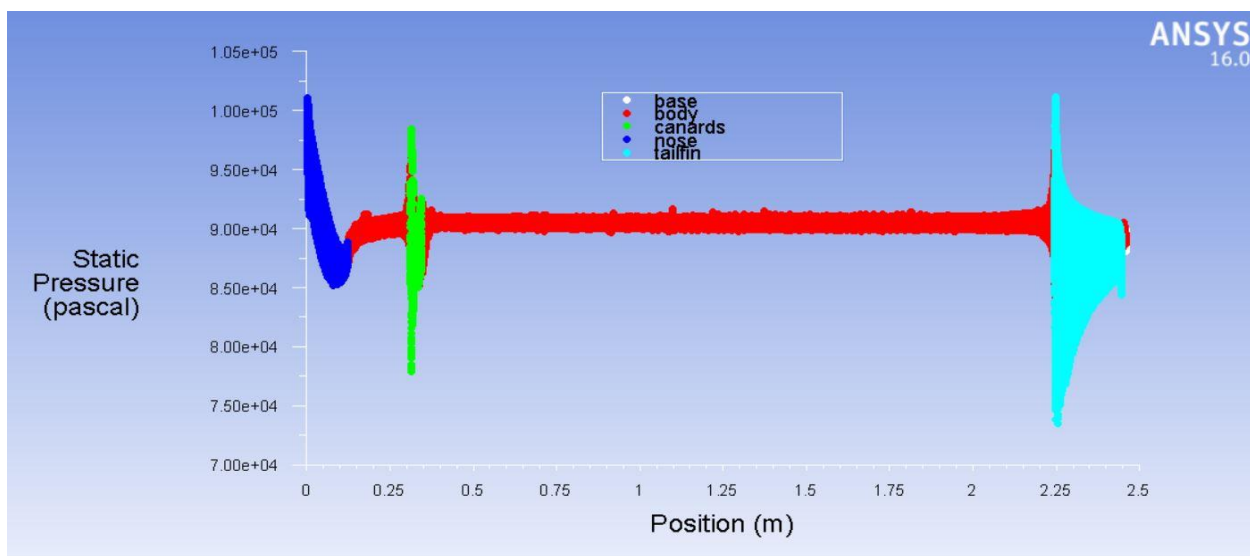


Figure 79 Static pressure distribution along missile for 0° control deflection and angle of attack $\alpha = 10^\circ$

Figure 80 shows the simulation case with -10 degrees angle of attack and 0 degree pitch control surface deflection. The contours of pressure in Figure 80 show increased pressure towards the upper part of the missile's nose due to the angled flow of -10 degrees.

The static pressure contours shown in Figure 80 show the pressure increase towards the upper area of the canards control surfaces and the tail fin. Hence, the force increases accordingly along the missile's axis which results in extra drag on the missile. In addition, the normal force decreases due to the angled flow of -10 degrees. The base drag effects can also be seen in Figure 80 through the drop of static pressure contours in that area.

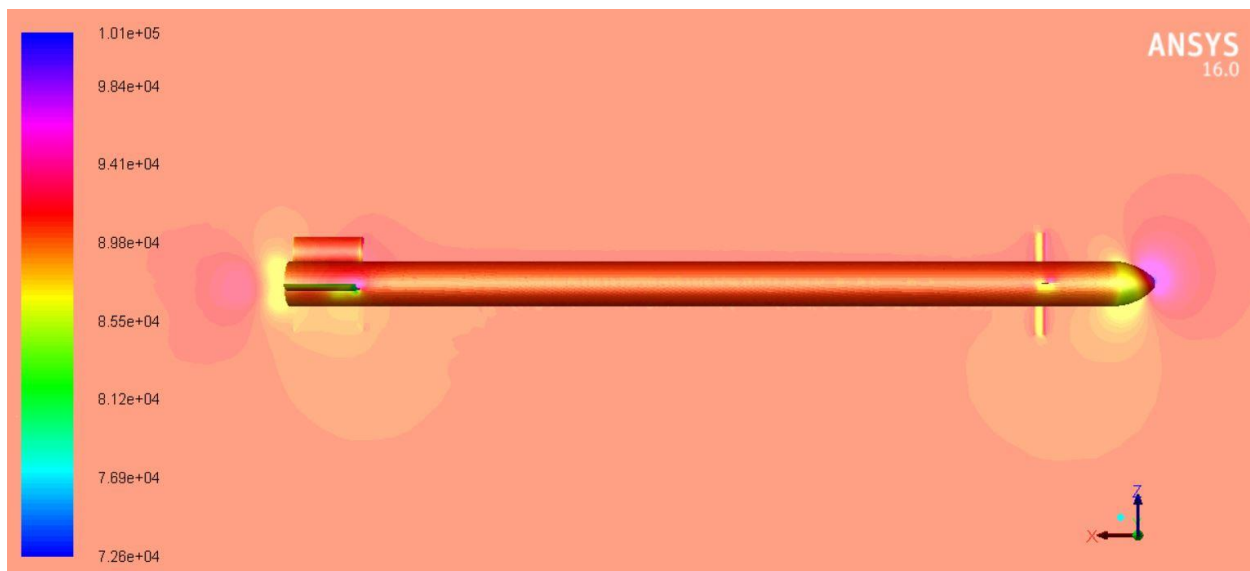


Figure 80 Static pressure contours for 0° control deflection and angle of attack $\alpha = -10^\circ$

Figure 81 shows the static pressure distribution along the whole missile's parts. The static pressure shows sudden increase in static pressure towards the nose, the canard control surfaces, and the tail fin. This is expected due to the direct exposure to the air flow.

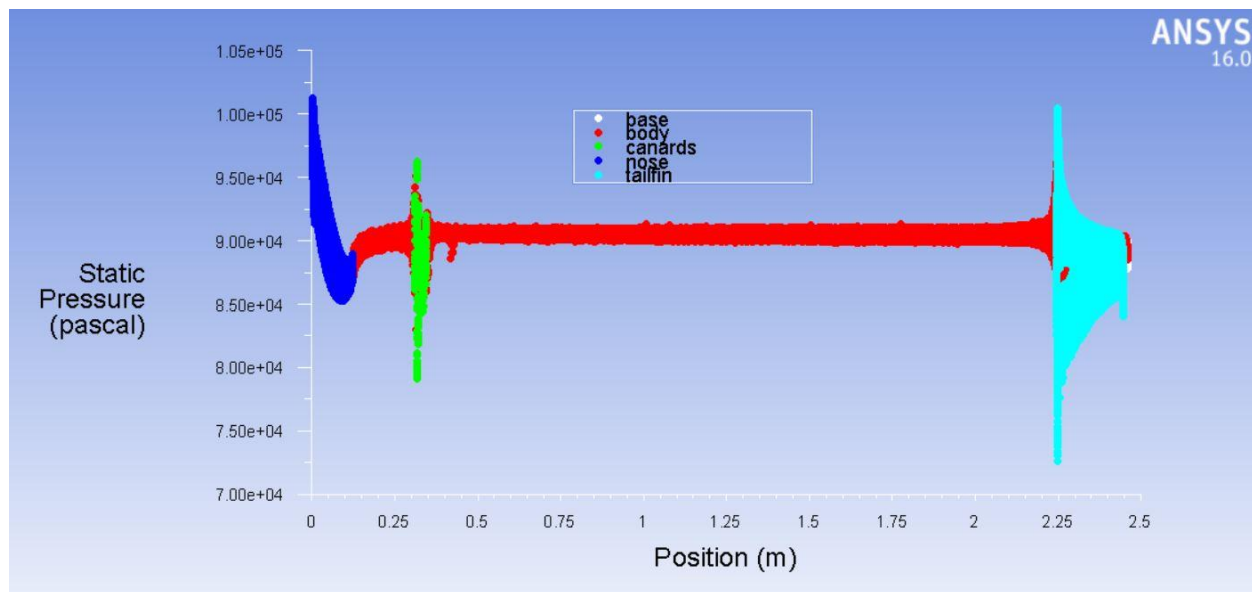


Figure 81 Static pressure distribution along missile for 0° control deflection and angle of attack $\alpha = -10^\circ$

4.2.2.2. 10 degrees deflection

The Contours of static pressure with 10 degrees control surface deflection are presented in Figure 82 - Figure 102 for different angles of attack.

Figure 82 shows the simulation case with 0 degree angle of attack and 10 degrees pitch control surface deflection. The static pressure contours presented in Figure 82 show ordinary pressure distribution

for 0 degree angle of attack. However, it is important to note that the increased pressure towards the leading edge of the control surfaces is caused by the deflected control surface.

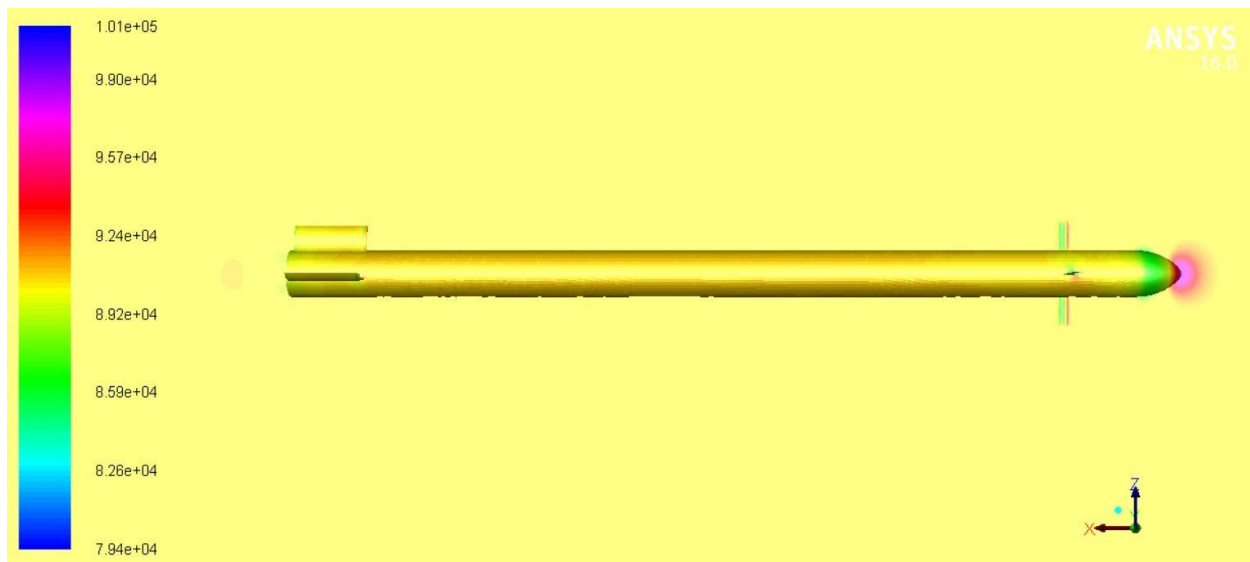


Figure 82 Static pressure contours for 10 ° control deflection and angle of attack $\alpha = 0^\circ$

Figure 83 shows the static pressure distribution along the whole missile's parts. It is important to point out that the canard control surfaces are exposed to greater pressure when comparing to Figure 61 which is due to the greater control deflection.

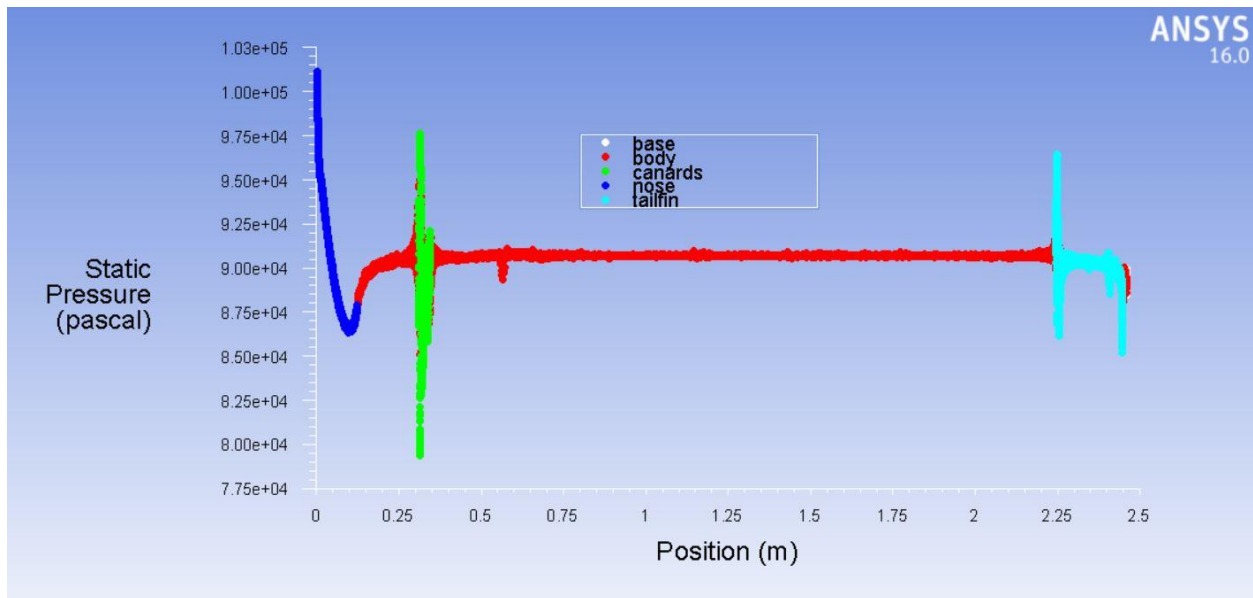


Figure 83 Static pressure distribution along missile for 10 ° control deflection and angle of attack $\alpha = 0^\circ$

Figure 84 shows the simulation case with 2 degrees angle of attack and 10 degrees pitch control surface deflection. The contours show clear pressure increases around some parts of the missile. The pressure increase around the control surfaces in these contours is greater than the contours in the Figure 62. This is caused by the control surface deflection of 0 degree. In addition, the pressure increases towards the lower area of the control surface's leading edge which is expected due to the 10 degrees deflection.

It is important to point out that the flow facing the axis of the control surface is the sum of 2 degrees angle of attack and the 10 degrees control deflection. Thus, the control surfaces are facing a total of 12 degrees angles of attack with respect to the chord line. That is why the pressure increase is greater than the case in Figure 62 where the control deflection is 0 degree.

Furthermore, the contours shown in Figure 84 indicate increased pressure towards the lower area of the front nose and tail fin leading edge of the missile. This is caused by the angled flow represented by 2 degrees angle of attack. Hence, the drag increases accordingly. In addition, the normal force components increases on the missile. These normal force components act upwards which is expected for positive angle of attack flow. However, the base drag effects can also be seen in Figure 84 through the drop of static pressure contours in that area.

The total normal force acting on the missile is directed upwards according to the normal force coefficients results presented in Figure 24. In addition, the pitch moment acting on the missile is positive which corresponds to anti-clockwise moment direction [pitch up direction]. That is according to the pitch moment coefficient results presented in Figure 23.

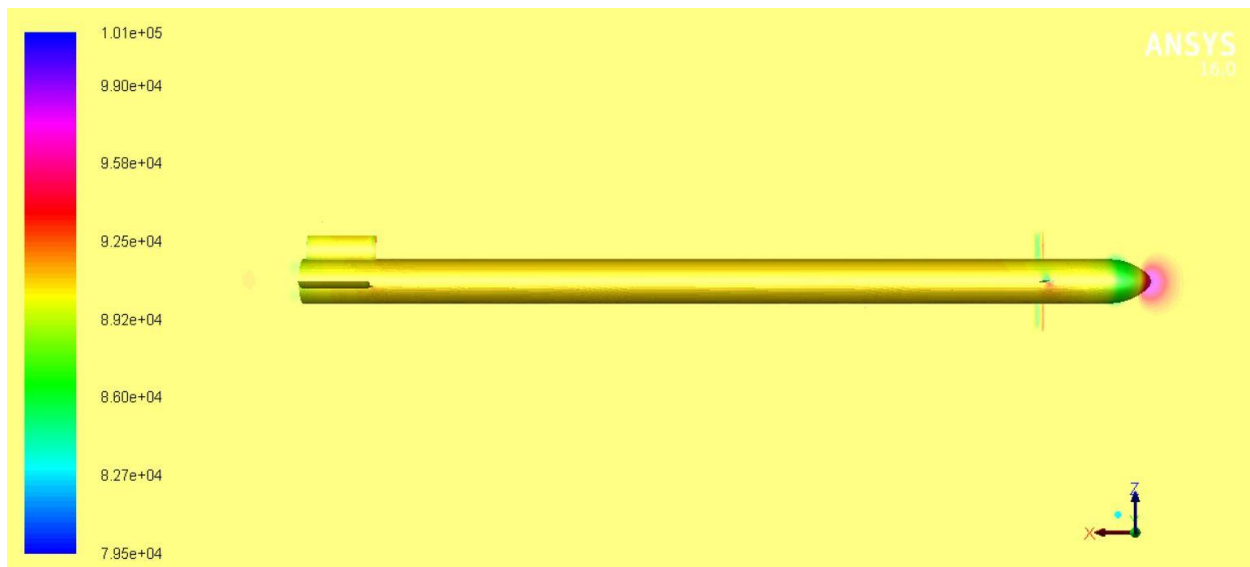


Figure 84 Static pressure contours for 10 ° control deflection and angle of attack $\alpha = 2^\circ$



Figure 85 shows the static pressure distribution along the whole missile's parts. It is important to point out that the canard control surfaces are exposed to greater pressure when comparing to Figure 63 which is due to the greater control deflection.

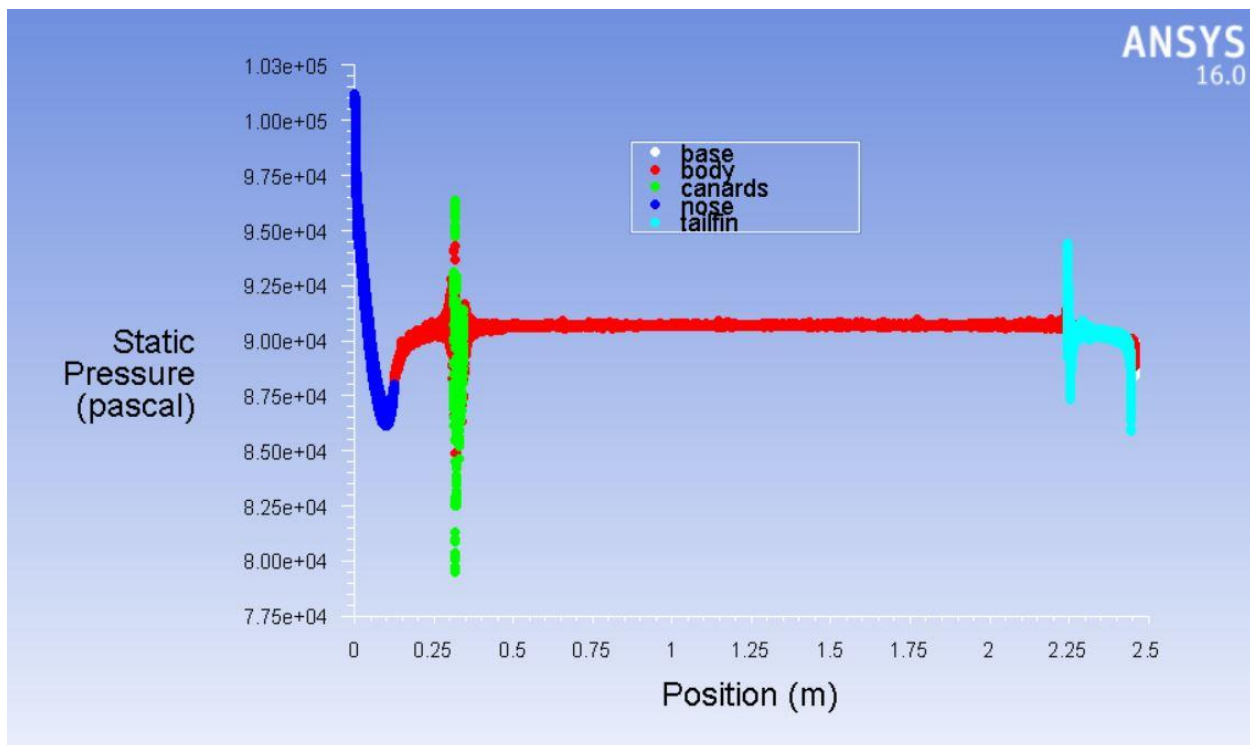


Figure 85 Static pressure distribution along missile for 10 ° control deflection and angle of attack $\alpha = 2^\circ$

Figure 86 shows the simulation case with -2 degrees angle of attack and 10 degrees pitch control surface deflection. The contours show clear pressure increases around some parts of the missile. The pressure increase around the control surfaces in these contours is greater than the contours in the Figure 64. This is caused by the control surface deflection of 0 degree. In addition, the pressure



increases towards the lower area of the control surface's leading edge which is expected due to the 10 degrees deflection.

It is important to point out that the flow facing the axis of the control surface is the sum of -2 degrees angle of attack and the 10 degrees control deflection. Thus, the control surfaces are facing a total of 8 degrees angles of attack with respect to the chord line. That is why the pressure increase is greater than the case in Figure 64 where the control deflection is 0 degree.

Furthermore, the contours shown in Figure 86 indicate increased pressure towards the upper area of the front nose and tail fin leading edge of the missile. This is caused by the angled flow represented by -2 degrees angle of attack. Hence, the drag increases accordingly. In addition, the normal force components increase on the missile. These normal force components act downwards which is expected for negative angle of attack flow. However, the base drag effects can also be seen in Figure 86 through the drop of static pressure contours in that area.

The total normal force acting on the missile is almost zero according to the normal force coefficients results presented in Figure 24. In addition, the pitch moment acting on the missile is positive which corresponds to anti-clockwise moment direction [pitch up direction]. That is according to the pitch moment coefficient results presented in Figure 23.



Figure 86 Static pressure contours for 10° control deflection and angle of attack $\alpha = -2^\circ$

Figure 87 shows the static pressure distribution along the whole missile's parts. It is important to point out that the canard control surfaces are exposed to greater pressure when comparing to Figure 65 which is due to the greater control deflection.

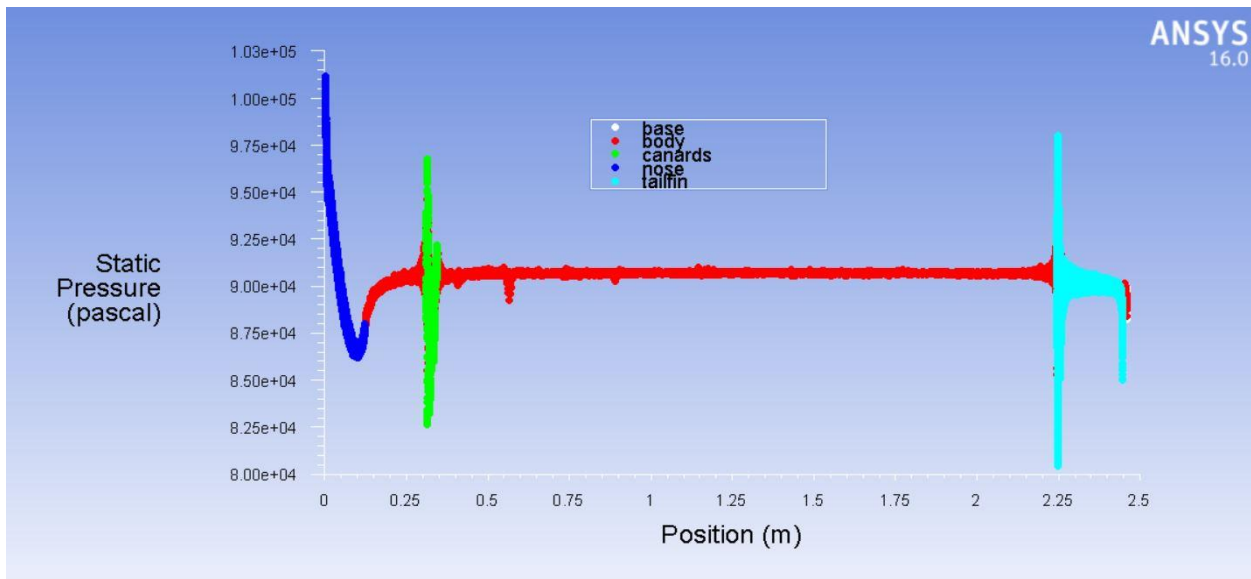


Figure 87 Static pressure distribution along missile for 10° control deflection and angle of attack $\alpha = -2^\circ$



Figure 88 shows the simulation case with 4 degrees angle of attack and 10 degrees pitch control surface deflection. The contours show clear pressure increases around some parts of the missile. The pressure increase around the control surfaces in these contours is greater than the contours in the Figure 66. This is caused by the control surface deflection of 0 degree. In addition, the pressure increases towards the lower area of the control surface's leading edge which is expected due to the 10 degrees deflection.

It is important to point out that the flow facing the axis of the control surface is the sum of 4 degrees angle of attack and the 10 degrees control deflection. Thus, the control surfaces are facing a total of 14 degrees angles of attack with respect to the chord line. That is why the pressure increase is greater than the case in Figure 66 where the control deflection is 0 degree.

Furthermore, the contours shown in Figure 88 indicate increased pressure towards the lower area of the front nose and tail fin leading edge of the missile. This is caused by the angled flow represented by 4 degrees angle of attack. Hence, the drag increases accordingly. In addition, the normal force components increases on the missile. These normal force components act upwards which is expected for positive angle of attack flow. However, the base drag effects can also be seen in Figure 88 through the drop of static pressure contours in that area.

The total normal force acting on the missile is directed upwards According to the normal force coefficients results presented in Figure 24. In addition, the pitch moment acting on the missile is zero since trim angle of attack is almost 4 degrees. That is according to the pitch moment coefficient results presented in Figure 23.

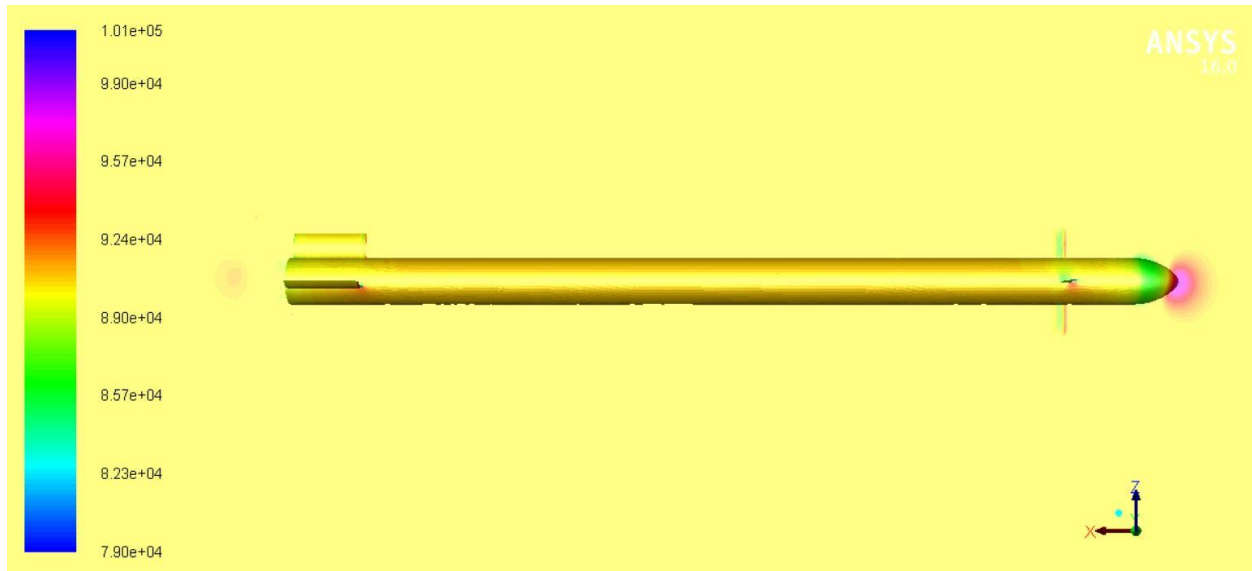


Figure 88 Static pressure contours for 10° control deflection and angle of attack $\alpha = 4^\circ$

Figure 89 shows the static pressure distribution along the whole missile's parts. It is important to point out that the canard control surfaces are exposed to greater pressure when comparing to Figure 67 which is due to the greater control deflection.

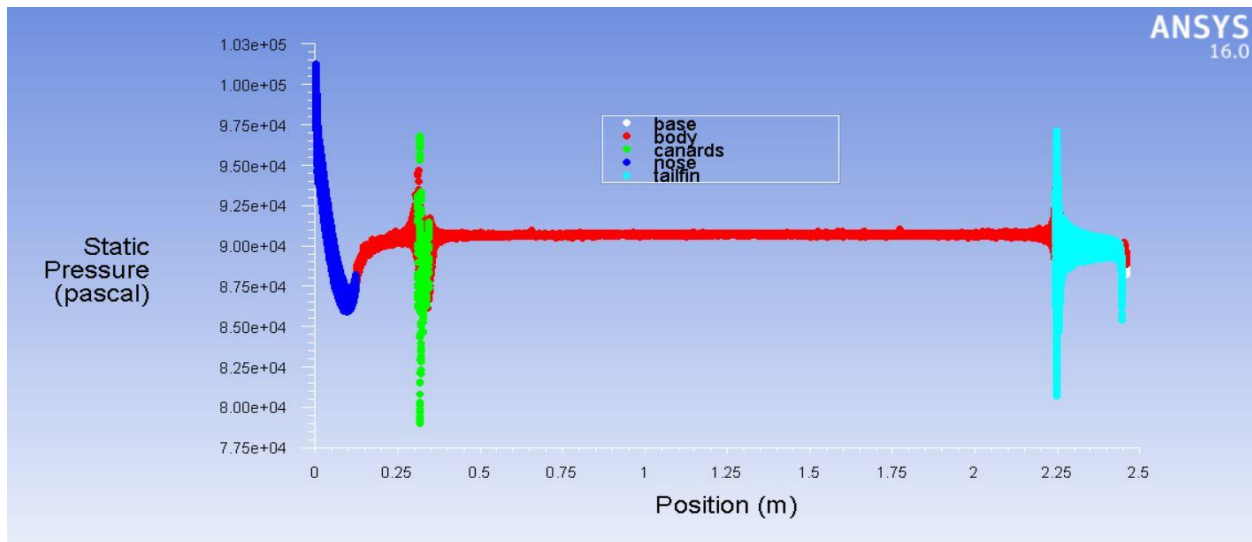


Figure 89 Static pressure distribution along missile for 10 ° control deflection and angle of attack $\alpha = 4^\circ$

Figure 90 shows the simulation case with -4 degrees angle of attack and 10 degrees pitch control surface deflection. The contours show clear pressure increases around some parts of the missile. The pressure increase around the control surfaces in these contours is greater than the contours in the Figure 68. This is caused by the control surface deflection of 0 degree. In addition, the pressure increases towards the lower area of the control surface's leading edge which is expected due to the 10 degrees deflection.

It is important to point out that the flow facing the axis of the control surface is the sum of -4 degrees angle of attack and the 10 degrees control deflection. Thus, the control surfaces are facing a total of 6 degrees angles of attack with respect to the chord line. That is why the pressure increase is greater than the case in Figure 68 where the control deflection is 0 degree.

Furthermore, the contours shown in Figure 90 indicate increased pressure towards the upper area of the front nose and tail fin leading edge of the missile. This is caused by the angled flow represented by -4 degrees angle of attack. Hence, the drag increases accordingly. In

addition, the normal force components increases on the missile. These normal force components act downwards which is expected for negative angle of attack flow. However, the base drag effects can also be seen in Figure 90 through the drop of static pressure contours in that area.

The total normal force acting on the missile is directed downwards. According to the normal force coefficients results presented in Figure 24. In addition, the pitch moment acting on the missile is positive which corresponds to anti-clockwise moment direction [pitch up direction]. That is according to the pitch moment coefficient results presented in Figure 23.



Figure 90 Static pressure contours for 10° control deflection and angle of attack $\alpha = -4^\circ$

Figure 91 shows the static pressure distribution along the whole missile's parts. It is important to point out that the canard control surfaces are exposed to greater pressure when comparing to Figure 69 which is due to the greater control deflection.

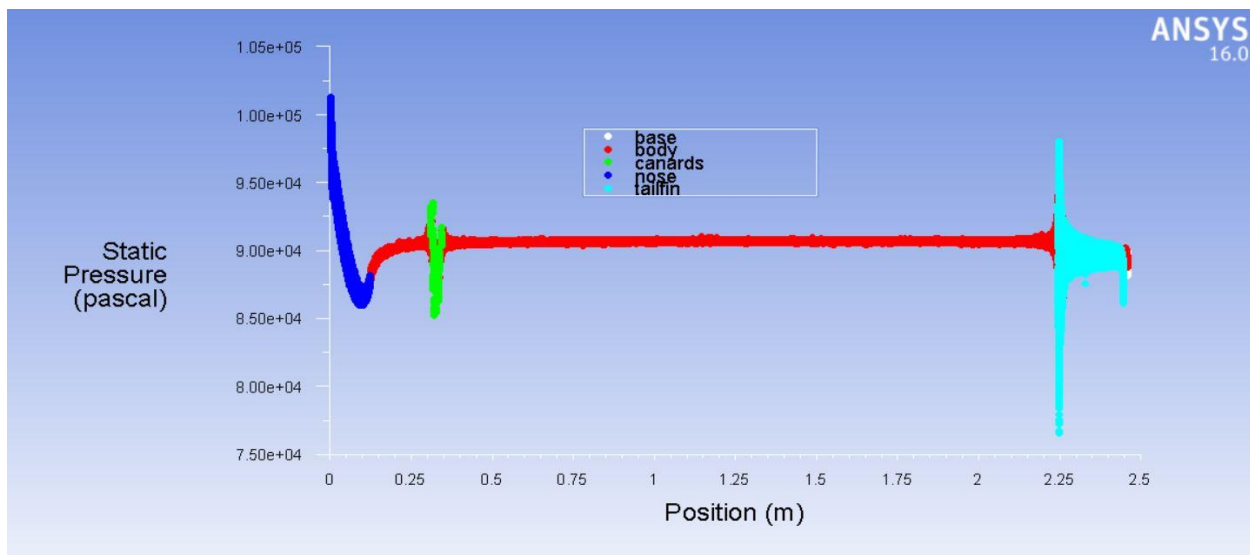


Figure 91 Static pressure distribution along missile for 10 ° control deflection and angle of attack $\alpha = -4^\circ$

Figure 92 shows the simulation case with 6 degrees angle of attack and 10 degrees pitch control surface deflection. The contours show clear pressure increases around some parts of the missile. The pressure increase around the control surfaces in these contours is greater than the contours in the Figure 70. This is caused by the control surface deflection of 0 degree. In addition, the pressure increases towards the lower area of the control surface's leading edge which is expected due to the 10 degrees deflection.

It is important to point out that the flow facing the axis of the control surface is the sum of angle of attack of 6 degrees plus the 10 degrees control deflection. Thus, the control surfaces are facing a total of 16 degrees angles of attack with respect to the chord line. That is why the pressure increase is greater than the case in Figure 70 where the control deflection is 0 degree.

Furthermore, the contours shown in Figure 92 indicate increased pressure towards the lower area of the front nose and tail fin leading edge of the missile. This is caused by the angled flow represented by

6 degrees angle of attack. Hence, the drag increases accordingly. In addition, the normal force components increases on the missile. These normal force components act upwards which is expected for positive angle of attack flow. However, the base drag effects can also be seen in Figure 92 through the drop of static pressure contours in that area.

The total normal force acting on the missile is directed upwards. According to the normal force coefficients results presented in Figure 24. In addition, the pitch moment acting on the missile is negative which corresponds to clockwise moment direction [pitch down direction]. That is according to the pitch moment coefficient results presented in Figure 23.

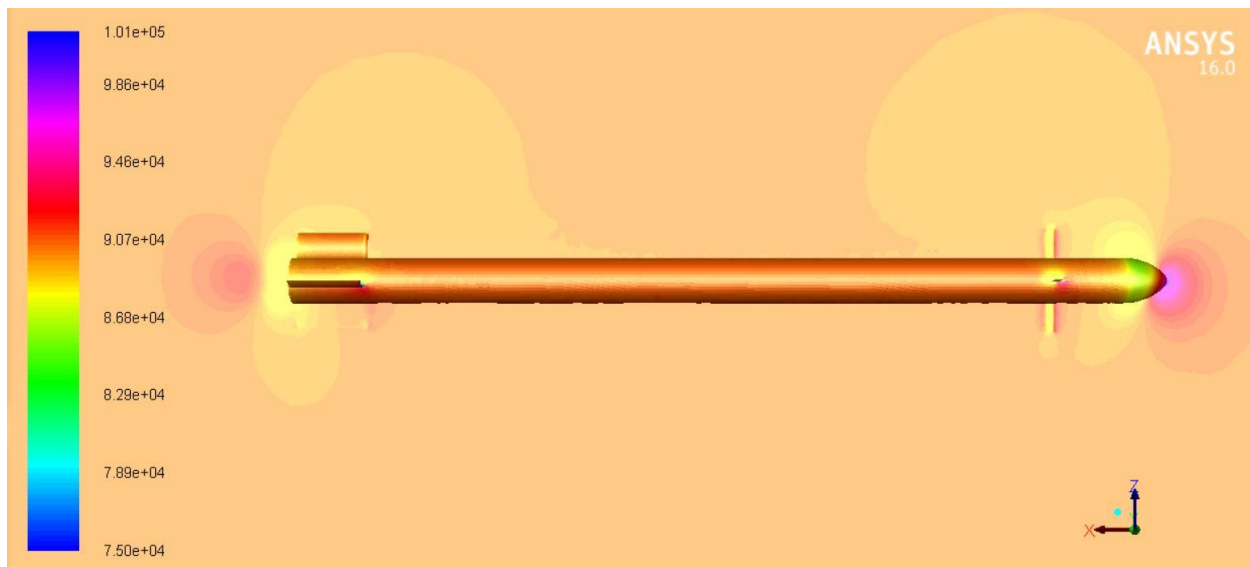


Figure 92 Static pressure contours for 10 ° control deflection and angle of attack $\alpha = 6^\circ$

Figure 93 shows the static pressure distribution along the whole missile's parts. It is important to point out that the canard control



surfaces are exposed to greater pressure when comparing to Figure 71 which is due to the greater control deflection.

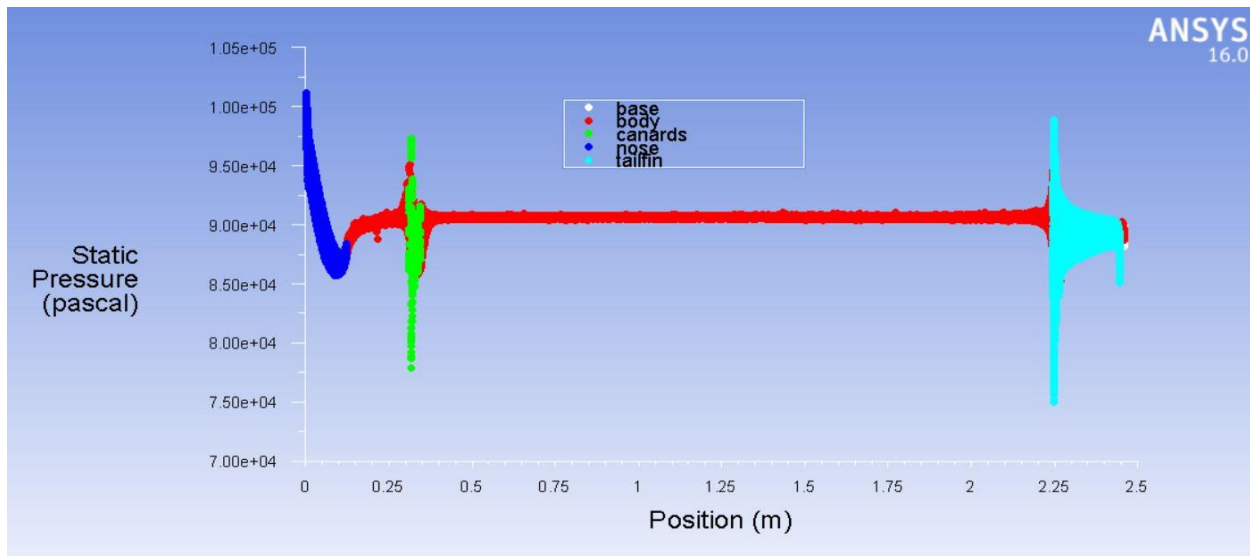


Figure 93 Static pressure distribution along missile for 10 ° control deflection and angle of attack $\alpha = 6^\circ$

Figure 94 shows the simulation case with -6 degrees angle of attack and 10 degrees pitch control surface deflection. The contours show clear pressure increases around some parts of the missile. The pressure increase around the control surfaces in these contours is greater than the contours in the Figure 72. This is caused by the control surface deflection of 0 degree. In addition, the pressure increases towards the lower area of the control surface's leading edge which is expected due to the 10 degrees deflection.

It is important to point out that the flow facing the axis of the control surface is the sum of -6 degrees angle of attack and the 10 degrees control deflection. Thus, the control surfaces are facing a total of 4 degrees angles of attack with respect to the chord line. That is why the pressure increase is greater than the case in Figure 72 where the control deflection is 0 degree.

Furthermore, the contours shown in Figure 94 indicate increased pressure towards the upper area of the front nose and tail fin leading edge of the missile. This is caused by the angled flow represented by -6 degrees angle of attack. Hence, the drag increases accordingly. In addition, the normal force components increases on the missile. These normal force components act downwards which is expected for negative angle of attack flow. However, the base drag effects can also be seen in Figure 94 through the drop of static pressure contours in that area.

The total normal force acting on the missile is directed downwards according to the normal force coefficients results presented in Figure 24. In addition, the pitch moment acting on the missile is positive which corresponds to anti-clockwise moment direction [pitch up direction]. That is according to the pitch moment coefficient results presented in Figure 23.

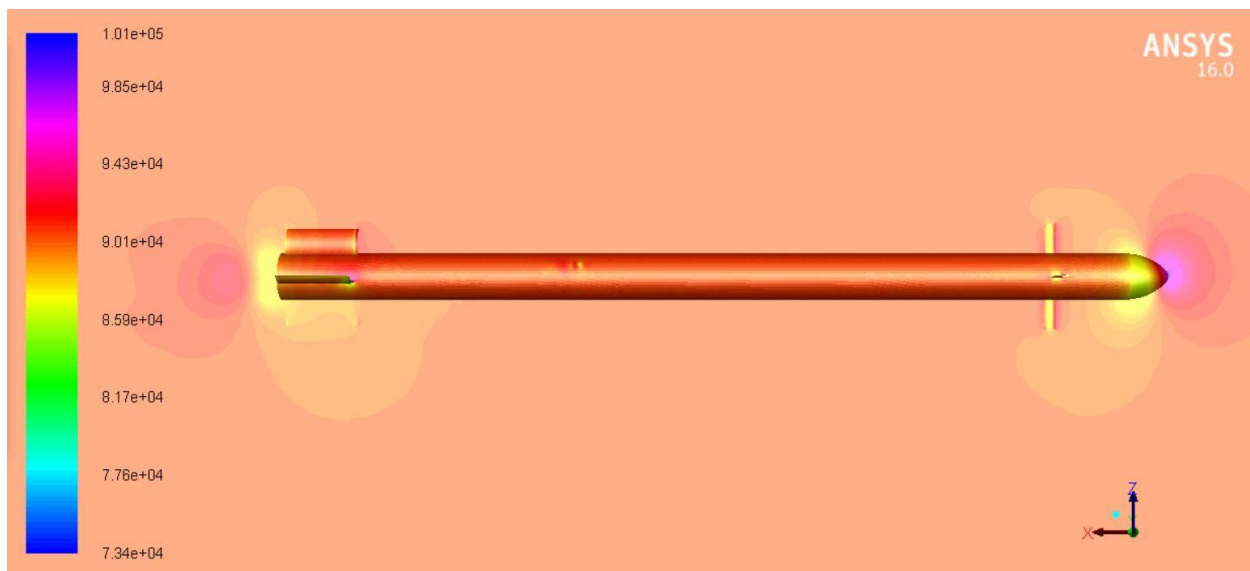


Figure 94 Static pressure contours for 10° control deflection and angle of attack $\alpha = -6^\circ$



Figure 95 shows the static pressure distribution along the whole missile's parts. It is important to point out that the canard control surfaces are exposed to greater pressure when comparing to Figure 73 which is due to the greater control deflection.

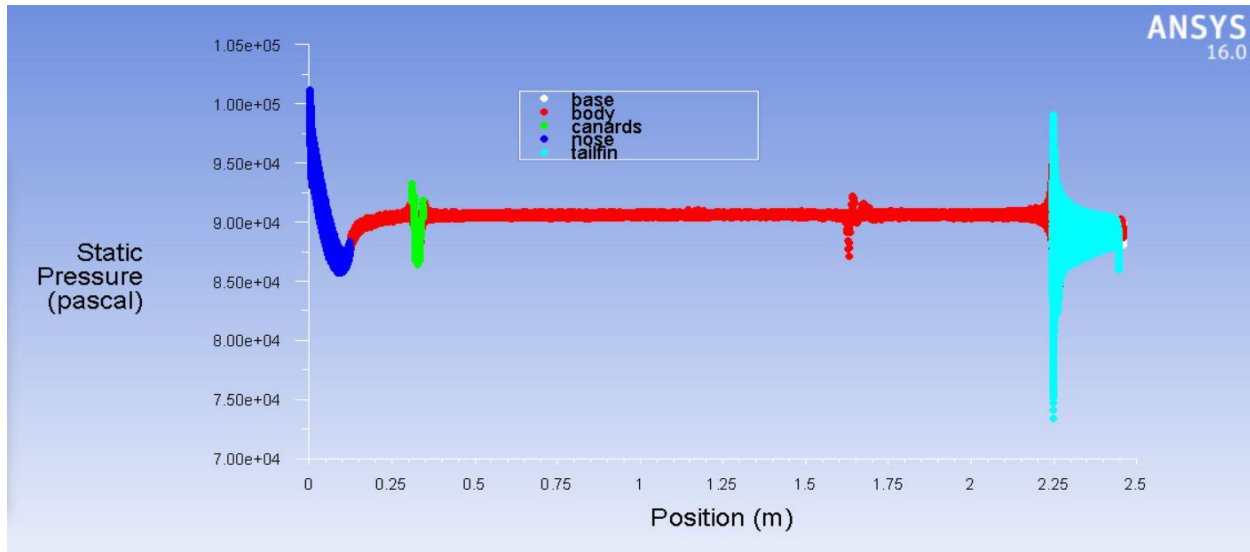


Figure 95 Static pressure distribution along missile for 10° control deflection and angle of attack $\alpha = -6^\circ$

Figure 96 shows the simulation case with 8 degrees angle of attack and 10 degrees pitch control surface deflection. The contours show clear pressure increases around some parts of the missile. The pressure increase around the control surfaces in these contours is greater than the contours in the Figure 74. This is caused by the control surface deflection of 0 degree. In addition, the pressure increases towards the lower area of the control surface's leading edge which is expected due to the 10 degrees deflection.

It is important to point out that the flow facing the axis of the control surface is the sum of 8 degrees angle of attack and the 10 degrees control deflection. Thus, the control surfaces are facing a total of 18 degrees angles of attack with respect to the chord line.



That is why the pressure increase is greater than the case in Figure 74 where the control deflection is 0 degree.

Furthermore, the contours shown in Figure 96 indicate increased pressure towards the lower area of the front nose and tail fin leading edge of the missile. This is caused by the angled flow represented by 8 degrees angle of attack. Hence, the drag increases accordingly. In addition, the normal force components increases on the missile. These normal force components act upwards which is expected for positive angle of attack flow. However, the base drag effects can also be seen in Figure 96 through the drop of static pressure contours in that area.

The total normal force acting on the missile is directed upwards According to the normal force coefficients results presented in Figure 24. In addition, the pitch moment acting on the missile is negative which corresponds to clockwise moment direction [pitch down direction]. That is according to the pitch moment coefficient results presented in Figure 23.



Figure 96 Static pressure contours for 10° control deflection and angle of attack $\alpha = 8^\circ$

Figure 97 shows the static pressure distribution along the whole missile's parts. It is important to point out that the canard control surfaces are exposed to greater pressure when comparing to Figure 75 which is due to the greater control deflection.

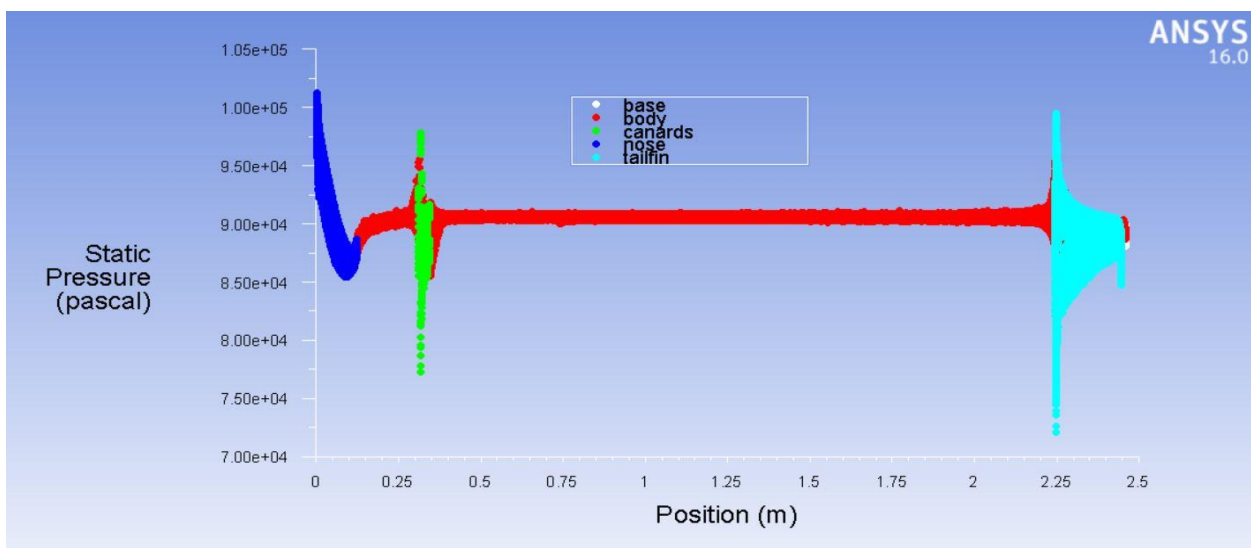


Figure 97 Static pressure distribution along missile for 10° control deflection and angle of attack $\alpha = 8^\circ$



Figure 98 shows the simulation case with -8 degrees angle of attack and 10 degrees pitch control surface deflection. The contours show clear pressure increases around some parts of the missile. The pressure increase around the control surfaces in these contours is greater than the contours in the Figure 76. This is caused by the control surface deflection of 0 degree. In addition, the pressure increases towards the higher area of the control surface's leading edge. This is expected due to the interaction between the 10 degrees deflection with the -8 angle of attack.

It is important to point out that the flow facing the axis of the control surface is the sum of -8 degrees angle of attack and the 10 degrees control deflection. Thus, the control surfaces are facing a total of 2 degrees angles of attack with respect to the chord line. That is why the pressure increase is greater than the case in Figure 76 where the control deflection is 0 degree.

Furthermore, the contours shown in Figure 98 indicate increased pressure towards the upper area of the front nose and tail fin leading edge of the missile. This is caused by the angled flow represented by -8 degrees angle of attack. Hence, the drag increases accordingly. In addition, the normal force components increases on the missile. These normal force components act downwards which is expected for negative angle of attack flow. However, the base drag effects can also be seen in Figure 98 through the drop of static pressure contours in that area.

The total normal force acting on the missile is directed downwards According to the normal force coefficients results presented in Figure 24. In addition, the pitch moment acting on the missile is positive which corresponds to anti-clockwise moment direction [pitch up direction]. That is according to the pitch moment coefficient results presented in Figure 23.

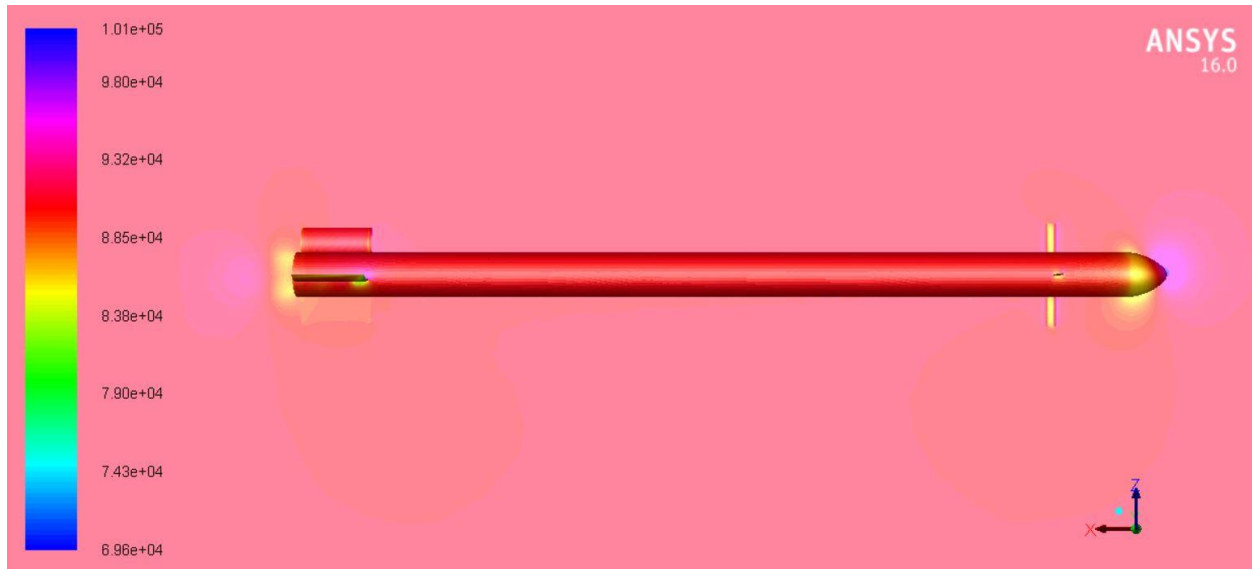


Figure 98 Static pressure contours for 10° control deflection and angle of attack $\alpha =$

Figure 99 shows the static pressure distribution along the whole missile's parts. It is important to point out that the canard control surfaces are exposed to greater pressure when comparing to Figure 77 which is due to the greater control deflection.

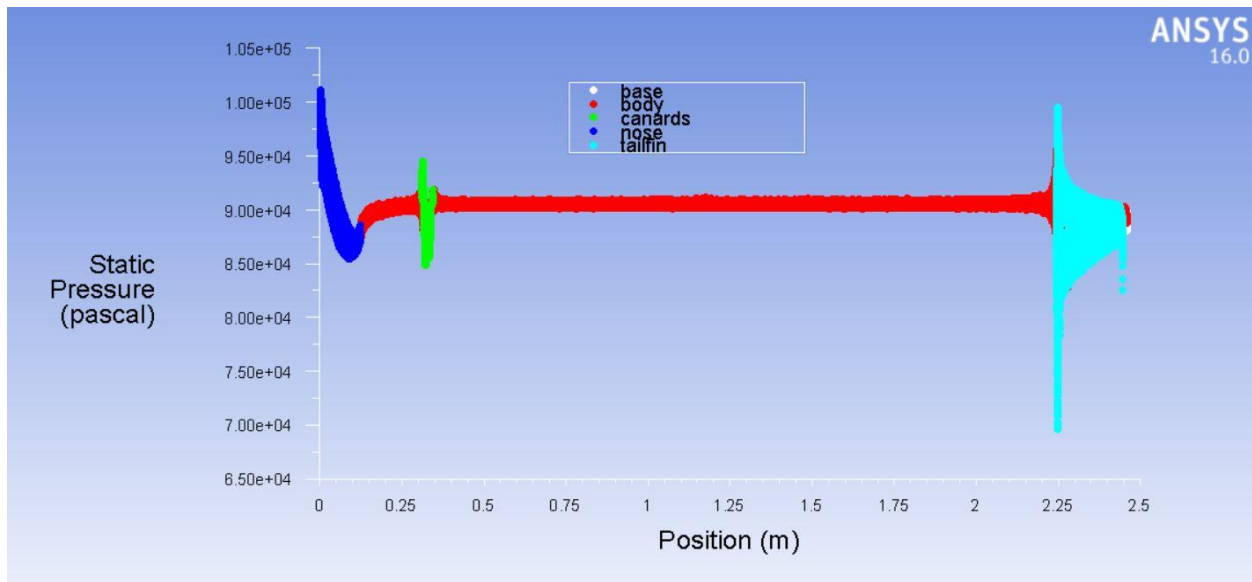


Figure 99 Static pressure distribution along missile for 10 ° control deflection and angle of attack $\alpha = -8^\circ$

Figure 100 shows the simulation case with 10 degrees angle of attack and 10 degrees pitch control surface deflection. The contours show clear pressure increases around some parts of the missile. The pressure increase around the control surfaces in these contours is greater than the contours in the Figure 78. This is caused by the control surface deflection of 0 degree. In addition, the pressure increases towards the lower area of the control surface's leading edge which is expected due to the 10 degrees deflection.

It is important to point out that the flow facing the axis of the control surface is the sum of 10 degrees angle of attack and the 10 degrees control deflection. Thus, the control surfaces are facing a total of 20 degrees angles of attack with respect to the chord line. That is why the pressure increase is greater than the case in Figure 78 where the control deflection is 0 degree.

Furthermore, the contours shown in Figure 100 indicate increased pressure towards the lower area of the front nose and tail fin leading edge of the missile. This is caused by the angled flow represented by 10 degrees angle of attack. Hence, the drag increases accordingly. In

addition, the normal force components increases on the missile. These normal force components act upwards which is expected for positive angle of attack flow. However, the base drag effects can also be seen in Figure 100 through the drop of static pressure contours in that area.

The total normal force acting on the missile is directed upwards. According to the normal force coefficients results presented in Figure 24. In addition, the pitch moment acting on the missile is negative which corresponds to clockwise moment direction [pitch down direction]. That is according to the pitch moment coefficient results presented in Figure 23.

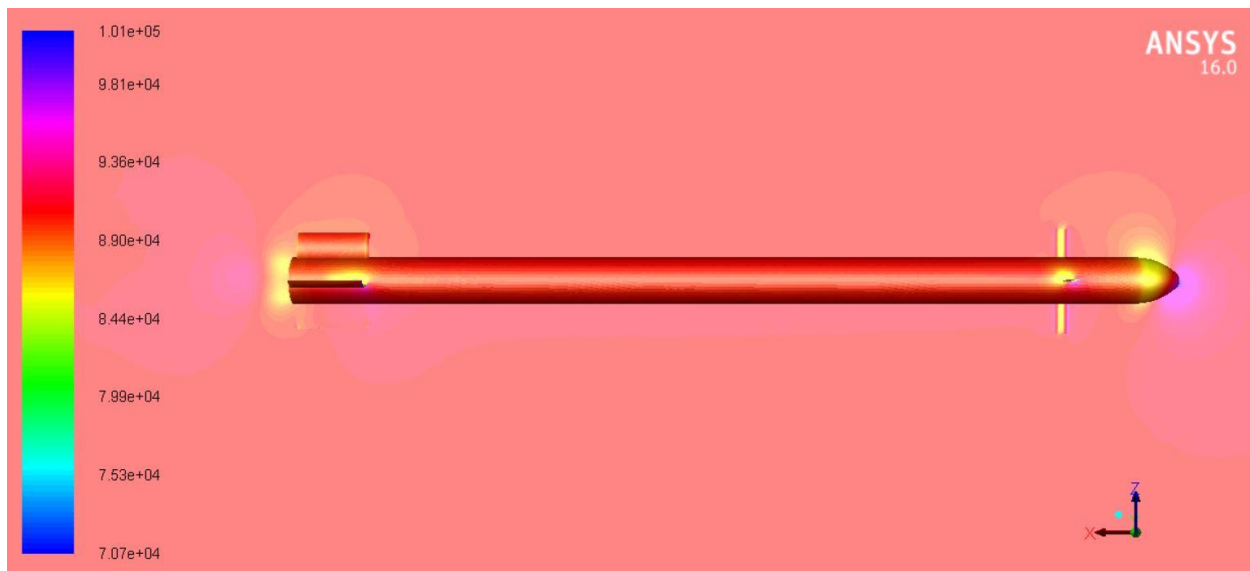


Figure 100 Static pressure contours for 10° control deflection and angle of attack $\alpha = 10^\circ$

Figure 101 shows the static pressure distribution along the whole missile's parts. It is important to point out that the canard control surfaces are exposed to greater pressure when comparing to Figure 79 which is due to the greater control deflection.

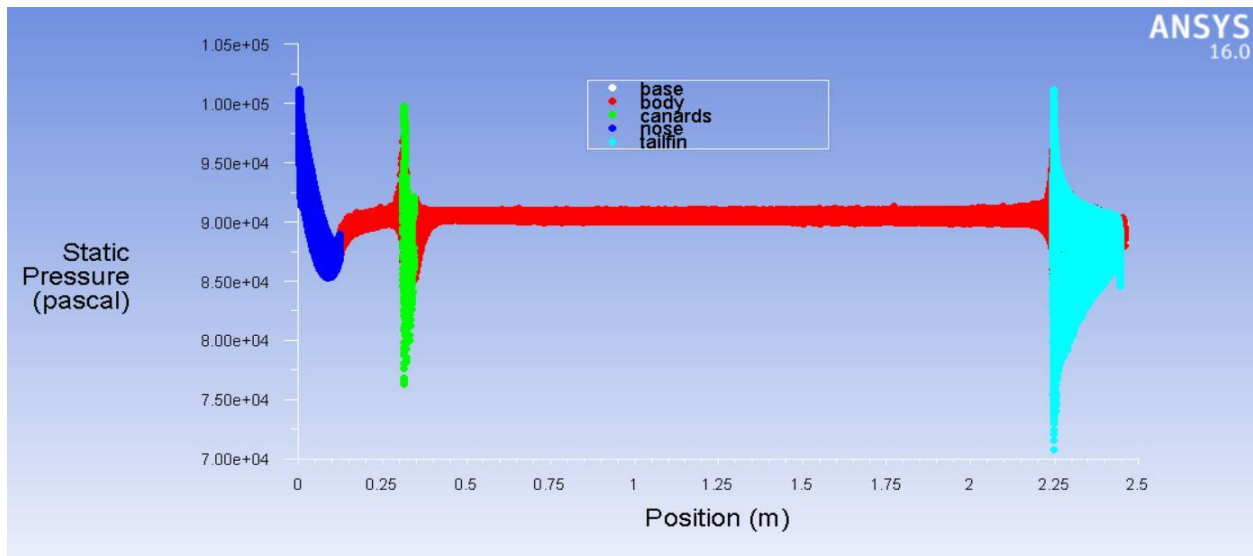


Figure 101 Static pressure distribution along missile for 10 ° control deflection and angle of attack $\alpha = 10^\circ$

Figure 102 shows the simulation case with -10 degrees angle of attack and 10 degrees pitch control surface deflection. The contours show clear pressure increases around some parts of the missile. The pressure increase around the control surfaces in these contours is greater than the contours in the Figure 80. This is caused by the control surface deflection of 0 degree. In addition, the pressure increases towards the upper area of the control surface's leading edge. This means that the control surfaces deflection cannot counter -10 degrees angle of attack.

It is important to point out that the flow facing the axis of the control surface is the sum of -10 degrees angle of attack and the 10 degrees control deflection. Thus, the control surfaces are facing a total of 0 degree angles of attack with respect to the chord line. That is why the pressure increase is greater than the case in Figure 80 where the control deflection is 0 degree.

Furthermore, the contours shown in Figure 102 indicate increased pressure towards the upper area of the front nose and tail fin leading edge of the missile. This is caused by the angled flow represented by

-10 degrees angle of attack. Hence, the drag increases accordingly. In addition, the normal force components increases on the missile. These normal force components act downwards which is expected for negative angle of attack flow. However, the base drag effects can also be seen in Figure 102 through the drop of static pressure contours in that area.

The total normal force acting on the missile is directed downwards. According to the normal force coefficients results presented in Figure 24. In addition, the pitch moment acting on the missile is positive which corresponds to anti-clockwise moment direction [pitch up direction]. That is according to the pitch moment coefficient results presented in Figure 23.

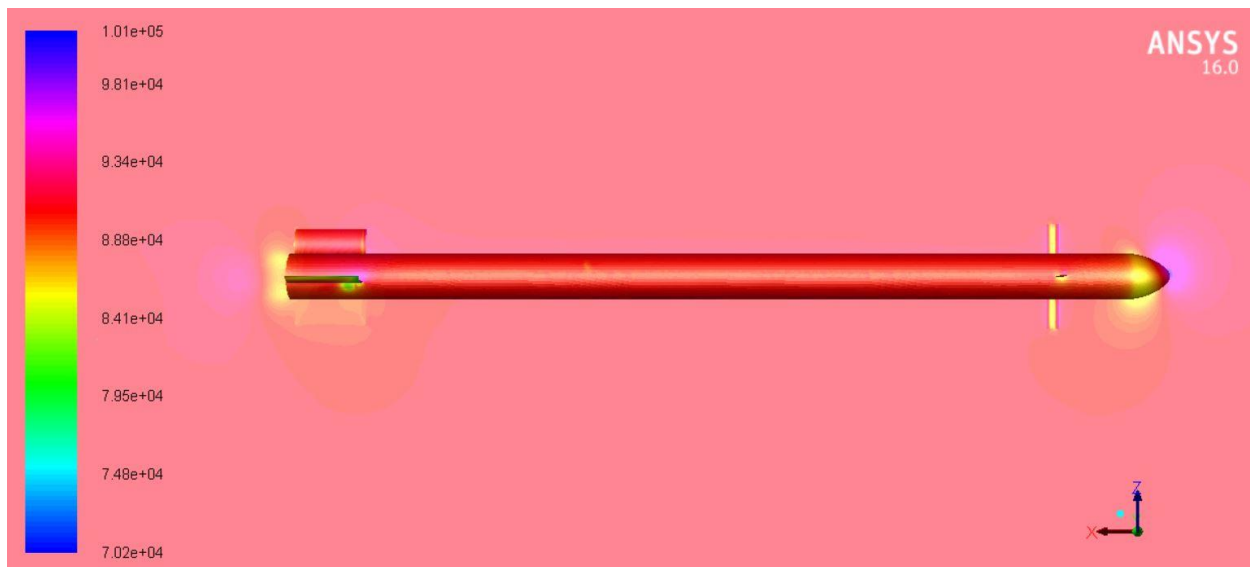


Figure 102 Static pressure contours for 10° control deflection and angle of attack $\alpha = -10^\circ$

Figure 103 shows the static pressure distribution along the whole missile's parts. It is important to point out that the canard control surfaces are exposed to greater pressure when comparing to Figure 81 which is due to the greater control deflection.

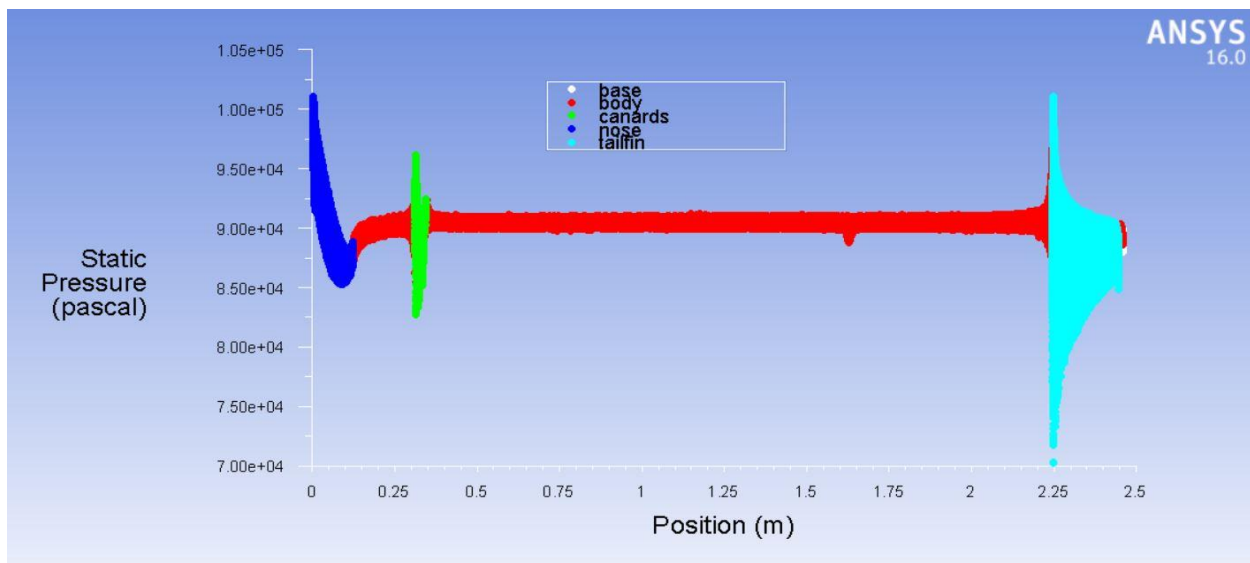


Figure 103 Static pressure distribution along missile for 10 ° control deflection and angle of attack $\alpha = -10^\circ$

4.2.2.3. 15 degrees deflection

The contours of static pressure with 15 degrees control surface deflection are presented in Figure 104 - Figure 124 for different angles of attack.

Figure 104 shows the simulation case with 0 degrees angle of attack and 15 degrees pitch control surface deflection. The contours of pressure show smooth pressure distribution due to the simulated zero angle of attack flow. However, the pressure increase in the lower area in front of the control surface is clear in Figure 104 which is due to the deflected control surface.

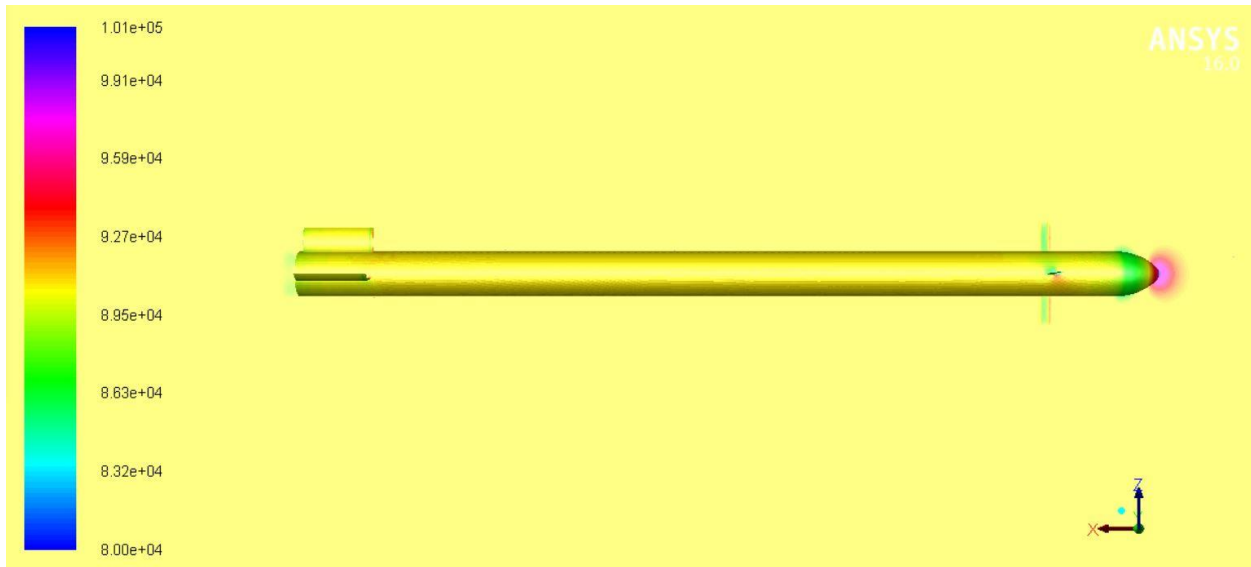


Figure 104 Static pressure contours for 15° control deflection and angle of attack $\alpha = 0^\circ$

Figure 105 shows the static pressure distribution along the whole missile's parts. It is important to point out that the canard control surfaces are exposed to greater pressure when comparing to Figure 83 which is due to the greater control deflection.

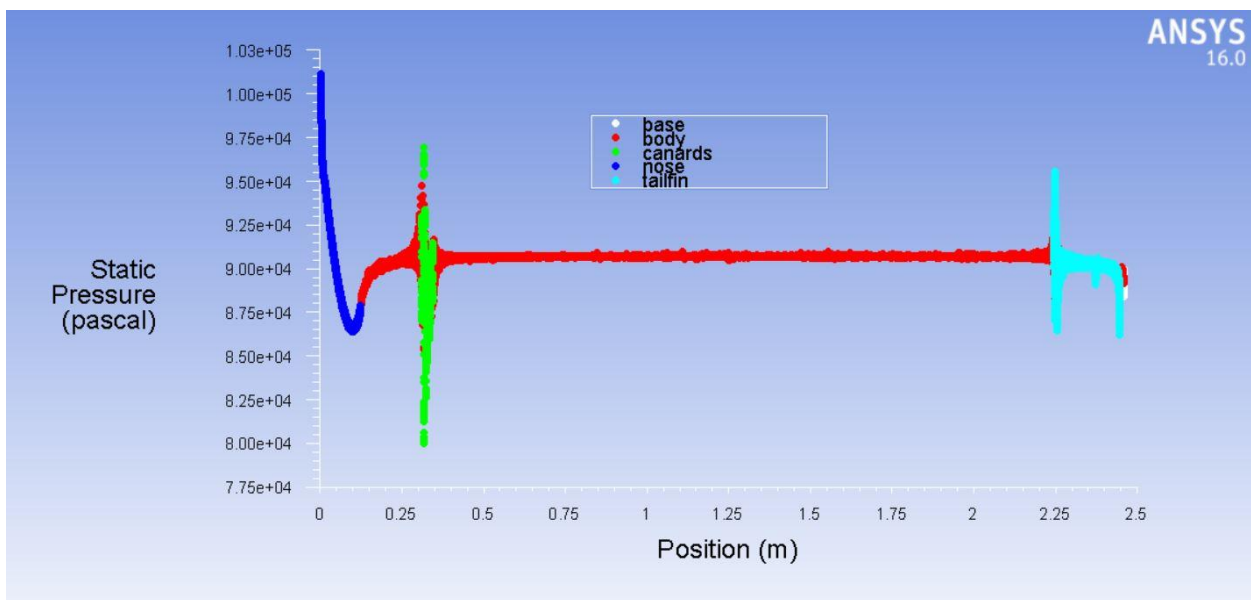


Figure 105 Static pressure distribution along missile for 15° control deflection and angle of attack $\alpha = 0^\circ$



Figure 106 shows the simulation case with 2 degrees angle of attack and 15 degrees pitch control surface deflection. The contours show clear pressure increases around some parts of the missile. The pressure increase around the control surfaces in these contours is greater than the contours in the Figure 84. This is caused by the control surface deflection of 10 degrees. In addition, the pressure increases towards the lower area of the control surface's leading edge which is expected due to the 15 degrees deflection.

It is important to point out that the flow facing the axis of the control surface is the sum of 2 degrees angle of attack and the 15 degrees control deflection. Thus, the control surfaces are facing a total of 17 degrees angles of attack with respect to the chord line. That is why the pressure increase is greater than the case in Figure 84 where the control deflection is 10 degrees.

Furthermore, the contours shown in Figure 106 indicate increased pressure towards the lower area of the front nose and tail fin leading edge of the missile. This is caused by the angled flow represented by 2 degrees angle of attack. Hence, the drag increases accordingly. In addition, the normal force components increases on the missile. These normal force components act upwards which is expected for positive angle of attack flow. However, the base drag effects can also be seen in Figure 106 through the drop of static pressure contours in that area.

The total normal force acting on the missile is directed upwards. According to the normal force coefficients results presented in Figure 24. In addition, the pitch moment acting on the missile is positive which corresponds to anti-clockwise moment direction [pitch up

direction]. That is according to the pitch moment coefficient results presented in Figure 23.

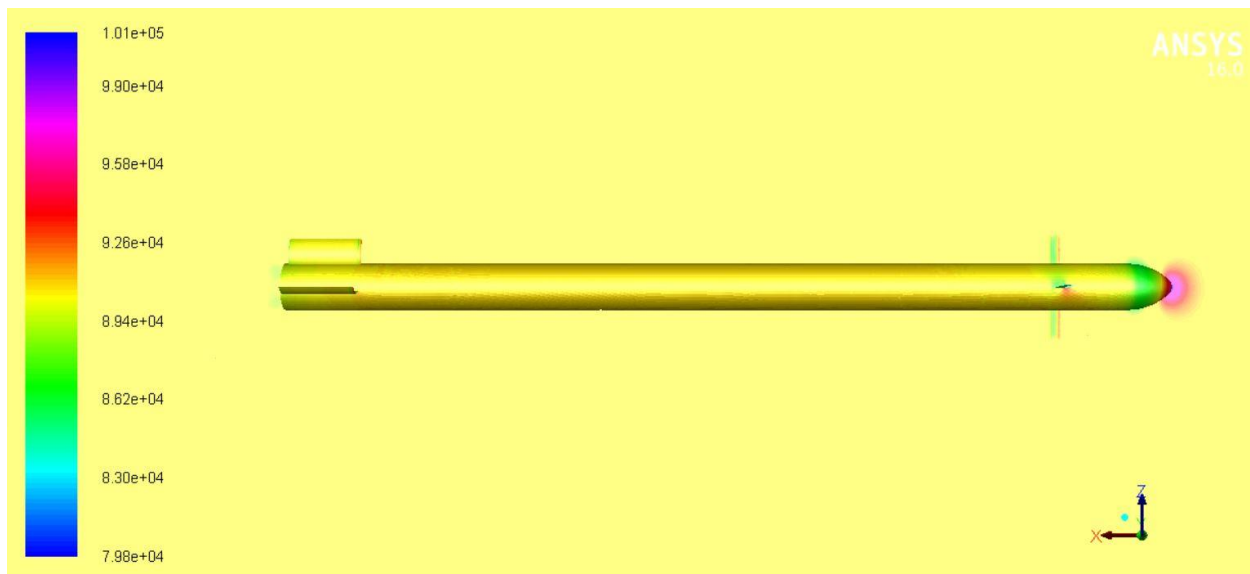


Figure 106 Static pressure contours for 15° control deflection and angle of attack $\alpha = 2^\circ$

Figure 107 shows the static pressure distribution along the whole missile's parts. It is important to point out that the canard control surfaces are exposed to greater pressure when comparing to Figure 85 which is due to the greater control deflection.

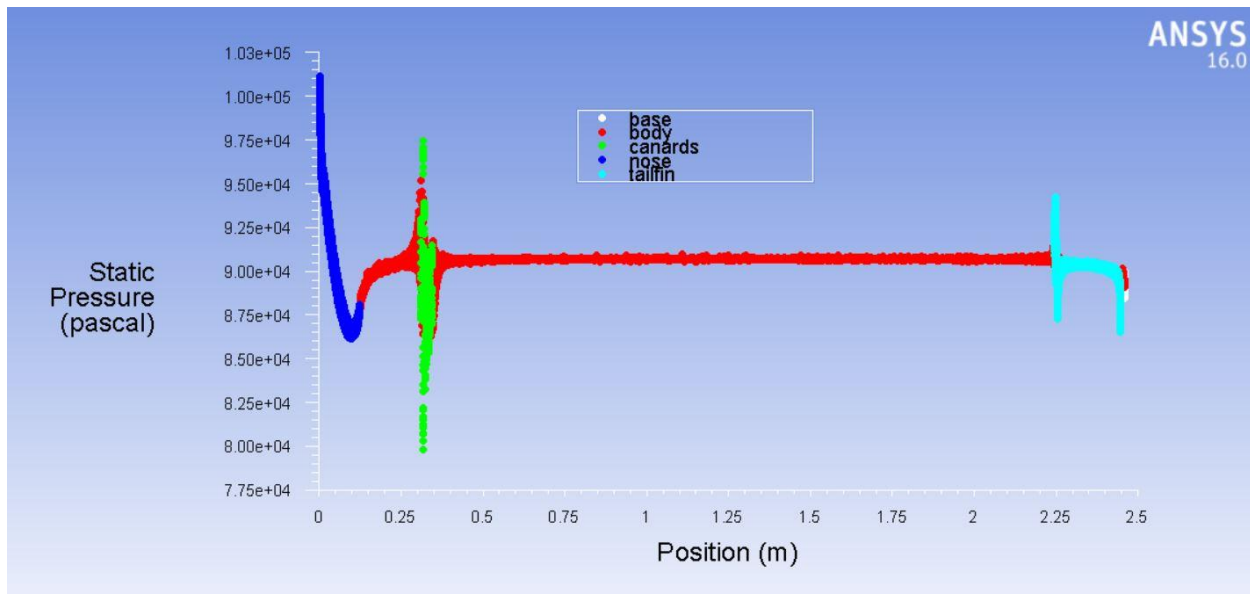


Figure 107 Static pressure distribution along missile for 15 ° control deflection and angle of attack $\alpha = 2^\circ$

Figure 108 shows the simulation case with -2 degrees angle of attack and 15 degrees pitch control surface deflection. The contours show clear pressure increases around some parts of the missile. The pressure increase around the control surfaces in these contours is greater than the contours in the Figure 86. This is caused by the control surface deflection of 10 degrees. In addition, the pressure increases towards the lower area of the control surface's leading edge which is expected due to the 15 degrees deflection.

It is important to point out that the flow facing the axis of the control surface is the sum of -2 degrees angle of attack and the 10 degrees control deflection. Thus, the control surfaces are facing a total of 8 degrees angles of attack with respect to the chord line. That is why the pressure increase is greater than the case in Figure 86 where the control deflection is 10 degrees.

Furthermore, the contours shown in Figure 108 indicate increased pressure towards the upper area of the front nose and tail fin leading edge of the missile. This is caused by the angled flow represented by

-2 degrees angle of attack. Hence, the drag increases accordingly. In addition, the normal force components increases on the missile. These normal force components act downwards which is expected for negative angle of attack flow. However, the base drag effects can also be seen in Figure 108 through the drop of static pressure contours in that area.

The total normal force acting on the missile is almost zero according to the normal force coefficients results presented in Figure 24. In addition, the pitch moment acting on the missile is positive which corresponds to anti-clockwise moment direction [pitch up direction]. That is according to the pitch moment coefficient results presented in Figure 23.

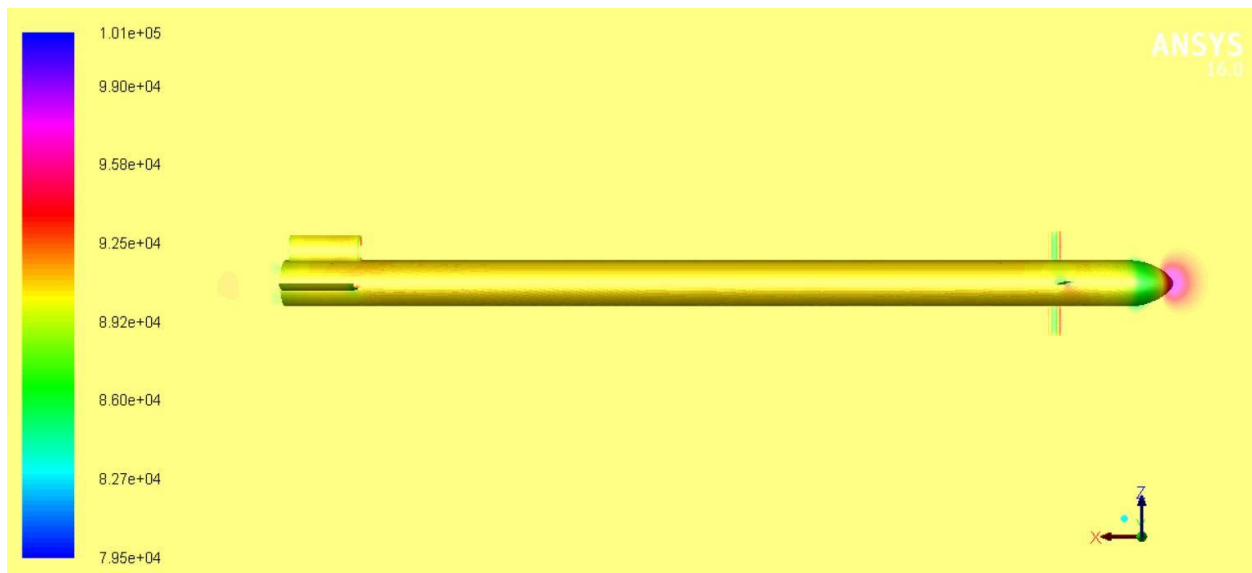


Figure 108 Static pressure contours for 15 ° control deflection and angle of attack $\alpha = -2^\circ$

Figure 109 shows the static pressure distribution along the whole missile's parts. It is important to point out that the canard control surfaces are exposed to greater pressure when comparing to Figure 87 which is due to the greater control deflection.

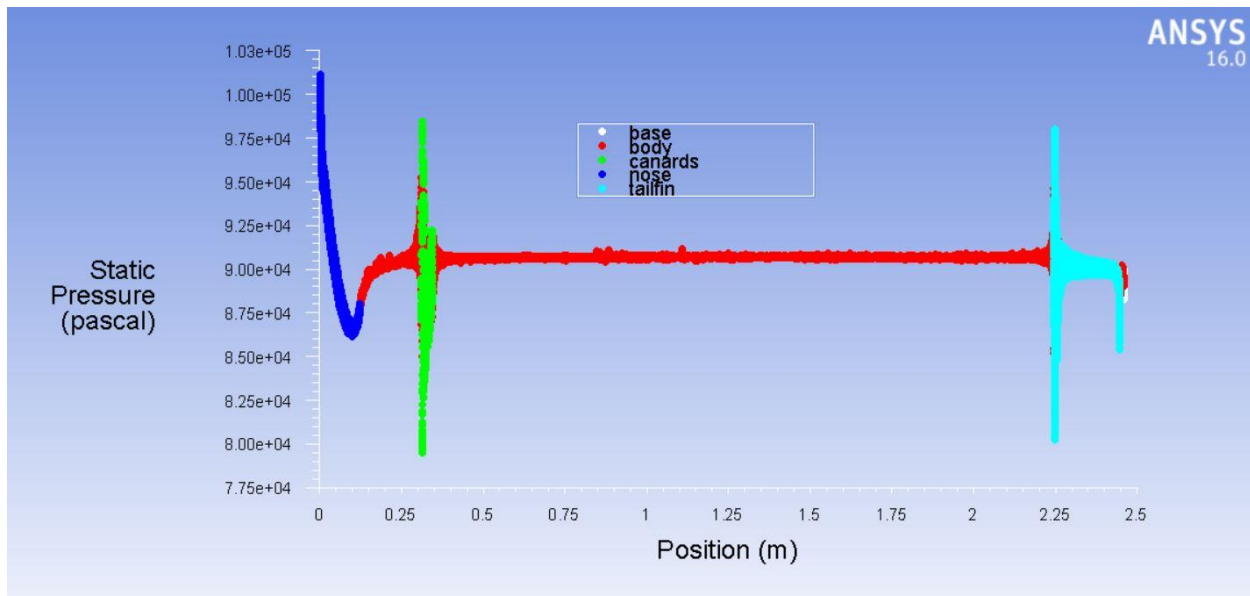


Figure 109 Static pressure distribution along missile for 15 ° control deflection and angle of attack $\alpha = -2^\circ$

Figure 110 shows the simulation case with 4 degrees angle of attack and 15 degrees pitch control surface deflection. The contours show clear pressure increases around some parts of the missile. The pressure increase around the control surfaces in these contours is greater than the contours in the Figure 88. This is caused by the control surface deflection of 10 degrees. In addition, the pressure increases towards the lower area of the control surface's leading edge which is expected due to the 15 degrees deflection.

It is important to point out that the flow facing the axis of the control surface is the sum of 4 degrees angle of attack and the 15 degrees control deflection. Thus, the control surfaces are facing a total of 19 degrees angles of attack with respect to the chord line. That is why the pressure increase is greater than the case in Figure 88 where the control deflection is 10 degrees.

Furthermore, the contours shown in Figure 110 indicate increased pressure towards the lower area of the front nose and tail fin leading edge of the missile. This is caused by the angled flow represented by 4 degrees angle of attack. Hence, the drag increases accordingly. In addition, the normal force components increases on the missile. These normal force components act upwards which is expected for positive angle of attack flow. However, the base drag effects can also be seen in Figure 110 through the drop of static pressure contours in that area.

The total normal force acting on the missile is directed upwards According to the normal force coefficients results presented in Figure 24. In addition, the pitch moment acting on the missile is zero since trim angle of attack is almost 4 degrees. That is according to the pitch moment coefficient results presented in Figure 23.

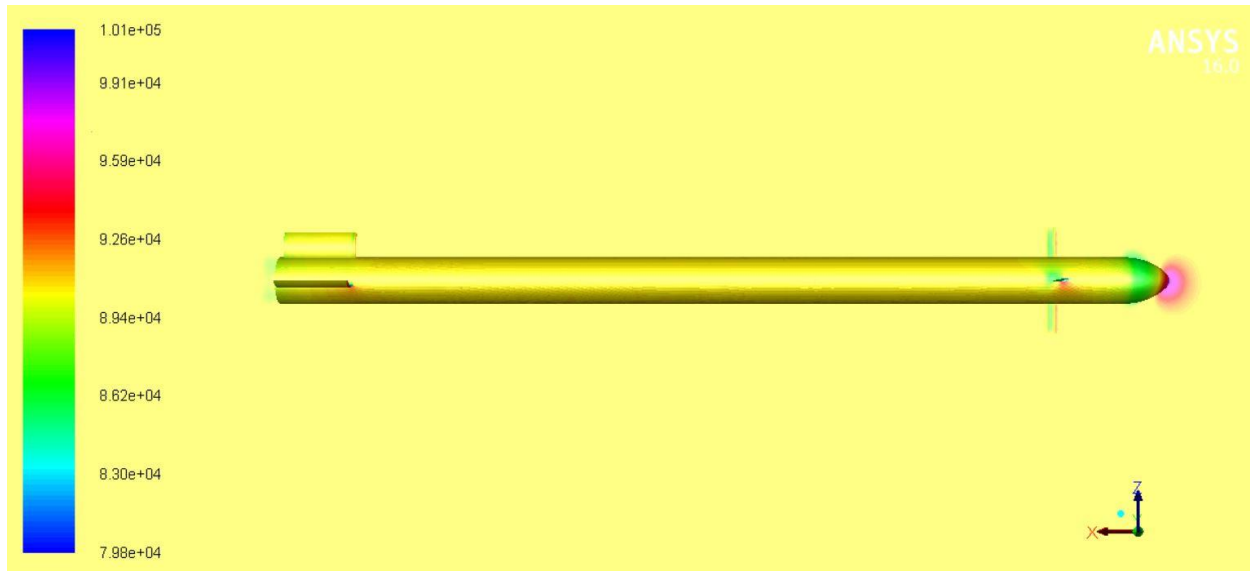


Figure 110 Static pressure contours for 15 ° control deflection and angle of attack $\alpha = 4^\circ$

Figure 111 shows the static pressure distribution along the whole missile's parts. It is important to point out that the canard control

surfaces are exposed to greater pressure when comparing to Figure 89 which is due to the greater control deflection.

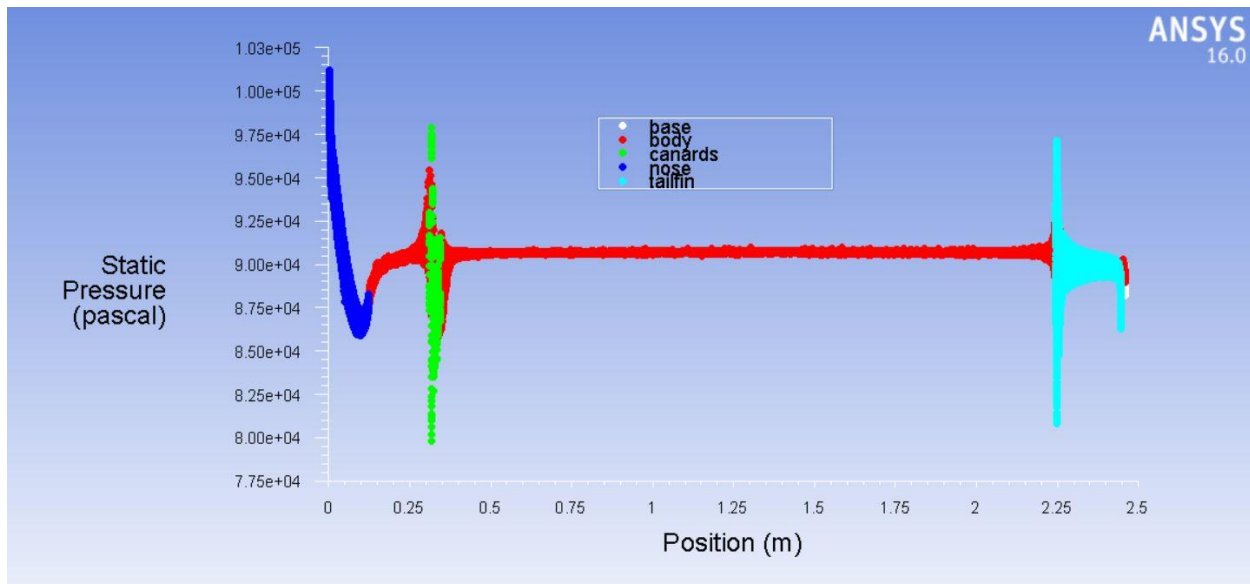


Figure 111 Static pressure distribution along missile for 15 ° control deflection and angle of attack $\alpha = 4^\circ$

Figure 112 shows the simulation case with -4 degrees angle of attack and 15 degrees pitch control surface deflection. The contours show clear pressure increases around some parts of the missile. The pressure increase around the control surfaces in these contours is greater than the contours in the Figure 90. This is caused by the control surface deflection of 10 degrees. In addition, the pressure increases towards the lower area of the control surface's leading edge which is expected due to the 15 degrees deflection.

It is important to point out that the flow facing the axis of the control surface is the sum of -4 degrees angle of attack and the 15 degrees control deflection. Thus, the control surfaces are facing a total of 11 degrees angles of attack with respect to the chord line. That is why the pressure increase is greater than the case in Figure 90 where the control deflection is 10 degrees.

Furthermore, the contours shown in Figure 112 indicate increased pressure towards the upper area of the front nose and tail fin leading edge of the missile. This is caused by the angled flow represented by -4 degrees angle of attack. Hence, the drag increases accordingly. In addition, the normal force components increases on the missile. These normal force components act downwards which is expected for negative angle of attack flow. However, the base drag effects can also be seen in Figure 112 through the drop of static pressure contours in that area.

The total normal force acting on the missile is directed downwards. According to the normal force coefficients results presented in Figure 24. In addition, the pitch moment acting on the missile is positive which corresponds to anti-clockwise moment direction [pitch up direction]. That is according to the pitch moment coefficient results presented in Figure 23.

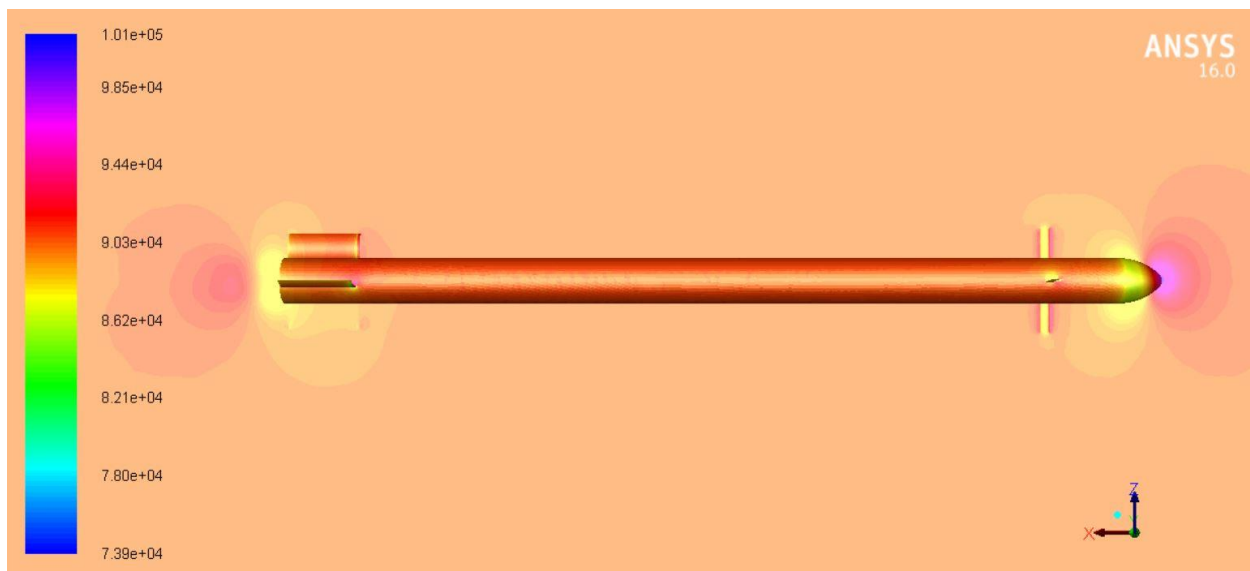


Figure 112 Static pressure contours for 15° control deflection and angle of attack $\alpha = -4^\circ$

Figure 113 shows the static pressure distribution along the whole missile's parts. It is important to point out that the canard control surfaces is exposed to greater pressure when comparing to Figure 91 which is due are the greater control deflection.

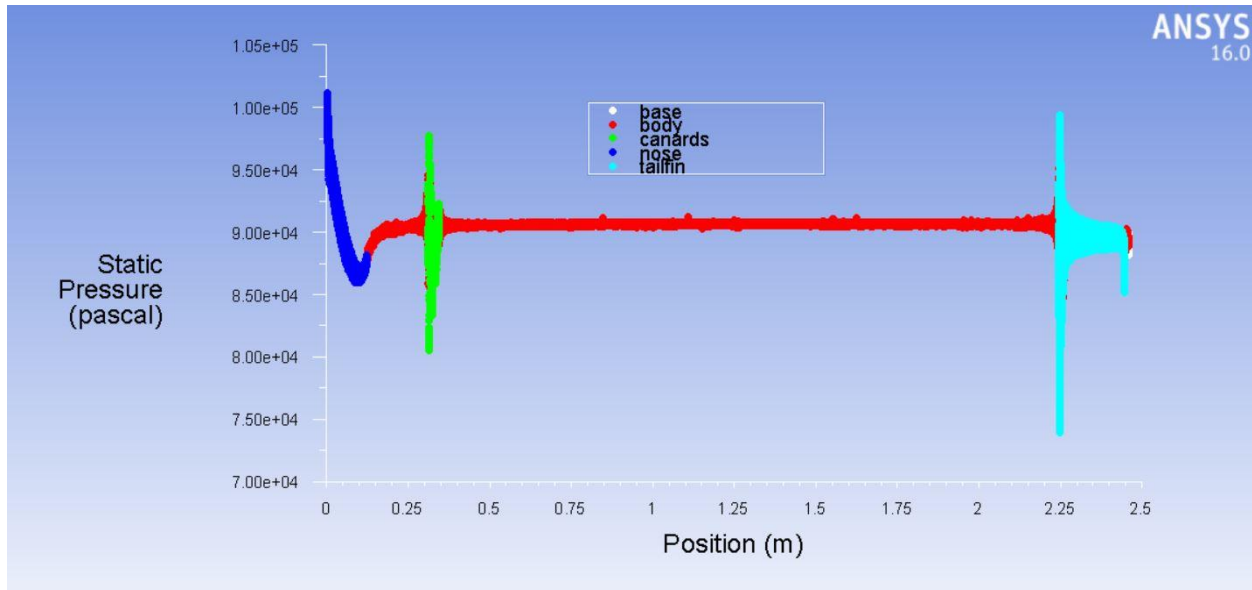


Figure 113 Static pressure distribution along missile for 15 ° control deflection and angle of attack $\alpha = -4^\circ$

Figure 114 shows the simulation case with 6 degrees angle of attack and 15 degrees pitch control surface deflection. The contours show clear pressure increases around some parts of the missile. The pressure increase around the control surfaces in these contours is greater than the contours in the Figure 92. This is caused by the control surface deflection of 10 degrees. In addition, the pressure increases towards the lower area of the control surface's leading edge which is expected due to the 15 degrees deflection.

It is important to point out that the flow facing the axis of the control surface is the sum of 6 degrees angle of attack and the 15 degrees control deflection. Thus, the control surfaces are facing a total of 21 degrees angles of attack with respect to the chord line.



That is why the pressure increase is greater than the case in Figure 92 where the control deflection is 10 degrees.

Furthermore, the contours shown in Figure 114 indicate increased pressure towards the lower area of the front nose and tail fin leading edge of the missile. This is caused by the angled flow represented by 6 degrees angle of attack. Hence, the drag increases accordingly. In addition, the normal force components increases on the missile. These normal force components act upwards which is expected for positive angle of attack flow. However, the base drag effects can also be seen in Figure 114 through the drop of static pressure contours in that area.

The total normal force acting on the missile is directed upwards. According to the normal force coefficients results presented in Figure 24. In addition, the pitch moment acting on the missile is negative which corresponds to clockwise moment direction [pitch down direction]. That is according to the pitch moment coefficient results presented in Figure 23.

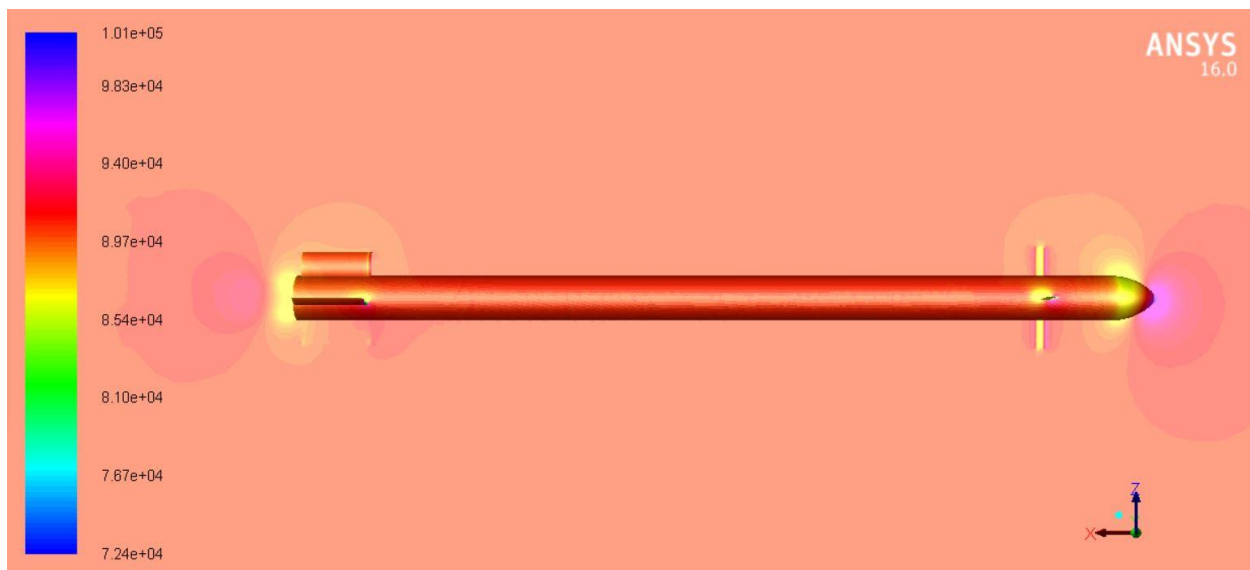


Figure 114 Static pressure contours for 15 ° control deflection and angle of attack $\alpha = 6^\circ$

Figure 115 shows the static pressure distribution along the whole missile's parts. It is important to point out that the canard control surfaces are exposed to greater pressure when comparing to Figure 93 which is due to the greater control deflection.

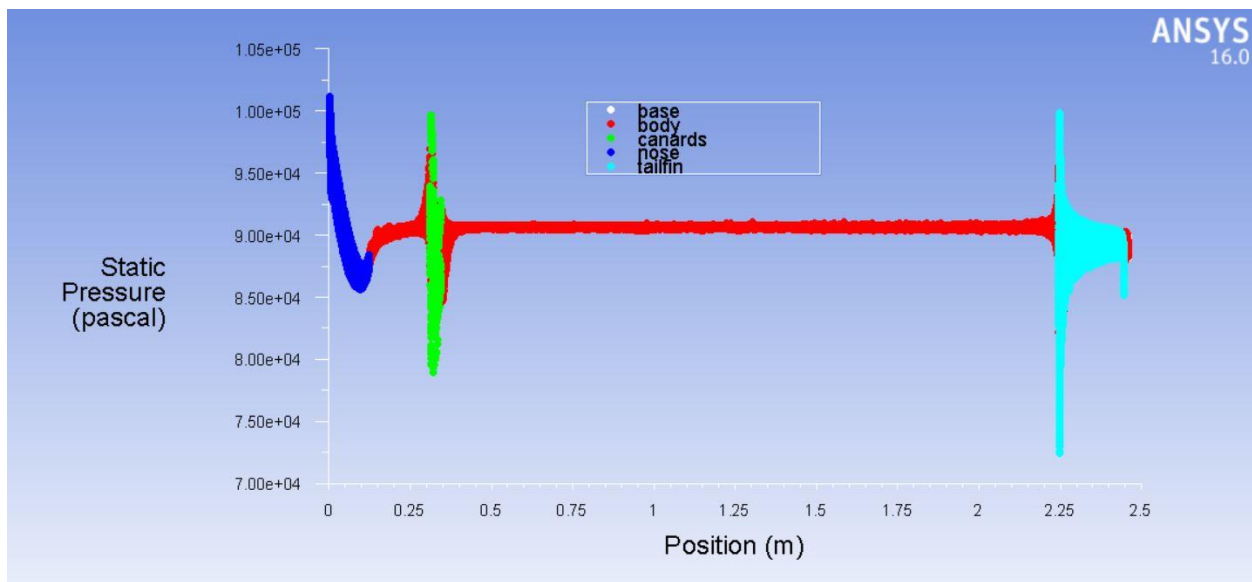


Figure 115 Static pressure distribution along missile for 15 ° control deflection and angle of attack $\alpha = 6^\circ$

Figure 116 shows the simulation case with -6 degrees angle of attack and 15 degrees pitch control surface deflection. The contours show clear pressure increases around some parts of the missile. The pressure increase around the control surfaces in these contours is greater than the contours in the Figure 94. This is caused by the control surface deflection of 10 degrees. In addition, the pressure increases towards the lower area of the control surface's leading edge which is expected due to the 15 degrees deflection.

It is important to point out that the flow facing the axis of the control surface is the sum of -6 degrees angle of attack and the 15



degrees control deflection. Thus, the control surfaces are facing a total of 9 degrees angles of attack with respect to the chord line. That is why the pressure increase is greater than the case in Figure 94 where the control deflection is 10 degrees.

Furthermore, the contours shown in Figure 116 indicate increased pressure towards the upper area of the front nose and tail fin leading edge of the missile. This is caused by the angled flow represented by -6 degrees angle of attack. Hence, the drag increases accordingly. In addition, the normal force components increases on the missile. These normal force components act downwards which is expected for negative angle of attack flow. However, the base drag effects can also be seen in Figure 116 through the drop of static pressure contours in that area.

The total normal force acting on the missile is directed downwards According to the normal force coefficients results presented in Figure 24. In addition, the pitch moment acting on the missile is positive which corresponds to anti-clockwise moment direction [pitch up direction]. That is according to the pitch moment coefficient results presented in Figure 23.

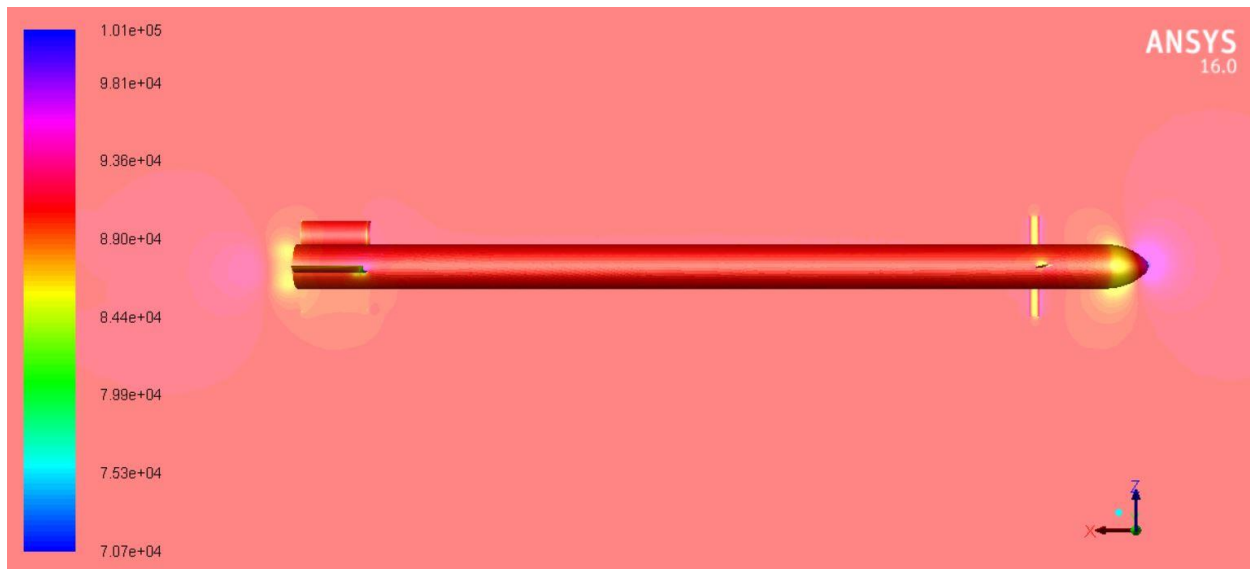


Figure 116 Static pressure contours for 15° control deflection and angle of attack $\alpha = -6^\circ$

Figure 117 shows the static pressure distribution along the whole missile's parts. It is important to point out that the canard control surfaces are exposed to greater pressure when comparing to Figure 95 which is due to the greater control deflection.

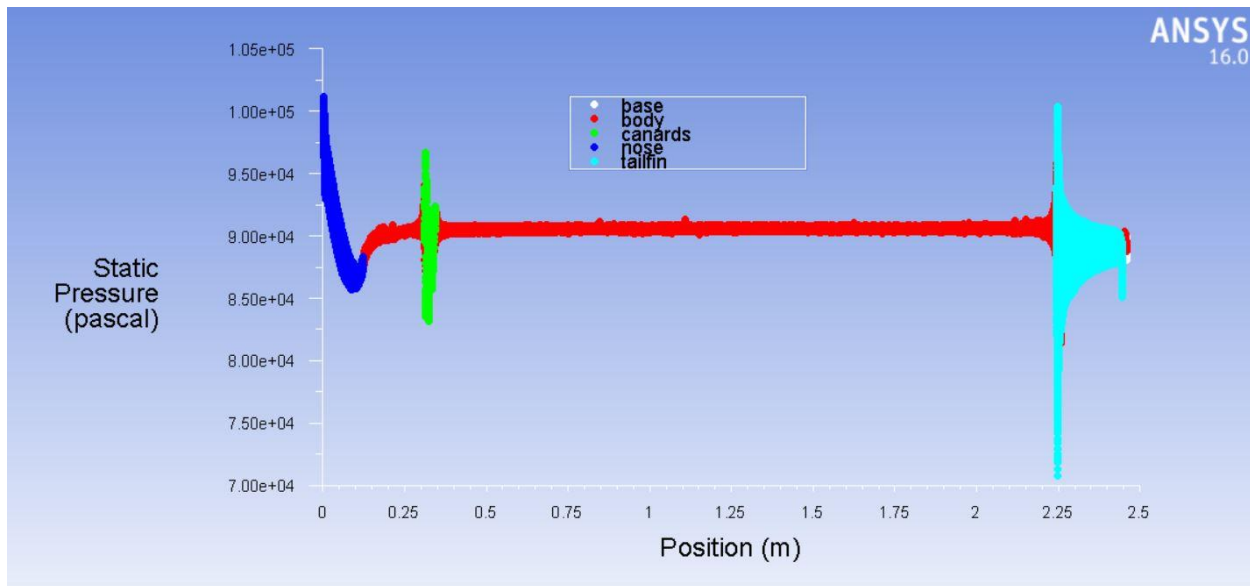


Figure 117 Static pressure distribution along missile for 15 ° control deflection and angle of attack $\alpha = -6^\circ$

Figure 118 shows the simulation case with 8 degrees angle of attack and 15 degrees pitch control surface deflection. The contours show clear pressure increases around some parts of the missile. The pressure increase around the control surfaces in these contours is greater than the contours in the Figure 96. This is caused by the control surface deflection of 10 degrees. In addition, the pressure increases towards the lower area of the control surface's leading edge which is expected due to the 15 degrees deflection.

It is important to point out that the flow facing the axis of the control surface is the sum of 8 degrees angle of attack and the 15 degrees control deflection. Thus, the control surfaces are facing a total of 23 degrees angles of attack with respect to the chord line. That is why the pressure increase is greater than the case in Figure 96 where the control deflection is 10 degrees.

Furthermore, the contours shown in Figure 118 indicate increased pressure towards the lower area of the front nose and tail fin leading edge of the missile. This is caused by the angled flow represented by

8 degrees angle of attack. Hence, the drag increases accordingly. In addition, the normal force components increases on the missile. These normal force components act upwards which is expected for positive angle of attack flow. However, the base drag effects can also be seen in Figure 118 through the drop of static pressure contours in that area.

The total normal force acting on the missile is directed upwards. According to the normal force coefficients results presented in Figure 24. In addition, the pitch moment acting on the missile is negative which corresponds to clockwise moment direction [pitch down direction]. That is according to the pitch moment coefficient results presented in Figure 23.

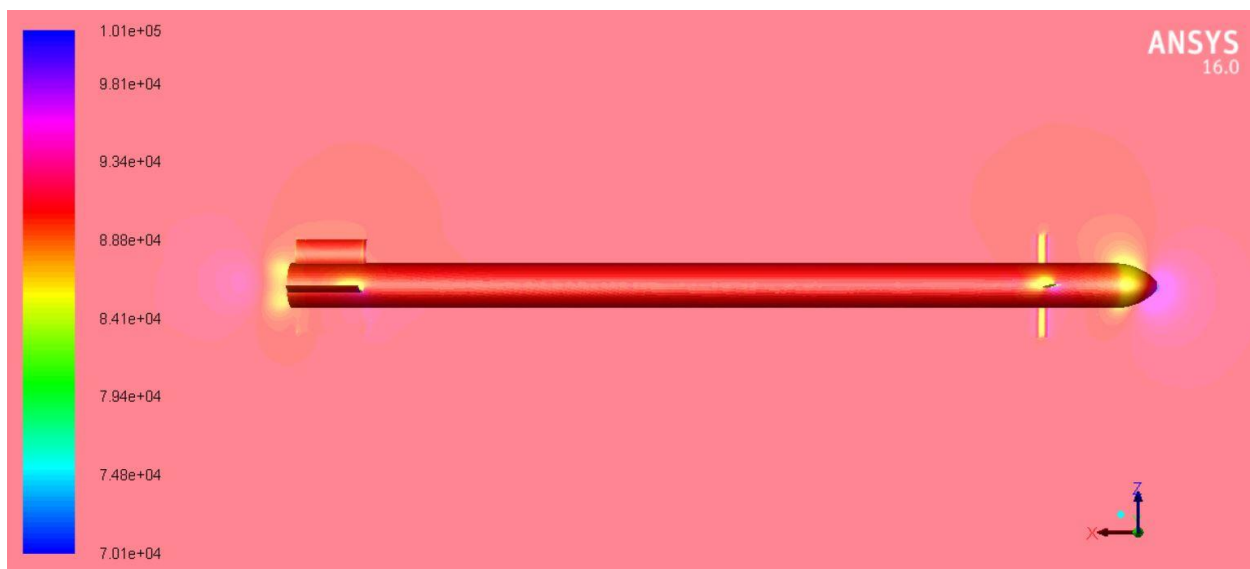


Figure 118 Static pressure contours for 15° control deflection and angle of attack $\alpha = 8^\circ$

Figure 119 shows the static pressure distribution along the whole missile's parts. It is important to point out that the canard control surfaces are exposed to greater pressure when comparing to Figure 97 which is due to the greater control deflection.

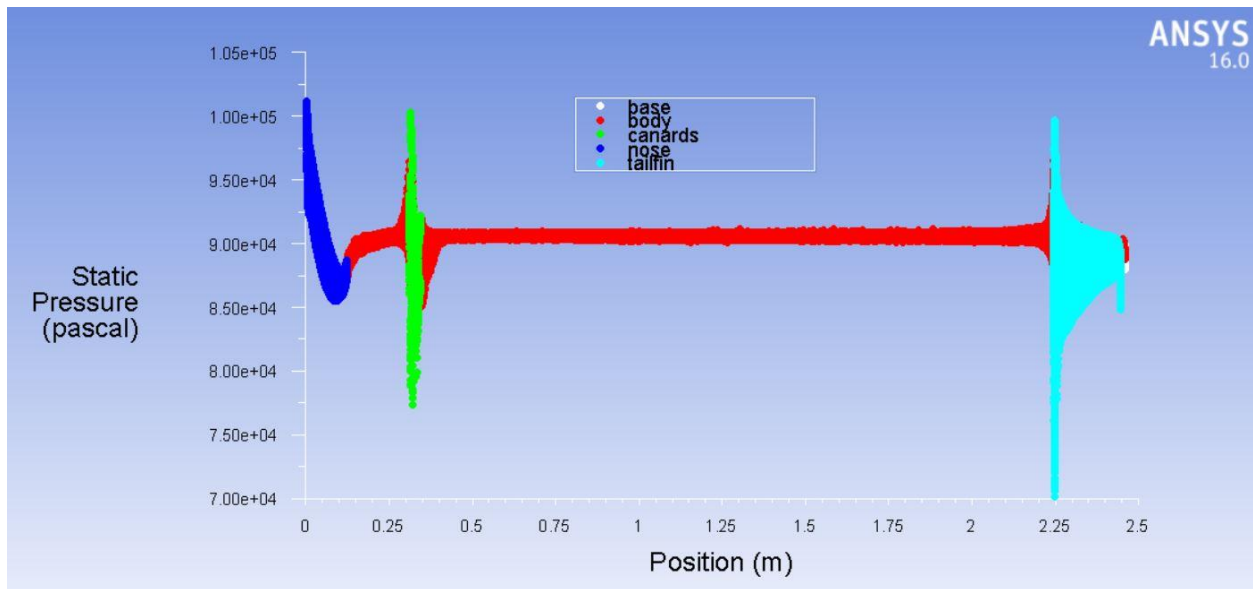


Figure 119 Static pressure distribution along missile for 15 ° control deflection and angle of attack $\alpha = 8^\circ$

Figure 120 shows the simulation case with -8 degrees angle of attack and 15 degrees pitch control surface deflection. The contours show clear pressure increases around some parts of the missile. The pressure increase around the control surfaces in these contours is greater than the contours in the Figure 98. This is caused by the control surface deflection of 10 degrees. In addition, the pressure increases towards the lower area of the control surface's leading edge which is expected due to the 15 degrees deflection.

It is important to point out that the flow facing the axis of the control surface is the sum of -8 degrees angle of attack and the 15 degrees control deflection. Thus, the control surfaces are facing a total of 7 degrees angles of attack with respect to the chord line. That is why the pressure increase is greater than the case in Figure 98 where the control deflection is 10 degrees.

Furthermore, the contours shown in Figure 120 indicate increased pressure towards the upper area of the front nose and tail fin leading

edge of the missile. This is caused by the angled flow represented by -8 degrees angle of attack. Hence, the drag increases accordingly. In addition, the normal force components increases on the missile. These normal force components act downwards which is expected for negative angle of attack flow. However, the base drag effects can also be seen in Figure 120 through the drop of static pressure contours in that area.

The total normal force acting on the missile is directed downwards According to the normal force coefficients results presented in Figure 24. In addition, the pitch moment acting on the missile is positive which corresponds to anti-clockwise moment direction [pitch up direction]. That is according to the pitch moment coefficient results presented in Figure 23.

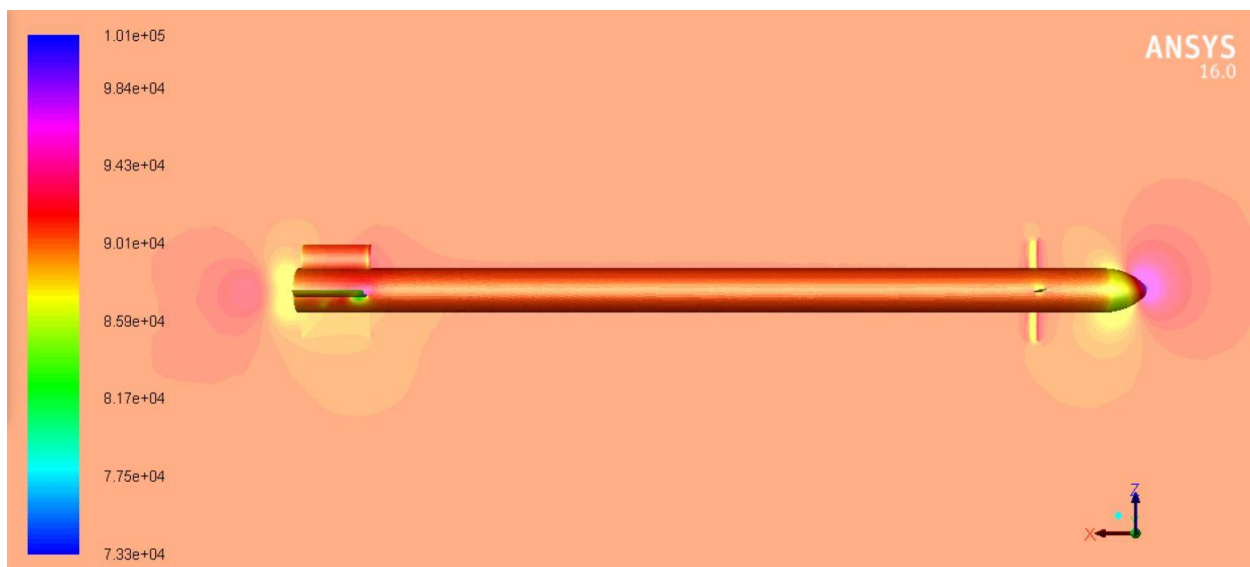


Figure 120 Static pressure contours for 15° control deflection and angle of attack $\alpha = -8^\circ$

Figure 121 shows the static pressure distribution along the whole missile's parts. It is important to point out that the canard control

surfaces are exposed to greater pressure when comparing to Figure 99 which is due to the greater control deflection.

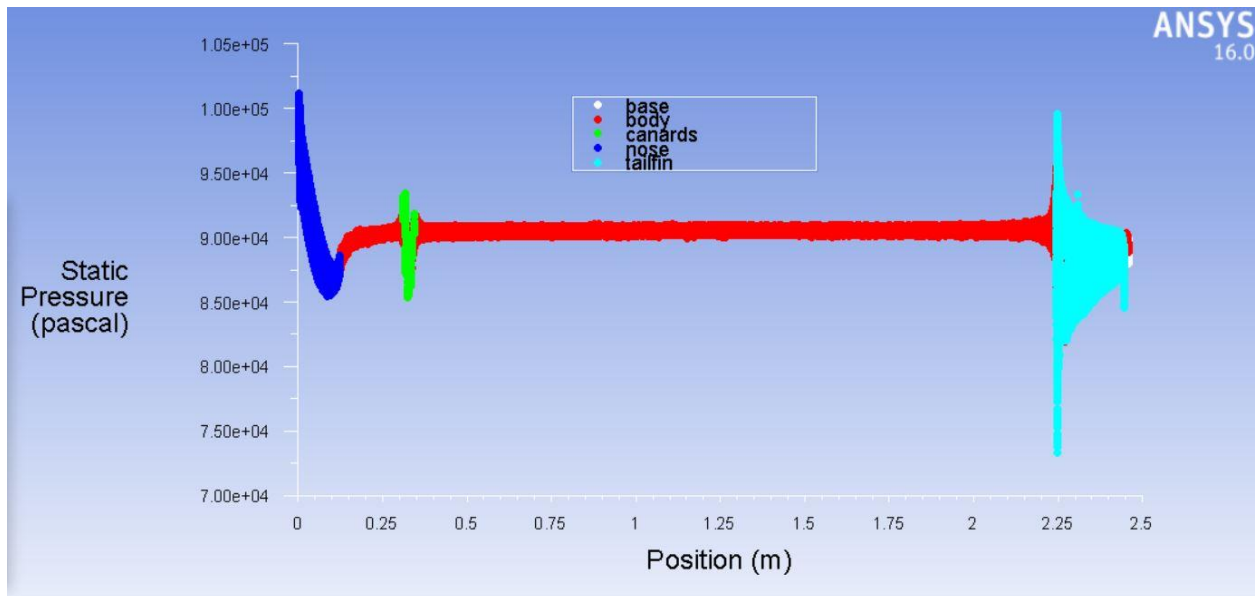


Figure 121 Static pressure distribution along missile for 15° control deflection and angle of attack $\alpha = -8^\circ$

Figure 122 shows the simulation case with 10 degrees angle of attack and 15 degrees pitch control surface deflection. The contours show clear pressure increases around some parts of the missile. The pressure increase around the control surfaces in these contours is greater than the contours in the Figure 100. This is caused by the control surface deflection of 10 degrees. In addition, the pressure increases towards the lower area of the control surface's leading edge which is expected due to the 15 degrees deflection. However, the static pressure contours show a significant drop in pressure behind the trailing edge of the control surface which indicates the beginning of flow separation.

It is important to point out that the flow facing the axis of the control surface is the sum of 10 degrees angle of attack and the 15 degrees control deflection. Thus, the control surfaces are facing a

total of 25 degrees angles of attack with respect to the chord line. That is why the pressure increase is greater than the case in Figure 100 where the control deflection is 10 degrees.

Furthermore, the contours shown in Figure 122 indicate increased pressure towards the lower area of the front nose and tail fin leading edge of the missile. This is caused by the angled flow represented by 10 degrees angle of attack. Hence, the drag increases accordingly. In addition, the normal force components increases on the missile. These normal force components act upwards which is expected for positive angle of attack flow. However, the base drag effects can also be seen in Figure 122 through the drop of static pressure contours in that area.

The total normal force acting on the missile is directed upwards. According to the normal force coefficients results presented in Figure 24. In addition, the pitch moment acting on the missile is negative which corresponds to clockwise moment direction [pitch down direction]. That is according to the pitch moment coefficient results presented in Figure 23.

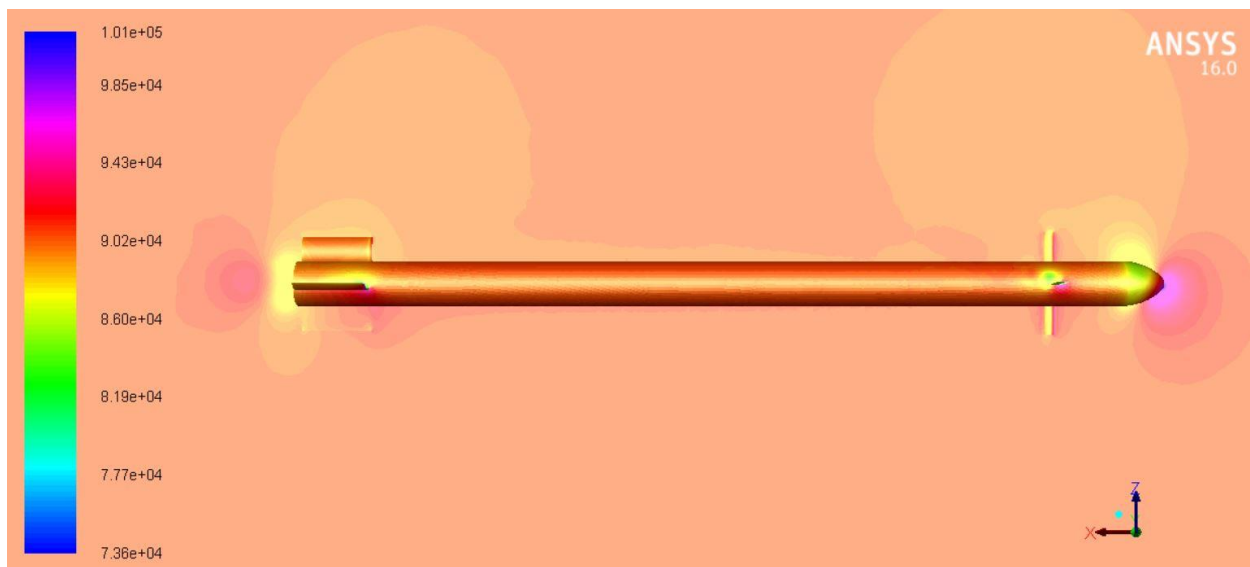


Figure 122 Static pressure contours for 15 ° control deflection and angle of attack $\alpha = 10^\circ$



Figure 123 shows the static pressure distribution along the whole missile's parts. It is important to point out that the canard control surfaces are exposed to greater pressure when comparing to Figure 101 which is due to the greater control deflection.

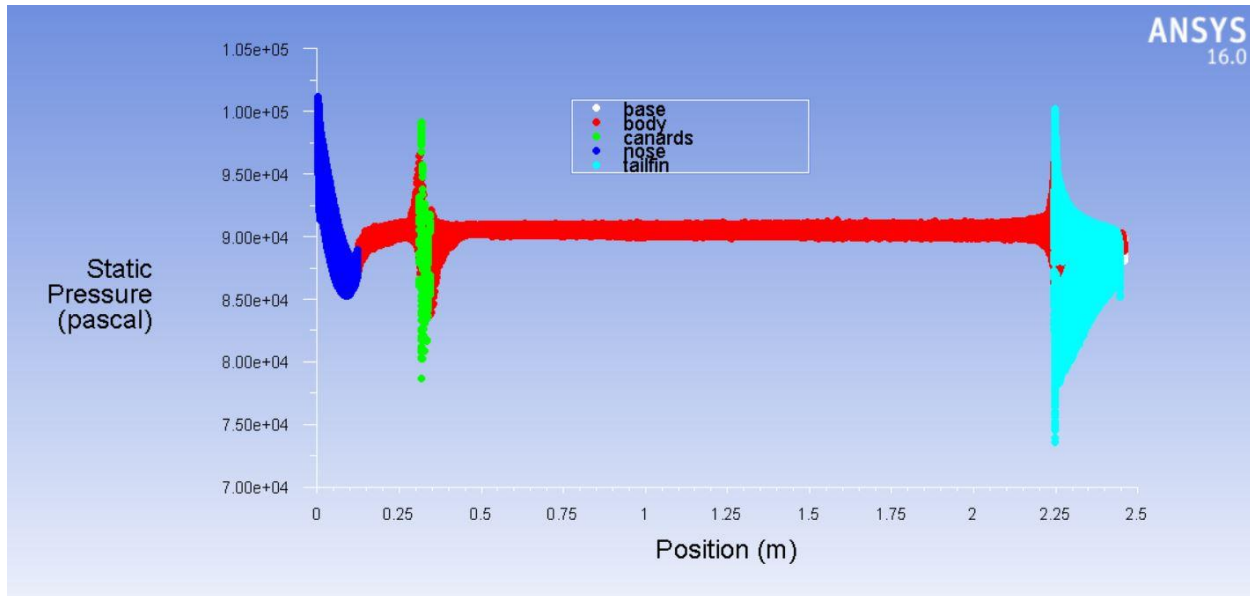


Figure 123 Static pressure distribution along missile for 15 ° control deflection and angle of attack $\alpha = 10^\circ$

Figure 124 shows the simulation case with -10 degrees angle of attack and 15 degrees pitch control surface deflection. The contours show clear pressure increases around some parts of the missile. The pressure increase around the control surfaces in these contours is greater than the contours in the Figure 102. This is caused by the control surface deflection of 10 degrees. In addition, the pressure increases towards the upper area of the control surface's leading edge. This means that the control surfaces deflection cannot counter -10 degrees angle of attack.

It is important to point out that the flow facing the axis of the control surface is the sum of -10 degrees angle of attack and the 15 degrees control deflection. Thus, the control surfaces are facing a



total of 5 degrees angles of attack with respect to the chord line. That is why the pressure increase is greater than the case in Figure 102 where the control deflection is 10 degrees.

Furthermore, the contours shown in Figure 124 indicate increased pressure towards the upper area of the front nose and tail fin leading edge of the missile. This is caused by the angled flow represented by -10 degrees angle of attack. Hence, the drag increases accordingly. In addition, the normal force components increases on the missile. These normal force components act downwards which is expected for negative angle of attack flow. However, the base drag effects can also be seen in Figure 124 through the drop of static pressure contours in that area.

The total normal force acting on the missile is directed downwards According to the normal force coefficients results presented in Figure 24. In addition, the pitch moment acting on the missile is positive which corresponds to anti-clockwise moment direction [pitch up direction]. That is according to the pitch moment coefficient results presented in Figure 23.

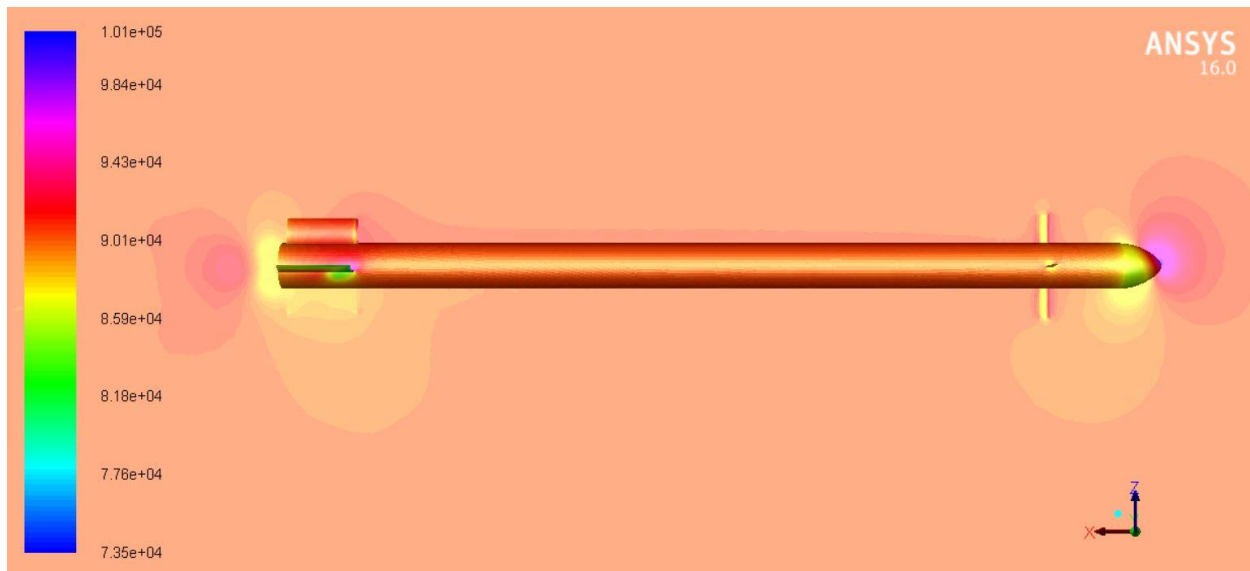


Figure 124 Static pressure contours for 15° control deflection and angle of attack $\alpha = -10^\circ$

Figure 125 shows the static pressure distribution along the whole missile's parts. It is important to point out that the canard control surfaces are exposed to greater pressure when comparing to Figure 103 which is due to the greater control deflection.

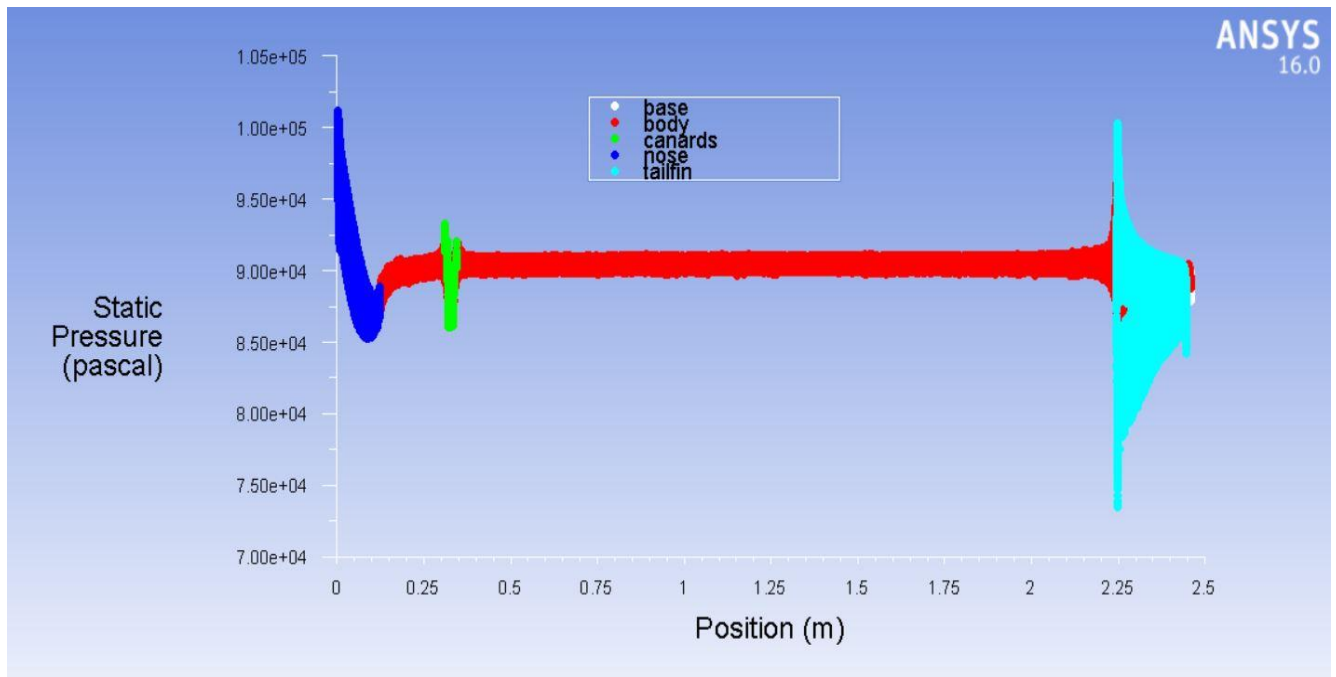


Figure 125 Static pressure distribution along missile for 15° control deflection and angle of attack $\alpha = -10^\circ$

5. Experiment Set up

5.1. Wind tunnel facility

The wind tunnel facility used for testing the model is located in the Military Technical Institute in Belgrade, Republic of Serbia. The wind tunnel facility is capable of testing missiles as well as aircraft. Moreover, the military technical institute provides four types of wind tunnels for different testing purposes.

For the testing conditions required, T-35 subsonic wind tunnel is used. T-35 wind tunnel is a large closed-circuit wind tunnel. The external view of the T-35 wind tunnel is shown in Figure 126 (23)



Figure 126 External view of the wind tunnel facility

5.2. Wind tunnel testing section

T-35 wind tunnel is capable of providing flow speed from Mach 0.1 to 0.5 with several angles of attack as well as sideslip angles. It also allows the model to rotate around the stinger to measure dynamic derivatives.

The testing section sizing is 4.4 m x 3.2 m which can help testing full scale models without the need of scaling down the model. A view of the testing section is shown in Figure 127.



Figure 127 Test section view during experiment preparation

5.3. Wind tunnel testing results

5.3.1. Pitch moment coefficients

Figure 128 shows the pitch moment coefficients vs. angle of attack for all control deflections. The pitch moment curve increases in value as the pitch control deflection increases. It is important to note that there is no significant increase of pitch moment curve between 10 degrees to 15 degrees especially towards the high angle of attack. This proves that the missile's pitch moment control surfaces start to lose effectiveness near 15 degrees as previously proved in the CFD results.

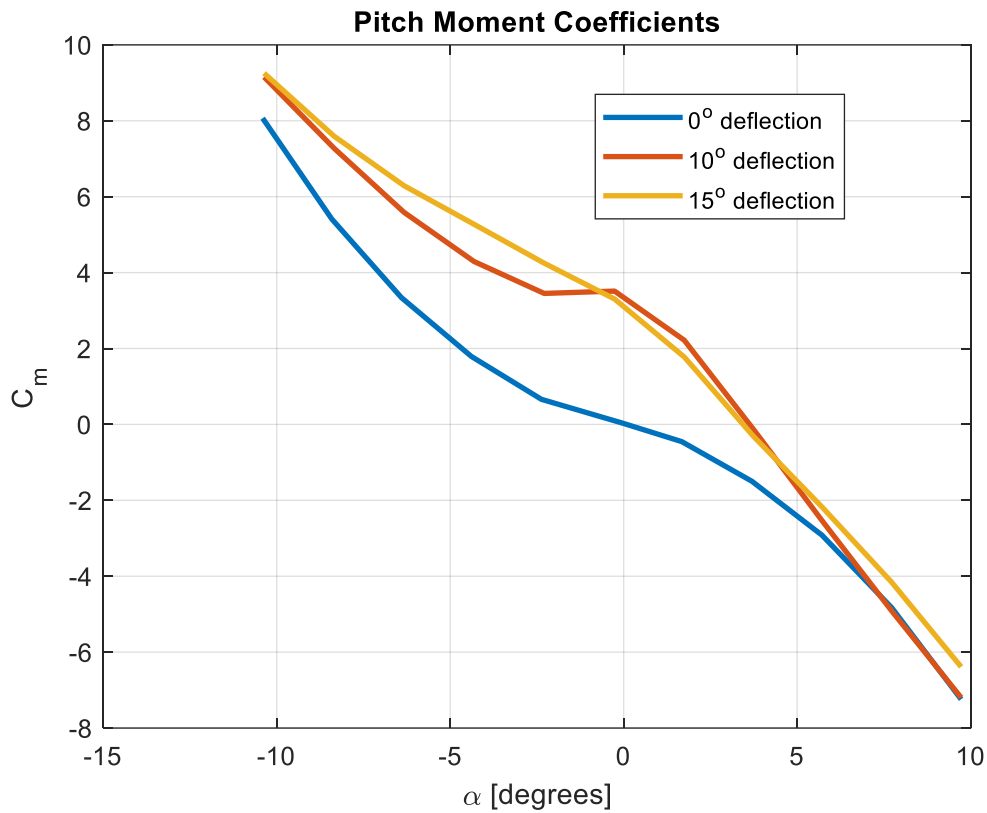


Figure 128 Wind tunnel pitch moment coefficients

5.3.2. Normal force coefficients

The normal force coefficients for all control deflections vs. angle of attack are shown in Figure 129. It is important to point out that the missile starts to lose control surfaces effectiveness at 15 degrees deflection near higher angle of attack as shown in Figure 130. The plot in Figure 130 is a zoomed version of the plot shown in Figure 129.

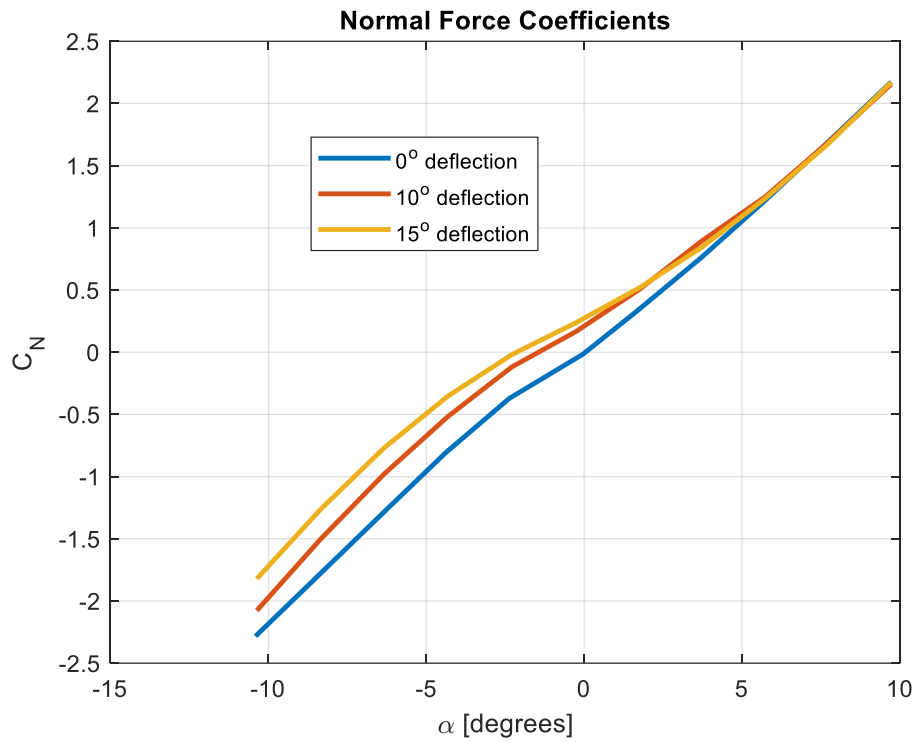


Figure 129 Wind tunnel normal force coefficients

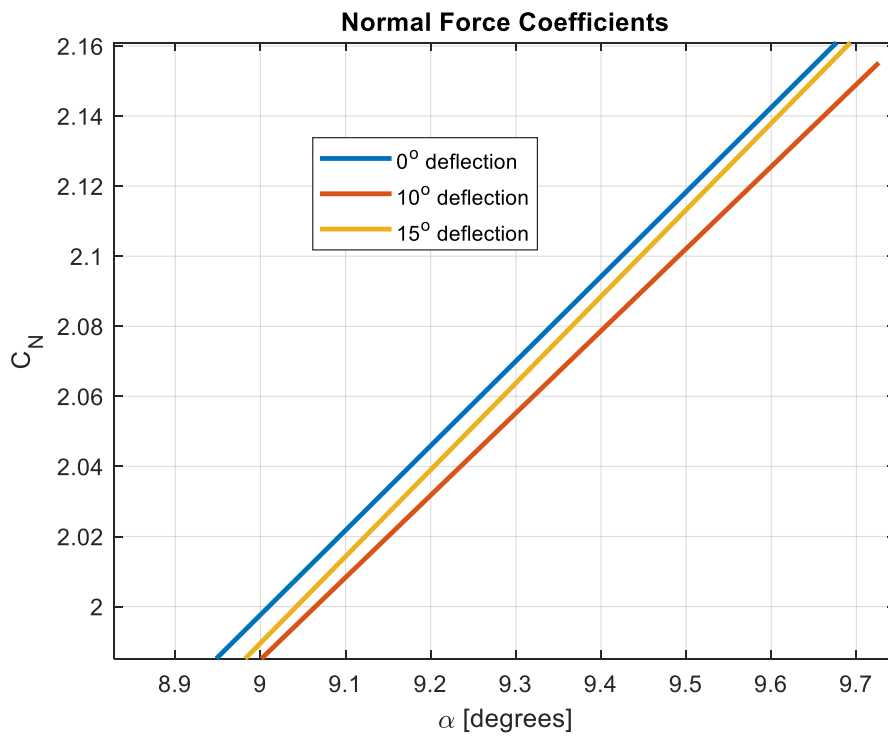


Figure 130 Wind tunnel normal force coefficients - zoomed



5.3.3. Axial force coefficients

Figure 131 shows the axial force coefficients vs. angle of attack for all control deflections obtained from the wind tunnel testing. The axial force curve increases in value as the pitch control deflection increases. It is important to note that there is a slight increase in the axial force coefficient for 10 and 15 degrees control deflection towards the high angle of attack. This increase is approximately 26% and 20% of the minimum axial force coefficient for 10 and 15 degrees control deflection respectively [increase between CA at angle of attack -10 degrees and 10 degrees].

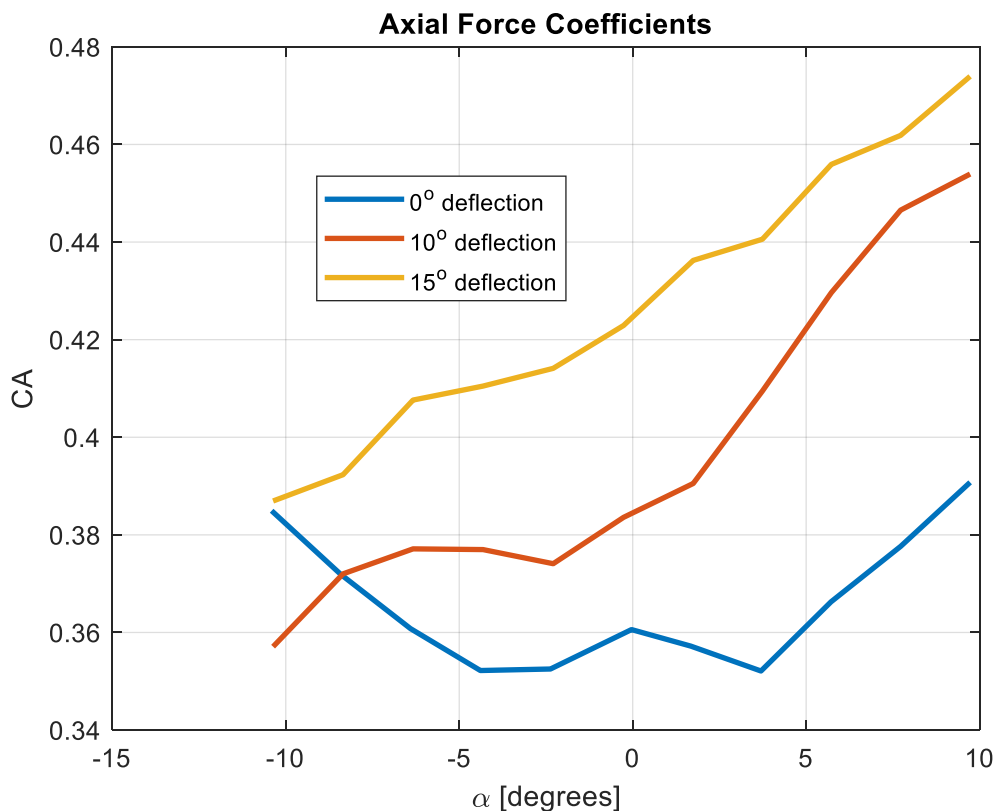


Figure 131 Wind tunnel axial force coefficients



5.3.4. Roll moment coefficients

Figure 132 shows the roll moment coefficients vs. angle of attack for 0 and 10 degrees control deflections obtained from the wind tunnel testing. The roll moment coefficient data for 15 degrees is not measured in wind tunnel testing. As seen in Figure 132, the roll moment coefficient curves are almost identical and small in magnitude. It is important to highlight that the control deflections simulation are for the pitch plane control. This means that there should be no roll moment. However, this roll is caused by the shape of tail fin [wrap around fin]. Therefore, the plot represents the wrap around fin effect on the roll plane.

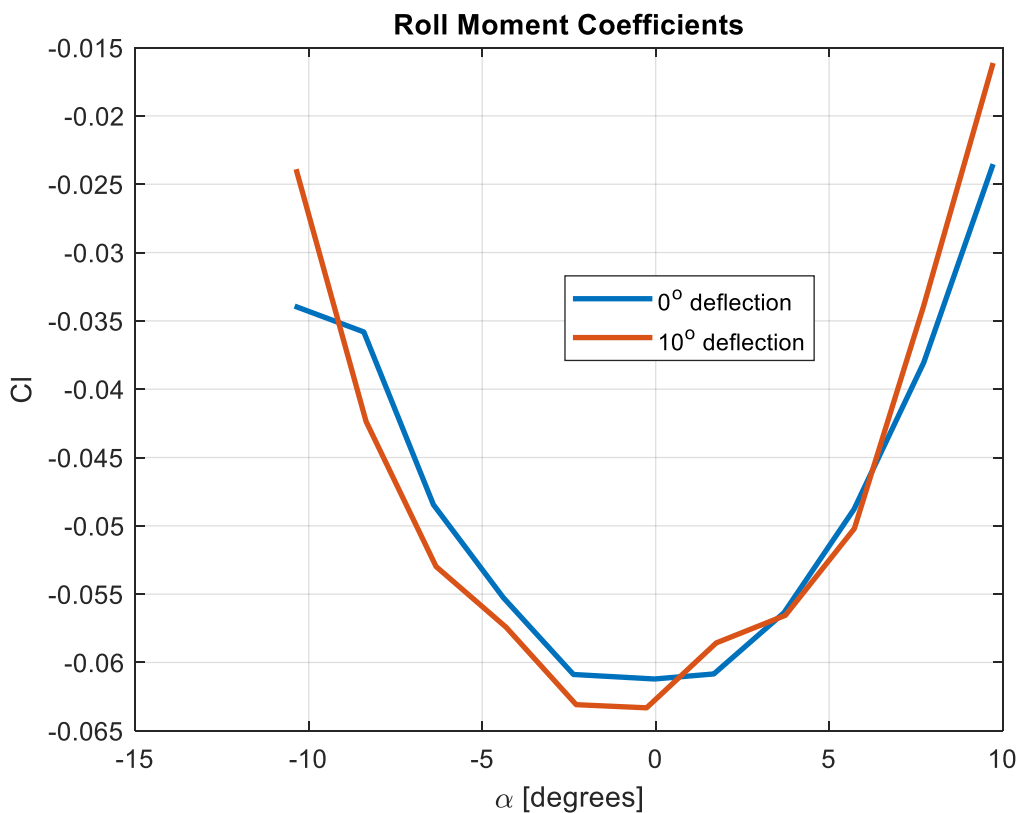


Figure 132 Wind tunnel roll moment coefficients



6. Semi Empirical Methods

Semi-empirical methods are commonly used for aerodynamic modelling of flying projectiles (24). Several codes utilize the semi-empirical methods such as Missile DATCOM (25) and AeroPrediction Code (AP98) (26). AeroPrediction Code (AP98) has been improved throughout the years to be more comprehensive as well as more optimized (27). However, the code used for the semi-empirical methods calculations in this paper is Missile DATCOM. Its biggest advantage is the quick set-up along with quick solution. Moreover, Missile DATCOM utilizes build-up methods for the coefficients identification (28). Even though Missile DATCOM has many limitations in terms of the results quality, it proved to be a good competitor to other calculation methods (29), (30), (31), and (32).

Figure 133 (33) presents the lift force coefficient of a missile at Mach number of 1.5 and varying angles of attack from 4 to 18 degrees. It is important to highlight that Missile DATCOM results are in good agreement with the experimental data. However, slight deviation is occurs towards high angles of attack.

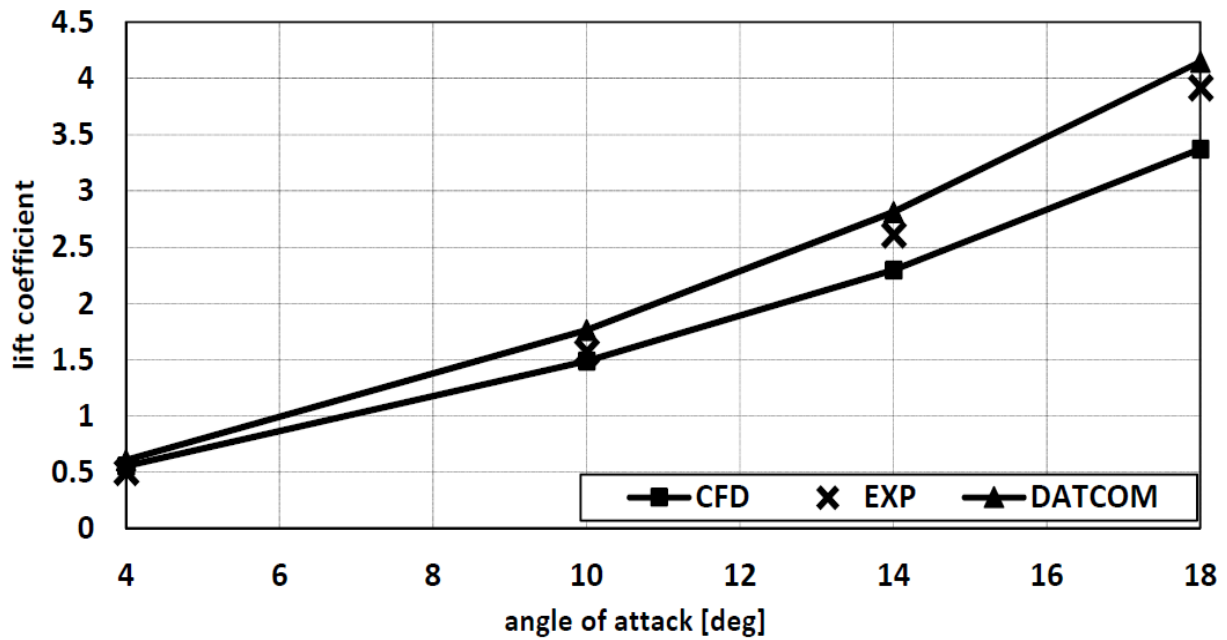


Figure 133 Lift coefficient for Missile DATCOM vs. other methods

Figure 134 (33) presents the axial force coefficient for the same missile with the same conditions as previously mentioned. It is important to highlight that Missile DATCOM results are in good agreement with the experimental data.

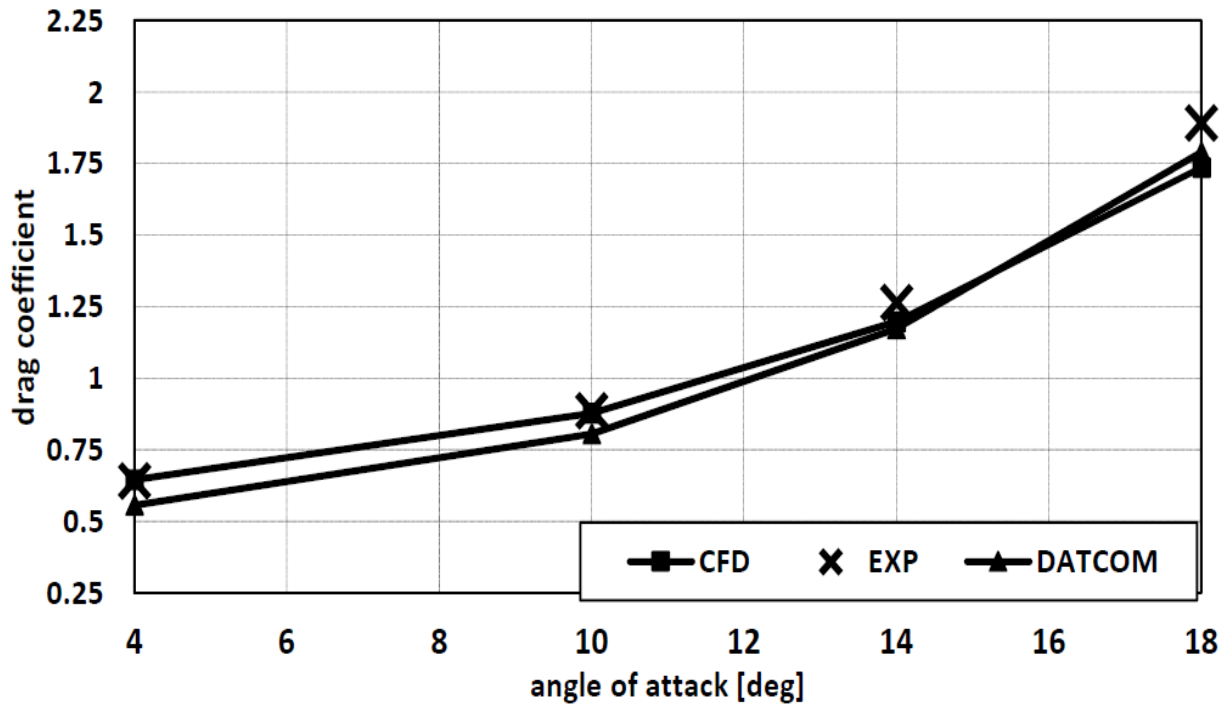


Figure 134 Drag coefficient for Missile DATCOM vs. other methods

Figure 135 (30) presents the pitch moment coefficient of a body-wing-tail missile at Mach number of 1.42 and varying angles of attack from 0 to 25 degrees. Two semi-empirical aerodynamic prediction codes used are AeroPrediction Code (AP98) and Missile DATCOM. It is important to highlight that both codes have discrepancies in the coefficient of pitch moment especially towards high angle of attack. Moreover, AP98 results have better agreement with experimental data.

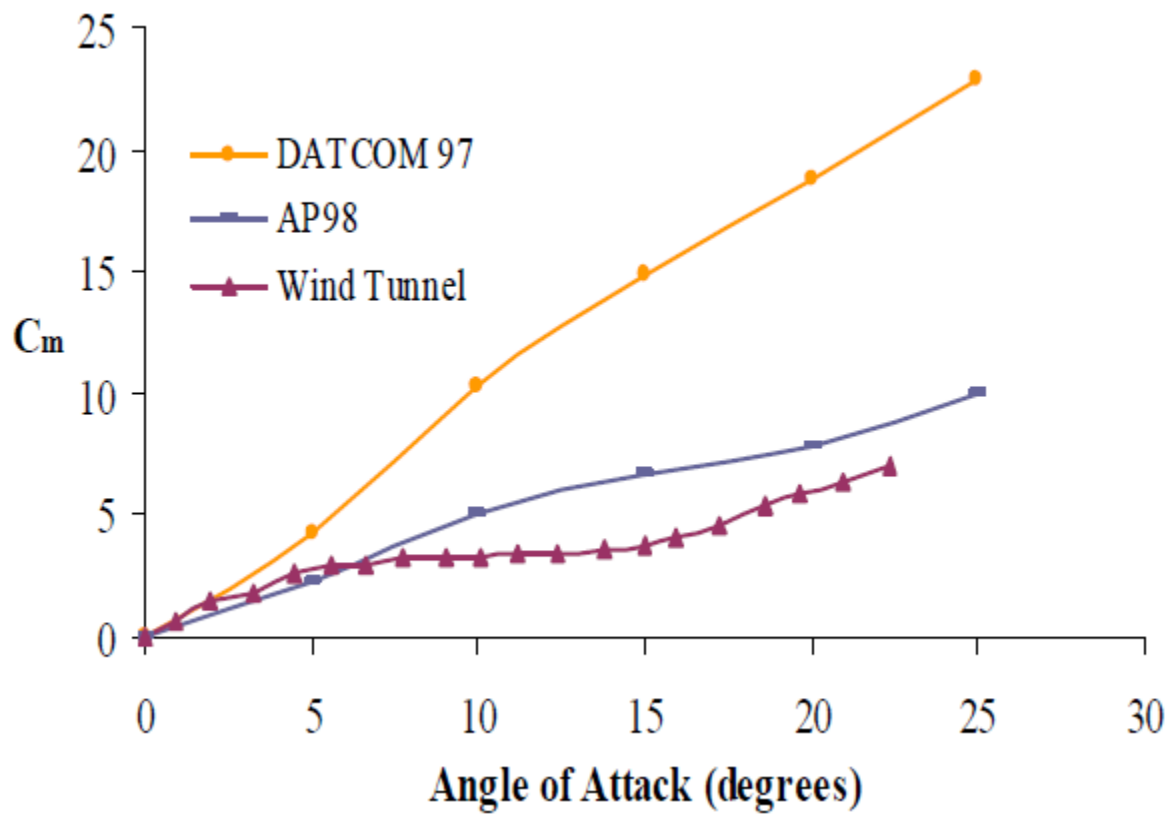


Figure 135 Pitch moment coefficient for Missile DATCOM vs. other methods

6.1. Missile DATCOM

The Aerodynamic coefficients are obtained using Missile DATCOM for identical model with same flow conditions for further comparison. However, it is crucial to point out that the model used in Missile DATCOM does not have wrap around tail fin stabilizer. Instead, it has straight fins and that is due to Missile DATCOM's model setup limitations. Figure 136 shows a view of the model used in Missile DATCOM.

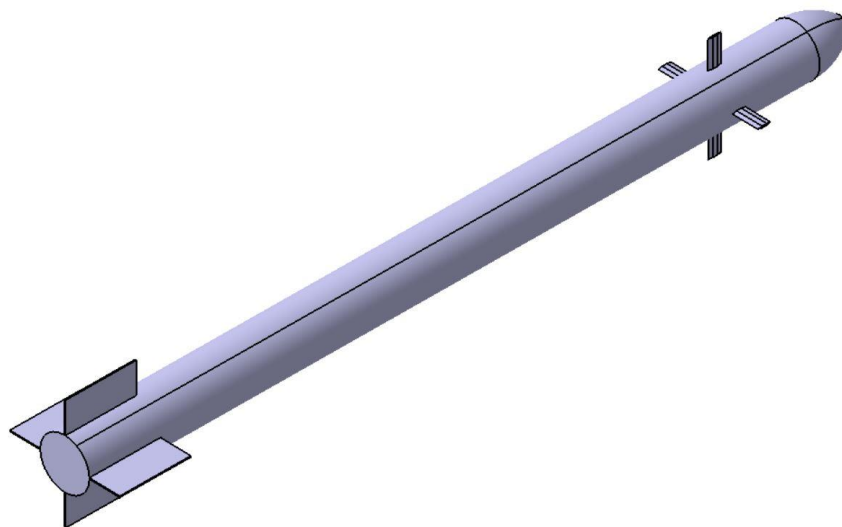


Figure 136 Missile DATCOM model

6.1.1. Pitch Moment Coefficients

Figure 137 shows the pitch moment coefficients vs. angles of attack for all control deflections simulated in Missile DATCOM. The pitch moment curve increases in value as the pitch control deflection



increases. It is important to note that there is no significant increase of pitch moment curve between 10 degrees to 15 degrees especially towards high angle of attack. This proves that the missile's pitch moment control surfaces start to lose effectiveness near 15 degrees.

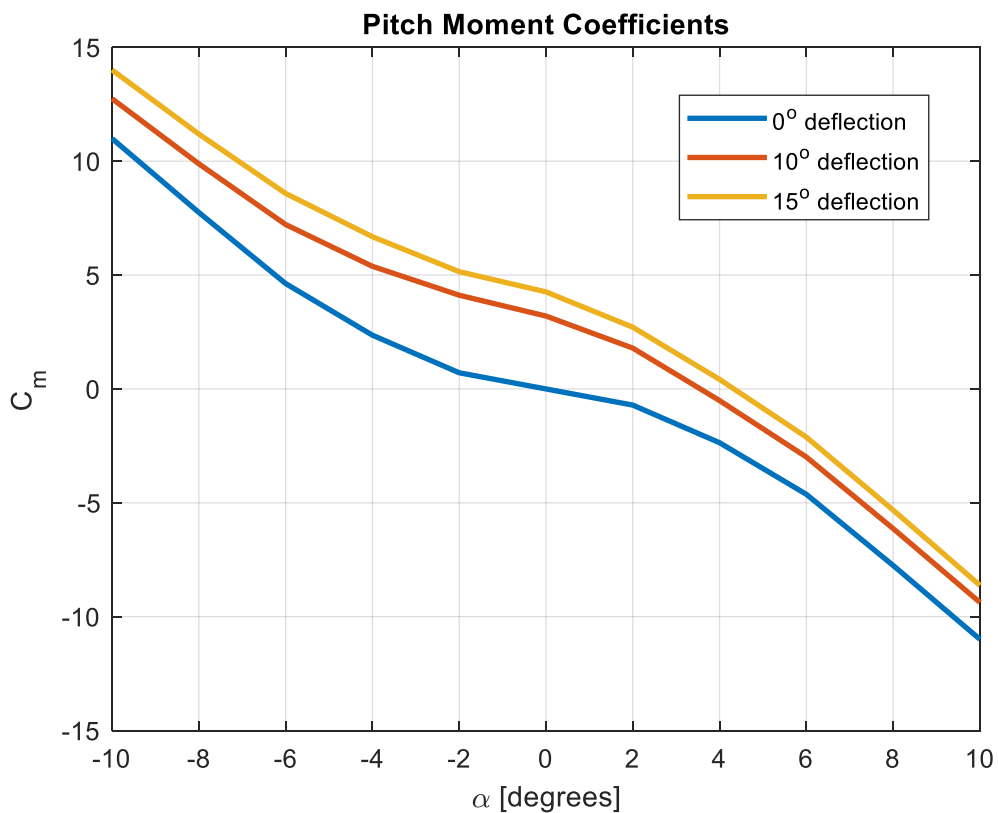


Figure 137 Missile DATCOM pitch moment coefficients

6.1.2. Normal Force Coefficients

The normal force coefficients for all control deflections vs. angles of attack are shown in Figure 138. It is important to highlight that the normal force coefficient curve of 10 and 15 degrees are almost



identical. This also proves that the missile starts to lose lift force when approaching 15 degrees pitch control deflection.

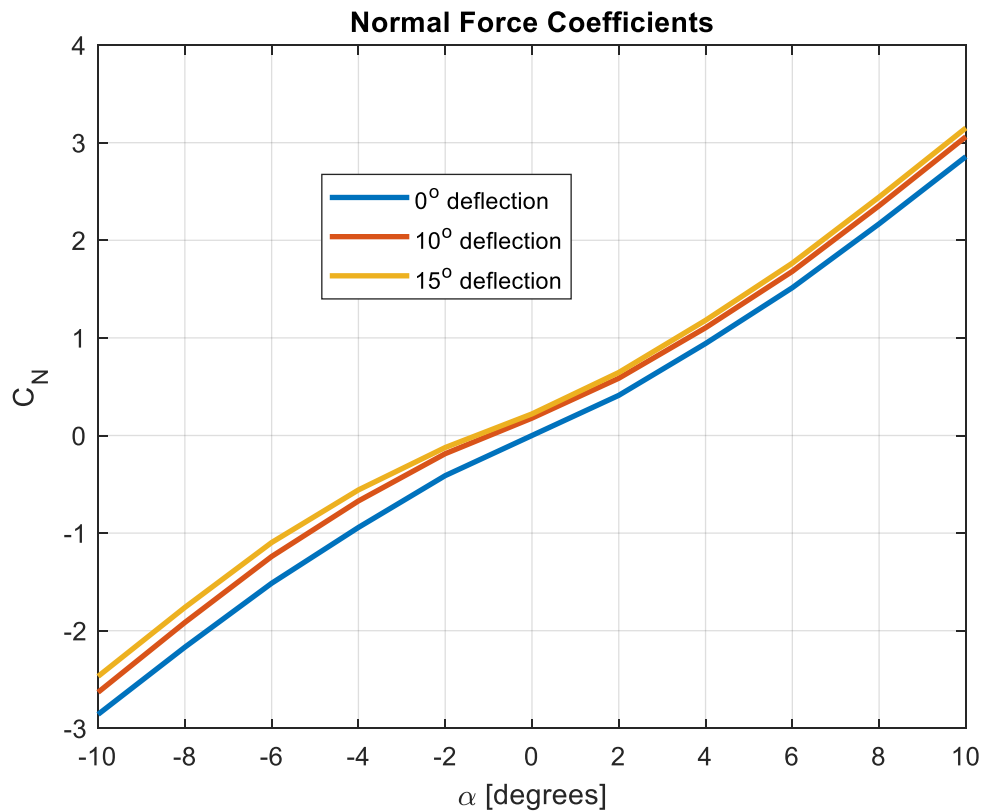


Figure 138 Missile DATCOM normal force coefficients

6.1.3. Axial Force Coefficients

Figure 139 shows the axial force coefficients vs. angles of attack for all control deflections simulated by Missile DATCOM. The axial force curve increases in value as the pitch control deflection increases. In addition, it is important to point out that there is a significant increase in the axial force coefficient for 10 and 15 degrees control deflection towards high angles of attack. This increase is nearly twice the values for lower angles of attack.

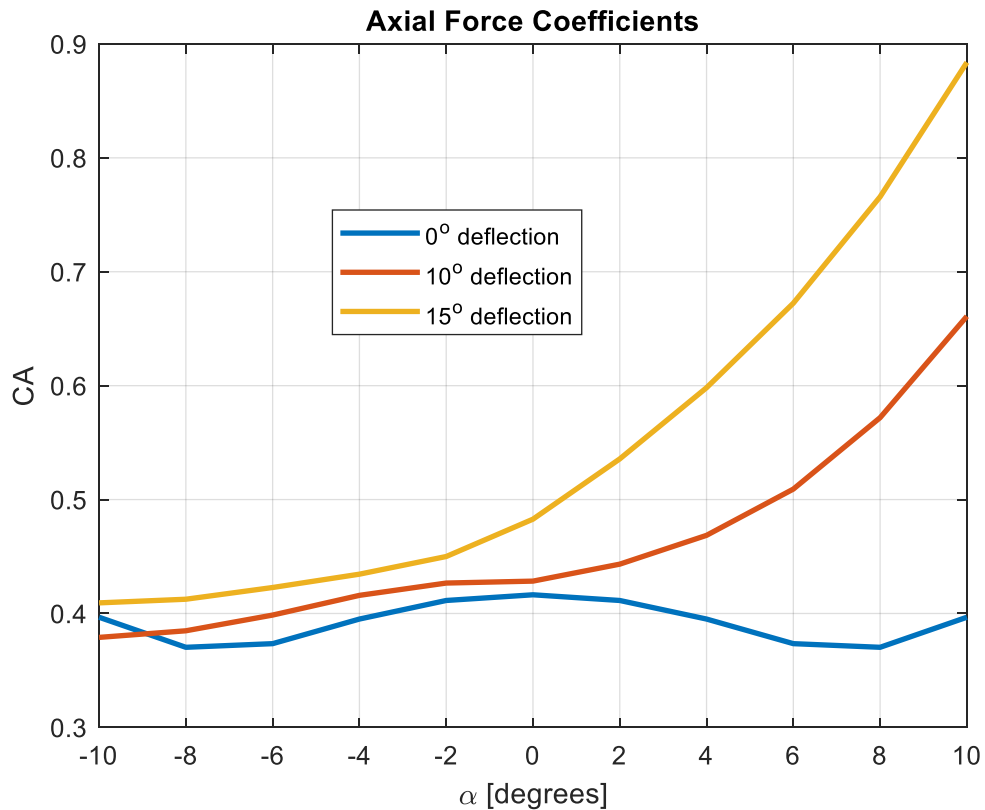


Figure 139 Missile DATCOM axial force coefficients

7. Results Comparison

The CFD results are compared with different methods of coefficients identification such as wind tunnel and Missile DATCOM semi-empirical methods. It is important to point out that the simulated model is identical in all methods to assure consistent comparison. However, the model used in Missile DATCOM is slightly different as mentioned previously.



All results are given in terms of the aerodynamic coefficient vs. different values of angles of attack for different cases. Each data set includes a certain case of canard pitch control deflection.

The wind tunnel results are obtained and compared with the theoretical results. It is important to note that all simulated flying conditions are identical to the tested conditions. Therefore, the theoretical methods can be verified.

This comparison section is divided according to the canard pitch control cases as seen in 7.1, 7.2 and 7.3

7.1. No deflection

Figure 140, Figure 141, Figure 142, and Figure 143 represent the results comparison between theoretical and experimental methods for 0 degrees control surface deflection. All the aerodynamic coefficients are presented in terms of different angles of attack.

Figure 140 shows the normal force coefficient comparison for 0 degrees control deflection. The theoretical results follow the same curve pattern as the experimental which seen in Figure 140. Figure 140 shows that normal force coefficients determined by the applied CFD approach are in better agreement with the wind tunnel results than the results from Missile DATCOM. It is also important to note that the applied CFD approach provided extremely accurate results towards high angles of attack.

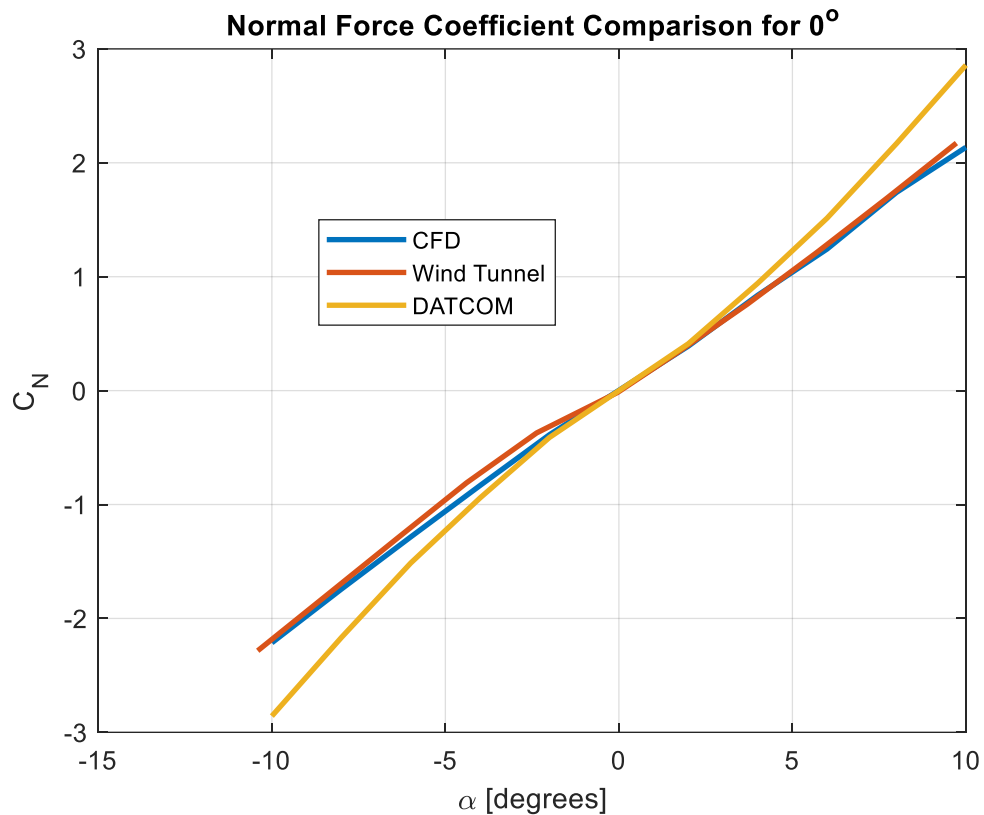


Figure 140 Normal force coefficient comparison for 0° control surface deflection

Figure 141 shows the pitch moment coefficient comparison for 0 degrees control deflection. The theoretical results follow the same curve pattern as the experimental which is seen in Figure 141. Figure 141 shows that the pitch moment coefficients determined by the applied CFD approach are in better agreement with the wind tunnel results than the results from Missile DATCOM. Moreover, it is important to note that the applied CFD approach provided extremely accurate results towards high angles of attack.

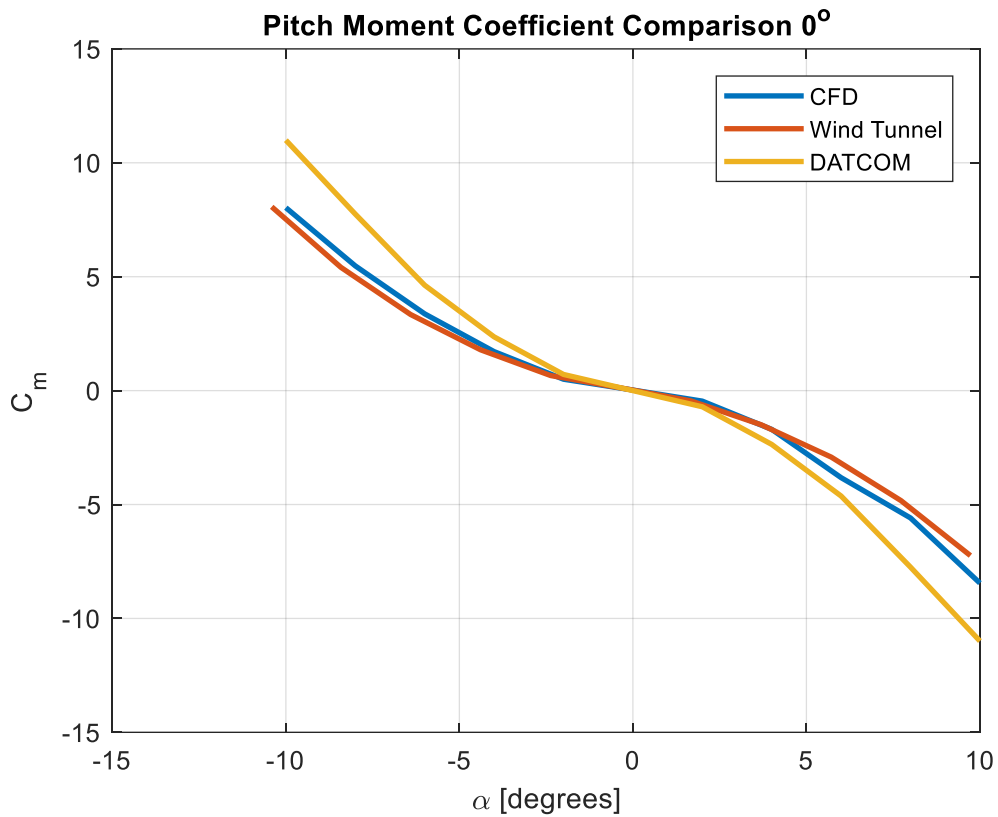


Figure 141 Pitch moment coefficient comparison for 0 ° control surface deflection

Figure 142 shows the axial force coefficient comparison for 0 degrees control deflection. The comparison shows decent agreement between theoretical and experimental results in terms of pattern. However, the CFD results are slightly off in magnitude when comparing to the wind tunnel data. Missile DATCOM shows better agreement with wind tunnel in terms of magnitude. It is important to point out that the applied simulation approach in CFD is not optimized for axial force calculation.

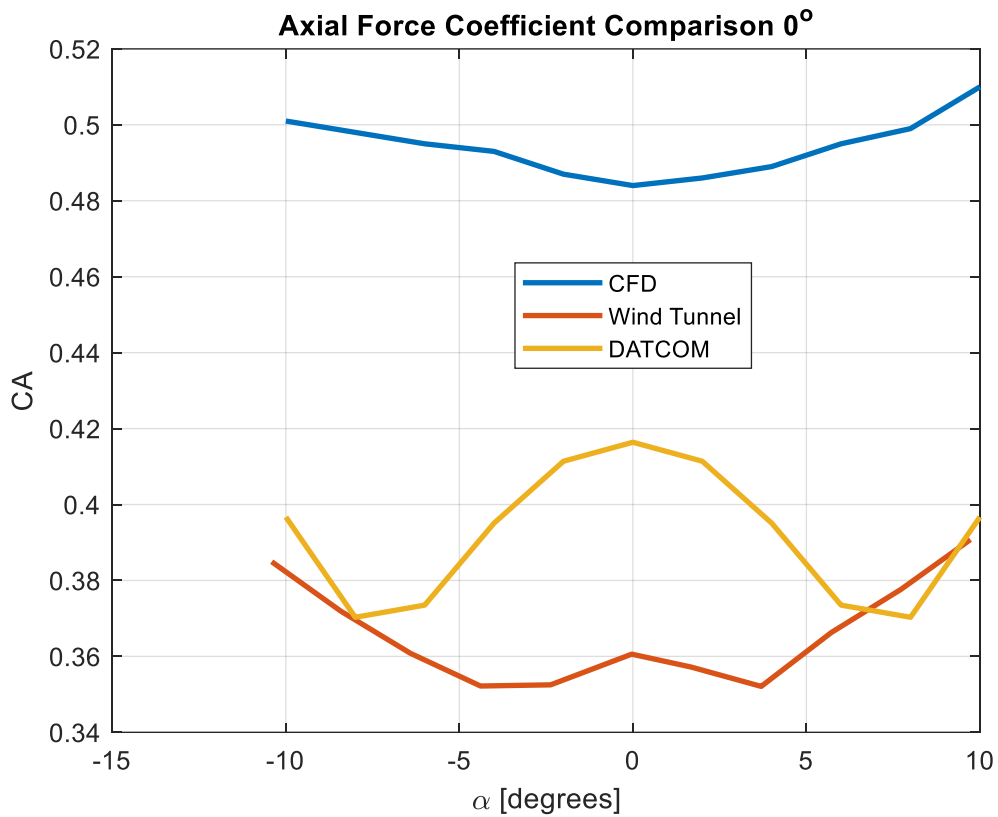


Figure 142 Axial force coefficient comparison for 0 ° control surface deflection

Figure 143 shows the roll moment coefficient comparison for 0 degrees control deflection. The comparison shows good agreement between CFD and experimental results in terms of pattern. However, the CFD results are slightly off in magnitude when comparing to the wind tunnel data. It is important to point out that Missile DATCOM results are not available for roll moment due to the limitation of Missile DATCOM.

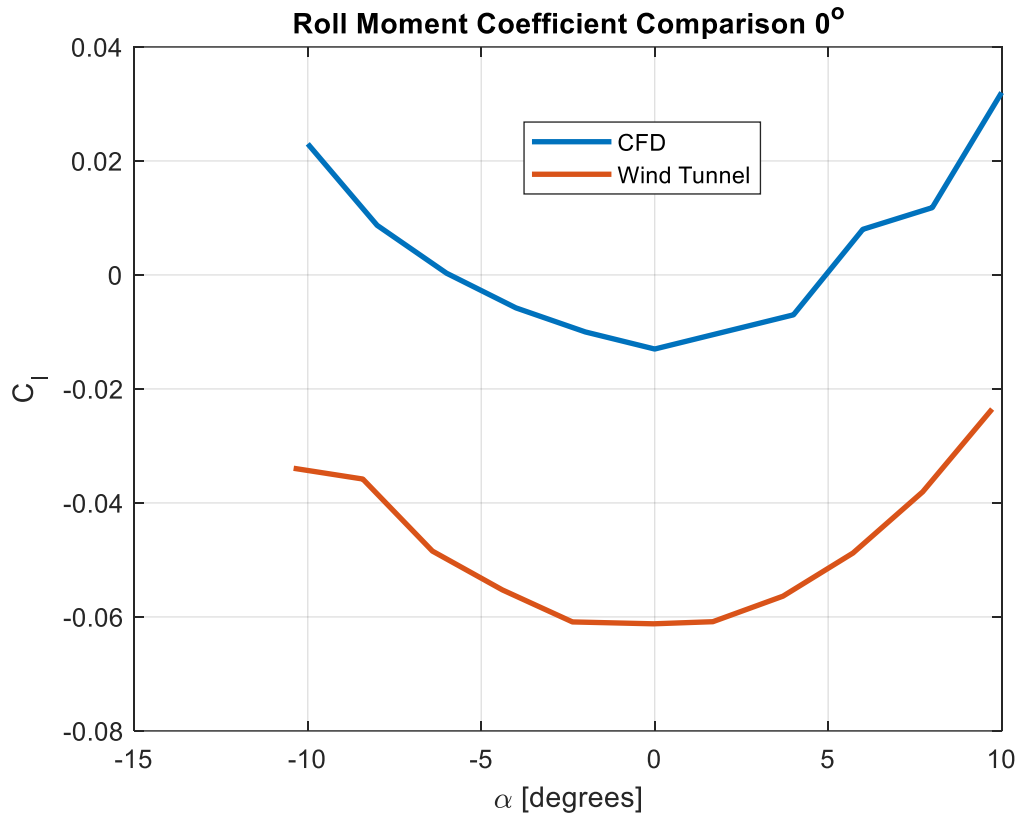


Figure 143 Roll moment coefficient comparison for 0° control surface deflection

7.2. 10 degrees deflection

Figure 144, Figure 145, Figure 146, and Figure 147 represent the results comparison between theoretical methods and experimental for 10 degrees control surface deflection. All the aerodynamic coefficients are presented in terms of different angles of attack.

Figure 144 shows the normal force coefficient comparison for 10 degrees control deflection. The theoretical results follow the same curve pattern as the experimental which is seen in Figure 144. Figure 144 shows that the normal force coefficients determined by the applied CFD approach are in better agreement with wind tunnel results than the



results from Missile DATCOM. It is also important to note that the applied CFD approach provided extremely accurate results towards high angles of attack.

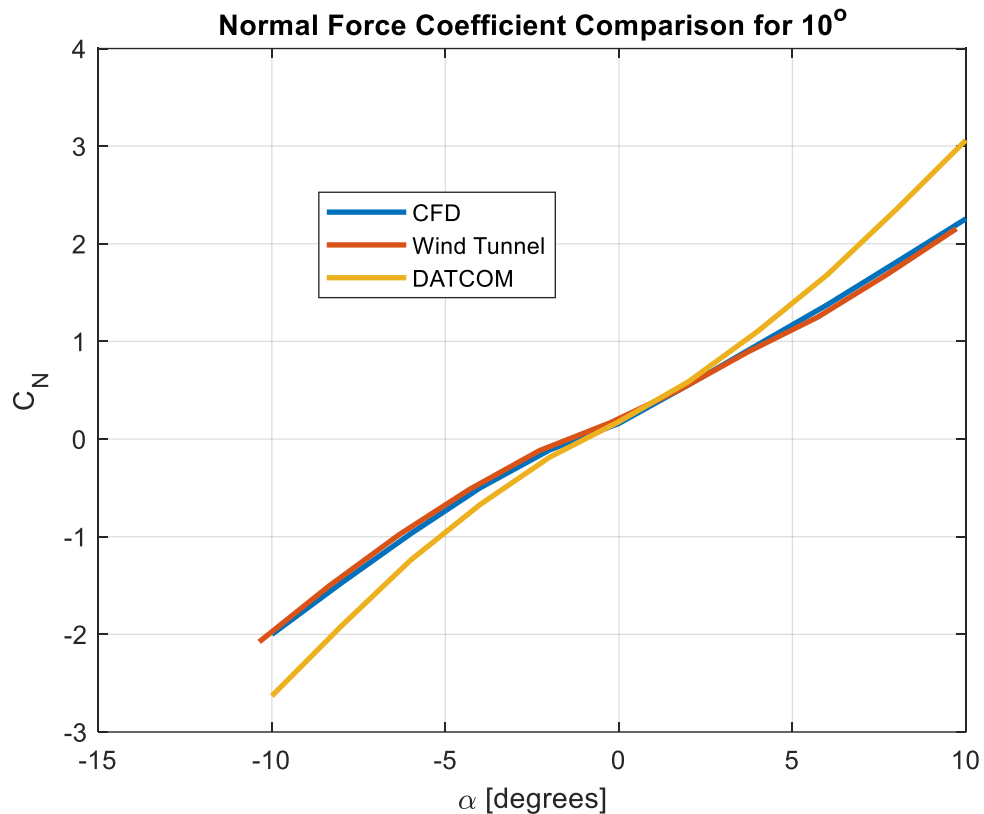


Figure 144 Normal force coefficient comparison for 10 ° control surface deflection

Figure 145 shows the pitch moment coefficient comparison for 10 degrees control deflection. The theoretical results follow the same curve pattern as the experimental which is seen in Figure 145. Figure 145 shows that the pitch moment coefficients determined by the applied CFD approach are in better agreement with wind tunnel results than the results from Missile DATCOM. Moreover, it is important to note that the applied CFD approach provided extremely accurate results towards high angles of attack where Missile DATCOM results highly deviated.

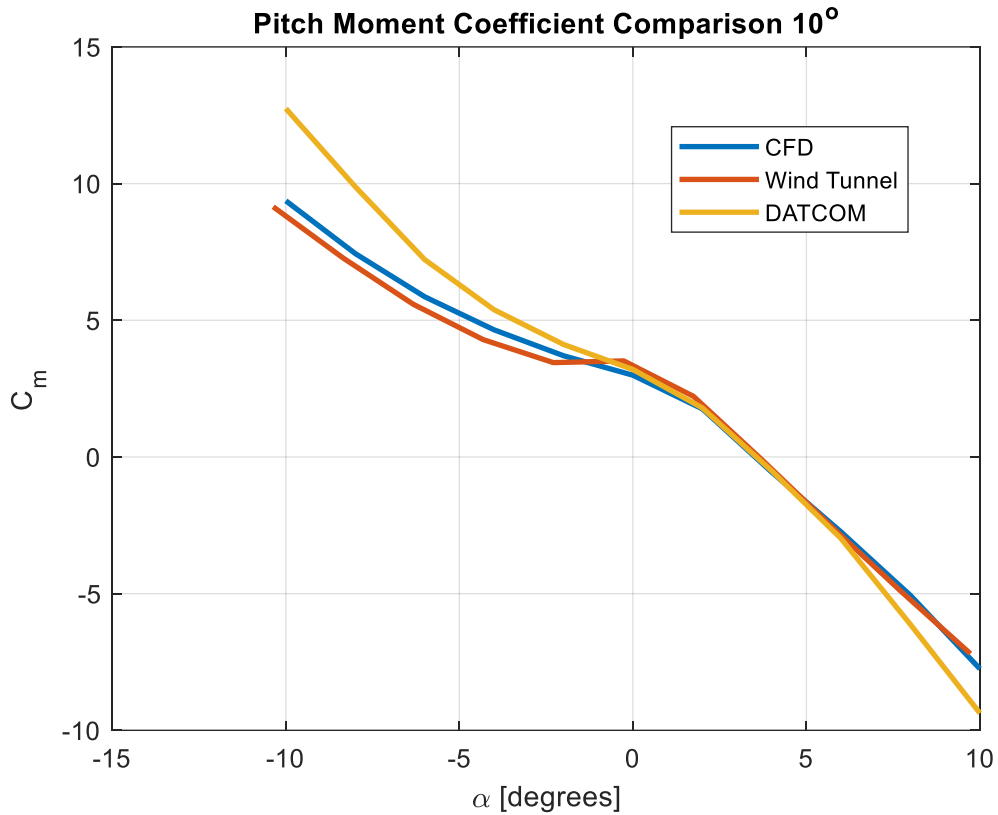


Figure 145 Pitch moment coefficient comparison for 10 ° control surface deflection

Figure 146 shows the axial force coefficient comparison for 10 degrees control deflection. The comparison shows decent agreement between theoretical and experimental results in terms of pattern. However, the CFD results are slightly off in magnitude when comparing to the wind tunnel data. Missile DATCOM shows better agreement with wind tunnel in terms of magnitude. Moreover, it is important to point out that Missile DATCOM results starts to exponentially deviate towards angles of attack 5 degrees and higher.

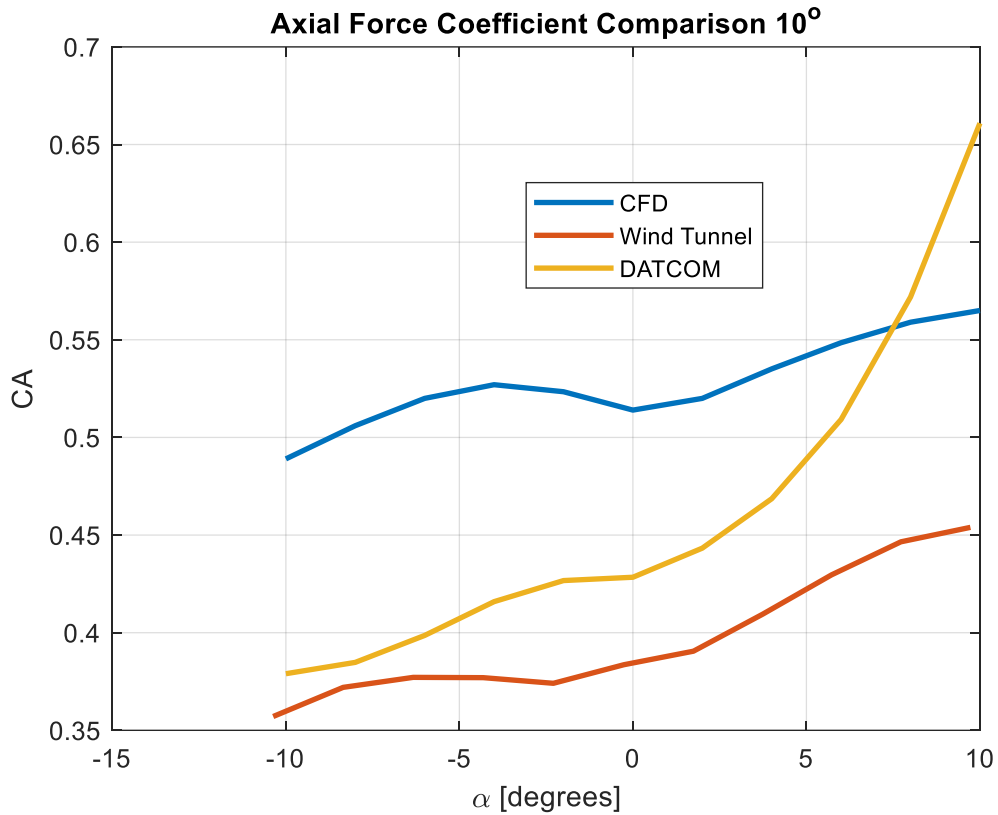


Figure 146 Axial Force coefficient comparison for 10 ° control surface deflection

Figure 147 shows the roll moment coefficient comparison for 10 degrees control deflection. The comparison shows good agreement between the CFD and experimental results in terms of pattern. However, the CFD results are slightly off in magnitude when comparing to the wind tunnel data. It is important to point out that Missile DATCOM results are not available for roll moment due to the limitation of Missile DATCOM as explained previously.

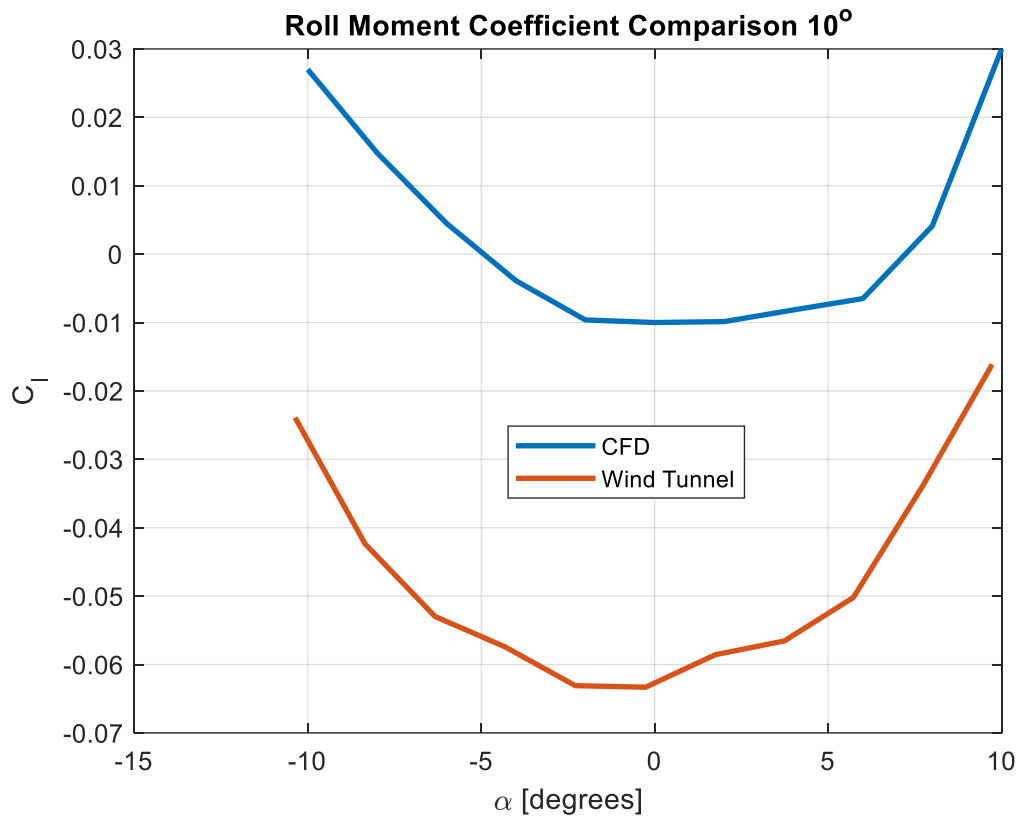


Figure 147 Roll moment coefficient comparison for 10 ° control surface deflection

7.3. 15 degrees deflection

Figure 148, Figure 149, and Figure 150 represent the results comparison between the theoretical and experimental methods for 15 degrees control surface deflection. All the aerodynamic coefficients are presented in terms of different angles of attack.

Figure 148 shows the normal force coefficient comparison for 15 degrees control deflection. The theoretical results follow the same curve pattern as the experimental which is seen in Figure 148. Figure 148 shows that the normal force coefficients determined by the applied CFD approach are in better agreement with wind tunnel results than the



results from Missile DATCOM. It is also important to note that the applied CFD approach provided extremely accurate results towards high angles of attack.

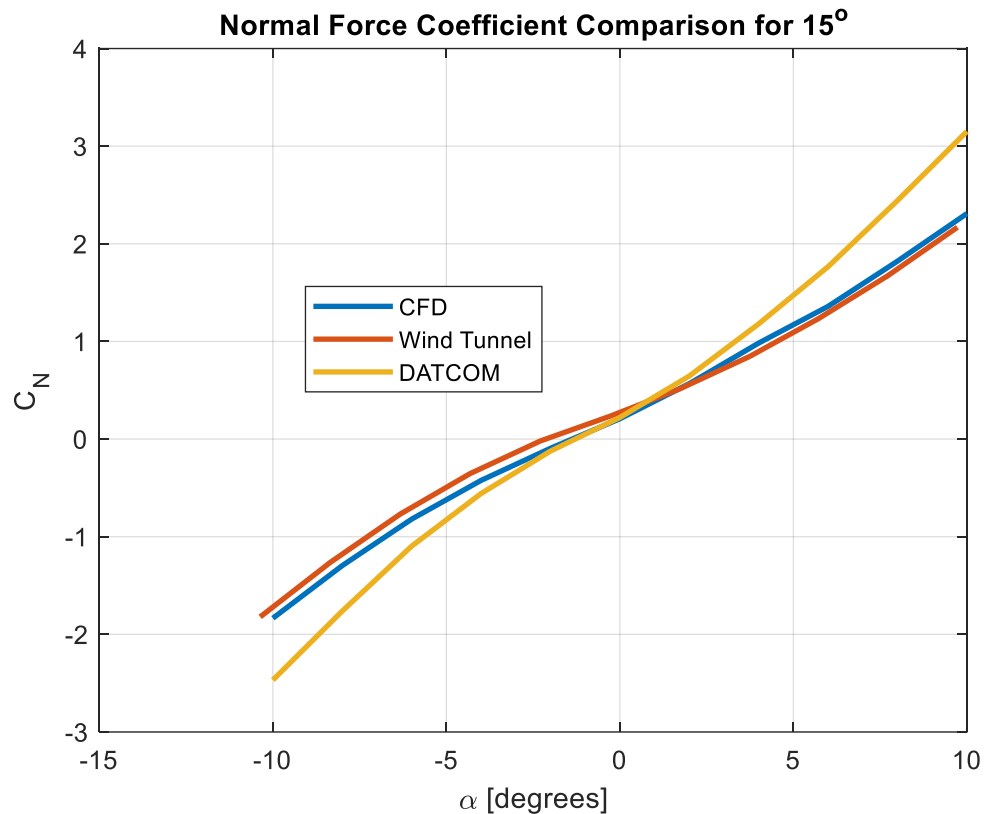


Figure 148 Normal force coefficient comparison for 15 ° control surface deflection

Figure 149 shows the pitch moment coefficient comparison for 15 degrees control deflection. The theoretical results follow the same curve pattern as the experimental which is seen in Figure 149. Figure 149 shows that the pitch moment coefficients determined by the applied CFD approach are in better agreement with wind tunnel results than the results from Missile DATCOM. Moreover, it is important to note that the applied CFD approach provided extremely accurate results towards high angles of attack where Missile DATCOM results deviated.

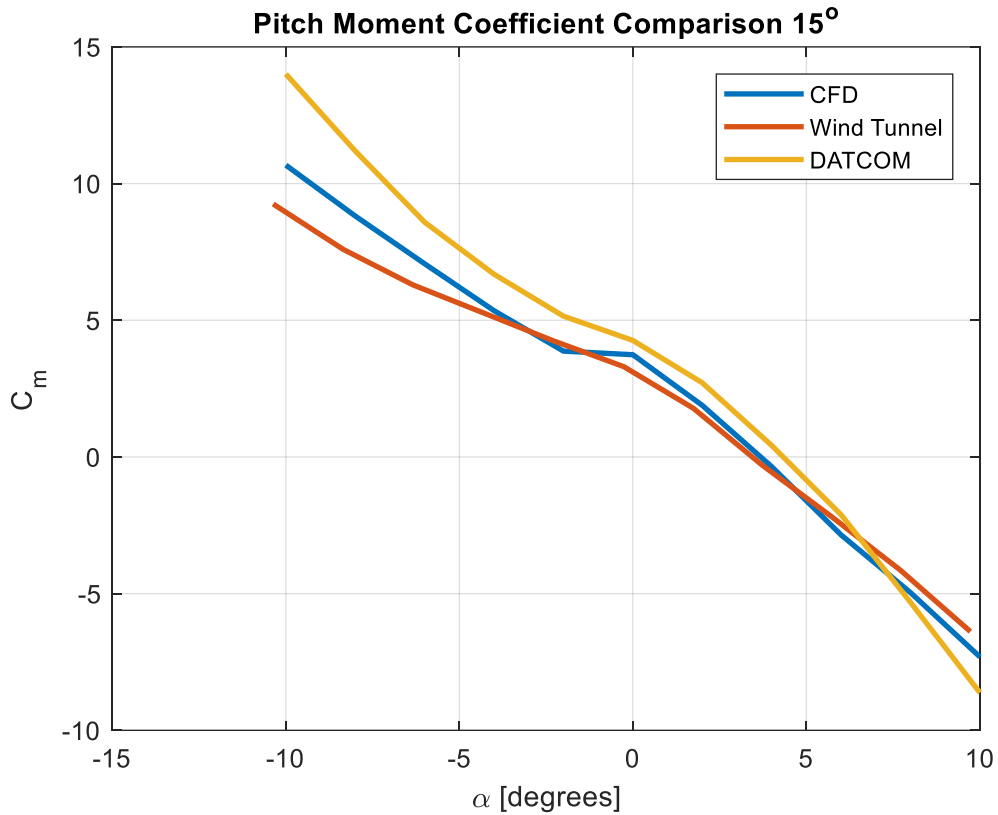


Figure 149 Pitch moment coefficient comparison for 15 ° control surface deflection

Figure 150 shows the axial force coefficient comparison for 15 degrees control deflection. The comparison shows decent agreement between theoretical and experimental results in terms of pattern. However, the CFD results are slightly off in magnitude when comparing to the wind tunnel data.

Missile DATCOM shows better agreement with wind tunnel in terms of magnitude. Moreover, it is important to point out that Missile DATCOM axial force coefficient results start to exponentially deviate towards angles of attack 2 degrees and higher. According to the results presented in both Figure 150 and Figure 146, Missile DATCOM has



limitations on predicting axial force for high angles of attack. This limitation increases as pitch control deflection increases.

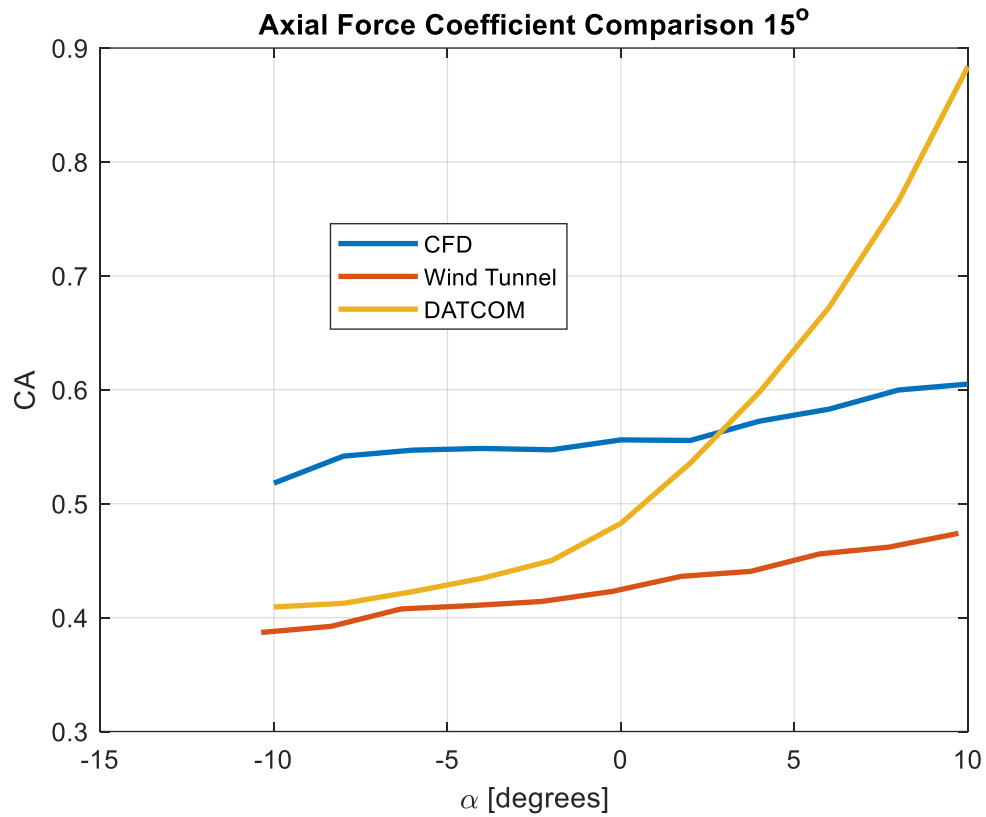


Figure 150 Axial force coefficient comparison for 15 ° control surface deflection



8. Conclusions

This paper presented and discussed a successful numerical approach by finite volume method. The method is realized by improving the mesh utilizing the pressure gradient methods. As seen in the paper, the CFD simulation results showed a good agreement with the experimental results performed in the wind tunnel for Mach 0.4.

Moreover, the CFD normal force and pitch moment coefficients showed better agreement with the wind tunnel data than Missile DATCOM results. However, there were slight discrepancies as angles of attack and pitch control deflections increase. These deviations are mainly caused by the high non-linear characteristics of the simulated flow. The maximum deviation occurred for pitching moment coefficient was at 15 degrees control deflection. However, the error was less than 20%. Therefore, the employed CFD approach can be considered accurate for identification of normal force and pitch moment coefficients in subsonic flow regime for this configuration. In addition, it is important to highlight that the employed approach in CFD mainly utilized Spalart Allmaras turbulence model along with Three Coefficient Method of Sutherland's law for viscosity calculation. Moreover, the pressure gradient mesh adaptation played a crucial role in accurate identification of the results.

The CFD results showed that the missile control surfaces start to lose effectiveness at 15 degrees pitch control deflection. This is also supported by the wind tunnel results. The drop in control surfaces effectiveness is greater towards high angles of attack. This is also supported by the contours generated which showed flow separation in the same simulation cases. Hence, the results conclude that the simulated model starts to lose control surface effectiveness towards high control deflection along with high angles of attack. This should be considered when designing the model control autopilot.



The roll moment coefficients represent the wrap around fin effect with angle of attack variations. The roll moment coefficients predicted by CFD followed the wind tunnel results trend extremely closely. However, the curve of CFD is off by a magnitude. It is important to point out that the employed approach in CFD simulations is neither optimized for wrap around fin roll moment nor axial force coefficient.

Missile DATCOM axial force coefficients results showed better agreement with wind tunnel data than CFD. However, this good agreement is only in lower angles of attack region. It is crucial to point out that Missile DATCOM axial force coefficients exponentially deviated in high angles of attack region. In addition, as the pitch control deflection increases, the axial force coefficient starts to deviate earlier [lower angles of attack]. Therefore, Missile DATCOM has a big disadvantage with the drag estimation for this missile configuration in high angles of attack as well as high control deflections.

The employed CFD approach proved numerous advantages even over the wind tunnel testing. It provided much more insights in the flow field. It is much faster and more economical than the wind tunnel testing given the right computational resources. It can also reduce the cost of testing different configurations in the wind tunnel. However, the wind tunnel is always needed to validate the results since CFD has limitations on certain flow conditions such as flow separation, transient flow, and transonic flow. In addition, it also has limitations for certain simulated model geometries.

The solution method explained in this paper covers the subsonic flow regime with pressure based solver type. Since the obtained CFD and experimental data correlate sufficiently in subsonic flow regime, the study will be further extended to transonic and supersonic velocities with different solver type. Moreover, different types of mesh adaptation will also be researched. In this research, the only turbulence model used is Spalart Allmaras. Therefore, different turbulence models will also be studied. In addition, Sutherland's law



for viscosity calculation will be replaced with different types of viscosity calculation methods for further studies.

9. References

1. *Computational Methods for Stability and Control (COMSAC): The Time Has Come*. **Hall, Robert M., et al.** San Francisco : AIAA, 2005. Atmospheric Flight Mechanics Conference and Exhibit.
2. *Practical Applications of a Building Method to Construct Aerodynamic Database of Guided Missile Using Wind Tunnel Test Data*. **Kim, Duk-hyun and Lee, Hyoung-Jin.** 2018, International Journal of Aeronautical & Space Sciences.
3. *Numerical Simulations on Aerodynamic Characteristics of a Guided Rocket Projectile*. **Peng, Jiazhong, Zhao, Liangyu and Jiao, Longyin.** Taiyuan : s.n., 2016. 3rd International Conference on Materials Engineering, Manufacturing Technology and Control. pp. 1004-1007.
4. *SUBSONIC FLOW CFD INVESTIGATION OF CANARD-CONTROLLED MISSILE WITH PLANAR AND GRID FINS*. **DeSpirito, James, Vaughn Jr., Milton E. and Washington, W. David.** Reno : s.n., 2003. 41st Aerospace Sciences Meeting and Exhibit.
5. *Aerodynamic prediction of a projectile fitted with fins*. **Decroq, Cedric, et al.** Lyon : s.n., 2017. 52nd 3AF International Conference on Applied Aerodynamics.
6. *Flight Performance of a Small Diameter Munition with a Rotating Wing Actuator*. **Fresconi, Frank, DeSpirito, James and Celmins, Ilmars.** 2015, Journal Spacecraft and Rockets, pp. 305-319.
7. *Flight Behavior of an Asymmetric Body through Spark Range Experiments using Roll-Yaw Resonance for Yaw Enhancement*. **Fresconi, et al.** San Diego : AIAA SciTech, 2016. AIAA Atmospheric Flight Mechanics Conference.
8. *Experimental Flight Characterization of Asymmetric and Maneuvering Projectiles from Elevated Gun Firings*. **Fresconi, Frank and Harkins, Tom.** 2012, Journal of Spacecraft and Rockets, pp. 1120-1130.
9. **Anderson, John Jr. D.** *Computational Fluid Dynamics: The Basic with Application*. Maryland : McGraw-Hill, Inc., 1995.
10. *Analysis of aerodynamic characteristics of a modular assembled missile with canard rudder and arc tail*. **Chen, Han, et al.** Kumming : s.n., 2017. The 9th International Conference on Modelling, Identification and Control.
11. *Flight Behaviors of a Complex Projectile using a Coupled CFD-based Simulation Technique: Free Motion*. **Sahu, Jubaraj and Fresconi, Frank.** Dallas : AIAA Aviation, 2015. 33rd AIAA Applied Aerodynamics Conference.
12. *Lateral jet control of a supersonic missile - CFD predictions and comparison to force and moment measurements*. **Srivastava, B.** Reno : AIAA, 1997. 35th Aerospace Sciences Meeting & Exhibit.



13. *Studies on Aircraft Store with Rotating Tail*. **Kumar, Rakesh, Quamar, Md. Shahid and T, Vishak**. s.l. : AIAA SciTech Forum, 2017. 55th AIAA Aerospace Science Meeting.
14. *Forced motions design for aerodynamic identification and modeling of a generic missile configuration*. **Allen, Jacob and Ghoreyshi, Mehdi**. 2018, Elsevier.
15. *CFD Computation of Magnus Moment and Roll-Damping Moment of a Spinning Projectile*. **DeSpirito, James and Heavey, Karen R**. Providence : AIAA, 2004. Atmospheric Flight Mechanics and Exhibit.
16. *Aerodynamic characteristic of a canard guided rocket*. **Chen, Yong-Chao, et al**. 2017, International Journal of Modeling, Simulation, and Scientific Computing, pp. 1750001-1750022.
17. *Computational and Experimental Free-Flight Motion of a Subsonic Canard-Controlled Body*. **Sahu, Jubaraj and Fresconi, Frank**. Denver : AIAA Aviation Form, 2017. 35th AIAA Applied Aerodynamics Conference.
18. **Versteeg, H K and Malalasekera, W**. *An Introduction to Computational Fluid Dynamics*. Harlow : Pearson Education Limited, 2007.
19. *A One-Equation Turbulence Model for Aerodynamic Flows*. **Spalart, P. R. and Allmaras, S. R**. Reno : AIAA, 1992. 30th Aerospace Sciences Meeting & Exhibit.
20. *CFD INVESTIGATION OF CANARD-CONTROLLED MISSILE WITH PLANAR AND GRID FINS IN SUPERSONIC FLOW*. **DeSpirito, James, Vaughn Jr., Milton E. and Washington, W. David**. Monterey : AIAA, 2002. Atmospheric Flight Mechanics Conference and Exhibit.
21. *GRID ADAPTATION FOR THE 2-D EULER EQUATIONS*. **Dannenhoffer, John F. and Baron, Judson R**. Reno : AIAA, 1985. 23rd Aerospace Sciences Meeting.
22. **ANSYS Inc**. ANSYS FLUENT 12.0 Theory Guide. April 2009.
23. **Military Technical Institute**. EXPERIMENTAL AERODYNAMICS LABORATORY. [Online] [Cited: September 3, 2018.]
24. *Approximate Method to Calculate Nonlinear Rolling Moment due to Differential Fin Deflection*. **Moore, F. G. and Moore, L. Y**. 2012, Journal of Spacecraft and Rockets, pp. 250-260.
25. **Blake, William B**. *Missile DATCOM USER'S MANUAL - 1997 FORTRAN 90 REVISION*. s.l. : AIR FORCE RESEARCH LABORATORY, 1998.
26. **Hymer, Thomas C., Moore, Frank G. and Tracor, Cornell Downs**. User's Guide For an Interactive Personal Computer Interface for the 1998 Aeroprediction Code (AP98). Dahlgren : Naval Surface Warfare Center, June 1998.
27. *Application of the 1998 Version of the Aeroprediction Code*. **Moore, F. G., McInville, R. M. and Hymer, T. C**. 1999, Journal of Spacecraft and Rockets, pp. 633-645.
28. *Missile DATCOM - Aerodynamic prediction of conventional missiles using component build-up techniques*. **Vukelich, S. R. and Jenkins, J. E**. Reno : AIAA, 1984. 22nd Aerospace Sciences Meeting.



29. *High angle of attack aerodynamic predictions using missile datcom.* **Abney, Eric J. and McDaniel, Melissa A.** Toronto : s.n., 2005. AIAA Applied Aerodynamics Conference.

30. *AERODYNAMIC PREDICTIONS, COMPARISONS, AND VALIDATIONS USING MISSILE DATCOM (97) AND AEROPREDICTION 98 (AP98).* **Sooy, Thomas J. and Schmidt, Rebecaa Z.** Reno : AIAA, 2004. 42nd AIAA Aerospace Sciences Meeting and Exhibit.

31. **Maurice, Andrew F.** Aerodynamic performance predictions of a SA-2 Missile using missile datcom. Monterey : s.n., September 2009.

32. *A Comparison of Predictive Methodologies for Missile Configurations with Strakes.* **Rosema, Christopher C., et al.** Dallas : AIAA Aviation, 2015. 33rd AIAA Applied Aerodynamics Conference.

33. *EXPERIMENTAL, COMPUTATIONAL, AND EMPIRICAL EVALUATION OF SUPERSONIC MISSILE AERODYNAMIC COEFFICIENTS.* **El-Mahdy, L. A., et al.** Cairo : Military Technical College Kobry El-Kobbah, 2016. 17th International Conference on Applied Mechanics and Mechanical Engineering.

10. Appendix A

10.1. Velocity contours

10.1.1. No deflection

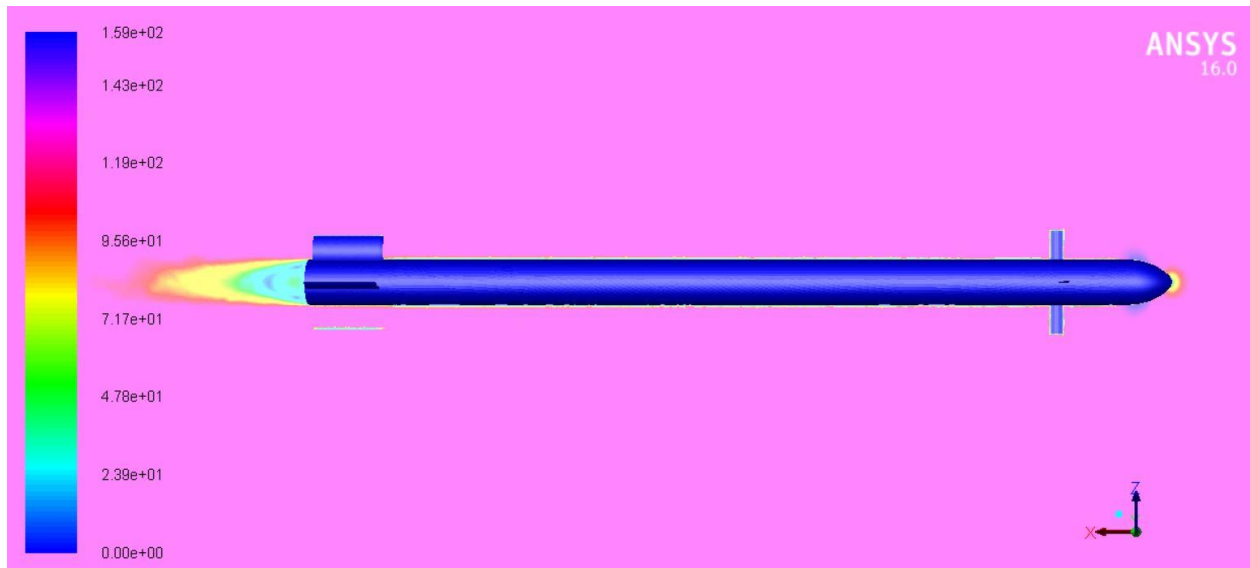


Figure 151 Velocity contours for 0° control deflection and angle of attack $\alpha = 0^\circ$

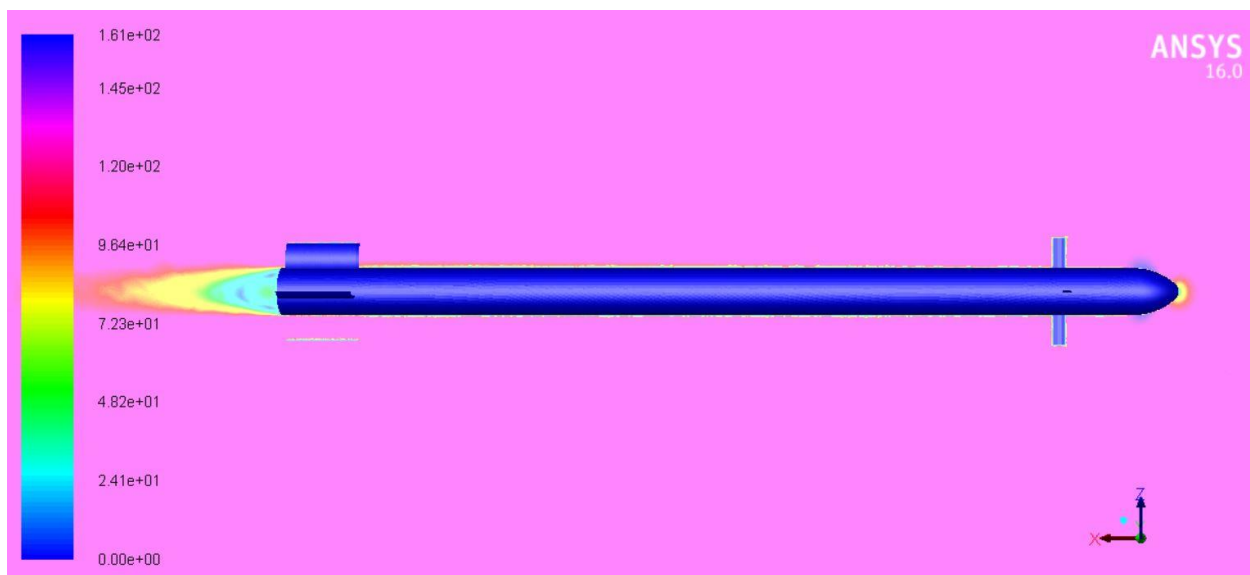


Figure 152 Velocity contours for 0° control deflection and angle of attack $\alpha = 2^\circ$

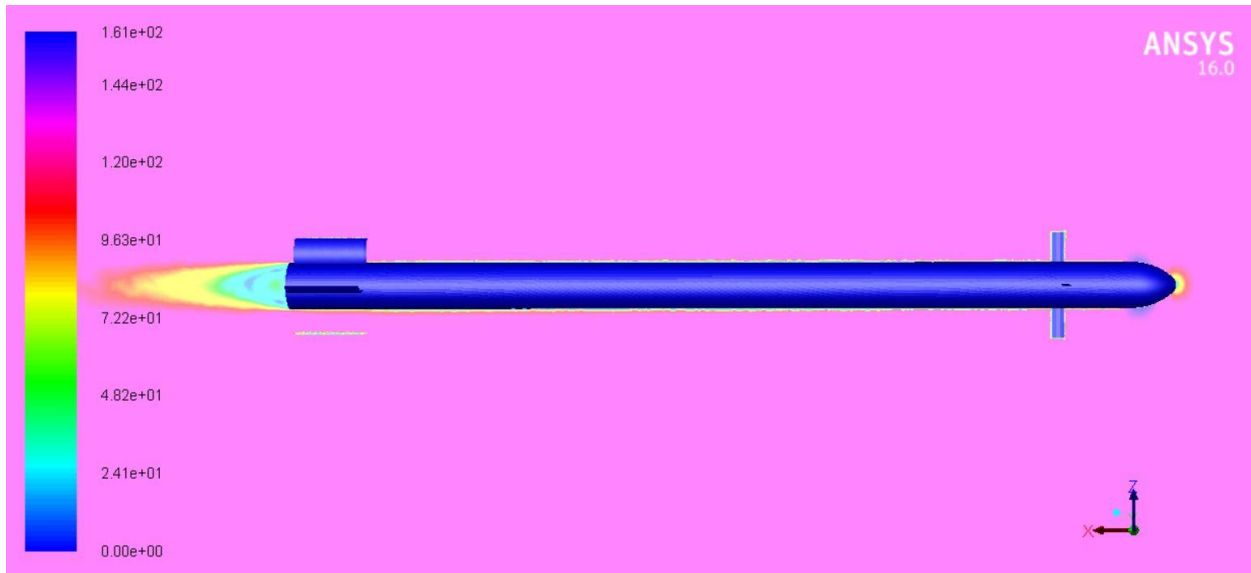


Figure 153 Velocity contours for 0° control deflection and angle of attack $\alpha = -2^\circ$

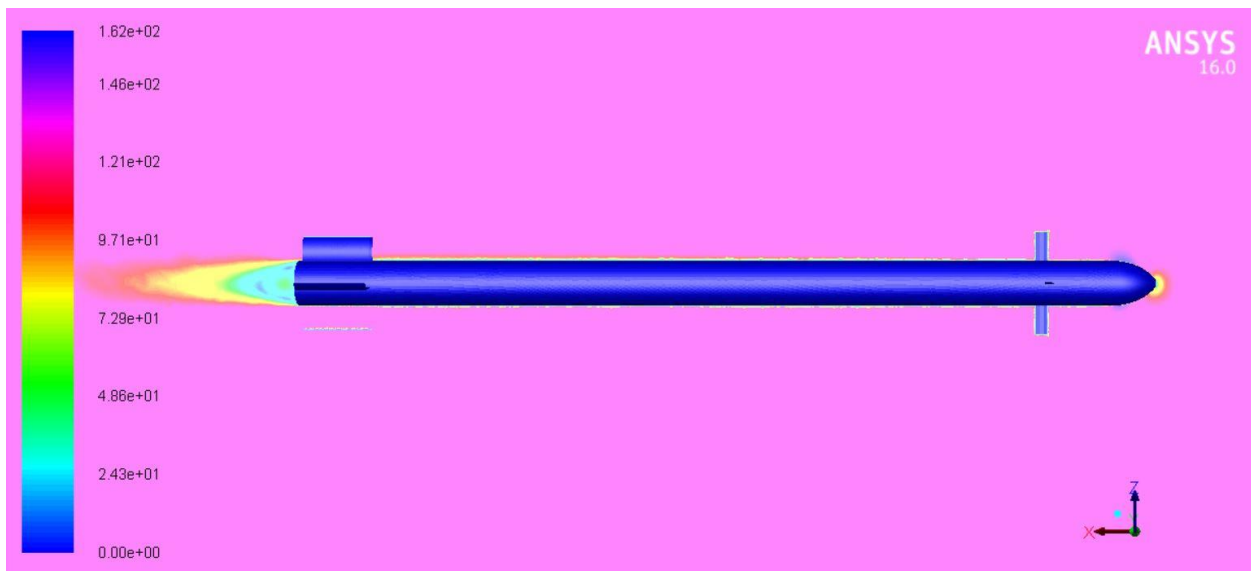


Figure 154 Velocity contours for 0° control deflection and angle of attack $\alpha = 4^\circ$

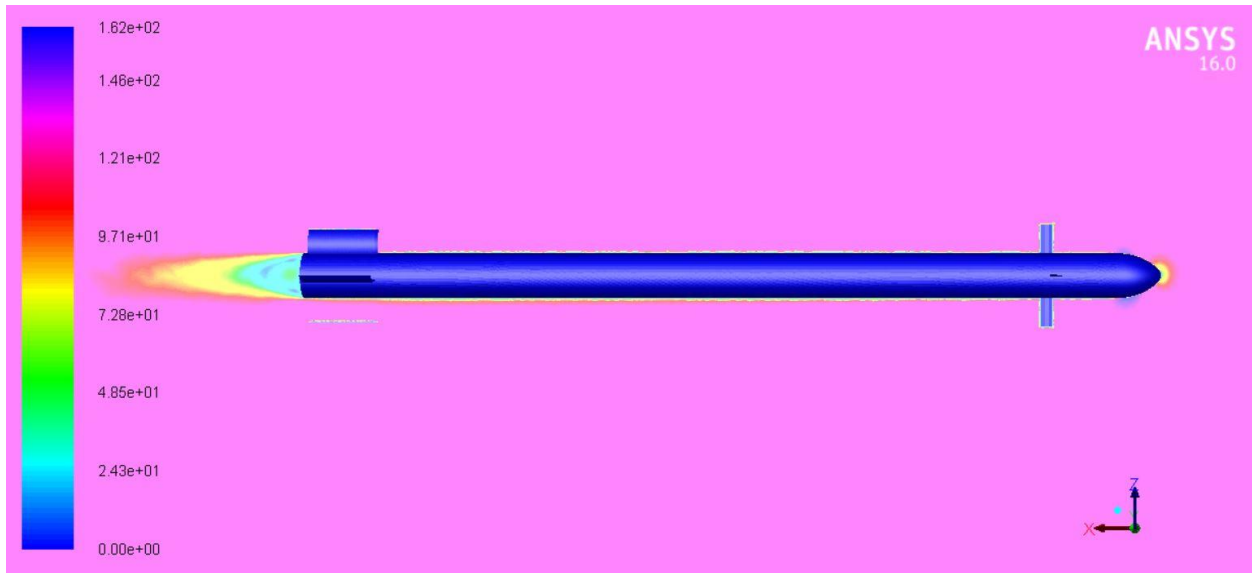


Figure 155 Velocity contours for 0° control deflection and angle of attack $\alpha = -4^\circ$

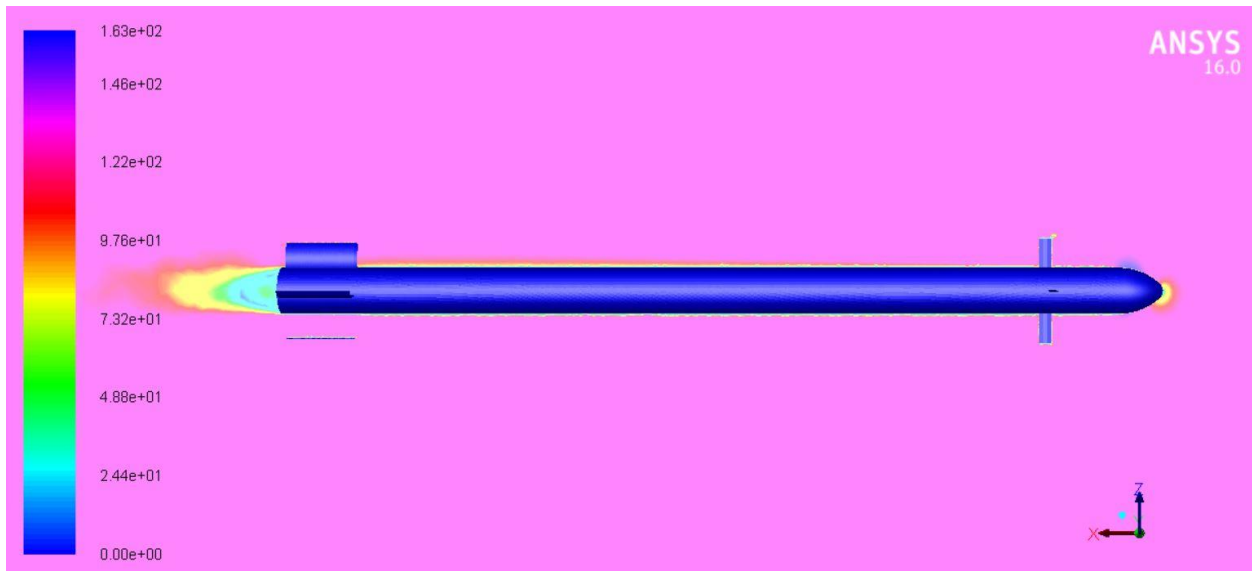


Figure 156 Velocity contours for 0° control deflection and angle of attack $\alpha = 6^\circ$

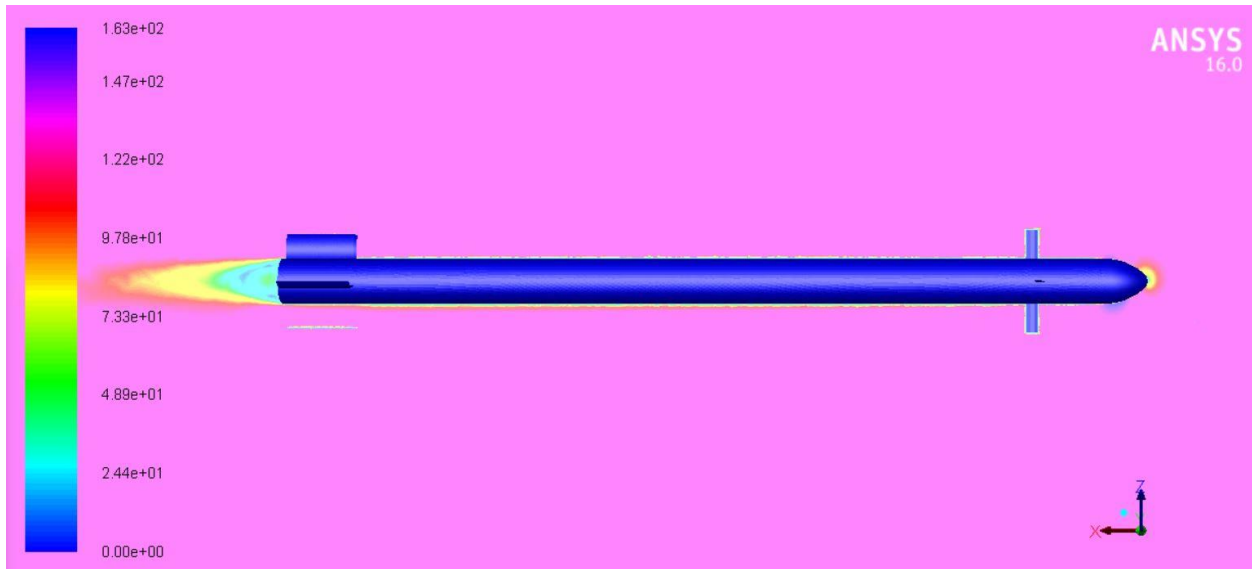


Figure 157 Velocity contours for 0° control deflection and angle of attack $\alpha = -6^\circ$

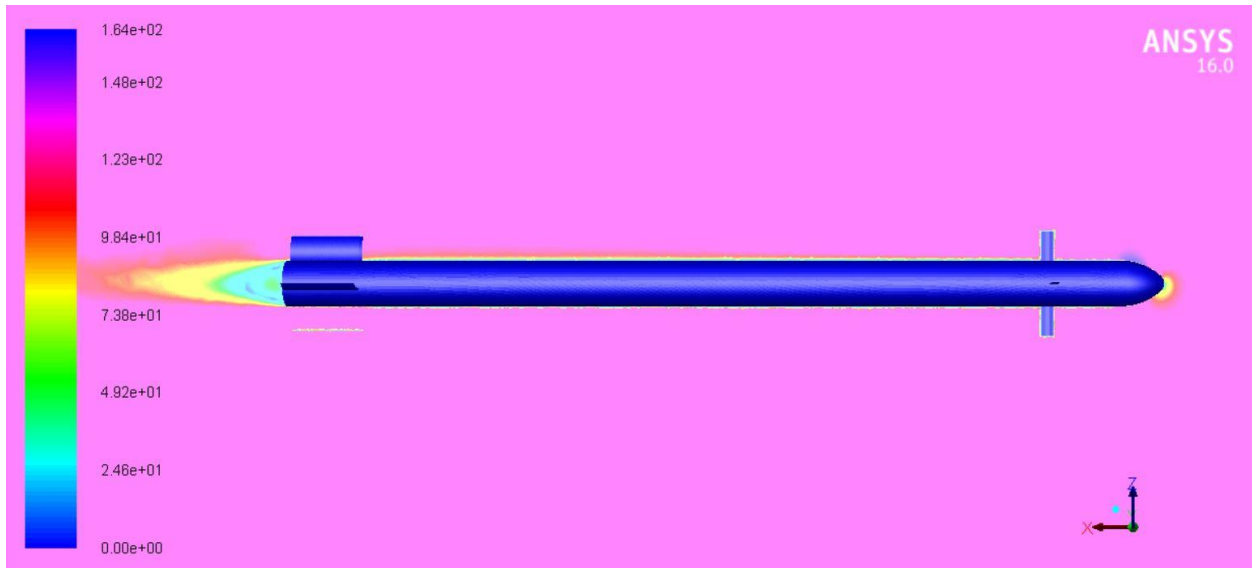


Figure 158 Velocity contours for 0° control deflection and angle of attack $\alpha = 8^\circ$

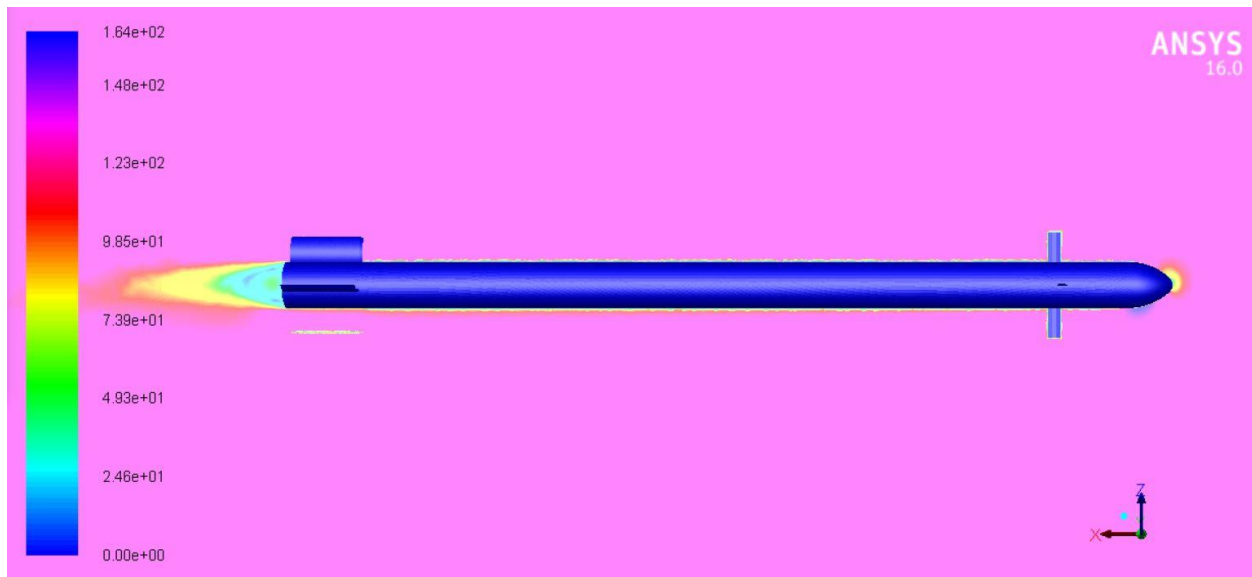


Figure 159 Velocity contours for 0° control deflection and angle of attack $\alpha = -8^\circ$

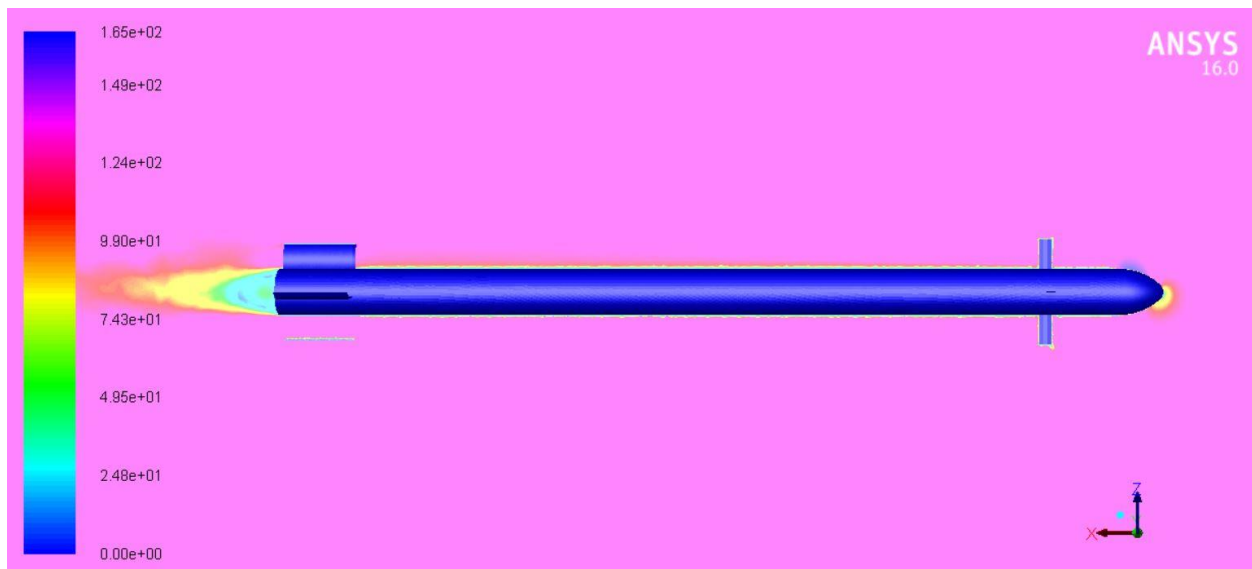


Figure 160 Velocity contours for 0° control deflection and angle of attack $\alpha = 10^\circ$

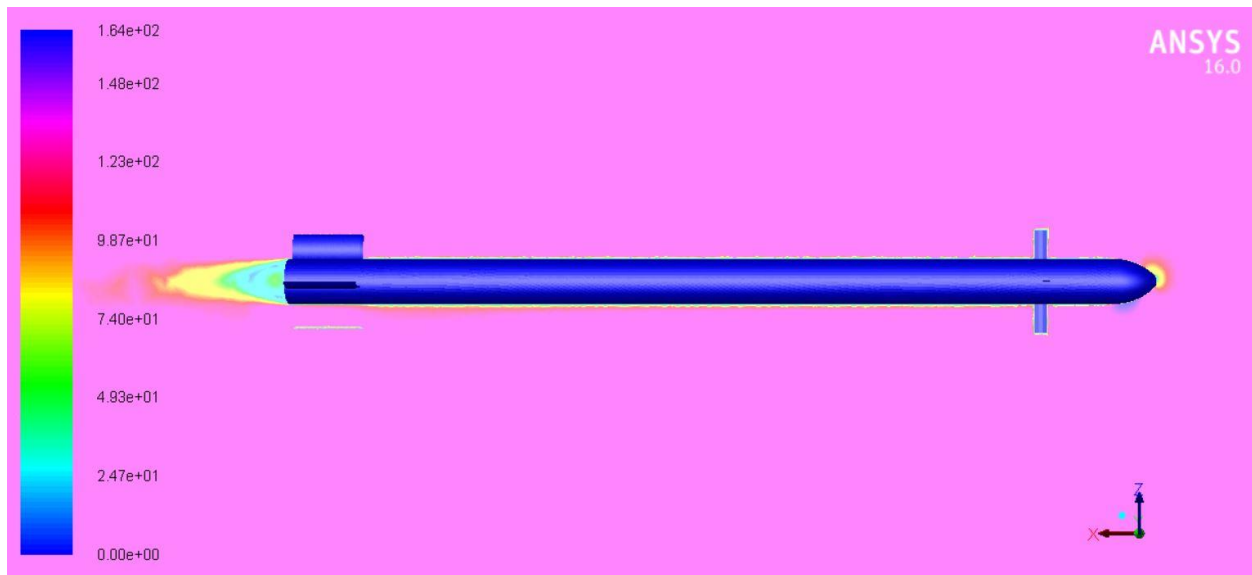


Figure 161 Velocity contours for 0° control deflection and angle of attack $\alpha = -10^\circ$

10.1.2. 10 degrees deflection

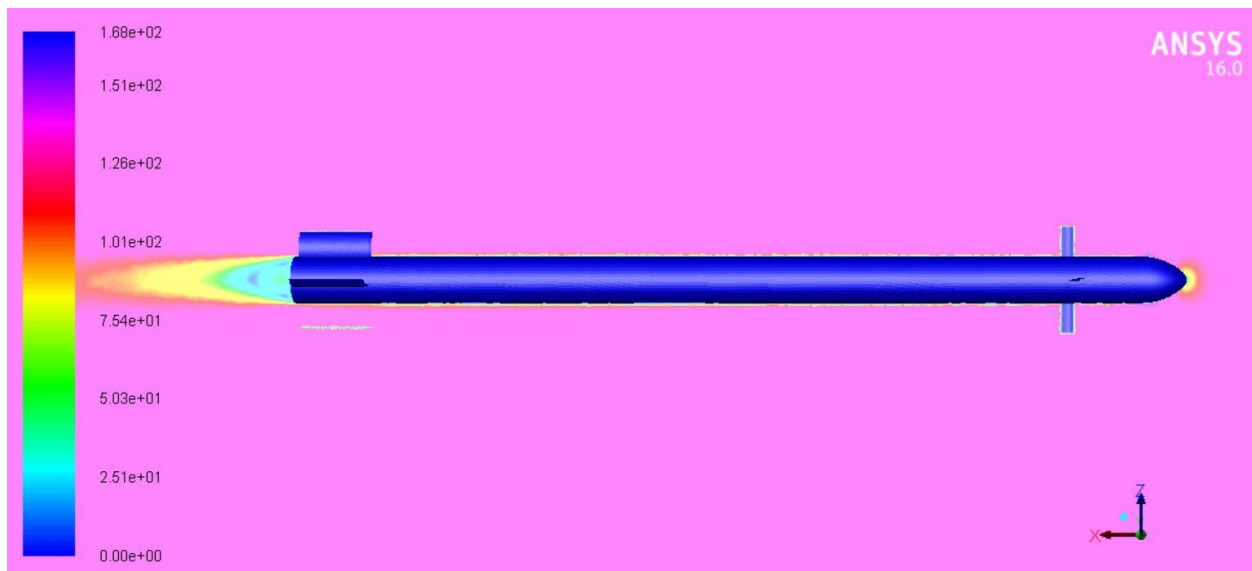


Figure 162 Velocity contours for 10° control deflection and angle of attack $\alpha = 0^\circ$

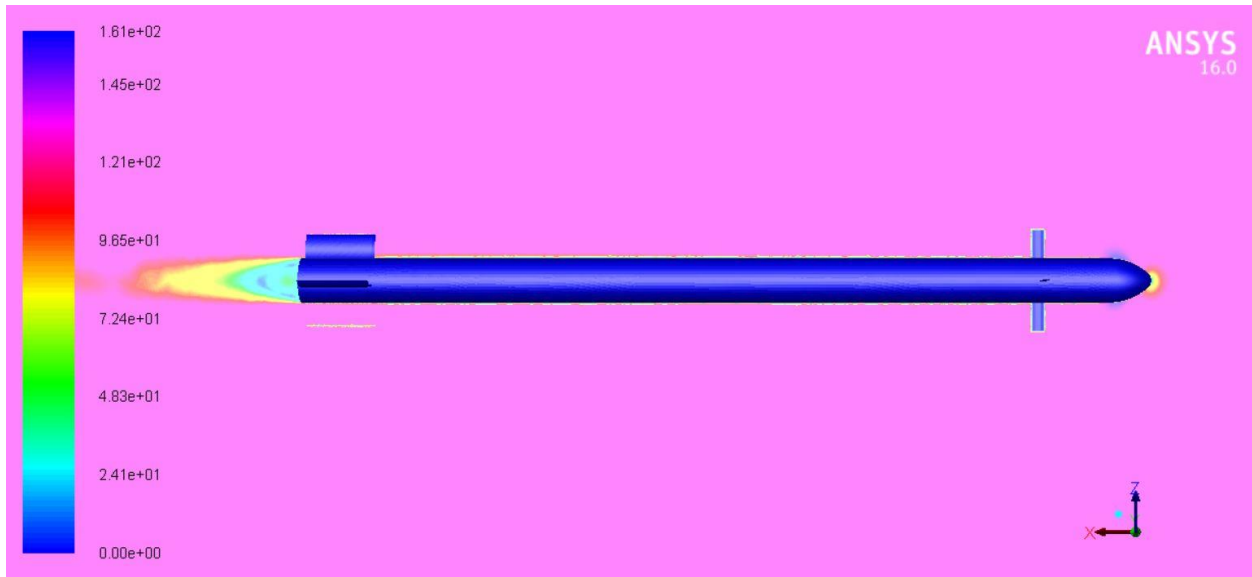


Figure 163 Velocity contours for 10 ° control deflection and angle of attack $\alpha = 2^\circ$

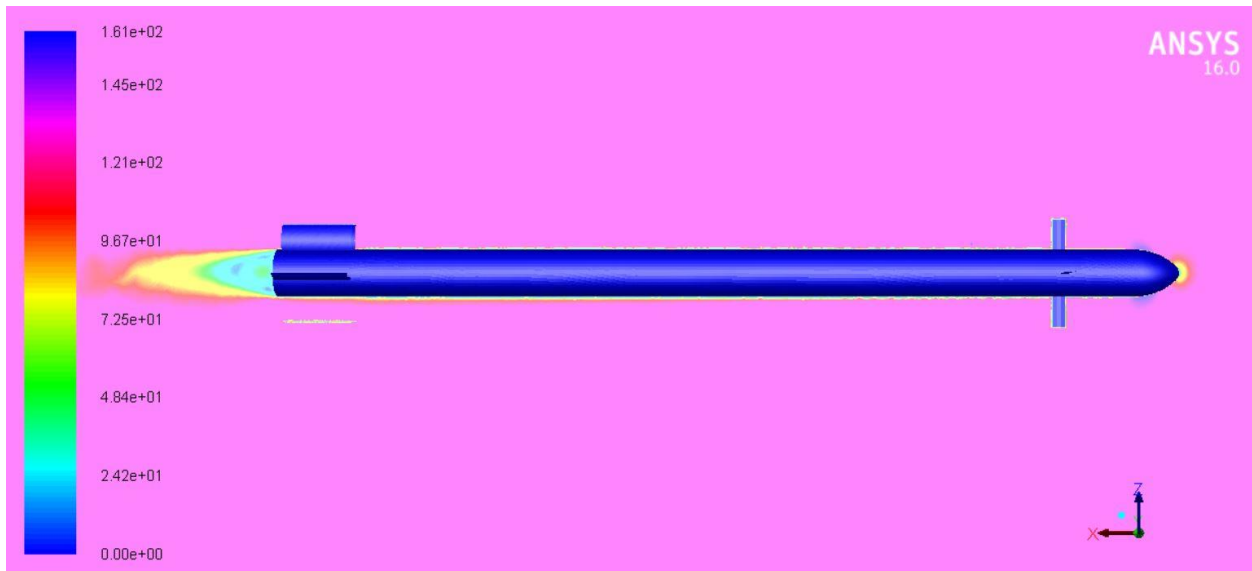


Figure 164 Velocity contours for 10 ° control deflection and angle of attack $\alpha = -2^\circ$

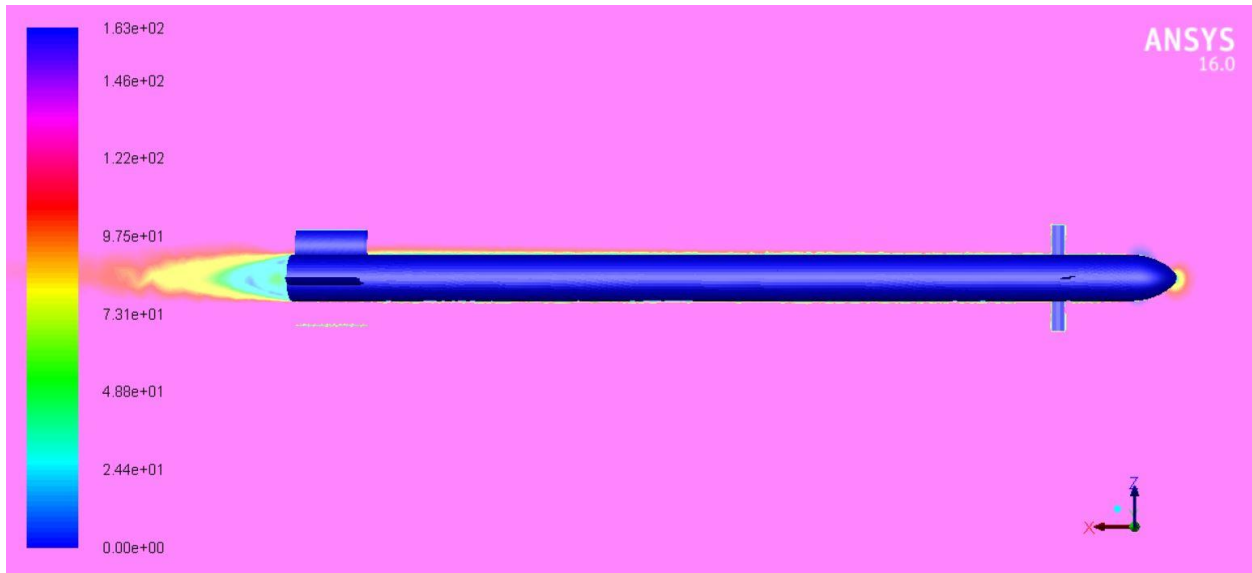


Figure 165 Velocity contours for 10 ° control deflection and angle of attack $\alpha = 4^\circ$



Figure 166 Velocity contours for 10 ° control deflection and angle of attack $\alpha = -4^\circ$

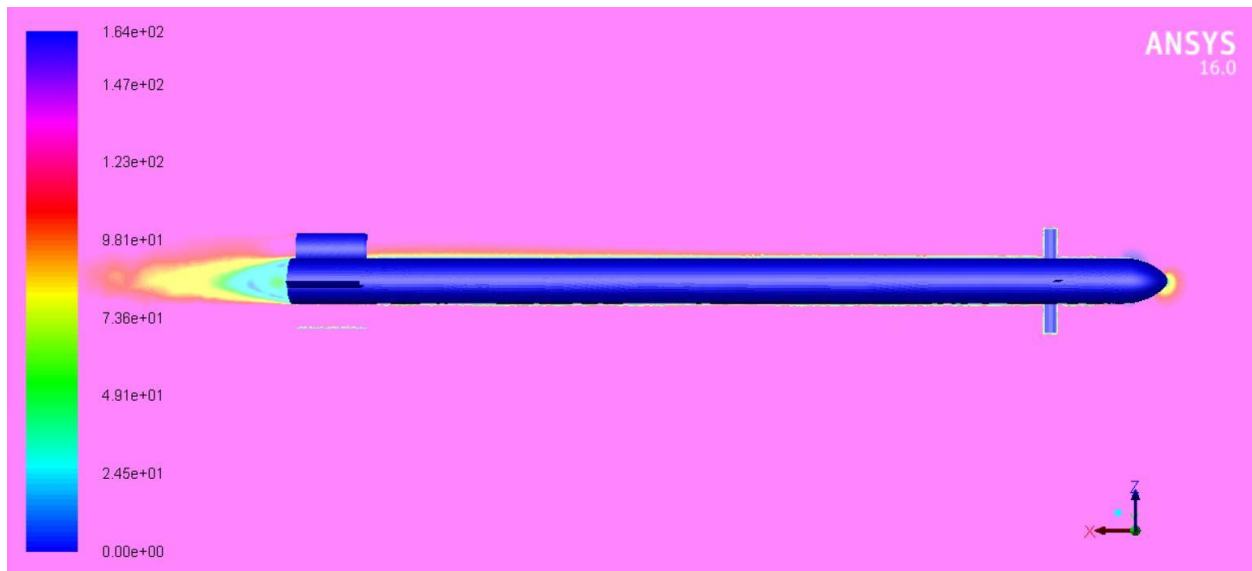


Figure 167 Velocity contours for 10° control deflection and angle of attack $\alpha = 6^\circ$

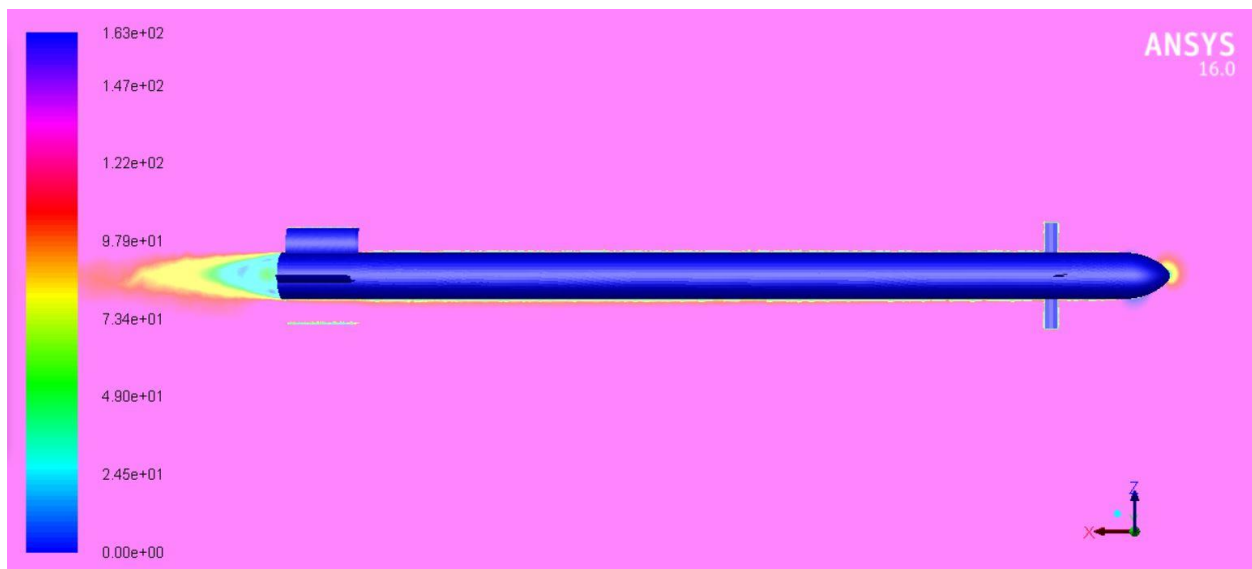


Figure 168 Velocity contours for 10° control deflection and angle of attack $\alpha = -6^\circ$

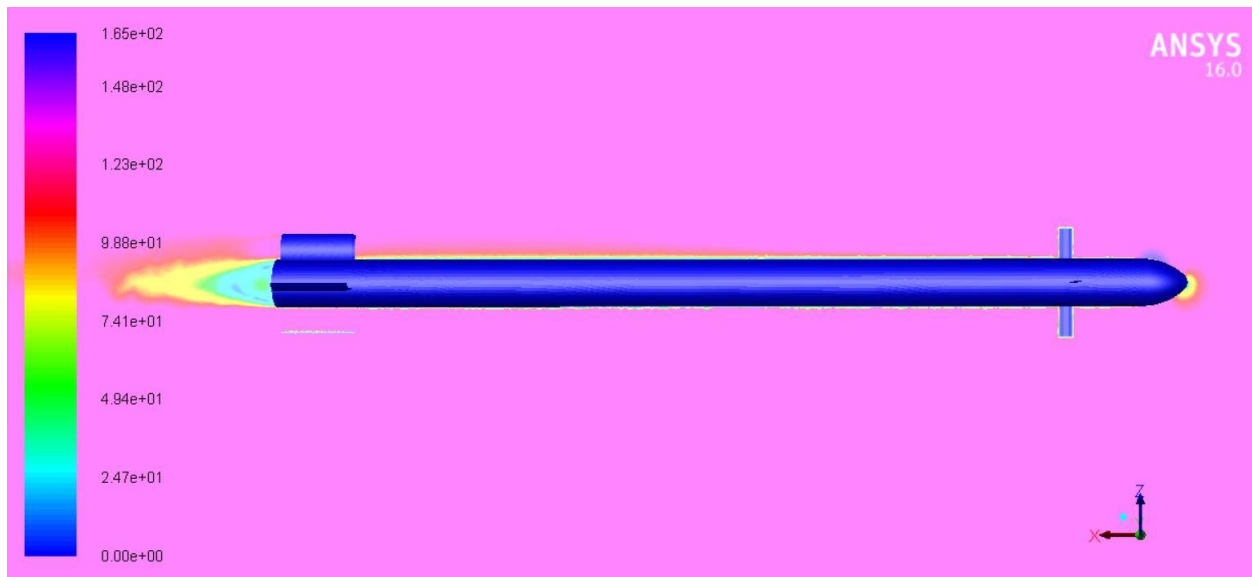


Figure 169 Velocity contours for 10° control deflection and angle of attack $\alpha = 8^\circ$

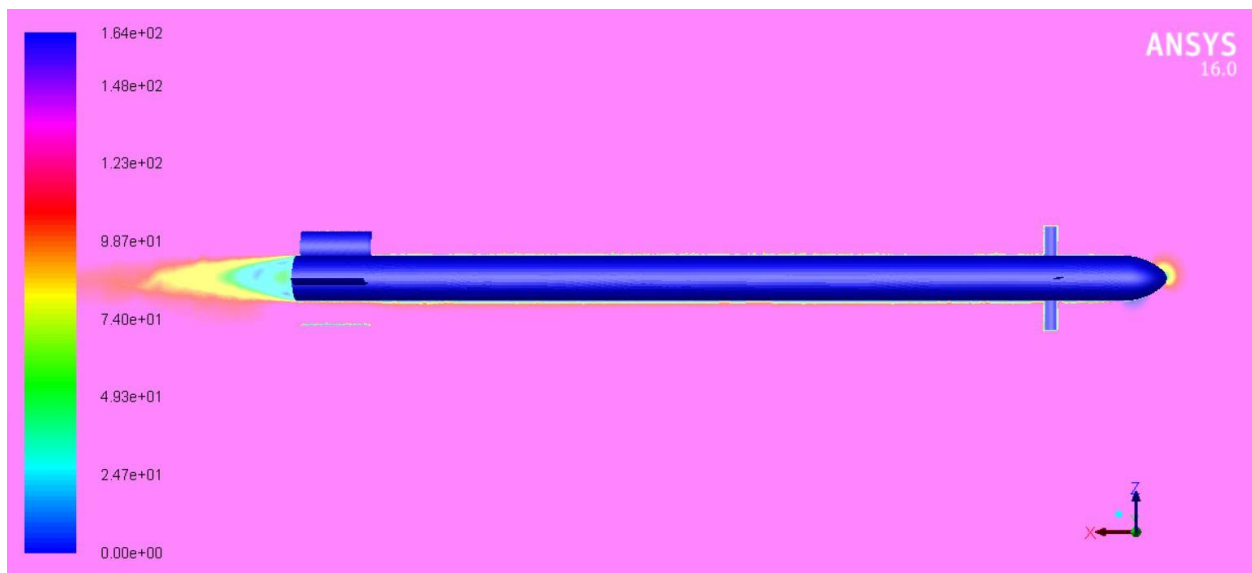


Figure 170 Velocity contours for 10° control deflection and angle of attack $\alpha = -8^\circ$

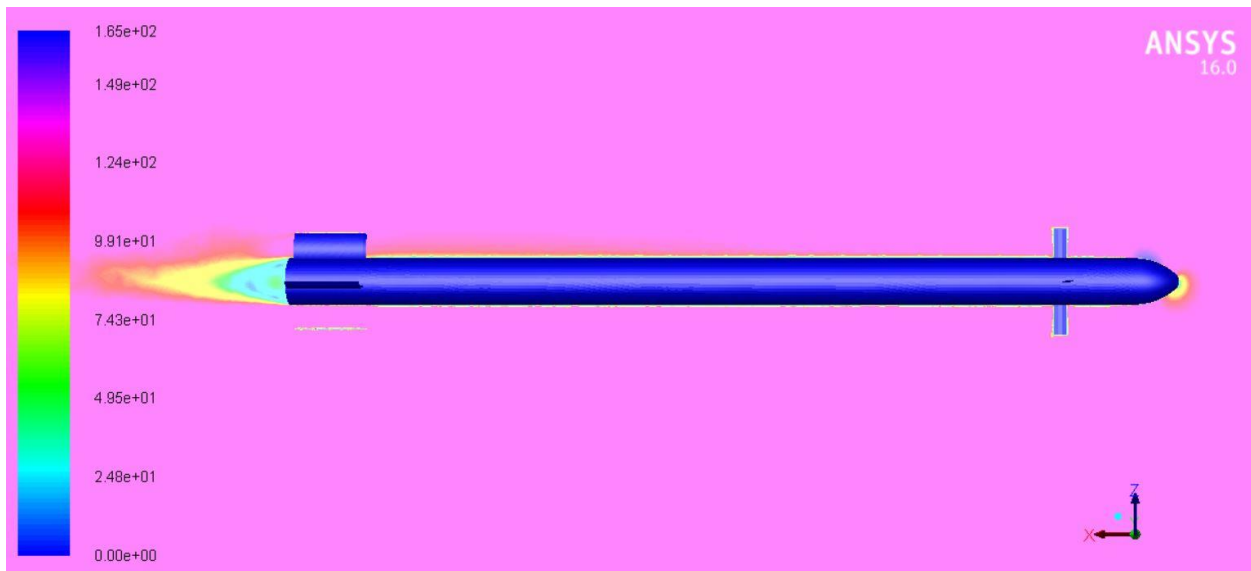


Figure 171 Velocity contours for 10 ° control deflection and angle of attack $\alpha = 10^\circ$

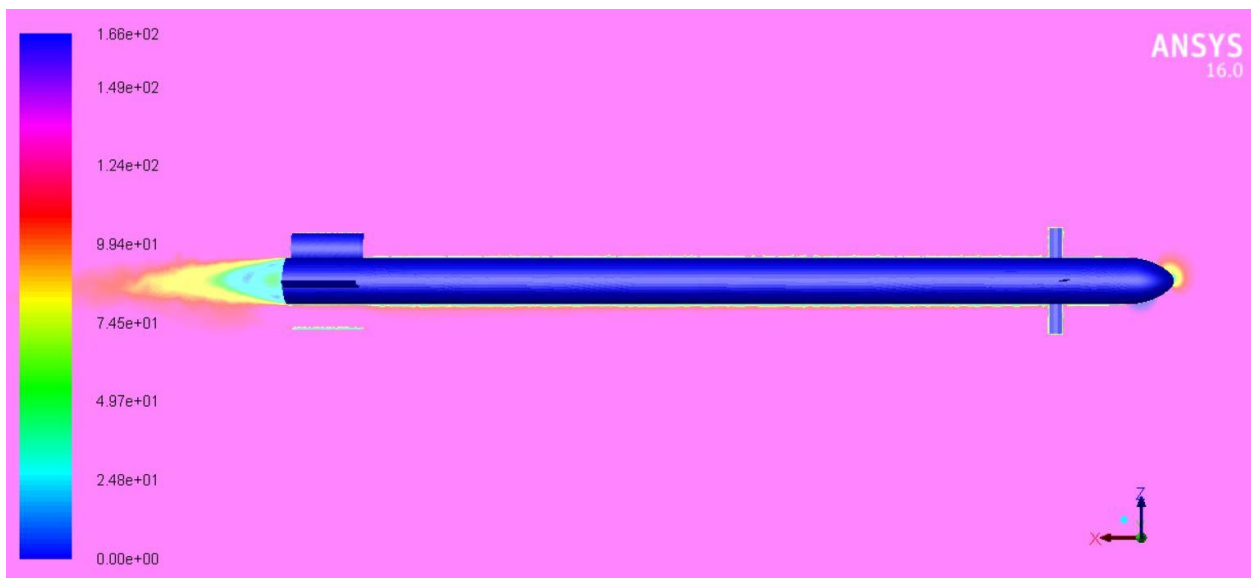


Figure 172 Velocity contours for 10 ° control deflection and angle of attack $\alpha = -10^\circ$

10.1.3. 15 degrees deflection

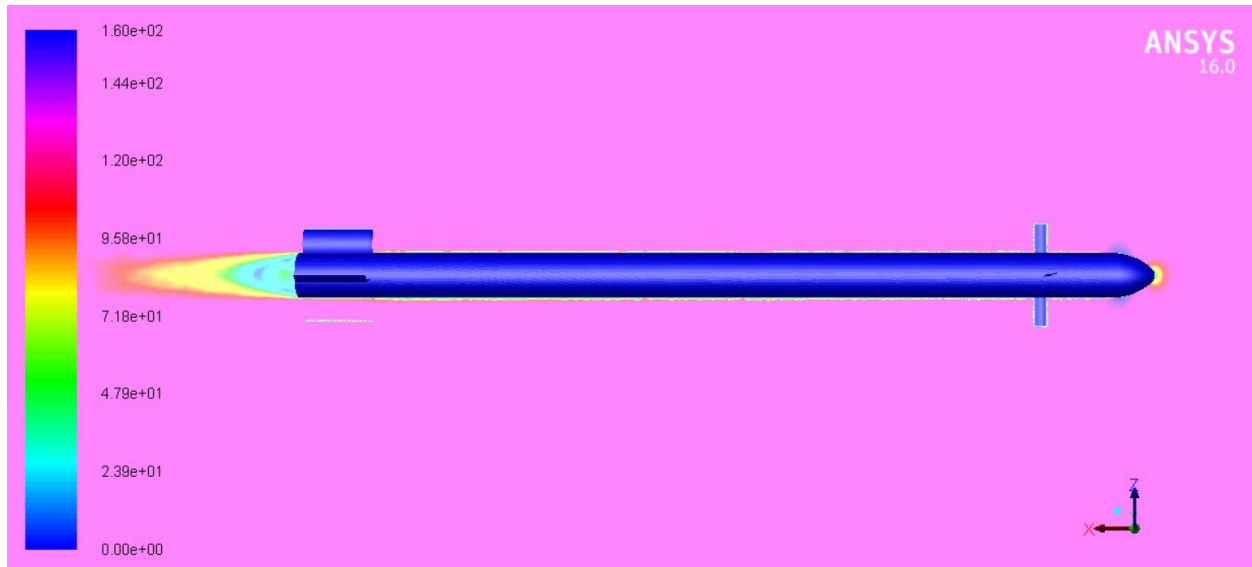


Figure 173 Velocity contours for 15 ° control deflection and angle of attack $\alpha = 0^\circ$

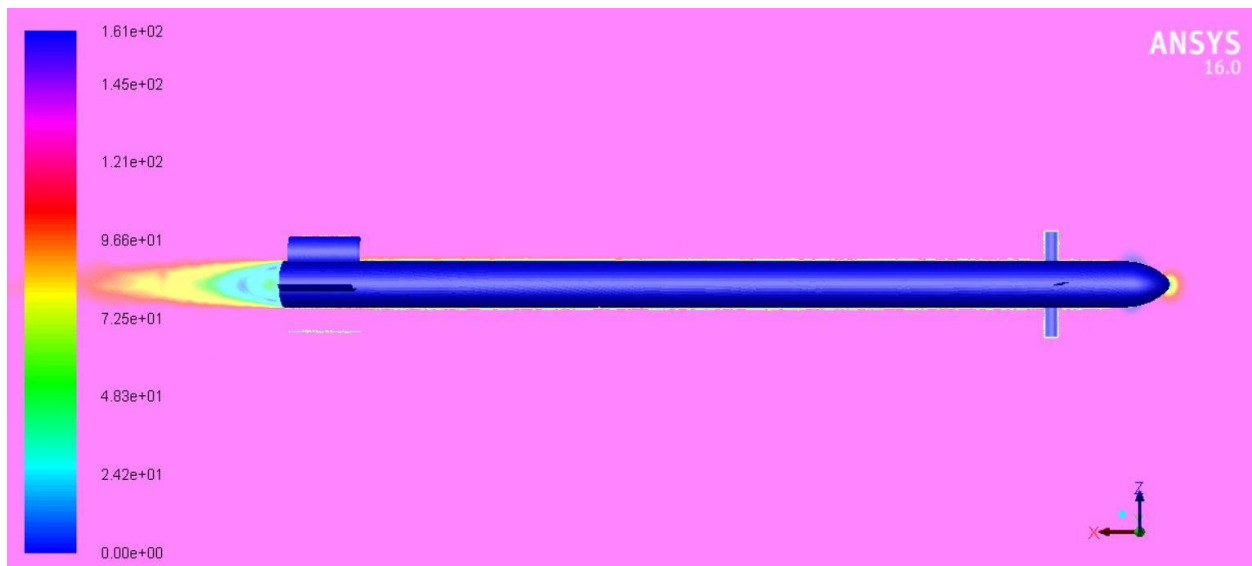


Figure 174 Velocity contours for 15 ° control deflection and angle of attack $\alpha = 2^\circ$

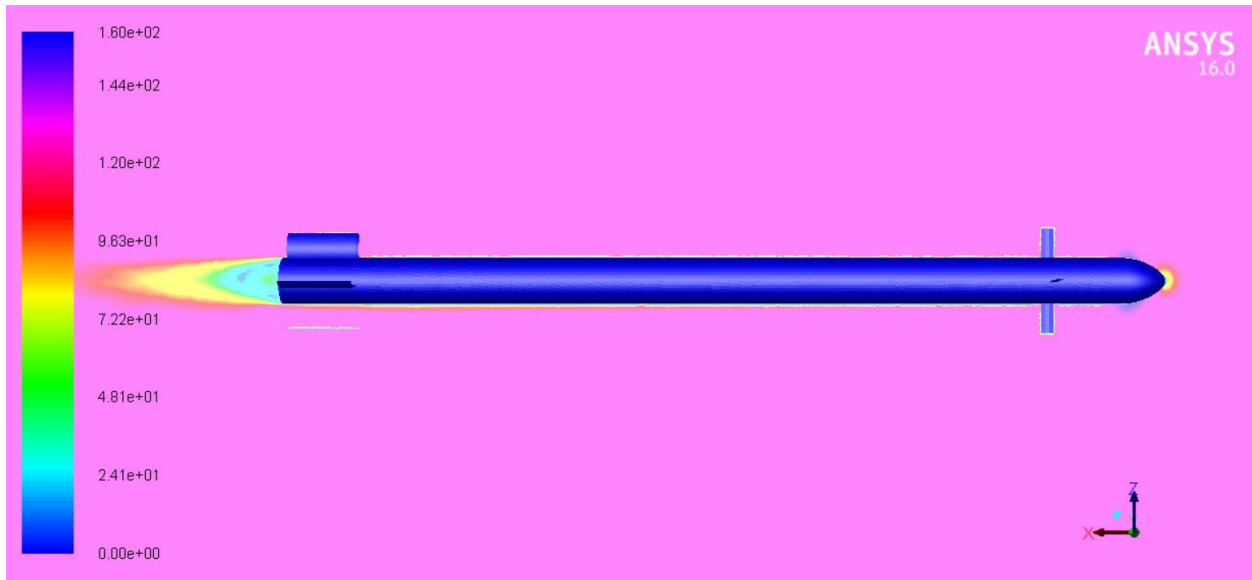


Figure 175 Velocity contours for 15 ° control deflection and angle of attack $\alpha = -2^\circ$

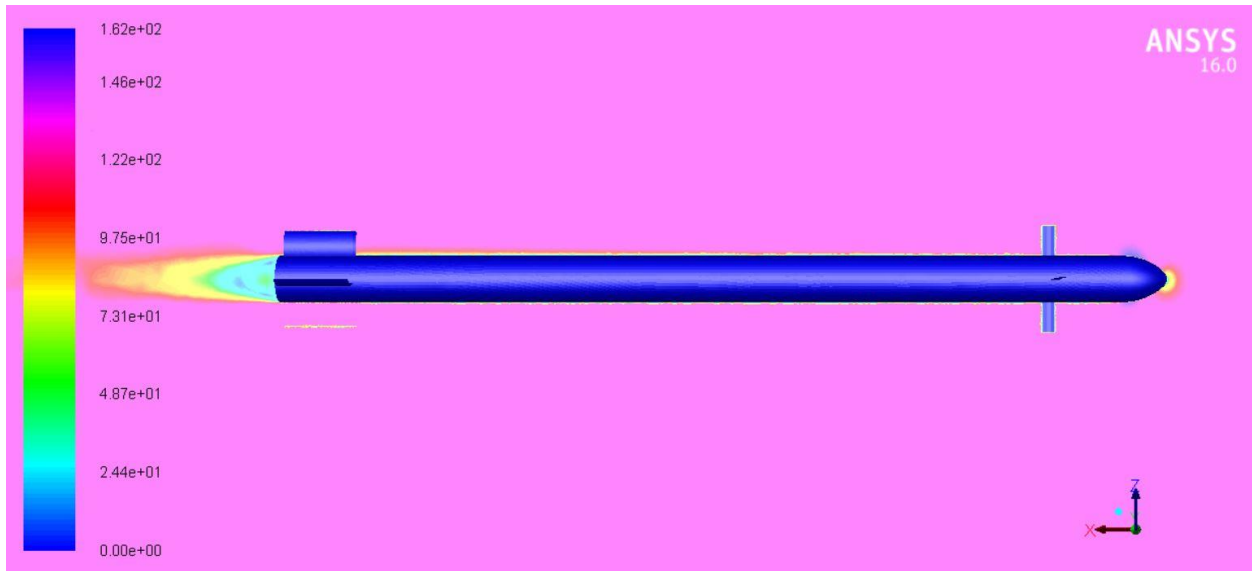


Figure 176 Velocity contours for 15 ° control deflection and angle of attack $\alpha = 4^\circ$

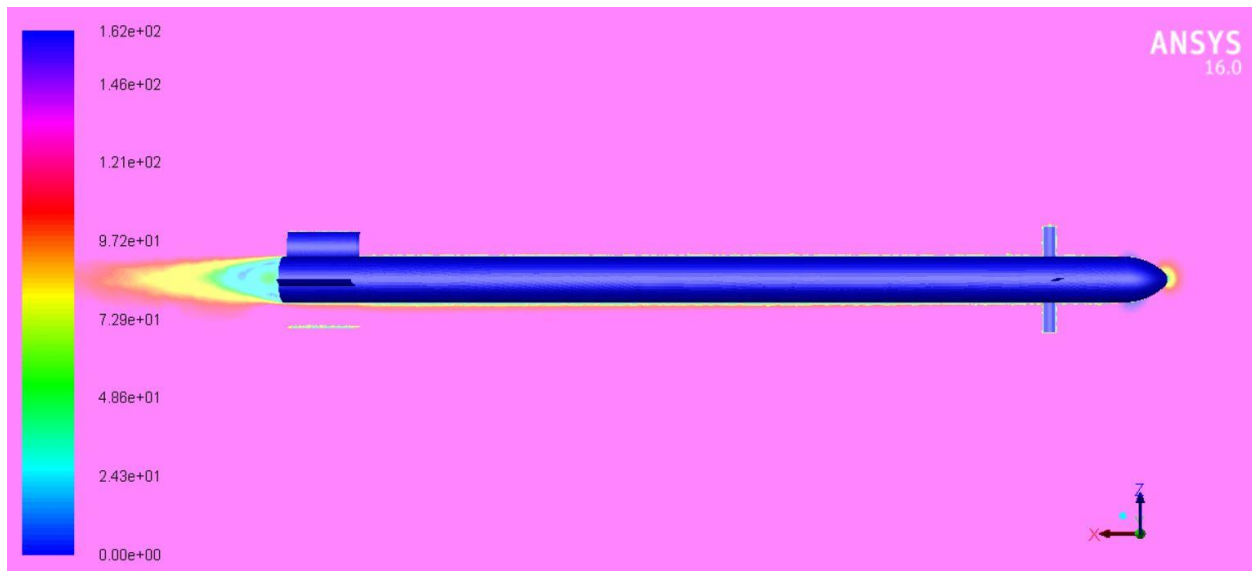


Figure 177 Velocity contours for 15 ° control deflection and angle of attack $\alpha = -4^\circ$

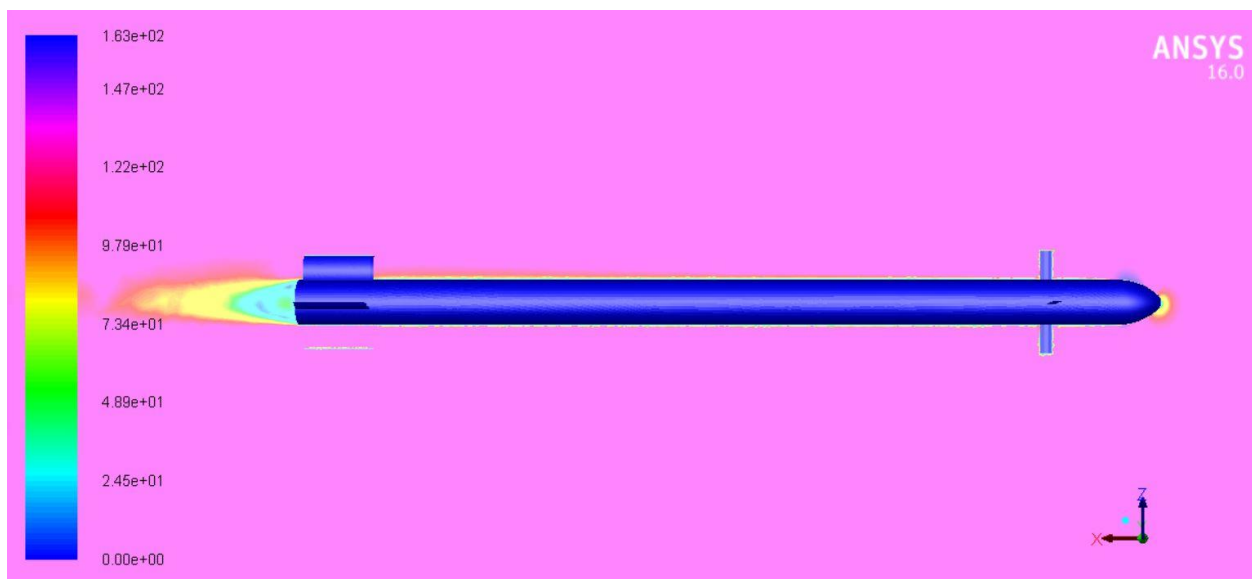


Figure 178 Velocity contours for 15 ° control deflection and angle of attack $\alpha = 6^\circ$

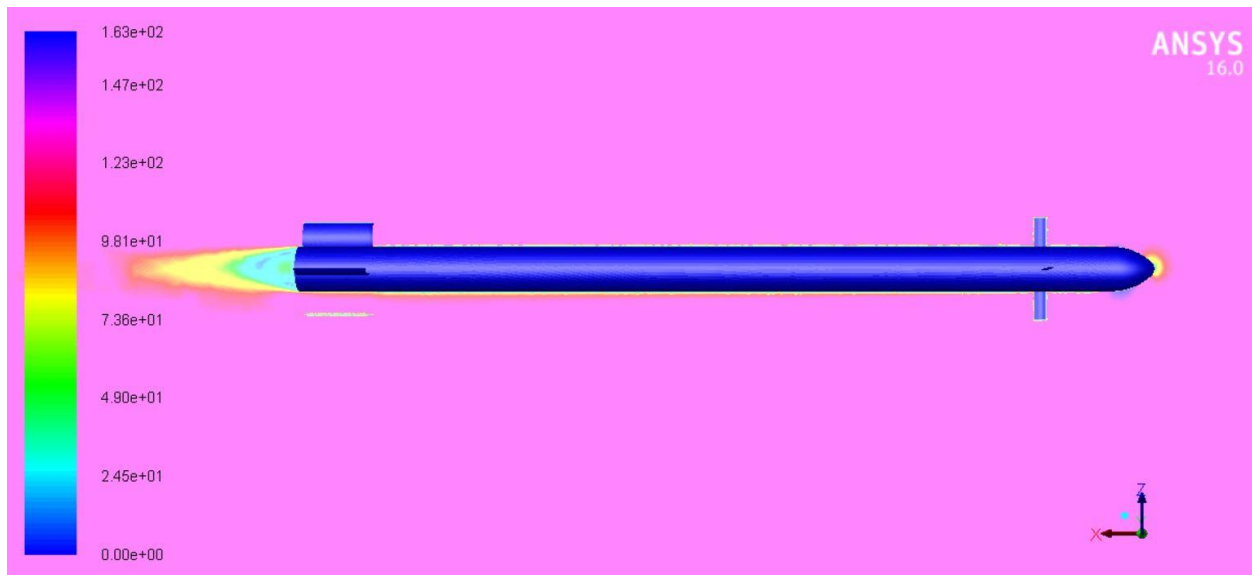


Figure 179 Velocity contours for 15 ° control deflection and angle of attack $\alpha = -6^\circ$

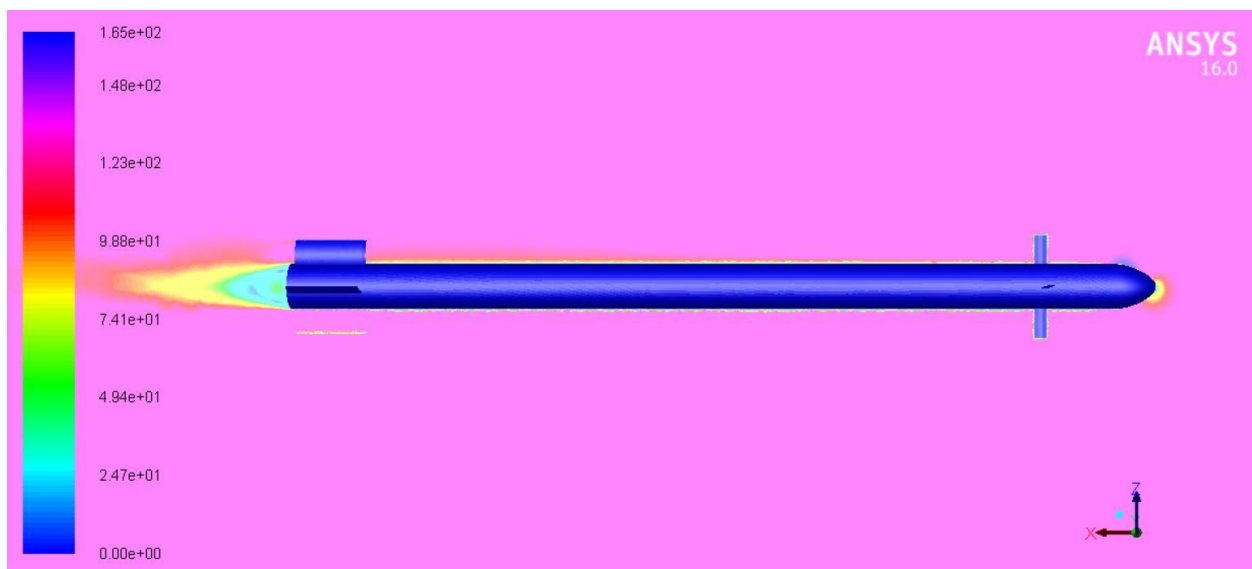


Figure 180 Velocity contours for 15 ° control deflection and angle of attack $\alpha = 8^\circ$

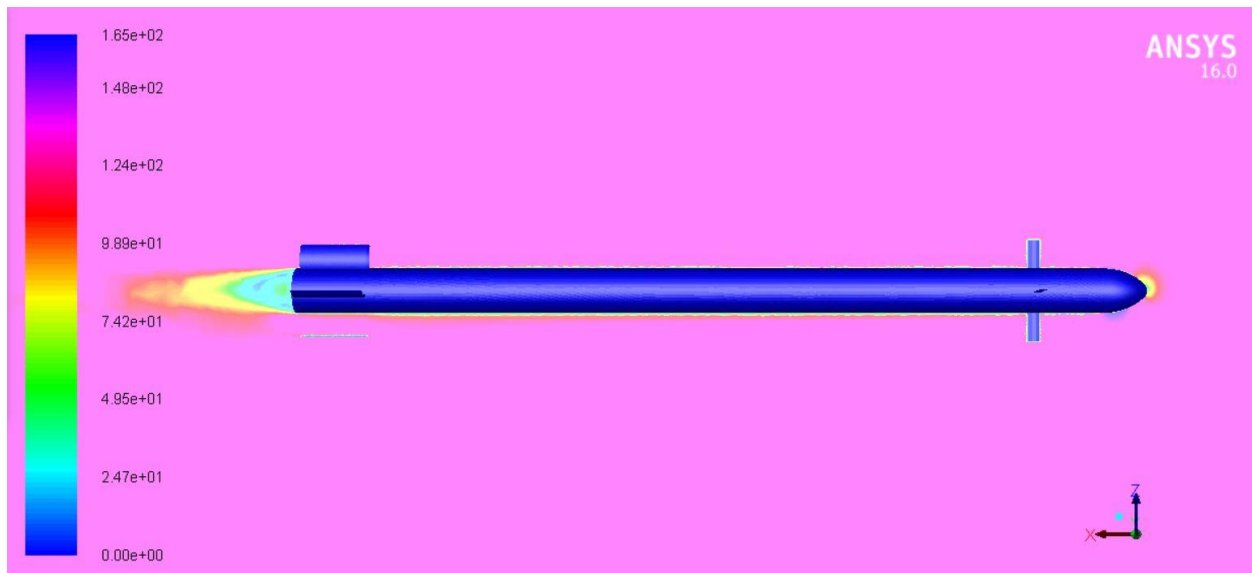


Figure 181 Velocity contours for 15 ° control deflection and angle of attack $\alpha = -8^\circ$

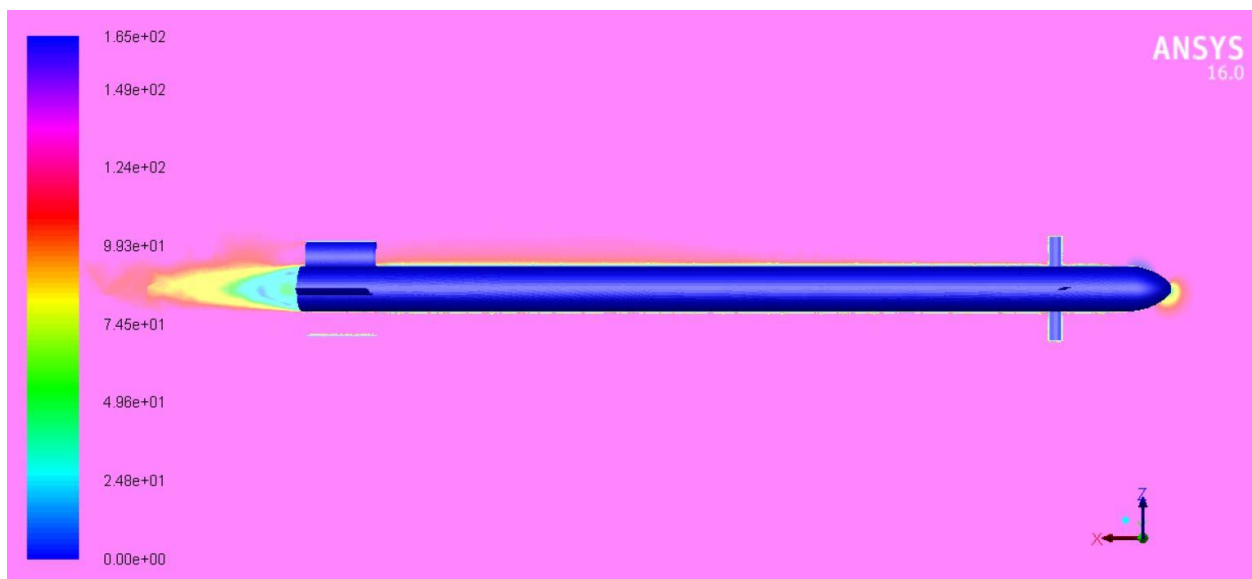


Figure 182 Velocity contours for 15 ° control deflection and angle of attack $\alpha = 10^\circ$

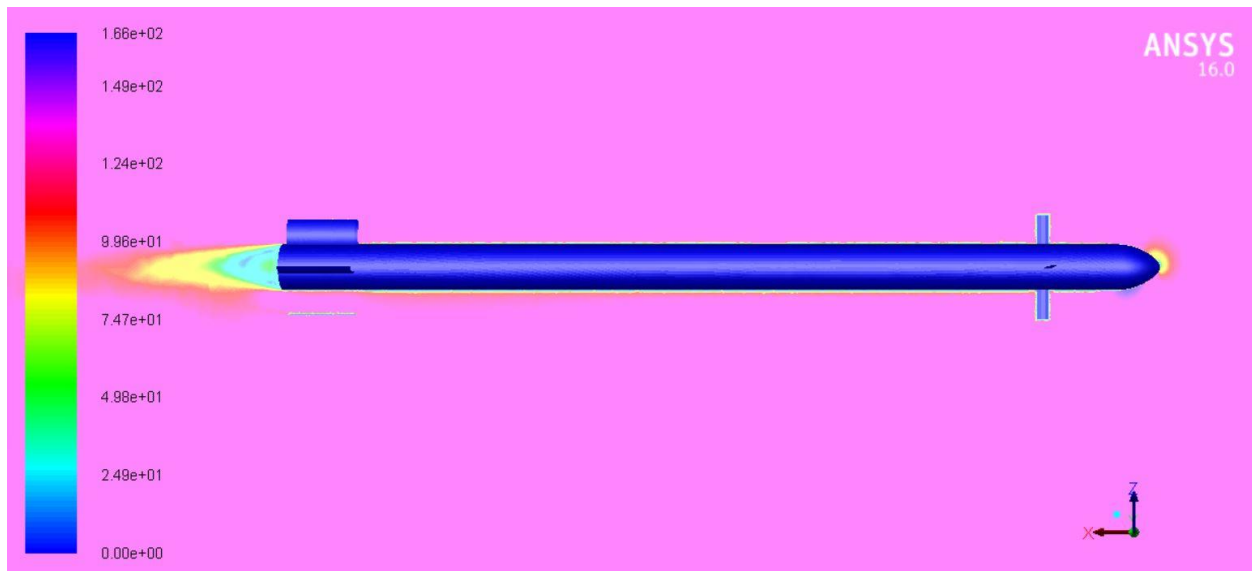


Figure 183 Velocity contours for 15 ° control deflection and angle of attack $\alpha = -10^\circ$

Прилог 1.

Изјава о ауторству

Потписани **Hamad Alkaabi**

број индекса **D35/2015**

Изјављујем

да је докторска дисертација под насловом

АЕРОДИНАМИЧКЕ КАРАКТЕРИСТИКЕ ОСНОСИМЕТРИЧНИХ ТЕЛА У НЕСИМЕТРИЧНОМ СТРУЈНОМ ПОЉУ (AERODYNAMIC CHARACTERISTICS OF AXI- SYMMETRIC BODIES IN NON-SYMMETRIC FLOW FIELDS)

- резултат сопственог истраживачког рада,
- да предложена дисертација у целини ни у деловима није била предложена за добијање било које дипломе према студијским програмима других високошколских установа,
- да су резултати коректно наведени и
- да нисам кршио/ла ауторска права и користио интелектуалну својину других лица.

Потпис докторанда

У Београду, 05.12.2018

Прилог 2.

**Изјава о истоветности штампане и електронске верзије
докторског рада**

Име и презиме аутора **Hamad Alkaabi**
Број индекса **D35/2015**
Студијски програм **Докторске академске студије**
Наслов рада **Аеродинамичке карактеристике осносиметричних
тела у несиметричном струјном пољу
(Aerodynamic characteristics of axi-symmetric bodies
in non-symmetric flow fields)**
Ментор **др Златко Петровић, ред. проф. у пензији**

Потписани **Hamad Alkaabi**

Изјављујем да је штампана верзија мог докторског рада истоветна електронској верзији коју сам предао за објављивање на порталу **Дигиталног репозиторијума Универзитета у Београду**.

Дозвољавам да се објаве моји лични подаци везани за добијање академског звања доктора наука, као што су име и презиме, година и место рођења и датум одбране рада.

Ови лични подаци могу се објавити на мрежним страницама дигиталне библиотеке, у електронском каталогу и у публикацијама Универзитета у Београду.

Потпис докторанда

У Београду, 05.12.2018

Прилог 3.

Изјава о коришћењу

Овлашћујем Универзитетску библиотеку „Светозар Марковић“ да у Дигитални репозиторијум Универзитета у Београду унесе моју докторску дисертацију под насловом:

**АЕРОДИНАМИЧКЕ КАРАКТЕРИСТИКЕ ОСНОСИМЕТРИЧНИХ ТЕЛА У
НЕСИМЕТРИЧНОМ СТРУЈНОМ ПОЉУ (AERODYNAMIC CHARACTERISTICS OF AXI-
SYMMETRIC BODIES IN NON-SYMMETRIC FLOW FIELDS)**

која је моје ауторско дело.

Дисертацију са свим прилозима предао сам у електронском формату погодном за трајно архивирање.

Моју докторску дисертацију похрањену у Дигитални репозиторијум Универзитета у Београду могу да користе сви који поштују одредбе садржане у одабраном типу лиценце Креативне заједнице (Creative Commons) за коју сам се одлучио/ла.

①. Ауторство

2. Ауторство - некомерцијално
3. Ауторство – некомерцијално – без прераде
4. Ауторство – некомерцијално – делити под истим условима
5. Ауторство – без прераде
6. Ауторство – делити под истим условима

(Молимо да заокружите само једну од шест понуђених лиценци, кратак опис лиценци дат је на полеђини листа).

Потпис докторанда

У Београду, 05.12.2018

1. Ауторство - Дозвољаваате умножавање, дистрибуцију и јавно саопштавање дела, и прераде, ако се наведе име аутора на начин одређен од стране аутора или даваоца лиценце, чак и у комерцијалне сврхе. Ово је најслободнија од свих лиценци.
2. Ауторство – некомерцијално. Дозвољаваате умножавање, дистрибуцију и јавно саопштавање дела, и прераде, ако се наведе име аутора на начин одређен од стране аутора или даваоца лиценце. Ова лиценца не дозвољава комерцијалну употребу дела.
3. Ауторство - некомерцијално – без прераде. Дозвољаваате умножавање, дистрибуцију и јавно саопштавање дела, без промена, преобликовања или употребе дела у свом делу, ако се наведе име аутора на начин одређен од стране аутора или даваоца лиценце. Ова лиценца не дозвољава комерцијалну употребу дела. У односу на све остале лиценце, овом лиценцом се ограничава највећи обим права коришћења дела.
4. Ауторство - некомерцијално – делити под истим условима. Дозвољаваате умножавање, дистрибуцију и јавно саопштавање дела, и прераде, ако се наведе име аутора на начин одређен од стране аутора или даваоца лиценце и ако се прерада дистрибуира под истом или сличном лиценцом. Ова лиценца не дозвољава комерцијалну употребу дела и прерада.
5. Ауторство – без прераде. Дозвољаваате умножавање, дистрибуцију и јавно саопштавање дела, без промена, преобликовања или употребе дела у свом делу, ако се наведе име аутора на начин одређен од стране аутора или даваоца лиценце. Ова лиценца дозвољава комерцијалну употребу дела.
6. Ауторство - делити под истим условима. Дозвољаваате умножавање, дистрибуцију и јавно саопштавање дела, и прераде, ако се наведе име аутора на начин одређен од стране аутора или даваоца лиценце и ако се прерада дистрибуира под истом или сличном лиценцом. Ова лиценца дозвољава комерцијалну употребу дела и прерада. Слична је софтверским лиценцама, односно лиценцама отвореног кода.